THE UNIVERSITY *of* EDINBURGH

An experimental study of REE carbonate and fluorocarbonate synthesis as a basis for understanding hydrothermal REE mineralisation

Matthew Holloway

Thesis submitted for the degree of Doctor of Philosophy
The University of Edinburgh
2018

Abstract

Many of the world's economic rare earth element (REE) deposits are formed from, or have been subsequently upgraded by, hydrothermal fluids. Some of the most important REE minerals are the light REE (LREE) enriched fluorocarbonates and carbonates, which are commonly found in carbonatites. Textural and mineralogical evidence from these and other sites point towards wall rock composition as a major control on the observed REE mineralisation, with the supply of carbonate, and possibly fluoride, thought to be the limiting factor. Despite theoretical and experimental studies focussed on REE speciation in hydrothermal fluids, and a few on REE mineral solubility, there remains a lack of understanding of the processes occurring at the fluid-rock interface during REE carbonate and fluorocarbonate mineralisation. Many of the issues surrounding this topic stem from the difficulty of working at elevated temperatures, low REE concentrations, and with the corrosive fluoride ion.

The synthesis of REE carbonates under simple, low temperature conditions is a useful starting point for understanding REE mineralisation, and as such has been the focus of research for decades. Despite this, cross-series trends are rarely assessed together under the same conditions, and multi-REE-bearing systems – useful for assessing REE fractionation – have scarcely been explored. Furthermore, wall rock experiments, whereby REE-rich fluids are reacted directly with carbonate rocks, are absent from the literature. The same is true for systems containing fluoride, necessary for studying the formation of fluorocarbonates. A fuller understanding of REE mineralisation cannot be achieved until empirical experimental results can be compared with theoretical data and field observations.

This thesis documents the laboratory synthesis of single- and multiple-REE-bearing carbonates and fluorocarbonates, and compares the findings with a mineralogical and textural study of two REE-bearing carbonatite deposits. The REEs La, Nd, Gd, Er and Yb were investigated as representatives of the entire series. The experiments constituted titrations of REE chloride solutions with sodium carbonate, and 'wall rock reactions' of REE chloride with dolomite, or dolomite plus fluorite. Batch and flow-through setups were used, and the experiments were performed, or the products aged, at temperatures ranging from ambient to 200 °C.

Products were characterised by techniques such as PXRD and SEM to document their structure and morphology as a function of temperature, and assess the influence of sin-

gle vs multiple REE on the final material (whether mixed or separate phases formed). Results showed that in titration experiments, the LREEs crystallised easily and at low temperatures (as low as room temperature), HREEs either do not crystallise (in some cases even at 200 °C) or are more difficult to crystallise, and mixed LREE + HREE precipitates behaved more like HREE-only examples. The HREEs and LREEs + HREEs mostly produced X-ray amorphous materials, identified as carbonates using FTIR. These were analysed by XAS (XANES and EXAFS) to assess whether they possessed the same short-range structure as the crystalline phase into which are known to form, thus adding to the non-classical nucleation pathway argument as previously suggested for these materials. Results suggested the short-range order of most phases analysed were similar to known bulk phases, but that these were probably different to the earlier precipitates formed in solution. Additionally, in the mixed LREE + HREE systems (Nd+Er), REEs were well dispersed (as opposed to Nd- and Er-rich clusters).

In contrast to the titration results were those of wall rock reactions, in which excellent crystallisation was observed for almost every REE configuration (single- or up to five-REE mix), or ageing duration. All but three of the phases produced were previously described natural or synthetic minerals. When fluorite was included in batch reactions the results were more varied: REE carbonates, fluorides and fluorocarbonates were all observed, but never together in the same sample (except in one example).

A textural and mineralogical assessment of two carbonatite deposits, Bayan Obo, China and Tundulu, Malawi, which were analysed by EMPA, revealed multiple stages of hydrothermal activity, some of which related to REE fluorocarbonate mineralisation. REE fluorocarbonates, identified at both sites, were typically LREE enriched. No REE carbonates or fluorides were observed, despite the presence of fluorite (REE-barren) and carbonates at Bayan Obo, and carbonates (low REE content) at Tundulu. However, at both sites apatite contained considerable REE. The REE fluorocarbonates were not solely associated with carbonate wall rocks, although the Ca-REE fluorocarbonate synchysite was only observed in the significantly more carbonate-rock-rich Tundulu samples. At Bayan Obo, bastnäsite and huanghoite (Ba-REE fluorocarbonate) were observed, the latter of which is reportedly replacing earlier Ca-REE fluorocarbonates.

The results demonstrate the varying behaviour of REEs during precipitation under different conditions, and highlights the influence of dissolved carbonate supply rate to morphology, structure and crystallinity of the products. The occurrence of only one class of REE mineral (carbonate, fluoride or fluorocarbonate) in the synthetic experiments with fluoride may help explain the lack of natural REE carbonates and fluorides – and predominance of REE fluorocarbonates – in hydrothermal systems, as was observed in the natural samples studied. In addition, the lack (absence?) of naturally occurring HREE carbonates and fluorocarbonates in the studied carbonatites

(and the literature) is suggested to result not from factors such as structural constraints, but instead from the relative crustal abundances of the individual REEs. It is shown that HREE carbonates and fluorocarbonates are valid species under certain conditions, but that these are not likely to occur naturally.

Lay Summary

Although not as well known as common metals like iron or copper, the rare earth elements (REEs) are a suite of metals essential for twenty-first century technologies and industry, including as components in smart phones, computers, televisions, wind turbines and fibre-optic cables. As with most other metals, REEs are mined from the ground, but only in places where they occur in high concentrations. The general processes that lead to metal accumulation are known, for example they are commonly deposited/crystallise from hot solutions (hydrothermal), but the specifics for different metals or at different deposits are not well understood.

A common mechanism for metal deposition/accumulation is the interaction of metal-laden fluids with rocks that cause changes in the fluid's chemistry - e.g. dissolution of a carbonate (carbon + oxygen) rock (e.g. calcite) that may neutralise the solution's acidity, which can limit the ability of the REEs to remain in solution. The most important economic REE mineral is bastnäsite, a compound with REE, carbonate and fluoride, which is most commonly found in carbonate-rich environments. Its formation has, therefore, been postulated to occur *via* dissolution of carbonate rocks by REE-bearing hydrothermal fluids. This mechanism is extensively cited in the literature, but surprisingly has not been tested experimentally.

This project presents the results of low temperature (up to 200 °C) hydrothermal experiments designed to synthesise first REE carbonate minerals (not so common in nature), then fluorocarbonates. Two main experimental pathways were taken, both using acidic, REE-rich solutions: 1) REE solutions were mixed with a solution containing a high concentration of dissolved carbonate, followed by ageing at temperature, and; 2) REE solutions were reacted with a carbonate rock (dolomite) at temperature. A modification of the second pathway included the mineral fluorite as a reactant phase, with the aim to form a fluorocarbonate mineral.

The results showed both methods were successful in precipitating REE carbonates, but that in the first setup some of these phases were amorphous (structureless) - i.e. not crystalline. These were probed at the atomic level by high-energy X-rays and shown to possess very similar short-range structures as the bulk phase into which they formed (at higher temperature or after longer ageing durations). Where crystalline material was formed, the morphologies were found to be dependent on the REE(s) used, and the temperature and length of the experiment.

For anyone interested enough to read this.

Declaration

I declare that all work in this thesis, unless otherwise referenced, is entirely my own. None of this work has been submitted for any degree or professional qualification other than that specified on the title page.

Signed: 

Date: 21/05/2018

Acknowledgements

The process of completing this project has been a long and sometimes unpleasant one, and it has taken from me more than I had imagined. Despite this, I am proud to say I have seen it through and am indebted to the following people for helping me get to where I am today.

I start with my supervisors Drs Bryne Ngwenya and Ian Butler. Without their expertise and guidance there is zero chance I would have succeeded. My third supervisor, Prof. Fred Mosselmans (Diamond Light Source), is also owed a big 'thank you' for his patience during our face-to-face, email and telephone correspondence with regard to EXAFS. University of Edinburgh staff I would like to thank are: Drs Nicola Cayzer (SEM), Nic Odling (XRD) and Chris Hayward (EMPA) for the assistance provided on their respective instruments, and Dr John Craven for his help with most other problems I had in the basement.

Natural carbonatite samples from Tundulu were kindly loaned to me by Dr Sam Broom-Fendley (Camborne School of Mines, The University of Exeter), and those from Bayan Obo were loaned from the Natural History Museum, London. A small number of fluorite samples used in the synthesis of REE fluorocarbonates were donated by Dr Linda Kirstein (UoE), who I also thank.

A special thanks is extended to all my colleagues in the Grant attic, especially Rūta, other members of my booth, and my flatmate Alice. I have met many lovely people during my four years in Edinburgh, and I will miss our Friday night excursions to John Leslie's. I must extend a heartfelt thanks to my drinking buddy and good friend Rory McKavney, without who I would not have made it through the worst times. I sincerely hope we remain friends for life.

To all my family and friends in Eastbourne and beyond: thank you for your patience and compassion during the final stages of this project, particularly when the money ran out!

Finally, I thank the Natural Environment Research Council (NERC) for funding this project and providing me the opportunity to gain not only a doctorate, but also experience four wonderful years living in Edinburgh, a city I have loved and will dearly miss.

Abbreviations, acronyms and lengths

UoE	University of Edinburgh
REE	Rare earth element
LREE	Light rare earth element
HREE	Heavy rare earth element
MREE	Middle rare earth element
PXRD	Powder X-ray diffraction
FTIR	Fourier transform infrared spectroscopy
ATR	Attenuated total reflectance
SEM	Scanning electron microscope
EMPA	Electron microprobe analyser
OM	Optical microscopy
HPLC	High performance liquid chromatography
XAS	X-ray absorption spectroscopy
XANES	X-ray absorption near edge structures
EXAFS	Extended X-ray absorption fine structures
PEEK	Poly ether ketone
PTFE	Polytetrafluoroethylene
Viton	Brand of synthetic fluoropolymers
μm	Micron, one millionth of a metre (10^{-6}m)
nm	Nanometre, one billionth of a metre (10^{-9}m)
Å	Ångström, one ten-billionth of a metre (10^{-10}m)

List of contents

List of Figures

List of Tables

Chapter 1

Thesis introduction

1.1 Project rationale

The exploitation of mineral deposits from the Earth's crust has been occurring for thousands of years (Coulson, 2012), but with increasing populations and even faster consumption growth, the world is facing a mineral resource crisis (Kesler and Simon, 2016). In the twenty-first century, no other metals better exemplify this problem than the rare earth elements (REE). Their use in modern technologies and applications has grown exponentially since the start of this century but there are significant geographical and geopolitical issues with their supply (e.g. Humphries, 2013; Golev et al., 2014; Weng et al., 2015).

Although a large number of REE-bearing mineral deposits are known (e.g. Kynicky et al., 2012; Mariano and Mariano, 2012; Jaireth et al., 2014; Goodenough et al., 2015), almost all are currently uneconomical to mine. In 2017, the majority of world supply originates from only a handful of deposits, the most important of which are in China (USGS, 2016). The importance of these metals, combined with the volatility of China's export policy, are driving forces behind their classification as 'critical' by a number of western governments and organisations - a measure of supply shortage concerns vs economic importance. The REEs often top, or sit high up these lists (e.g. European Commission, 2011, 2014).

Although primary magmatic deposits are known (e.g. Mountain Pass, California - Olson et al., 1954), the vast majority, including many of those currently in production, are of indisputable hydrothermal origin, or have been significantly altered/upgraded by hydrothermal processes (e.g. Ngwenya, 1994; Ruberti et al., 2008; Williams-Jones et al., 2012; Smith et al., 2015; Migdisov et al., 2016). Research focussing on the transport mechanisms of REEs in hydrothermal fluids, which exist as metal-ligand complexes, has been ongoing for several decades (e.g. Wood, 1990a; Haas et al., 1995; Migdisov et al., 2002; Mayanovic et al., 2006; Migdisov and Williams-Jones, 2014), and with

advancements in analytical techniques, for example X-ray absorption spectroscopy and molecular modelling, we now have a more comprehensive understanding of these processes.

During the formation of economic REE (and other metal) deposits, hydrothermal mobilisation is only half the story. It is of course important for metals to be fluid-mobile in order for ore-grade deposits to form, but there must also exist processes that lead to their deposition, and importantly accumulation, from these fluids. These processes require the physicochemical properties of the metal-laden fluid to change, thereby destabilising the fluid-mobile metal complexes. Examples include changes in fluid chemistry, including pH, brought about by the mixing of two (or more) fluids, often meteoric, or by dissolution of the rocks through which the fluid is migrating (wall rocks). The latter example highlights the importance of fluid-rock interactions during the concentration of REEs to exploitable grades.

Fluorocarbonates and carbonates of the REEs are some of the most important ore minerals, and provide the majority of the world supply of light REEs (LREEs) (e.g. USGS, 2016). At many of the world's largest REE deposits, the minerals bastnäsite ($REECO_3F$), parisite ($Ca(REE)_2(CO_3)_3F_2$) and synchysite ($CaREE(CO_3)_2F$) are the principal REE ore minerals, along with the phosphate monazite ($REEPO_4$). The carbonates hydroxylbastnäsnite ($REECO_3OH$) and kozoite ($REECO_3OH$) are also mined, but less common; REE carbonates and fluorocarbonates are almost exclusively LREE-enriched. These minerals are most commonly found in REE deposits associated with carbonatites, and often show complex relationships with each other, other REE minerals (e.g. monazite), and wall rocks (e.g. Ngwenya, 1994; Smith et al., 1999; Chakhmouradian and Wall, 2012; Ani and Sarapaa, 2013; Broom-Fendley et al., 2016). These mineralogical and textural relationships have led to various (often site-specific) theories on the behaviour of REEs during hydrothermal alteration/mobilisation and fluid-rock/mineral reactions. A theory suggested in the literature, but for which limited empirical experimental evidence has been collected, is that the dissolution of wall rock(s) triggers REE precipitation by providing the system with 'precipitation ligands' (e.g. CO_3^{2-}), and goes on to suggest that the ore mineral assemblage that forms is ultimately controlled by the chemistry of the wall rocks (Ngwenya, 1994; Migdisov et al., 2016; Trofanenko et al., 2016; Benaouda et al., 2017).

Experimental synthesis of mineral phases - under controlled conditions - provides valuable information on crystallisation mechanisms and pathways, and is essential for the tunable growth of crystals for various nano- and micro-technologies. The aforementioned theory (and others) can be tested by attempting to reproduce the mineral assemblages/textures found at real deposits. These often simple experiments, commonly involving direct mixing of REE-bearing and carbonate-bearing solutions, may also help

elucidate why natural carbonates and fluorocarbonate of REEs are almost exclusively LREE-enriched, despite previous studies having demonstrated that under certain conditions HREE carbonate synthesis is possible (e.g. Liu and Ma, 2007; Tahara et al., 2007; Michiba et al., 2011). Although experiments of this ilk have been ongoing for more than 60 years (e.g. Salutsky and Quill, 1950; Charles, 1965; Nagashima et al., 1973; Hsu, 1992; Liu et al., 1999a; Vallina et al., 2013), the results are difficult to compare because preparation techniques are inconsistent, which appears to have significant influence on the properties of the products (e.g. morphology and crystallinity). In general, the LREEs have been more extensively studied than the HREEs, while data for multiple-REE systems is scarce. This is of particular importance in the twenty-first century given the rise of nano-technologies in which REEs are essential components (e.g. Tan, 2012; Kaczmarek et al., 2015).

Simple mixing experiments are excellent for studying REE carbonate and fluorocarbonate crystallisation mechanisms, but the results are difficult to compare with natural REE mineralisation characteristics because the preparation techniques/conditions between lab and nature are often quite different. Experiments dedicated to rock/fluid interaction in the REE-carbonate-fluorine system, even at temperatures on the lower end of the natural scale, are a logical starting point to bridge this gap, yet their absence from the literature is striking. Such experiments may help to better understand the processes occurring during REE carbonate and fluorocarbonate mineralisation, and lead to more targeted exploration at mine sites, improve REE mineral processing, or have materials science applications *via* the controlled growth of crystals.

1.2 Research questions

The complexity of REE carbonate and fluorocarbonate mineralisation has been touched upon in the opening pages of this thesis, and a number of key areas in which experimental studies are required have been highlighted, including a number of previously hypothesised but as yet under-explored theories. In response, this thesis will address the following research questions:

1. Can carbonates of REE be synthesised *via* the reaction of soluble REEs and a carbonate rock under relatively low (< 200 °C) conditions, with a particular focus on HREE and multi-REE systems?

2. How are the precipitated REE-bearing phases influenced by temperature?

3. Are there differences in the behaviour of REEs when precipitated from a solution containing one REE compared with two or more? Do discrete mixtures of LREE or HREE differ in behaviour from mixtures combining both?

4. Given the experimental difficulties of working with dissolved fluoride at low temperatures (including the low solubility of REE fluoride-bearing minerals), can an experimental method be designed that enables the precipitation of REE fluorocarbonate minerals at low (< 200 °C) temperatures?

5. What do the results of experiments tell us about the conditions/processes occurring during REE accumulation/deposition in natural REE-bearing deposits?

1.3 Objectives and methods

Table 1.1 outlines the objectives of this project and the methods by which they will be achieved. The chapter in which the relevant detail can be found is shown in column three.

Research objective	**Research methods**	**Chapter**
Synthesise carbonates and fluorocarbonates of the REE.	Titration + batch reactions and wall rock experiments.	4, 6, 7
Investigate the effect of heating and ageing on the morphology and crystallinity of synthesised phases.	Vary temperature and ageing duration; characterise samples *via* FTIR, PXRD and SEM.	4, 6, 7
Determine if patterns or trends in the crystallinity and morphology of phases exist/can be identified across the REE series.	Use single- and multi-REE-bearing solutions; characterise products *via* FTIR, PXRD and SEM.	4, 6, 7
Assess the extent to which the local structure of solution- and fresh-precipitates compares with that of aged (amorphous or crystalline) products.	Extended X-ray absorption fine structures analyses.	5
Investigate the role of wall rocks to REE carbonate and fluorocarbonate synthesis during fluid/rock interactions.	Wall rock experiments, including some with a fluoride source.	6, 7
Identify textural relationships between REE minerals and wall rocks in natural carbonatite deposits; compare with experimental data.	Optical microscopy and micro chemical analyses and imaging (SEM, EMPA) of thin sections from two natural carbonatites.	7

Table 1.1: Research objectives and methods of this project.

1.4 Thesis structure

This thesis is presented with the following structure:

Chapter 2 introduces the REE, including their importance, issues and sources. It continues with literature related to the mineralogical and textural relationships between REE carbonates/fluorocarbonates and their wall rocks, and the synthesis of REE carbonate/fluorocarbonate phases.

Chapter 3 outlines in detail the experimental procedures and materials used during the project, and the techniques by which the samples were characterised, including synchrotron-based X-ray spectroscopy and its data processing and modelling procedures.

Chapters 4 through 7 present the project's results. Chapter 4 focusses on the synthesis of REE carbonates though titration-based batch experiments, and explores the influence of temperature and ageing on the products. This chapter also assesses the effect of atomic number on crystallisation by comparing results when using different representatives from across the rare earth series, and also in systems containing multiple REEs.

The local structure/coordination of the REEs during their precipitation from solution and subsequent crystallisation is investigated in Chapter 5. Synchrotron-based X-ray absorption spectroscopy was used in an attempt to explain cross-series differences in crystallinity of the REE carbonates presented in Chapter 4. A hypothesis that bulk crystalline structure is predetermined by that of the clusters/precipitates in solution, or that the precursor phase to mineralisation has the same local structure as the bulk, was tested. This work was undertaken at the UK's national synchrotron, The Diamond Light Source in Oxfordshire.

Chapter 6 focusses on the role carbonate wall rocks play during REE carbonate crystallisation, and presents a method by which these minerals can be synthesised. These experiments, dubbed 'wall rock reactions', involved the reaction of dolomite with a REE-bearing solution in a flow-through setup. As with the previous chapters, the influence of temperature, ageing length and REE content were assessed.

REE fluorocarbonate synthesis is attempted through a continuation of the wall rock reaction theme, this time in the presence of fluoride. The results comprise part of Chapter 7. These experiments involved the reaction of soluble REEs with pellets composed of dolomite plus fluorite. The remainder of this chapter is a mineralogical and textural study of two natural REE-bearing carbonatite deposits, Tundulu, Malawi, and Bayan

Obo, Mongolia. Where possible, comparisons are made between experimental data and the natural samples.

The closing chapter summarises the findings of chapters 4 - 7, collates the data and adds context by comparison with previous works, and ends with a critical evaluation of the project and ideas for future work.

Chapter 2

Background and literature review

2.1 Rare earth elements

2.1.1 Nomenclature

The term 'rare earth metals' (or 'rare earth elements' - REE) is an official term of the International Union of Pure and Applied Chemistry (IUPAC) to define a group of 17 chemically similar elements found in group 3 of the periodic table . It includes the 15 lanthanoides: lanthanum ($_{57}$La), cerium ($_{58}$Ce), praseodymium ($_{59}$Pr), neodymium ($_{60}$Nd), promethium ($_{61}$Pm), samarium ($_{62}$Sm), europium ($_{63}$Eu), gadolinium ($_{64}$Gd), terbium ($_{65}$Tb), dysprosium ($_{66}$Dy), holmium ($_{67}$Ho), erbium ($_{68}$Er), thulium ($_{69}$Tm) ytterbium ($_{70}$Yb) and lutetium ($_{71}$Lu), in addition to scandium ($_{21}$Sc) and yttrium ($_{39}$Y). Although official, 'rare earth elements' is rarely used by geologists and geochemists to describe all 17 elements, and is instead more commonly used as reference to the lanthanides alone, or the lanthanides plus yttrium (often given the abbreviation REY). In the current work, 'rare earth elements' is adopted as a general term when referring to any of the 17 elements.

The REE are commonly split into two (sometimes three) groups based predominantly on their mass and size: the light REE (LREE - La to approx. Sm) and heavy REE (HREE - Eu to Lu plus Y). Neither of these terms are official, with the boundaries varying across the literature. The middle REE (MREE) is a term sometimes used to (roughly) describe the elements Sm to Tb. Figure 2.1 shows the location of the rare earth elements in the periodic table and the common subdivisions of the group.

The names of rare earth minerals, i.e. those in which REEs are essential constituents, are suffixed by the predominant REE within their composition, for examples bastnäsite-(Ce) or bastnäsite-(Y), following the Levinson classification (Levinson, 1966).

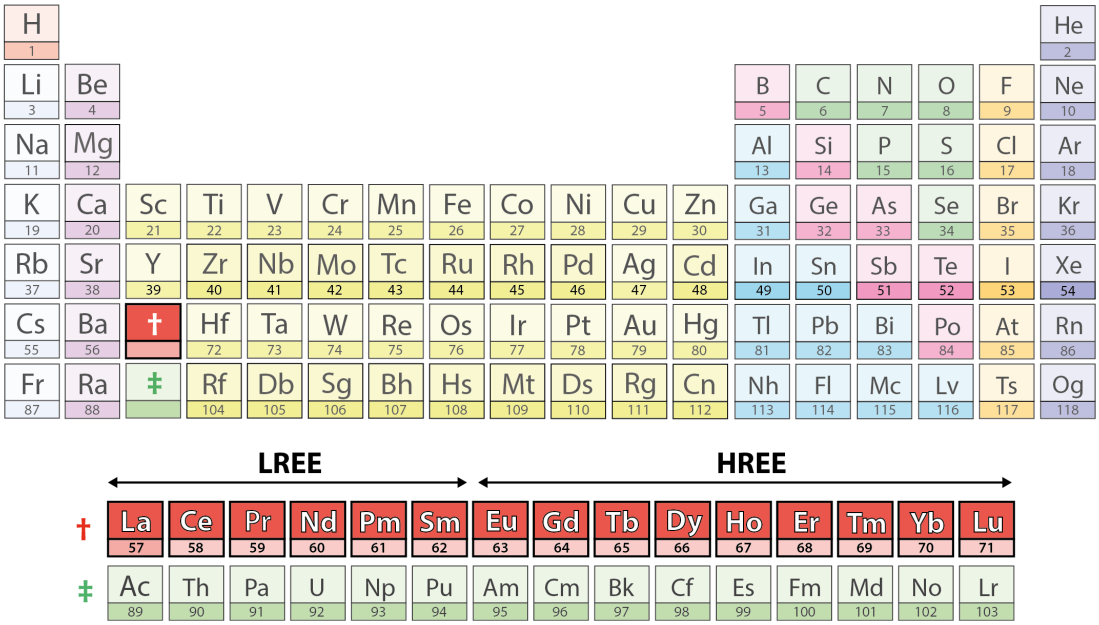

Figure 2.1: Periodic table of the elements. The rare earth elements La - Lu are highlighted (red), and the boundaries of the LREEs and HREEs are shown for reference.

2.1.2 General chemistry/geochemistry

The REEs are the largest group of elements to possess near coherent chemical and physical properties, yet it is their differences that make them so interesting from an academic and industrial perspective.

The general coherency stems from their electronic configuration: electrons are added to the $4f$ sub-shell as one moves across the series (La - $[Xe]4f^{0}5d^{1}6s^{2}$; Lu - $[Xe]4f^{14}5d^{1}6s^{2}$), leaving the outer shells (i.e. those involved in chemical reactions) unchanged. REEs never occur as native metals, nor can they be found as individual elements in minerals. The systematic addition of protons to the nucleus across the series results in an increased nuclear attraction and consequent contraction in ionic radius known as the 'lanthanide contraction' (Henderson, 1984). This change in size has implications for coordination number, which leads to mineral structure and substitution constraints. Fractionation can occur through the preferential incorporation of LREEs or HREEs into minerals; the mineralogy of a deposit therefore becomes a major factor when assessing the economic viability of mining. This is also true because some REE minerals are more difficult to process than others (e.g. carbonates vs oxides). Under most geological conditions the REEs all exhibit a +3 valence, another feature linking their behaviour. Under oxidising and reducing conditions, respectively, Ce may be +4 and Eu +2.

Average upper crustal abundances vary significantly across the series. Most abundant is Ce (63 ppm), while Lu is the least (0.1 ppm) (Rudnick and Gau, 2003). The REE promethium (Pm) is radioactive and has no long-lived isotope.

2.1.3 Uses, supply and demand

REEs are used in a huge number of modern technologies, many of which are essential for the development of low-carbon technologies, industrial processes and military applications (e.g. Charalampides et al., 2015; Kaczmarek et al., 2015). Their superior magnetic, optical, electrical and catalytic properties have been increasingly recognised over the past few decades, with uses now including: permanent magnets in computer hard drives, wind turbines and electric cars; phosphors in LCD televisions; glass polishing and cutting; catalytic converters, and; fluid cracking agents in oil refining (e.g. Alonso et al., 2012; Chakhmouradian and Wall, 2012; Charalampides et al., 2015; Weng et al., 2015). REEs are becoming increasingly important in nano-technologies, e.g. in medicine, electronics, catalysis and even cosmetics (e.g. Tan, 2012; Malathi et al., 2013; Katz et al., 2015). The increased efficiency that comes with incorporation or substitution of REEs has allowed the miniaturisation of numerous technologies synonymous with the twenty-first century (e.g. laptops, smart phones, tablets etc.), resulting in the sparse but widespread distribution of these metals in both Western and emerging markets.

During the twentieth century, demand was met by only a handful of deposits, one of the most important of which was Mountain Pass in California, USA (Castor, 2008). However, since the early twenty-first century, both supply and demand have been monopolised by China (with estimates up to 97 % of production in 2006 – e.g. Weng et al., 2015). In 2010, a year-on-year decrease in Chinese export quotas of 40 % amplified supply concerns, particularly in Western nations, such that these metals have now been classified as 'critical' – i.e. their use in essential technologies, and the risk to their supply, is high (e.g. European Commission, 2011; Golev et al., 2014). Supply deficits saw the prices of REEs dramatically rise, prompting renewed interest in domestic exploration and recycling (e.g. Adachi et al., 2010; Jaireth et al., 2014; Goodenough et al., 2015; Tunsu et al., 2015). Although a large number of deposits have now been identified, the vast majority are uneconomic and as such there is great interest in elucidating the processes by which deposits are 'upgraded' - particularly in the higher value HREEs - as it is hoped this will improve targeted exploration and mineral processing.

2.1.4 REE deposits and minerals

REE deposits occur in a variety of geological environments. Primary magmatic deposits are uncommon, but an example is Mountain Pass, once the most important

REE source in the world (Castor, 2008; Mariano and Mariano, 2012). In these examples, REEs are often incorporated into the rock forming minerals, e.g. carbonates or apatite, in addition to forming REE minerals (see below). More common are deposits of either mixed magmatic-hydrothermal or hydrothermal origin, including carbonatites, alkaline igneous rocks and other hydrothermal deposits unrelated to alkaline igneous rocks/provinces (e.g. Walters and Lusty, 2011; Chakhmouradian and Zaitsev, 2012). Here, REE are most commonly associated with late-stage hydrothermal vein/replacement mineralisation (e.g. Buhn et al., 2002; Ruberti et al., 2008; Xu et al., 2008; Gob et al., 2011; Smith et al., 2015; Mondillo et al., 2016). The REEs may be sourced directly from fluids emanating off an igneous body, or *via* the dissolution of earlier REE-bearing rock-forming phases or accessory minerals. A notable deposit of hydrothermal origin is Bayan Obo, China (currently the world's largest REE deposit).

Examples of sedimentary REE deposits include placers, laterites and ion-adsorption clays. The latter are extremely important because they are highly enriched in HREEs and are very simple to mine/process (Kynicky et al., 2012).

In 1984 it was reported that approximately 70 minerals were known to contain REEs as an essential component (Clark, 1984); by 2012 this had increased to approximately 280 (Chakhmouradian and Wall, 2012), at least 30 of which are described from a single location (Bayan Obo - e.g. Fan et al., 2016). The most important ore minerals are the fluorocarbonate bastnäsite, and phosphates monazite ($LREEPO_4$) and xenotime ($HREEPO_4$) (e.g. USGS, 2016). REEs are also extracted from apatite as a by-product of fertiliser production (e.g. Weng et al., 2015; Broom-Fendley et al., 2016). REEs can substitute into other rock forming or gangue minerals such as calcite, plagioclase, fluorite, zircon and allanite.

2.1.5 REE carbonates and fluorocarbonates

The rare earth carbonate group includes the following 'types' (e.g. Wickleder, 2002; Kaczmarek et al., 2015): normal, basic (or hydroxyl), oxyhydroxylcarbonate, oxycarbonate, dioxycarbonate, ternary and fluoride. Some examples are shown in Table 2.1.

In natural systems the most common occurrence of REE carbonates is as the fluoride mineral bastnäsite, and to a lesser extent synchysite and parisite (e.g. Chao et al., 1992; Samson et al., 2004; Chakhmouradian and Wall, 2012; Smith et al., 2015; USGS, 2016; Benaouda et al., 2017). Non-fluoride REE carbonates are less common (e.g. Maksimovic, 1985; Miyawaki et al., 2000; Graham et al., 2007), and include the minerals lanthanite, tengerite, kozoite and hydroxylbastnäsite. These are the most relevant minerals to the current investigation, and will be mentioned throughout this thesis. The hydroxylcarbonate has several polymorphs, including orthorhombic kozoite and hexag-

onal hydroxylbastnäsite. The former is isostructural with the common mineral ancylite (REE^{3+})$_x$(M^{2+})$_{2-x}$(CO_3)$_2$(OH)$_2$.(2-x)H_2O) (e.g. Dal Negro et al., 1975; Miyawaki et al., 2000; Tahara et al., 2007).

Type	**Formula**	**Mineral Name**
Normal	$La_2(CO_3)_3 \cdot 8\,H_2O$	Lanthanite-(La)
	$Y_2(CO_3)_3 \cdot 2\,H_2O$	Tengerite-(Y)
Basic (hydroxyl)	$NdOHCO_3$	Kozoite-(Nd)
	$NdOHCO_3$	Hydroxylbastnäsite-(Nd)
Oxyhydroxylcarbonate	$Yb_2O(OH)_2CO_3$	-
Dioxycarbonate	$La_2O_2CO_3$	-
	$Dy_2O_2CO_3$	-
Fluoride	$Ce(CO_3)F$	Bastnäsite-(Ce)
	$CaCe(CO_3)_2F$	Synchysite-(Ce)
	$CaCe_2(CO_3)_3F_2$	Parisite-(Ce)
	$BaCe(CO_3)_2F$	Huanghoite
Ternary	$Na_3Y(CO_3)_3 \cdot 3\,H_2O$	Shomiokite-(Y)
	$NaCe(CO_3)_2$	Carboceranite-(Ce)
	$KGd(CO_3)_2$	-

Table 2.1: Examples of REE carbonate and fluorocarbonate phases grouped by type. These include both natural and synthetic examples.

The size of a REE ion dictates its coordination number, and therefore into which minerals it may form/substitute. The lanthanite structure is only able to accommodate REE ions equal to or larger than Nd (i.e. the LREEs), while tengerite is more common for the heavier REEs (although it appears REE ions smaller than Tm cannot form this structure - Miyawaki et al., 1993). In the hydroxyl (basic) group, the orthorhombic 'kozoite-type' structure has been synthesised for REEs La - Er; heavier REEs formed a tetragonal structure (8 coordinated - e.g. Tahara et al., 2007; Vallina et al., 2015). The hexagonal species has also been synthesised for La - Er, but not Tm, Yb or Y (Michiba et al., 2011). The synthesis of REE carbonates and fluorocarbonates is reviewed later in this chapter.

There are more LREE-enriched examples of REE carbonates and fluorocarbonates, although natural examples in which HREEs dominate are known, e.g. tengerite-(Y) ($Y_2(CO_3)_3 \cdot 2{-}3\,H_2O$ - Miyawaki et al., 1993) and bastnäsite-(Y) (YCO_3F - Fleischer, 1972). In addition, there are dozens of examples in which the structure contains ad-

ditional cations and anions, e.g. burbankite-(Ce) ($(Na,Ca)_3(Sr,REE,Ba)_3(CO_3)_5$ - e.g. Nadeau et al., 2015), petersenite-(Ce) ($Na_4(REE)_2(CO_3)_5$ - Grice et al., 1994) and decrespignyite-(Y) ($(Y,REE)_4Cu(CO_3)_4Cl(OH) \cdot 2.5\,H_2O$ - Wallwork et al., 2002). A more in depth discussion of this, including examples, is presented in Chapter 6.

2.2 REE transport and precipitation mechanisms during carbonate and fluorocarbonate deposit genesis

Despite their importance to world REE supply, the conditions at which these minerals form is not well understood, although considerable progress has been made over the past decade or so. During the formation of any metal deposit, the two most important processes to understand are the form in which the metal is transported (i.e. its speciation), and the solubility of any minerals into which it will precipitate. The availability of the ligands (anionic species) required for either solution complexes or precipitation is controlled by the chemistry of the fluid, which itself will be influenced by numerous factors, for example the fluid source, temperature, pressure, pH, mixing with other fluids or interaction with wall rocks. Many of these are closely linked. The following sections review literature on the aqueous speciation of REE, followed by mineral solubility.

2.2.1 Speciation of REEs

The speciation of REE in low temperature solutions (e.g. groundwater, surface water and seawater) has been shown to exert a major control on their behaviour, particularly fractionation of the series *via* adsorption to colloids (e.g. Wood, 1990a; Sholkovitz, 1992; Byrne and Li, 1995; Johannesson et al., 1997). The thermodynamic data required to calculate REE speciation (i.e. formation/stability constants) have been determined at 25 °C and various ionic strengths for a number of important REE-ligand pairings including REE-chloride, -fluoride, -carbonate and –sulphate (e.g. Wood, 1990a; Luo and Byrne, 2001, 2004; Luo and Millero, 2004; Schijf and Byrne, 2004). These were determined using a variety of techniques, including potentiometry, ion exchange, mineral solubility studies and spectroscopy, and agreed values now exist for the majority of these pairings. The values obtained are generally consistent with Pearson's Rule (Pearson, 1963), which predicts the stability of REE complexes with monovalent ligands increases in the order:

$$F^- > OH^- > NO_3^- > Cl^- > Br^-$$

And for those with divalent ligands:

$$CO_3^{2-} > SO_4^{2-} > P_2O_5^{2-}$$

It also predicts that the stability of these complexes will increase with the hardness of the cation (i.e. moving across the series from La to Lu). This prediction is correct for some of these pairings (F^-, OH^-, CO_3^{2-}, $P_2O_5^{2-}$), although there is little difference in stability of REE sulfate, and a decrease in stability of REE-chloride complexes across the series at low T (e.g. Luo and Byrne, 2001; Schijf and Byrne, 2004).

Stability data for REE species necessary for understanding REE mobility in hydrothermal fluids are more difficult to determine. The early attempts were not actually empirical, but were instead extrapolations of low temperature data up to 300 °C (e.g. Wood, 1990b; Haas et al., 1995). These data produced mostly similar patterns to those at low temperature, and became routinely used in the literature to explain REE speciation/behaviour in fluids responsible for REE mineral deposition (e.g. Ngwenya, 1994; Poitrasson et al., 1996; Salvi and Williams-Jones, 1996; Smith et al., 1999; Forster, 2001; Ruberti et al., 2008), with most authors interpreting from the extrapolated data that REEs were invariably transported as fluoride complexes. Mineral deposition was then triggered by destabilisation of the REE fluoride complexes, often believed to occur by deposition of fluorite (a common gangue mineral) after mixing with Ca-rich fluids or interaction with Ca-bearing rocks. However, over the past 20 years, high temperature and pressure experiments utilising UV-vis spectroscopy, X-ray spectroscopy (e.g. XANES - X-ray absorption near edge structure, and EXAFS - extended X-ray absorption fine structures) and TRLFS (time-resolved laser fluorescence spectroscopy) have been undertaken for temperatures up to approximately 500 °C (e.g. Ragnarsdottir et al., 1998; Migdisov et al., 2002; Migdisov and Williams-Jones, 2007; Migdisov et al., 2008; Stepanchikova and Kolonin, 2005; Mayanovic et al., 2009a,b; Loges et al., 2013; Asakura et al., 2015), and although many of these experimentally-derived formation constants have proven to be similar to those predicted by extrapolation from low temperature data, a number of significant differences do exist.

Perhaps the most important of these differences in terms of REE ore deposition was the data for REE chloride and fluoride species. The extrapolated data is now known to have significantly overestimated the stability of REE fluoride complexes, with the difference increasing with temperature and atomic number (Figure 2.2 - Migdisov and Williams-Jones, 2007; Williams-Jones et al., 2012; Migdisov and Williams-Jones, 2014). REE chloride species behave in a similar way to REE fluorides, except their stability is orders of magnitude lower (Figure 2.2). REE sulfate complexes exhibit similar stabilities across the series, with experimental and theoretical predictions mostly in agreement (Migdisov et al., 2008).

To date, no high temperature REE carbonate complex data has been measured, which is important because at ambient temperature they form some of the strongest complexes (e.g. Luo and Byrne, 2004).

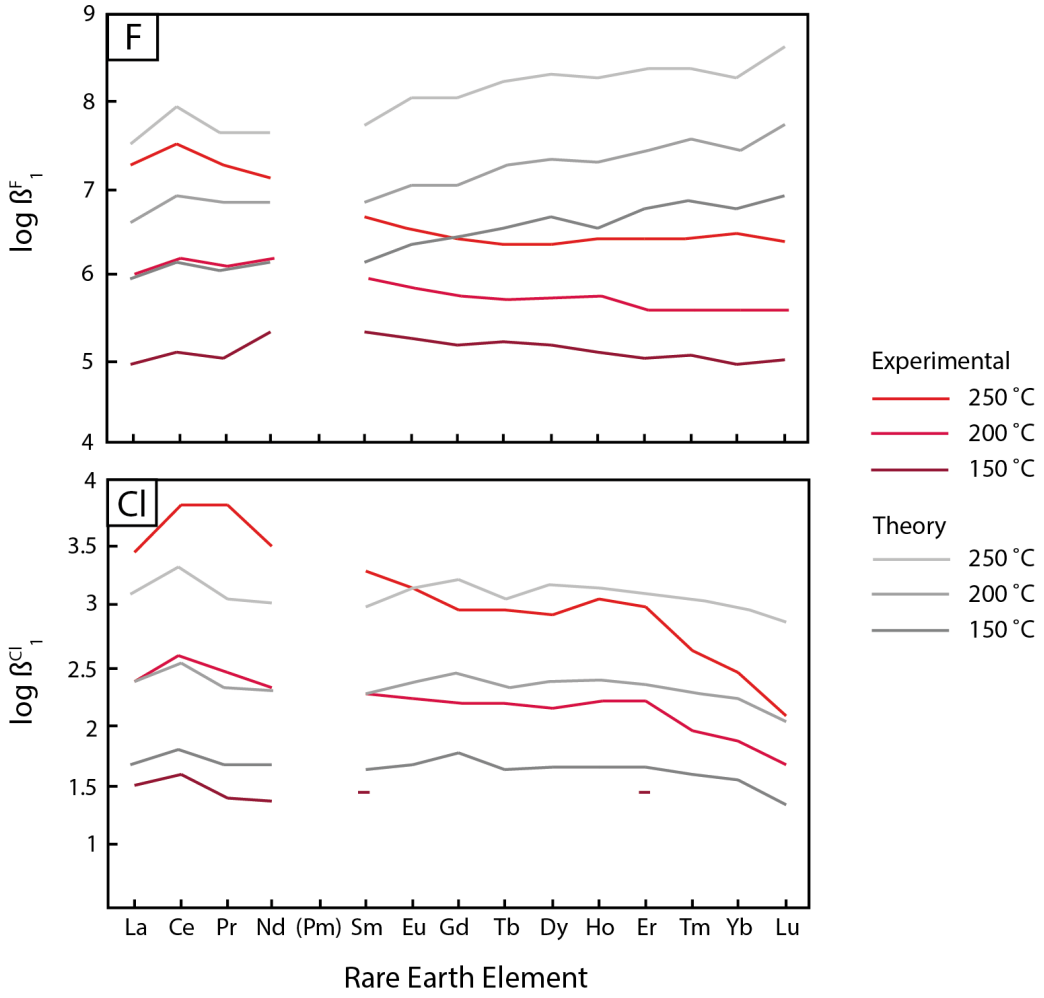

Figure 2.2: Comparison of formation constant values calculated by Migdisov et al. (2009) and extrapolated by Haas et al. (1995) for REE fluoride (top) and chloride complexes (bottom).

2.2.2 REE carbonate and fluorocarbonte mineral solubilities

There are very few studies dedicated to calculating the solubilities or thermodynamic properties of REE carbonates and fluorocarbonates, meaning these minerals cannot be included in modelling hydrothermal REE mobility.

Although few minerals have been studied, REE carbonates, fluorocarbonate and fluorides are known to be highly insoluble. This is evident from the frequent occurrence of minerals like bastnäsite, and to a lesser extent synchysite, parisite, fluocerite ($REEF_3$), hydroxylbastnäsite, kozoite and other carbonates. A recent solubility study of synthetic hydroxylbastnäsite-(La), -(Nd) and kozoite-(Nd) at 25 °C has determined the former two are more stable than the latter, but that the difference between the former two is minimal (Voigt et al., 2016).

Thermochemical properties of natural bastnäsite-(Ce) and parisite-(Ce) were investigated by Gysi and Williams-Jones (2015) at temperatures between 50 and 750 °C. The results were used to construct a quantitative fluid-mineral stability diagram for bastnäsite, parisite, fluocerite and calcite, which revealed the importance of temperature, pH and the activities of fluoride, chloride, calcium and REE on the stability fields of the various minerals.

In a similar study, Shivaramaiah et al. (2016) calculated thermodynamic properties of synthetic bastnäsite-(La) and -(Ce), and of synthetic $LaCO_3OH$ (hex and orth), $CeCO_3OH$ (orth), $NdCO_3OH$ (hex), $DyCO_3OH$ (orth) and YCO_3OH (orth). The results revealed that the lighter the REE, the more stable the minerals, and also that the fluoro-minerals were stable to higher temperatures. This was used as evidence to explain why bastnäsite is a more common mineral than hydroxylbastnäsite.

These data/observations agree with some other studies in which REE flurocarbonates have been synthesised (review in Section 2.3).

2.2.3 REE carbonate and fluorocarbonate depositional mechanisms and models

A fundamental oversight in previous interpretations of REE transport in hydrothermal fluids was the low solubility of REE carbonate, fluorocarbonate and fluoride minerals. Studies reporting the salinity of hydrothermal fluids are common - something routinely accomplished by fluid inclusion studies - but very few have reported the concentrations of REEs or fluoride. One such study, whose data has been used for modelling purposes is that Banks et al. (1994), whose solution chemistry was simplified for modelling by Migdisov and Williams-Jones (2014) to 10 wt.% NaCl, 500 ppm fluoride, 2 wt.% sulfate and 200 ppm Nd. Using data for Nd chloride (Migdisov et al., 2009), fluoride (Migdisov and Williams-Jones, 2007) and sulfate (Migdisov et al., 2008) complexes, it is now shown that the stability fields of REE fluoride complexes are closely matched by those of REE fluoride solids, effectively meaning transport by the former is limited by the low solubility of the latter. Taken together, the revised speciation data and mineral solubilities point to REEs being transported in hydrothermal fluids as complexes with chloride, not fluoride (e.g. Migdisov and Williams-Jones, 2014; Migdisov et al., 2016). However, the presence of fluoride-bearing minerals still requires some soluble fluoride, which is proposed in some systems to be present as undissociated hydrofluoric acid. This HF dissociates once fluid conditions change (e.g. pH or temperature rise). Although few data exist for the solubility of REE carbonates and fluorocarbonates, or for the strength of REE carbonate complexes, carbonate ions are proposed as being important depositional ligands given the predominance of REE fluorocarbonate minerals like bastnäsite.

An important point from the previous paragraph is the influence that ligand availability has on REE mobility. A commonly cited mechanism for chemical change to a solution is the rising of pH by dissolution of carbonate rocks. Not only does this change the pH, but it also provides the system with dissolved carbonate ions necessary for REE carbonate and fluorocarbonate precipitation. An early theoretical study of the $REE(CO_3)F-CaCO_3-F_2(CO_3)-H_2O$ system, conducted using mostly qualitative, literature-sourced data, was that of Williams-Jones and Wood (1992). In that study phase diagrams were constructed, and the stability of phases predicted, with an important conclusion that changes between the different fluorocarbonate minerals cannot occur with changes in the activity of F^- alone, but can do so from variations in either Ca^{2+} or CO_3^{2-} activities. These theoretical interpretations, combined with observations from natural mineral assemblages, highlight the importance of Ca^{2+} and CO_3^{2-} supply when precipitating REE carbonate and fluorocarbonate minerals.

Based on textural relationships and mineral chemistries at the Tundulu carbonatite, Malawi, and following on from the conclusions of Williams-Jones and Wood (1992), Ngwenya (1994) suggested that differences in REE-fluorocarbonate assemblages identified in different classes of carbonatites (calcite-, ankerite- and apatite-carbonatites) resulted from the ability of the wall rocks to supply the hydrothermal system with Ca^{2+} or CO_3^{2-}. Bastnasite was interpreted as forming where this was low (i.e. ankerite carbonatites) and synchysite where it was high. This interpretation also required the existence of a hypothetical aqueous $REECO_3F$ complex, the existence of which has not been proven to this day. Another important study is that of Smith et al. (1999), who studied the reaction relationships between REE fluorocarbonates, REE phosphates, apatite fluorite and calcite at Bayan Obo, China. This study also highlighted the importance of Ca^{2+} or CO_3^{2-} activities, and those of HF^0 and PO_4^{3-}, with the conclusion that transformations between the observed minerals is controlled by the pH of the solution and therefore the buffering capacity of the rocks - i.e. the availability of dolomite/calcite, or by fluoritisation.

Since those studies numerous others have cited the dissolution of carbonate rocks as a mechanism for REE fluorocarbonate (and Ca-fluorocarbonte) deposition, including at the Jbel Boho alkaline igneous complex, Morocco (Benaouda et al., 2017), the Barra Do Itapirapuã carbonatite, Brazil (Ruberti et al., 2008), the Silius fluorite vein system, Sardinia (Mondillo et al., 2016), the Palabor Carbonatite Complex, South Africa (Giebel et al., 2017) and the Nissi bauxite laterite deposit, Greece (Kalatha et al., 2017). Despite the common occurrence of REE carbonates and fluorocarbonates with carbonate rocks, and therefore the implied dependence of the latter on the formation of the former, there are no related empirical experimental data in the literature. This is the basis for the wall rock experiments presented in Chapters 6 and 7 of this thesis.

2.3 Synthesis of REE carbonates and fluorocarbonates

The synthesis of nano- and micro-sized REE carbonates is reviewed by Kaczmarek et al. (2015), and a comprehensive guide to the structures of inorganic REE compounds (including carbonates) can be found in Wickleder (2002). Although studies concerned with the controlled synthesis of REE carbonate and fluorocarbonate phases go back over 60 years (e.g. Salutsky and Quill, 1950), only in the past few decades (e.g. Matijevic, 1988) has this area become so important because the use of REEs in nano- and micro-technologies - particularly for their luminescent properties - requires the REE-bearing material to possess tunable size, shape and crystallinity (structure). Controlled synthesis of these phases under known conditions can help reveal the crystallisation pathways they take on their journey to the most thermodynamically-stable state, which can be used to determine their thermodynamic properties and ultimately be included in geochemical modelling of natural systems. The following is a review of the literature related to the synthesis of first REE carbonates, then fluorocarbonates, with a particular emphasis on works relevant to the current investigation.

2.3.1 REE carbonates

Over the years a number of methods have been used for REE carbonate synthesis, including solution mixing followed by hydrothermal synthesis (e.g. Foger et al., 1992; Shang et al., 2009; Vallina et al., 2015), microwave assisted hydrothermal synthesis (e.g. Ikuma et al., 2002), low temperature urea homogeneous precipitation (e.g. Nagashima et al., 1973; Lu and Wang, 2002; Refat, 2004), ultrasound irradiation (e.g. Jeevanandam et al., 2001), hydrolysis of lanthanide trichloroacetates (e.g. Salutsky and Quill, 1950; Charles, 1965; Wakita and Nagashima, 1972), among others.

Carbonates of all 15 REEs have been synthesised using these methods, however, their morphology, structure and size is known to be highly sensitive to the preparation method (e.g. Rahimi-Nasrabadi et al., 2017). Plates and sheets (e.g. Liu et al., 1999a; Ikuma et al., 2002; Vallina et al., 2013; Rodriguez-Blanco et al., 2014), rods, tubes and needles (e.g. Jeevanandam et al., 2001; Zhang et al., 2009), dendrites (e.g. Shang et al., 2009; Vallina et al., 2014), spheres (e.g. Ikuma et al., 2002; Zhang et al., 2007), 'dumbbell' (e.g. Zhang et al., 2009), cruciform (e.g. Rodriguez-Blanco et al., 2014), triangular pyramids (e.g. Vallina et al., 2014) and 'micro-gears' (e.g. Zhang et al., 2015) are just some of the morphologies produced. A few examples are shown in Figure 2.3. It is also worth noting that in many cases, the products are 'amorphous' in terms of their structures. Factors affecting the size, shape, and crystallinity of the products are numerous and include the concentration and type of reagents used, reaction time and temperature, use of CO_2 atmospheres, the presence of organic ligands or seeds, the drying conditions and even whether or not a solution is agitated.

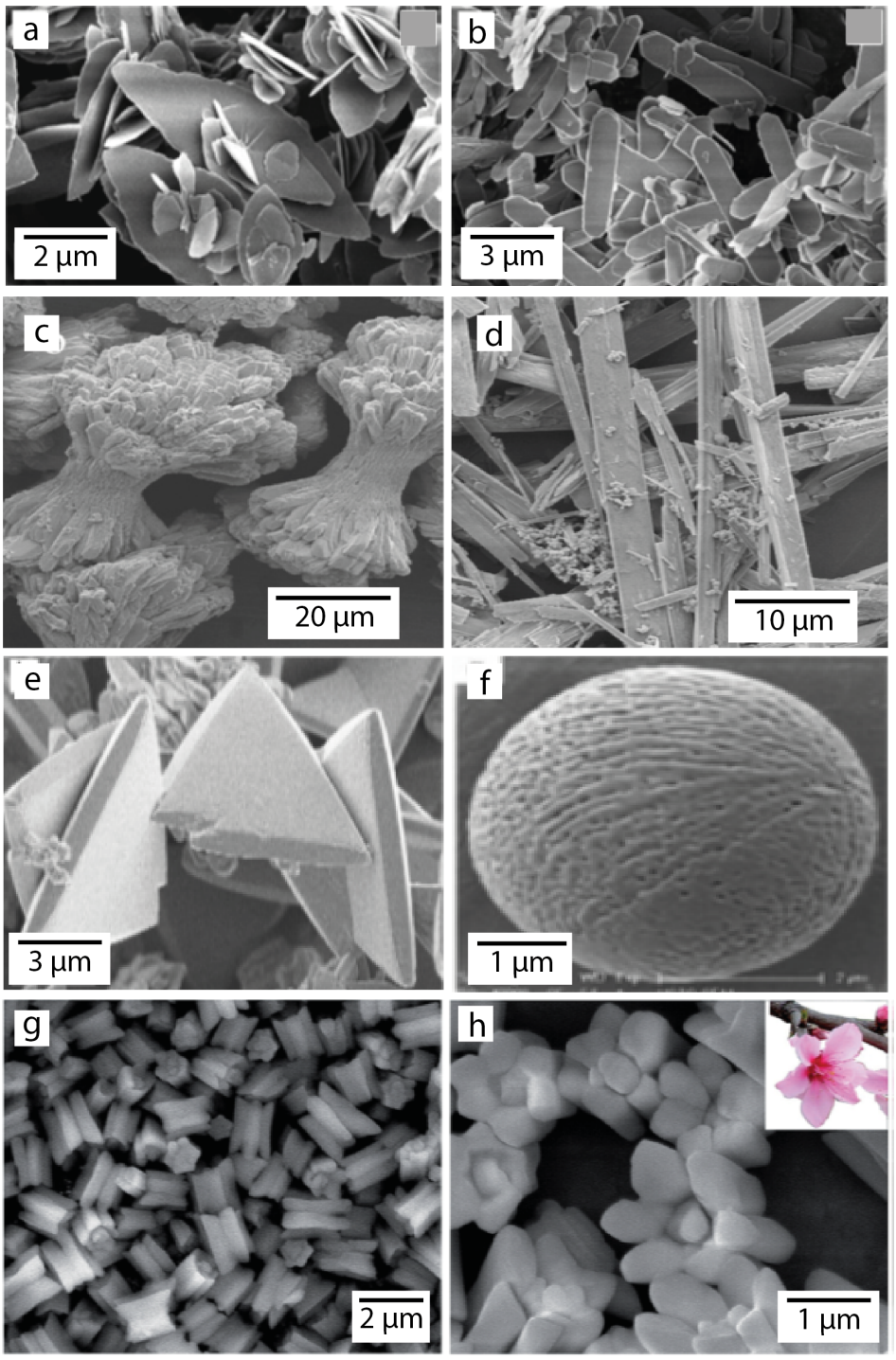

Figure 2.3: SEM images showing example morphologies of REE carbonates synthesised *via* various methods and at different conditions. a and b) plates and cruciform habits of La and Ce lanthanite ($REE_2(CO_3)_3 \cdot 8\,H_{20}$), respectively, formed at 21 °C and after 17 hours of a REE nitrate and sodium carbonate solution being mixed (images from Rodriguez-Blanco et al., 2014); c and d) 'dumbbell' YCO_3OH and acicular tengerite ($Y_2(CO_3)_3 \cdot 2{-}3\,H_2O$) formed by heating a Y nitrate solution in the presence of urea at 150 °C for 22 hours - the dumbbell morphology was formed when the ratio of Y nitrate to urea was 1:1, and the acicular crystals formed at a ratio of 1:3 (images from Zhang et al., 2009); e) triangular pyramids of Nd hydroxylbastnäsite (hexagonal $NdCO_3OH$) formed by heating a mixed solution of Nd chloride and sodium carbonate in a pre-heated oven at 165 °C for one week (image from Vallina et al., 2014); f) spherical La hydroxylbastnäsite formed after heating a mixture of urea and La nitrate at 230 °C for 8 hours (image from Zhang et al., 2007); g and h) 'micro-gear' morphology La hydroxylbastnäsite formed after mixing of a La nitrate solution with one containing glycerol and urea, and heating at 200 °C for 6 hours (image from Zhang et al., 2015).

One of the most common methods for the synthesis of REE carbonates is the mixing of two solutions, one containing an alkali carbonate/bicarbonate and the other soluble REEs (e.g. as nitrates or chlorides), followed by ageing, often at temperature. In a series of papers, Lui & Ma (and sometimes additional authors) were able to precipitate normal carbonates of Ce, Nd, Eu, Tb, Ho, Y and Er by mixing REE chloride solutions with ammonium bicarbonate and leaving at room temperature (RT) for one week (Liu and Ma, 1996a,b; Liu et al., 1999a,b, 2000; Liu and Ma, 2007). The authors chose ammonium bicarbonate for the precipitant as they noted the products were always crystalline when analysed by PXRD, unlike some previous studies using alkali carbonates . The results of their investigations revealed the lower atomic number (Z) elements (Ce and Nd) were most similar in structure to lanthanite (e.g. $La_2(CO_3)_3 \cdot 8\,H_2O$) and the middle to high Z REEs (Eu, Tb, Y, Ho and Er) had a tengerite-type structure ($REE_2(CO_3)_3 \cdot 2{-}3\,H_2O$). When using the REEs Yb and Lu (Liu and Ma, 1997b,a), a hydrated basic or oxyhydroxide carbonate was formed, e.g. $Yb_2(OH)(CO_3)_2 \cdot 5\,H_2O$. The Lu example was crystalline enough to produce Bragg peaks when analysed by PXRD, but the SEM revealed plate-like morphologies admixed with fine-grained 'amorphous' material.

In a similar style, Foger et al. (1992) precipitated REE carbonates (La, Ce, Sm, Tb, Er and Yb) using either ammonium bicarbonate or sodium carbonate added to rare earth nitrate solutions. However, in contrast to the results described above, this investigation found that using ammonium bicarbonate did not form crystalline products, but when using sodium carbonate all the phases were mixtures of hydroxycarbonates and normal carbonates. The only exception was La, which formed a normal carbonate using either precipitant. The use of Na_2CO_3 afforded normal crystalline carbonates of La, Sm, Tb and, in contradiction to some other studies (e.g. Nagashima et al., 1973), Yb. The Sm and Tb examples were hydrated with approx three water molecules each, giving them tengerite-like formulae. Their hydration indicates that heavier REEs are harder to dehydrate, something also noted by Charles (1965). Cerium was found to precipitate as $CeOCO_3$ using either precipitant.

Using higher pressures and temperatures, Christensen (1973b) synthesised the hydroxylcarbonates of La, Nd and Sm using potassium bicarbonate as precipitant, and solved the crystal structure of the Nd variety. The products were washed with CO_2-saturated water and then heated in Ag-lined pressure vessels at between 300 °C (La and Sm) and 420 °C (Nd) for 48 hours. The products, $REE(OH)CO_3$, had hexagonal structures (i.e. the mineral now known as hydroxylbastnäsite).

Nagashima et al. (1973), having noted the variability of products obtained *via* different methods of REE carbonate precipitation in the literature, decided to conduct a comparative study of the most popular methods. They chose precipitation by alkali carbon-

ate/bicarbonate, hydrolysis of trichloroacetates, and heating urea and REE solutions. Their experiments were carried out over a range of temperatures from 25 to 130 °C, and the results showed that five different types of carbonates formed: tengerite-type; lanthanite-type; monoxocarbonates; double carbonates and X-ray amorphous material (identified as carbonate based on IR spectra). The use of alkali carbonates/bicarbonates as precipitant in producing 'double (or ternary) carbonates' has also been reported by other authors (Quill and Salutsky, 1952; Refat, 2004). Interestingly, it was shown that the product composition was influenced by temperature but was independent of the precipitation method, with the exception of the double carbonates that only formed when Na_2CO_3 was used. These results are clearly in contradiction to the other studies mentioned here. The results of that study are summarised in Figure 8.3.

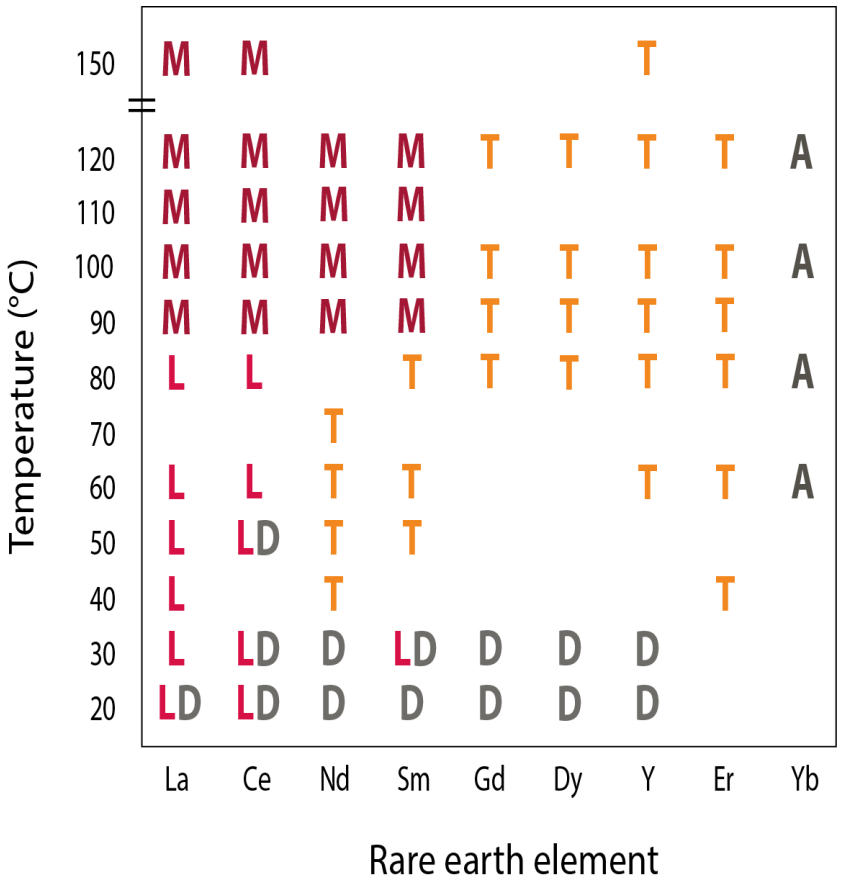

Figure 2.4: Summary of the results obtained by Nagashima et al. (1973) for each of the REE at different temperatures using the methods described in text. The results highlight the different structures formed as a function of REE Z and temperature. M = monoxocarbonate; T = tengerite; L = lanthanite; D = double carbonate (e.g. hydrated carbonate of REE anf Na); A = amorphous.

In general, the lower Z elements form lanthanite-type and monoxocarbonate-type structures at lower and higher temperatures respectively, and the higher Z elements form tengerite-type structures from around 40 °C upwards. The highest Z REE in their study, ytterbium, was always found to produce X-ray amorphous material.

Even from the few studies cited here, the complexity and sensitivity of the products to the preparation method is highlighted. However, a general trend does appear to be increased difficulty when crystallising carbonates containing the heavier REEs, which is also evident by the number of published studies working with La and Nd compared with some of the HREEs.

In a series of recent studies, the crystallisation pathways of La, Ce, Pr, Nd and Dy carbonates have been investigated (Vallina et al., 2013, 2014; Rodriguez-Blanco et al., 2014; Vallina et al., 2015), which were precipitated by mixing solutions of REE chlorides or nitrates with sodium carbonate. Unlike the other studies mentioned above, these also studied the material straight after solution mixing (i.e. the fresh or non-aged precipitate), and found it to be 'amorphous' in all cases. Transmission electron microscopy (TEM) revealed this material to consist of 10-20 nm spheres. The lifetime of this material varied: that composed of the lightest REE (La) only remained stable for about two minutes when left in the mother solution at room temperature, whereupon the sole product was lanthanite, whereas that composed of the heaviest REE studied (Dy) was stable for more than 24 hours. In fact, the authors noted a linear relationship between REE Z and lifetime of this 'amorphous' phase for the REEs studied. This adds further to the idea of HREEs being more difficult, i.e. requiring more energy or time to crystallise.

When heated in solutions the 'amorphous' phase went on to crystallise. In La experiments the sequence was lanthanite, followed by kozoite (orthorhombic $REECO_3OH$) and finally hydroxylbastnäsite (hexagonal $REECO_3OH$); Nd followed the same pathway but with tengerite forming between lanthanite and kozoite (Vallina et al., 2015); Dy formed tengerite, then kozoite (no hexagonal phase was detected - Vallina et al., 2013). This led the authors to propose a crystallisation pathway controlled by dehydration, the rate of which was also shown (in the Nd system) to influence the morphology of the crystals (Vallina et al., 2014).

Precipitation of REE carbonates from solutions containing more than one REE are less common and a more recent endeavour than single-REE synthesis. However, the luminescent properties of a few REEs (e.g. Eu, Tb) means their doping into different REE carbonate types is becoming more common, with the structure of the host known to influence the efficiency of desired properties (Kaczmarek et al., 2015). The hexagonal dioxycarbonate has been shown to be the most suitable host for phosphors (Kaczmarek et al., 2015). A study by Zhou et al. (2015) synthesised Eu doped normal carbonate of Tb (tengerite structure) *via* reaction of ammonium bicarbonate and various ratios of Tb and Eu chloride at 60 °C for one week, producing 'dumbbell'-shaped crystals. As with single-REE experiments, the crystal size and morphology was influenced by the

reaction duration and reagent concentrations (in this case the ammonium carbonate). However, the authors did not note a change in morphology resulting from up to 15 % molar ratio doping of Eu. These authors did not make any measurements of the early-formed material (i.e. only aged).

A similar study (Lechevallier et al., 2010), this time with the carbonate prepared *via* urea-assisted precipitation of REE nitrates at 85 °C, doped Eu into Gd carbonate (normal - tengerite structure). These authors studied the morphology/crystallinity as a function of time, and noted the same 'amorphous' spherical phase after 2 hours, which had crystallised to Gd tengerite after 7 hours.

A few additional examples of Eu- and Tb-doped carbonate phases include $CeCO_3OH$ (Qian et al., 2012), $Y_2(CO_3) \cdot xH_2O$ (Chang et al., 2011) and $Y_2O_2CO_3$ (Koyabu et al., 2006).

These results provide a framework on which to base an investigation into the behaviour of heavier REEs, and assess whether the linear relationship of increasing dehydration energy with REE Z holds. The nature of the X-ray amorphous precursor phase is also of interest, as it is currently unknown whether the first crystalline phase in the sequence forms *via* the dissolution-precipitation of the amorphous phase, or transforms directly from it. It is also unclear from the previous results whether this material possesses short-range order comparable to that observed for crystalline materials, as previously shown for the $CaCO_3$ system (e.g. Dietzsch et al., 2017). These areas of research make up the first half of this thesis.

2.3.2 REE fluorocarbonates

According to a review of natural and synthetic fluoride carbonates (Grice et al., 2007), there were 22 of these minerals in 2007, 17 of which contained essential REEs (i.e. were REE minerals), although this number is higher today (e.g. Biagioni et al., 2013; Lin et al., 2015). There are significantly fewer studies devoted to the synthesis of REE fluorocarbonates compared with REE carbonates, and of those undertaken only a handful have been conducted at low temperatures (i.e. < 150 °C). The earliest study was that of Jansen et al. (1959), who successfully synthesised La and Ce bastnäsite by heating (in a steam bath) La or Ce carbonate in distilled water, adding dilute hydrofluoric acid and bubbling through CO_2, conducted over five days. The products were pure, and when using equal amounts of La and Ce in the starting solution, produced a bastnäsite with 1:1 ratio of these REEs. This method was later used (Pradip et al., 2013) to synthesise about 1 g of product, with which they calculated the solubility product and the stability constant, and proposed a speciation diagram (for the Ce-F-CO_3 system at 25 °C).

One of the few other studies conducted at < 100 °C is that of Shivaramaiah et al. (2016). La and Ce fluorobastnäsites were synthesised *via* urea hydrolysis in the presence of NH_4F at 90 °C for 20 hours. Using high-temperature calorimetry (700 °C), the enthalpies of formation were calculated, which when compared with data for some $REECO_3OH$ (orthorhombic and hexagonal), suggested the fluorobastnäsites to be more stable than their OH counterparts.

The conclusions of Shivaramaiah et al. (2016) support earlier work (e.g. Haschke, 1975; Hsu, 1992). Haschke (1975) investigated the hydrothermal phase equilibria along an isobaric and isothermal section of the La-OH-F-CO_3 system. The author first synthesised a hydroxylbastnäsite by hydrolysis of a normal carbonate of La, then studied the effects of fluoride, heat and pressure on this phase. The hydroxylbastnäsite was heated at 600 °C and 1200 atm in the presence of variable concentrations of NH_4F for up to 14 days. The results indicated that a complete solid solution exists between the OH and F end members, $La(OH)_{1-x}F_xCO_3$, but only when x is ≤ 1. For ≤ 1 x ≤ 3, carbonate begins to be replaced by fluorine, resulting in two phases, $LaFCO_3$ and LaF_3. At x ≥ 3, the only phase formed was LaF_3. The study concluded that mixed phase OH-F members do not form, or do so with difficulty, owing to the high degree of disorder in the structure.

Hsu (1992), studied the (Ce,La)−F−H−C−O system, hoping to better constrain the temperature at which fluorobastnäsites of La and Ce formed, including their OH counterparts. Cerium or lanthanum oxalate was heated at 580 °C and 1 kbar for one week in the presence of natural bastnäsite (from Mountain Pass) in order to synthesise the hydroxylbastnäsites. Fluorocarbonates were prepared in the same way but with the addition of HF. These phases were heated to 900 °C to assess their stability relationships. The $La(OH)CO_3$ and $LaFCO_3$ phases were stable up to 810 and 860 °C respectively; the Ce members were less stable owing to the influence of oxygen fugacity of the system (redox between Ce^{3+} and Ce^{4+}). The OH version was stable to 640 or 660 °C and the F member between 760 to 800 °C depending on the oxygen buffer used. IR spectra of these phases revealed additional bands in the OH members, attributed to changes in local symmetry as F replaces OH. The study concluded that the fluorobastnäsites are stable to higher temperatures than their OH counterparts, and that the former are able to form in environments low in F while the latter only occur when the system is essentially devoid of this element.

More recent high temperature (700 °C) synthesis of REE fluorocarbonates have synthesised 'pure' bastnäsite for REEs up to Eu, in addition to various Ba-fluorocarbonate minerals, e.g. huanghoite ($BaREE(CO_3)_2F$) and cebaite ($Ba_3REE(CO_3)_5F_2$) (Corbel et al., 2001).

The absence of lower temperature studies focussed on the synthesis of HREE or multi-REE fluorocarbonates is used in this thesis as the basis for the experiments presented in Chapter 7.

Chapter 3

Materials and methods

3.1 Introduction

In the review of REE carbonate synthesis outlined in the previous chapter, it is apparent that a large number of variables in the preparation technique exist, which clearly have significant influences on the characteristics of the products. When fluoride is introduced, the complexity of the system is increased because under different conditions it can either form strong complexes with REEs, facilitating transport, or act as a precipitation ligand, promoting REE precipitation (e.g. Migdisov et al., 2009; Migdisov and Williams-Jones, 2014; Migdisov et al., 2016). This makes the recreation of REE- and F-bearing fluids extremely challenging at temperatures thought to be applicable during REE carbonate and fluorocarbonate mineralisation/alteration (hydrothermal range, up to approx. 400 °C). Additionally, the corrosive effects of fluoride on a wide range of commonly used lab materials (e.g. glass or steel) requires construction of equipment from suitable materials.

This chapter presents the experimental techniques and procedures used throughout this thesis to synthesise REE carbonates and fluorocarbonates. The majority of experiments completed during this project fall under three broad categories:

1. titration of REE chloride solutions with sodium carbonate, followed by ageing at temperatures up to 200 °C;

2. batch and flow-through reactions of REE chloride solutions with dolomite chips conducted at temperatures up to 200 °C (wall rock reactions);

3. batch reactions between REE chloride solutions and pellets made of dolomite + fluorite, at 90 °C.

The rationale was twofold:

1. previous and current literature has focussed/is focussing on the crystallisation pathways and mechanisms of REE carbonates represented by experimental setup 1 (as outlined in the previous chapter). The current project aims to build on those data, including using synchrotron-based X-ray absorption spectroscopy to probe (potential) structural evolution from nucleation to bulk carbonate, and;
2. reaction of REE-bearing fluids with rocks commonly associated with real REE deposits (e.g. dolomite) provides empirical evidence that might be useful for comparison with theoretical predictions and observed mineral assemblages at real deposits. Experiments of this nature were almost absent from the literature.

In addition to these experiments, a number of samples from two natural REE fluorocarbonate mineral-bearing carbonatite deposits were studied: the Bayan Obo deposit, China, and the Tundulu Carbonatite Complex, Malawi. The former were obtained on loan from the Natural History Museum (NHM), London, having been collected in the late 1990s, while the African samples were collected in 2013 by Sam Broom-Fendley, a colleague based at the Camborne School of Mines (The University of Exeter), Cornwall. Mineralogical and textural relationships from these were compared with the results of the synthetic experiments.

This chapter details the experimental methods and reagents used in the production of all synthetic research materials, and the techniques by which these and the natural samples were characterised. More details on the specific experimental matrices are presented in the relevant data chapter.

3.2 Research materials

3.2.1 Rare earth elements

During this project the REEs La, Nd, Gd, Er and Yb were used as representatives of the light, middle and heavy REEs. This provided the opportunity to study both the behaviour of end members, and any potential fractionation/change in behaviour when individual REEs were in the presence of others. These elements also include lower (La) and higher (Nd, Er, Yb) value REEs.

All REE salts used/purchased were of at least 99.9% purity. Sesquioxides (i.e. REE_2O_3) were used in the production of stock REE chloride solutions, from which all subsequent REE-bearing solutions used in this project were made. 'Normal', hydrated REE carbonates (i.e. $REE_2(CO_3)_3 \cdot xH_2O$) and anhydrous fluorides (i.e. $REEF_3$) were purchased for use as standards during synchrotron work.

Table 3.1 outlines the purity and source of all salts used during this project.

Name	Formula	% REO	Supplier
Lanthanum (III) oxide	La_2O_3	99.9	Fisher Scientific
Neodymium (III) oxide	Nd_2O_3	99.9	Fisher Scientific
Gadolinium (III) oxide	Gd_2O_3	99.9	Fisher Scientific
Erbium (III) oxide	Er_2O_3	99.9	Fisher Scientific
Ytterbium (III) oxide	Yb_2O_3	99.9	Fisher Scientific
Lanthanum (III) carbonate hydrate	$La_2(CO_3)_3 \cdot xH_2O$	99.99	Alfa Aesar REacton
Neodymium (III) carbonate hydrate	$Nd_2(CO_3)_3 \cdot xH_2O$	99.9	Alfa Aesar REacton
Erbium (III) carbonate hydrate	$Er_2(CO_3)_3 \cdot xH_2O$	99.99	Alfa Aesar REacton
Ytterbium (III) carbonate hydrate	$Yb_2(CO_3)_3 \cdot xH_2O$	99.9	Alfa Aesar REacton
Lanthanum (III) fluoride anhydrous	LaF_3	99.9	Alfa Aesar
Neodymium (III) fluoride anhydrous	NdF_3	99.9	Alfa Aesar
Erbium (III) fluoride anhydrous	ErF_3	99.9	Alfa Aesar
Ytterbium (III) fluoride anhydrous	YbF_3	99.9	Alfa Aesar

Table 3.1: Formula, purity and supplier of all REE materials used throughout this investigation

Stock REE chloride solutions were made to 0.2 M. This high concentration was chosen so that solutions containing multiple REEs could be mixed without diluting the individual REE to levels too low to use experimentally (i.e. to ensure adequate product yields). They were prepared by fully dissolving an accurately weighed aliquot of REE_2O_3 in concentrated HCl (Fisher, analytical reagent grade), evaporating this to dryness (producing the $REECl_3$ salt), then dissolving the products in the appropriate volume of 0.1 M HCl. The 0.1 HCl stock solution was itself prepared by diluting concentrated HCl in deionised water (18.2 $M\Omega \cdot cm$). The final pH of each REE chloride solution was between 0.8 and 0.9. Although such a low pH is undesirable given the extra buffering required, it was chosen to avoid hydrolysis of the REE. All solutions were stored in plastic bottles and kept in a cool, dark cupboard. Two sets of stock solutions were made for each REE during the project: one at the beginning (September 2013), and the other when that ran out (this was typically about the same time for all elements, somewhere around two years into the project). REE concentrations were not directly measured (e.g. by ICP-MS) at any point, and as such any evolution of the concentration (e.g. as a consequence of adsorption to the bottle) cannot be stated.

Chloride-rich, as opposed to fluoride, carbonate or sulphate solutions were chosen as the REE-bearing media for several reasons. The first is the common occurrence of chloride-rich fluids with hydrothermal/magmatic-hydrothermal-fluid-derived ore deposits of other metals (e.g. Cu-Zn-Pb VMS deposits; Zn-Pb SEDEX or MVT deposits; Cu-(Mo) porphyry deposits; uranium deposits), as demonstrated by fluid inclusion data (e.g. Poty and Pagel, 1988; Wilkinson, 2010; Gregory, 2017). The second is the highly

insoluble nature of REE fluorides and carbonates (e.g. Firsching and Mohammadzadel, 1986; Migdisov and Williams-Jones, 2007; Voigt et al., 2016), opposed to the high solubility of REE chlorides. Recent experimental work (Migdisov and Williams-Jones, 2014) has also indicated that REE chlorides are likely the most important species in the transport of REEs in ore-forming fluids.

3.2.2 Precipitation ligands

3.2.2.1 Carbonates

Consultation of the literature on REE carbonate synthesis reveals one of the most common choice for a dissolved carbonate ion source to be sodium carbonate (Na_2CO_3). In the current investigation, Na_2CO_3 was chosen to build upon recent experiments (e.g. Vallina et al., 2013, 2014; Rodriguez-Blanco et al., 2014) and hence provide comparable results. Using Fischer Scientific analytical grade Na_2CO_3 and deionised water, a stock 0.15 M solution was made; the pH of this solution was not measured. These solutions were stored in plastic bottles, but were made more frequently than the REE solutions (as more volume was used); solutions were typically made at the beginning of each set of experiments (daily). The concentration was chosen to ensure high yields from the experiments (i.e. the carbonate ion concentration was a minimum of 1.5 times that of the REE solutions). Results from the titration experiments completed during this project are presented in Chapters 4 and 5.

When designing the fluid-rock reaction experiments, the literature was reviewed on natural REE carbonate and fluorocarbonate mineral assemblages; the most common associated carbonate minerals are calcite and dolomite. Using this, a preliminary experiment involving the reaction of calcite with Nd chloride was undertaken, with the results quickly demonstrating this mineral's unsuitability. A 1 gram chip of calcite had completely dissolved within 30 minutes when reacted - in a sealed serum bottle - with 15 ml Nd chloride solution at 90 °C, with no neo-formed mineralisation observed. There was an audible release of gas when the bung was removed, suggesting the carbonate had turned to CO_2 more rapidly than it takes for the REE ions to precipitate as carbonates. When dolomite was used in a repeat of the experiment, it was found to be significantly less reactive. The rate of dissolved carbonate release was therefore slower, thus offering a greater chance for REE carbonate precipitation. Mineralisation was abundant, evident on both the dolomite chip and bottom of the serum bottle. Therefore, one kilogram of dolomite was subsequently sourced from a builders' merchant, which came as small (approx. 10 mm) pure-white chips. Randomly selected samples were checked for their purity through powder X-ray diffraction (PXRD), and found not to contain any detectable mineral impurities. Results from the fluid-rock interaction experiments are presented in Chapter 6.

3.2.2.2 Fluoride

REE fluoride solids have extremely low, and temperature-retrograde solubility (e.g. Migdisov et al., 2009, 2016), meaning the conditions under which stable aqueous REE fluoride complexes exist are narrow. Experiments involving REE fluoride complexes are therefore extremely challenging, and require specialist materials in order to accommodate low-pH, highly aggressive solutions. In order to control the supply of fluoride ions to solution, and hopefully avoid mass REE fluoride solid precipitation, fluorite was used during this investigation as a fluoride source. Pellets of intimately-mixed dolomite and fluorite were made, with the aim of producing $REECO_3F$. Natural fluorite samples, collected from the Peak District, UK, were donated by Dr Linda Kirstein of the Department of GeoSciences, University of Edinburgh. The results of these experiments are presented in Chapter 7.

3.2.3 Natural carbonatite samples

In order to compare the mineralogy and textures produced in synthetic growth experiments with those seen at natural REE fluorocarbonate-bearing deposits, it was necessary to obtain samples of the latter. After researching the location and background information (REE mineralogy, wall rock mineralogy, REE grades, previous literature, etc.), it was decided that Bayan Obo and Tundulu were good examples of REE-bearing deposits, particularly as the former is hosted almost exclusively in dolomite and the latter is a mixed calcite-dolomite-apatite carbonatite (e.g. Chao et al., 1992; Ngwenya, 1994; Smith et al., 2015; Broom-Fendley et al., 2016).

Bayan Obo is the world's largest REE-producing deposit (e.g. Smith et al., 2015), and a highly topical subject of research with a large body of literature on its mineralogy and genesis. A list of samples (including limited mineralogy) held by the NHM was obtained and reviewed, which led to 12 samples being chosen for further study. A number were already thin sections, and the remainder were rock samples. The latter were made into polished thin sections at the UoE, and prepared ready for analyses. The results of these investigations are presented in Chapter 7.

Tundulu was chosen because it was the original site at which Ngwenya (1994) based the hypothesis that wall rock chemistry controls the observed REE mineralogy. In addition a colleague, Dr Sam Broom-Fendley (Camborne School of Mines, The University of Exeter), had recently returned from the field and was in possession of dozens of samples. As with the Bayan Obo samples, the rocks provided by Sam were prepared into polished thins.

3.3 Experimental methods

3.3.1 Synthesis of REE carbonates *via* titrations

A variety of methods have been used for the precipitation of REE carbonates, and the previous chapter has highlighted the different nature of the products (morphology, crystallinity, etc.) as a consequence of small procedural variations. During the current investigation, Na_2CO_3 was added to the REE chloride solutions *via* titration with a burette, as opposed to direct mixing of the two. This approach meant the pH could be recorded as a function of Na_2CO_3 addition, and potentially provide additional information of the conditions experienced during REE precipitation, including the pH range over which it occurs.

Single and multiple REE-bearing solutions were used in these experiments. Single REE-bearing solutions were made to have REE concentrations equal to 0.1 M by 1:1 dilution of the stock 0.2 M REE chloride solutions and the stock HCl. Solutions containing two REEs had individual REE concentrations of 0.1 M by 1:1 mixing with each other. Three element solutions had individual REE concentrations of 0.066 M, made by mixing equal volumes of each stock REE chloride solution. Solutions containing five REEs were also made by mixing equal volumes of the stock REE solutions, resulting in individual REE concentrations of 0.04 M. The idea of using solutions containing > two REEs was only thought of after the one-REE and two-REE experiments had been completed, and therefore the concentrations of the former could not be matched to that of the latter.

An experiment consisted of the REE solution being placed into a glass beaker, which was sat on a magnetic stirrer, and titrated at room temperature with Na_2CO_3 over a period of approximately 10 minutes. This arbitrary length of time was chosen originally (back in 2013 at the project's beginning) on the assumption that this would allow enough time for initial crystallisation to occur, but not long enough for any transformation of this initial phase into something else. Later, it was shown by other authors that the onset of crystallisation varies as a function of Z (e.g. Rodriguez-Blanco et al., 2014); lanthanum was shown to crystallise after only two minutes after the direct mixing of a La chloride solution with one of Na_2CO_3, but that the same process takes around 100 minutes for Nd. As a large number of titration experiments had already been completed before the publication of Rodriguez-Blanco et al. (2014), the rapid titration used in the current investigation was not altered during the remaining experiments so that consistency could be maintained.

The solutions were stirred continuously with a PTFE-covered magnetic stir bar. The volume of Na_2CO_3 administered was recorded, and the solution pH monitored using a REFEX glass Ag/AgCl double junction combination pH electrode and Radiometer

Analytical PHM 220 pH meter, which was calibrated before each experiment with certified pH buffers (pH 4.0 and 7.0). The pH was observed to follow the pattern:

1. A sharp increase with minimal Na_2CO_3 addition (approx. 1:3 ratio Na_2CO_3:REE solution). This period was named **pre-pH stat**. The solution became slightly turbid;

2. A period of almost static pH, during which the addition of significant volumes of Na_2CO_3 resulted in minimal pH fluctuation (approx. ratio 1.5:1 Na_2CO_3:REE chloride solution). This period was named **pH stat**. The solution became opaque;

3. A second sharp increase in pH with minimal Na_2CO_3 addition.

All titrations were terminated at around pH 8.5, which equated to a final Na_2CO_3:REE chloride ratio of about 2:1. An example of the relationship between pH and volume of Na_2CO_3 added is shown in Figure 3.1. It must be noted at this point that the volume of Na_2CO_3 added was only recorded manually (i.e. by eye) after approximately every 1 ml had been dispensed, and the pH was also read manually from the pH meter. No automated equipment was used. Consequently, the patterns observed in Figure 3.1 are only indicative of broad trends, and cannot be used to extract additional information on, for example, the formation of certain metal-ligand complexes or buffering capacity of the solutions.

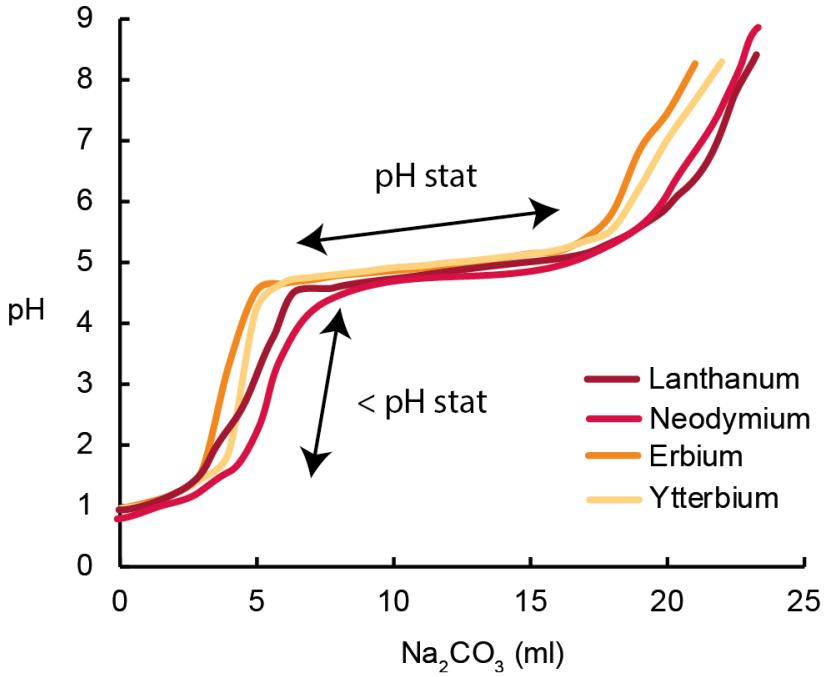

Figure 3.1: Example of the relationship between pH and volume of Na_2CO_3 added. The periods of initial rapid pH rise, pre-pH stat, and static pH, pH stat, are shown.

This rapid-rise - stabilisation - rapid-rise is attributed to the formation of the REE carbonate precipitates, with the period of static pH maintained (buffered) by the production of acid:

$$2\,REE^{3+}{}_{(aq)} + 3\,H_2CO_{3(aq)} \rightarrow REE_2(CO_3)_{3(s)} + 6\,H^+{}_{(aq)}$$

Previous studies of REE carbonate synthesis (e.g. Nagashima et al., 1973; Shang et al., 2009; Vallina et al., 2014) have shown structural and morphological differences in the products as a function of ageing temperature. In order to assess this variable, aliquots of the titration solutions were sampled and aged at different temperatures, the maximum limit of which was constrained by the upper working limit of the oven (220 °C). Products were aged from 40 to 200 °C for between 1 and 84 days; the higher temperature experiments were run only for a few days based on the results of comparable studies in the literature; lower temperature runs were typically run for six weeks, a figure used from the start of the project (before any results were generated), and repeated for consistency. As a result of the equipment used (see below), the number of different experiments that could be run concurrently at > 100 °C was limited to zero (i.e. only one at a time), whereas those at < 100 °C was limited by the size of the oven, which could easily accommodate 50 different samples. This, therefore, had an effect on the total number of experiments completed, and resulted in certain multi-REE solutions (i.e. the experiments completed later in the project) being prioritised over others. The experimental matrix for these titrations is presented in Chapter 4. The simpler experiments conducted at < 100 °C were completed during the earlier stages of the project, and were originally exploratory in nature. As the results were collected and analysed, the equipment required for taking the experiments to higher temperatures was designed and built in-house (see below).

The experiments heated at < 100 °C were completed in 15 ml volume serum bottles (total of 10 ml REE chloride per experiment). The bottles were stoppered shut with butyl rubber, crimp sealed and placed in a preheated oven at 40 or 90 °C, and left for the desired time period. The solutions were not agitated.

Experimental solutions heated at > 100 °C were placed into two PTFE screw-lid vessels (10 ml volume each) with PTFE O-rings, which were themselves placed into a larger steel reaction vessel (approx. 300 ml volume). Two vessels were required to yield enough product for characterisation using the analytical methods mentioned later in this chapter. The PTFE vessels were crafted from a single PTFE rod, and the steel vessel from a thick (12.5 cm diameter) bar of 304 grade stainless steel. Both were made in-house at the UoE. PTFE was chosen for its high chemical resistance to acids, including those containing fluorine (i.e. hydrofluoric acid). The 304 stainless steel was chosen for its good corrosion resistance (not to fluoride, however), its workability and

relatively low cost. The steel vessel was filled with 150 ml of deionised water to ensure the pressure was balanced between the inside of the PTFE and steel vessels when heated, avoiding distortion/destruction of the former. The steel vessel lid was held in place by six bolts, tightened to the main body with a torque wrench (set to 27 Nm). An O-ring (fluorinated propylene monomer, FPM, aka 'Viton') was situated between the lid and the main body of the vessel, ensuring a watertight face-seal. These runs were also not agitated. The steel vessel and PTFE vessel setup is shown in Figure 3.2.

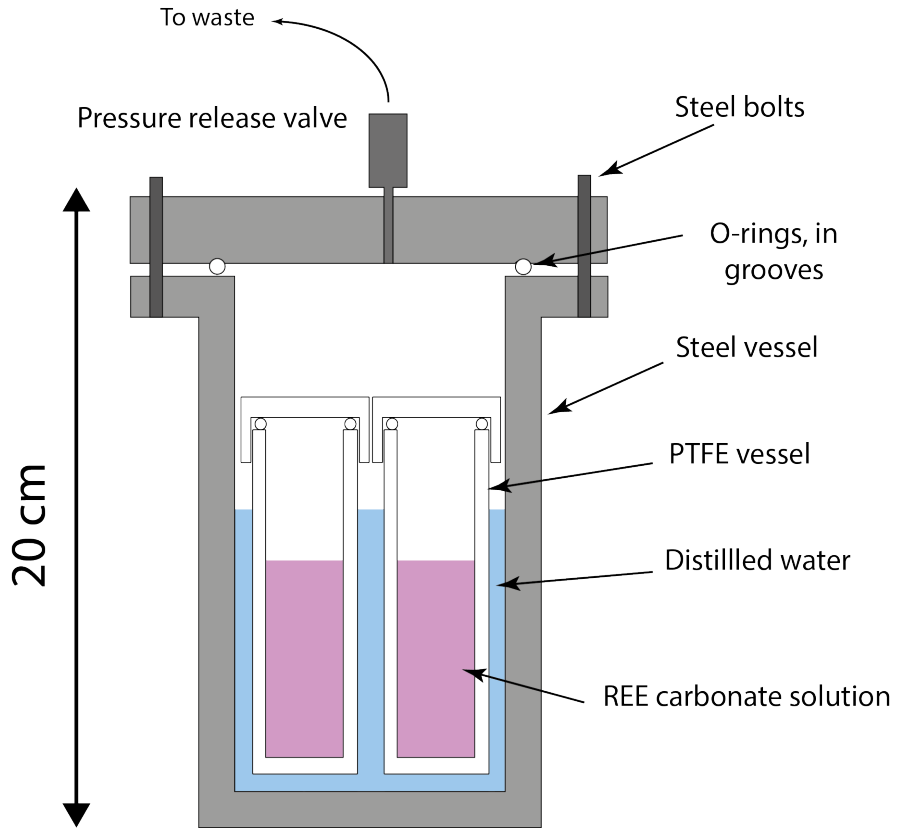

Figure 3.2: Schematic of the experimental setup required to heat the products of titrations at > 100 °C. PTFE vessel size slightly exaggerated; height value represents steel vessel.

At the termination of each titration, and the end of an ageing experiment, the precipitants were quenched, vacuum filtered on 0.45 μm mixed cellulose ester filters, repeatedly washed with deionised water and left to air-dry. This allowed comparison of 'fresh' and 'aged' precipitates. The 'fresh' precipitates were those filtered within a few seconds of the cessation of Na_2CO_3 addition. In all cases the filtrates were clear; washing the products with deionised water was not thought to cause any dissolution because of their low solubilities (although these were not explicitly known); SEM analyses did not reveal features consistent with dissolution. The experimental matrix for these titrations is also presented in Chapter 4.

An increasing number of studies on crystallisation (particularly $CaCO_3$), including pre- and post-nucleation stages, suggest that amorphous precursor materials may show short-range order similar to the bulk structure of the particular polymorph into which it crystallises (e.g. Rieger et al., 2007; Gebauer et al., 2008; Meldrum and Cölfen, 2008; Meldrum and Sear, 2008; Dietzsch et al., 2017). In order to determine whether the phases precipitated during the titrations followed this theory, a number of additional titrations were completed but this time at temperature (40 and 90 °C). Sub-sampling of the solutions just before/during the period of rapid pH rise (pre-pH stat), and the period of static pH (pH stat), meant the local structure of the precipitates could be assessed as a function of pH/time/Na_2CO_3 addition. This was done using X-ray absorption spectroscopy (see section 3.3.3.6).

These experiments were conducted in the same way as the room temperature titrations, with the exception that solutions were heated using the hot plate function of the magnetic stirrer (and the experiment was housed in a fume cupboard). The pH meter was calibrated at the appropriate temperature to compensate for the changes caused by temperature, and a glass thermometer was used to monitor the temperature. By insulating the beaker with enough tissue paper and a makeshift glass lid, it was possible to keep the REE chloride solutions at ± 3 °C at 40 °C and ± 6 °C at 90 °C for the duration of the experiments. The Na_2CO_3 was preheated to slightly above the temperatures of the REE chlorides (50 and 95 °C) in bunged serum bottles before being transferred to the burette. This ensured the temperature stayed as close to that of the REE solutions as possible. These titrations were conducted at a slightly faster rate than those described in the previous section (about five minutes) to minimise heat loss from the solutions.

Aliquots were sampled at pre-pH stat and pH stat. To avoid changes in speciation, oxidation or crystallisation, these samples were instantly frozen using liquid nitrogen. In order to do this, but also ensure the sample was in an appropriate form to be analysed by XAS, specialist cells were required. Ten cells were crafted from a single bar of 6080-T6 aluminium (25 mm wide by 6 mm thick) at the School of GeoSciences, UoE. Each cell was 20 mm in length, with a 10 mm inner diameter bore drilled through its longest and largest face, with two smaller holes bored perpendicular to this through the top face such that there was a connectivity between the three. The smaller bores were threaded to accommodate an M3 screw each. A schematic of the cell is shown in Figure 3.3.

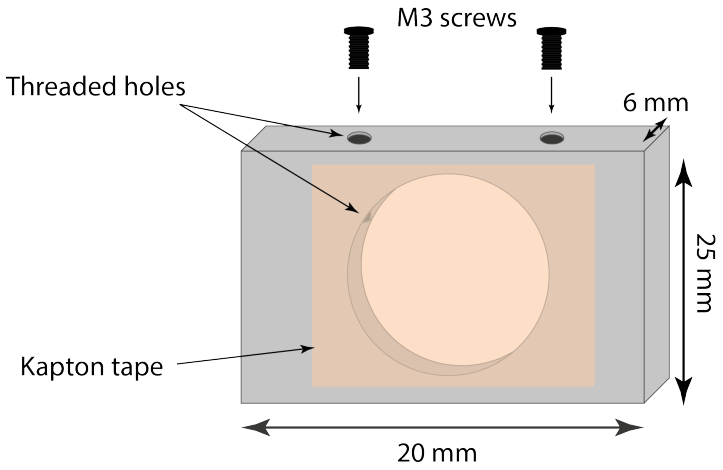

Figure 3.3: Schematic of the aluminium cells used in the analysis of solution (frozen) samples collected at pre-pH stat and pH stat. There is a piece of Kapton tape attached to each side of the cell. Once the solution had been pipetted into the cell through one of the threaded holes, the screws were tightened and the whole cell submerged in liquid nitrogen.

To make the cell watertight, but still allow the X-ray beam to come in contact with the sample, Kapton tape was used to cover each side of the large bore; Kapton is commonly used as window material during X-ray work because it has high transmittance to this radiation wavelength. At the appropriate point in the titration, a small volume of aliquot was removed from the beaker in a mechanical pipette and inserted into a (Kapton-bearing) cell, and the two remaining holes quickly plugged with M3 screws. The sealed cell was then submerged in liquid nitrogen and stored in a freezer. Approximately 10 seconds passed between extraction from the mother liquid and submergence in the LN_2. The frozen samples were transported to the synchrotron for XAS analyses in a polystyrene box filled with dry ice.

Fresh precipitates from the heated titrations were obtained as before by immediately filtering solutions at the end of an experiment. XAS analysis required the fresh and aged precipitates (i.e. the solids) to be in the form of pellets. This was achieved using a 13 mm diameter spectroscopic die press: approximately 0.01 g of sample was crushed in a mortar and pestle, then mixed with approximately 0.08 g cellulose and pressed into pellets about 1 mm thick. Cellulose is used because it acts as a binding agent but is relatively transparent to high energy (hard) X-rays (because it is composed of low Z elements).

3.3.2 Synthesis of REE carbonates and fluorocarbonates *via* fluid-rock reactions

The reaction of a metal-bearing fluid with the rocks through which it is flowing can result in physical/chemical changes to that fluid, which may increase or decrease its

ability to transport certain metals. These changes can lead to metal accumulation at ore grade levels. These observations, combined with the common occurrence of REE ore deposits with carbonate-rich rocks, led to the idea of conducting wall rock reactions between carbonate rocks and REE-bearing solutions. The aims/objectives of these experiments were threefold:

1. to confirm the reaction of a REE-bearing solution with a carbonate rock results in REE carbonate mineralisation;
2. assess the influence of temperature and REE solution content on potential products, and;
3. compare the results with those of the titration experiments.

A thorough search of the literature identified no other studies utilising the following method, although variations on hydrothermal fluid-rock interactions are very common (e.g. Hövelmann et al., 2010; Okamoto et al., 2010; Kato et al., 2013; Schepers and Milsch, 2013; Isobe and Yoshizawa, 2014; Wolterbeek et al., 2016). As such, the wall rock experiments presented in this project represent a new and unique view of REE carbonate and fluorocarbonate mineral genesis.

As with the titrations, two experimental setups were required depending on the temperature at which the solutions were heated. Those conducted at < 100 °C were done in serum bottles, and those at > 100 °C in a specially-made flow-through cell. The < 100 °C runs were, as with the titrations, completed earlier in the project (first year), whereas the higher temperature experiments required equipment to be designed and built at the UoE. The same temperatures as used in the titration experiments were used here, although there were a few variations on ageing lengths. This was based on the observation that mineralisation was occurring at the lower temperatures (90 °C) within (at maximum) five days, and therefore running these experiments for six weeks (as in the titrations) was unnecessary. A full experimental matrix can be found in Chapter 6.

In brief, the reaction cell containing the dolomite (explained below) was placed inside the oven and plumbed into a high pressure liquid chromatography (HPLC) pump, with a couple of filters (one 10 μm pre-filter and a second 2 μm filter) and a back-pressure regulator sitting between the two. A flow-through setup was chosen to better represent the type of reaction (i.e. 'open system') expected during natural REE carbonate deposition.

The reaction cell was designed and constructed in-house at the UoE. PEEK was chosen as the cell material because of its chemical resistance and mechanical properties. The cylindrical cell was constructed from a PEEK rod, and had a total length (including

caps) of 140 mm. The central 100 mm (i.e. without caps) was bored (4.5 mm diameter), resulting in a 1.5 ml reaction cell volume. Viton O-rings, chosen for their high chemical resistance, were placed between the caps (into each of which an appropriate O-ring-sized groove had been cut) and the main body of the cell, ensuring a watertight fit when assembled and tightened. M5 rods running parallel to the cell were tightened against steel plates situated at each end of the cell using M5 nuts. This held the cell together tightly. The setup for the > 100 °C experiments, including the PEEK reaction cell, is shown in Figure 3.4.

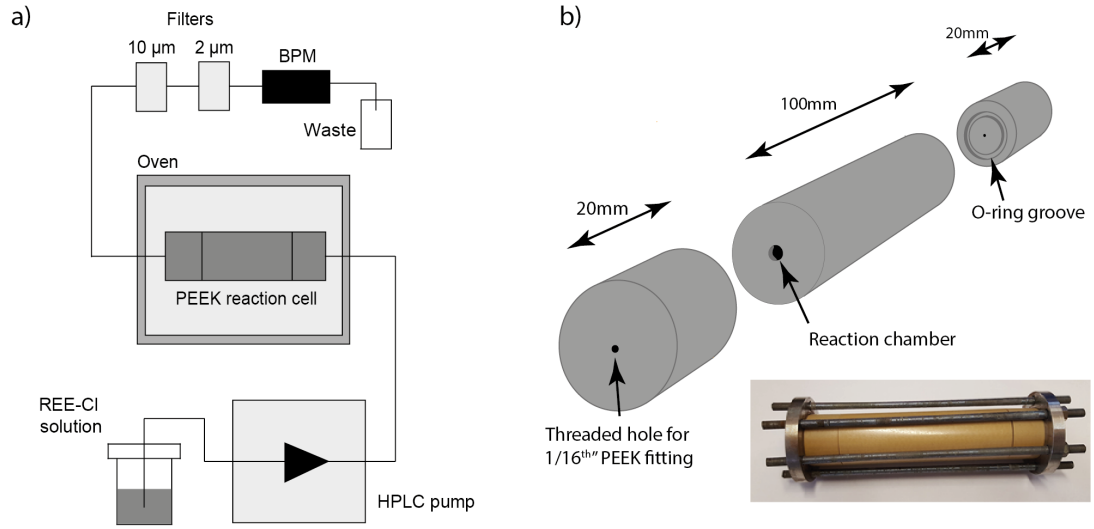

Figure 3.4: a) Schematic of the flow-through setup used in the > 100 °C experiments; b) schematic of the PEEK reaction cell. Inset photograph is the cell with metal end plates and M5 threaded rods in place, holding the PEEK pieces tightly in place.

Threads to accommodate finger-tight PEEK fittings were added to the outside edge of each cap, into which 1/16" HPLC tubing was connected and tightened. Tubing from one end of the cell fed out the oven to the HPLC pump, into which the reaction solution (the REE chlorides) was plumbed. The HPLC tubing from the other end of the reaction vessel led to waste via the two filters (one 10 μm and one 2 μm) and a 500 psi back-pressure regulator (BPR). The BPR ensured the pressure within the cell remained below 500 psi, thus avoiding tube blow-outs. The end of the tubing was fed to waste.

During exploratory experiments it was found that even at the lowest flow rate available from the pump (0.01 ml/min), the dolomite (0.5 g worth of chips, approx. 3 mm in length/width) was fully dissolved in < 48 hours at 90 °C. A shorter experiment, lasting

only three hours and at the same temperature, resulted in an approx. 15 % mass decrease but no visual change (i.e. no crystallisation) the dolomite chips, indicating the fluid residence time was too short. Based on the preliminary results, it was decided to use a hybrid system in this thesis, termed 'continuous batch reactions'. This involved the solution inside the cell being replenished once every 24 hours: e.g. experiments lasting four days would have the solution within the cell 'flushed through' three times (i.e. at 24, 48 and 72 hours) by turning the pump on at a known flow rate. Because the solution volume was refreshed every 24 hours, the concentration of starting solutions was decreased from 0.1 or 0.04 M (as used in titrations), to 0.02 M. This value was also chosen because during the exploratory experiments it was shown to be high enough to produce neo-mineralisation on the dolomite, and therefore use of more concentrated solutions was deemed wasteful (the REE salts were expensive and not limitless in their availability).

At the end of each experiment the cell was quenched, and the dolomite chips were removed, washed repeatedly with deionised water using the vacuum pump/filters described earlier and left to air-dry.

A further set of wall rock reaction experiments in which fluoride was a reactive component were performed to determine whether fluorocarbonates could be formed *via* this method. The reactions were only conducted at 90 °C due to time constraints (these experiments were completed in the final few weeks of the project before write-up commenced), and as such used the serum bottle method described above. Given the time constraints and small number of experiments completed, the results are exploratory/preliminary in nature. A preliminary experiment, in which a chip of dolomite and a chip of fluorite were reacted at 90 °C for five days in a REE chloride solution, found only REE carbonate (on dolomite) and REE fluoride (on fluorite). This indicated that both solids had dissolved, but that the precipitation of solid phases occurs very close to the dissolved ligand source, and as such the two reactant solids needed to be more intimately mixed. Dolomite plus fluorite pellets were made first by crushing the appropriate mass of solid in the mortar and pestle, ensuring the mix was homogeneous, then pressing the powder into a pellet using a pin press and hydraulic press. A mass of 0.15 g each of fluorite and dolomite was used to make each pellet, which was enough to create a robust, readily-handled pellet.

The same 0.02 M REE chloride solutions were used during these experiments, with pellets placed into 15 ml volume serum bottles along with 10 ml experimental solution. The bottles were bunged, crimped and heated in the oven at 90 °C for five days. As these experiments were conducted in the closing stages of the project, these temperatures and ageing lengths were based on the results from previous dolomite-only experiments. The contents of the serum bottles were vacuum filtered, repeatedly washed with deionised

water and left to air-dry at the end of each experiment. Results from these experiments are presented in Chapter 7.

3.3.3 Characterisation techniques

A number of techniques were used to gather as much information on the structure, morphology and chemistry of the experimental products, and on the mineralogical & textural relationships between minerals in the thin sections.

3.3.3.1 Optical microscopy

Some of the experimental products were large enough to see with the naked eye, but not large enough to make out any detail. In these cases a Nikon SMZ800 Stereo microscope with a Leica DFC 420C camera was used to reveal the crystal morphologies. Some of these images can be found in Chapter 6. The same equipment was used to make a first assessment of the textural relationships between phases in the thin sections (Chapter 7).

3.3.3.2 Scanning electron microscopy (SEM)

When viewed under the optical microscope, the crystallites or particles comprising the samples produced during titration and wall rock reactions were too small to be resolved. It was therefore necessary to examine them using a scanning electron microscope (SEM). The following is adapted from Goldstein et al. (2017).

SEM can produce nanometre-scale resolution images of samples, and identify their chemical constituents *via* the use of X-ray microanalysis. SEM analysis first requires the sample(s) to be gold or carbon coated, which prevents sample charging by forming a conductive layer between the sample surface and mount. In this investigation carbon was required because the samples, as well as being imaged, were to be analysed for their chemical constituents (using Au can cause interference peaks with other metals). This was useful for investigating the chemistry of precipitates formed from solutions containing more than one REE (i.e. whether they contained more than one REE).

In SEM analyses the sample is kept under vacuum and a focussed electron beam, generated in an electron gun, is fired at the target, scanning across the area of interest. The incident electron beam causes the atoms at the sample surface to emit secondary electrons (in 'secondary electron SEM', or SE-SEM) that are collected by the detector. The location at which the signal was collected in relation to the raster scan can then be used to form a 2D 'image', that, because of the width of the incident beam (generally $<$ 5 - 10 nm), creates an apparent 3D image. SE-SEM is commonly used for imaging.

The elements present in the sample can be identified using an energy dispersive detector (energy dispersive spectroscopy – EDS). Atoms will produce characteristic X-rays when their inner shell electrons are promoted to higher level, higher energy orbitals when the electron beam 'excites' them, and then 'relax' back to their original, lower energy state. The energy of the emitted X-rays is characteristic of the orbital transition, which is also elements specific. In SEM-EDS, the promotion of the electrons is a consequence of their interaction with high energy electrons. As the identification of sample chemistry was required in this study, but the excitation energy of REEs is high ($L\alpha$ of Yb = 7.41 kV), the accelerating voltage of the electrons was set to 20 kV.

During this investigation a Carl Zeiss SIGMA HD VP field emission gun scanning electron microscope was used for all SEM analyses. Qualitative/semi-quantitative chemical analyses were obtained using energy-dispersive X-ray spectrometry (EDS), with an Oxford Instruments Aztec analysis system.

3.3.3.3 Electron microprobe analyser (EMPA)

The following is adapted from Reed (2005).

EMPA is a commonly used technique for *in-situ*, non-destructive quantitative chemical analyses of minerals and other materials. Precise analyses over very small areas are achievable *via* EMPA, which make it a popular technique for analysing chemical compositions of minerals within rocks, or even chemical variations within single minerals. It is for this reason that EMPA was employed in the current investigation. Rock samples - made into polished thin sections - from two natural carbonatite deposits were analysed *via* EMPA, with a focus on REE concentrations (and textures) within both REE minerals and their host rocks.

An EMPA uses the same principals as outlined for SEM analyses, in that it utilises a micro-focussed electron beam to excite the target causing it to emit element-specific X-rays, but also has the additional capability of accurately determining the chemical composition of the sample by comparison with well characterised standards (details of the standards used can be found in Chapter 7). EDS, as on the SEM, can be used to gather information on the chemical constituents of the sample, and wavelength-dispersive spectroscopy (WDS) is used during quantitative chemical analyses. An analysis requires the elements of interest (i.e. the major constituents of the sample, plus the trace elements of interest) to be loaded into a file, which then runs the analysis, measuring the desired elements by isolating their X-rays (based on wavelengths using Bragg's Law - explained in the next subsection) using an (or several) analytical crystal(s).

At the UoE, the EMPA is a Cameca SX1000 electron probe microanalyser, which was operated at an accelerating voltage of 20 kV and had a beam current between 1 and 40 nA for major elements, and 40 and 100 nA for trace elements. As with the SEM, thin sections were carbon coated prior to analyses.

3.3.3.4 Powder X-ray diffraction (PXRD)

The majority of experiments in this investigation produced very fine grained materials, which, using SEM, were seen in many cases to consist of micro-sized crystals. Larger crystals were also formed in some of the wall rock reactions. In all cases, structural information was required in order to assess the influence of the experimental variables (e.g. method, temperature, etc.). In order to obtain this information, X-ray diffraction was required. Specifically, because of the nature of the materials (i.e. mostly very fine grained), powder XRD (PXRD) was used. The following is taken from Gill (1997) and Clegg (2003).

PXRD is a common technique for determining the bulk composition of a sample, which must be finely ground and homogenised. With the samples produced by the titration method, preparation for PXRD was simply achieved by scraping the dried products from the filters and grinding them in a mortar and pestle. To the powdered sample was added acetone, such that the powder was suspended, whereupon it was syringed and dripped onto a square glass plate (2 cm^2). The acetone then volatilised off, turning the solution into a paste. This method ensures a random orientation of the grains, which is important to avoiding bias in the results of PXRD analyses from preferred orientation of, for example, plate-like crystals. A larger and thicker glass plate was pressed against the first to ensure the sample had a flat surface.

PXRD is based on the constructive interference of monochromatic X-rays upon their scattering off the atoms in a material. In a crystal, which is made up of long range repeating units of the same atomic arrangement (unit cell, to form a crystal lattice), the X-rays will scatter in all directions, although most will interfere with or completely cancel each other out – known as destructive interference. However, under certain conditions, the reflections will interfere constructively when Bragg's Law is satisfied:

$$2dsin\theta = n\lambda$$

where n is a positive integer, λ is the wavelength of the X-ray and d is the inter-plane spacing of the crystalline material. This is possible because the spacings between planes of crystals are of a similar size to the wavelength of the X-rays produced by the diffractometer; in the current investigation this was Cu$K\alpha$ radiation ($\lambda = 0.154$ nm). Two instruments were used, a Bruker D8 Advance X-ray spectrometer (Department of GeoSciences, UoE) and a Bruker D2 PHASER desktop X-ray spectrometer (Depart-

ment of Chemistry, UoE). Constructive interference is illustrated in Figure 3.5. The angle between the incident beams and the crystal planes is θ, and the space between the planes is d.

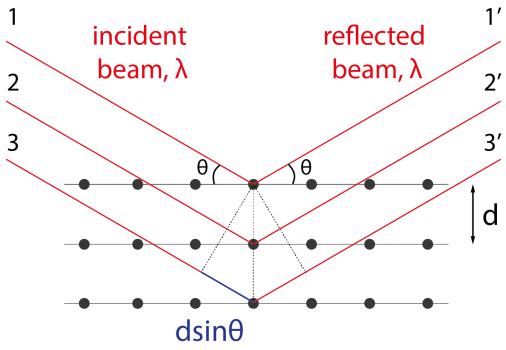

Figure 3.5: Schematic representation of Bragg's Law being satisfied, resulting in constructive interference of X-rays when diffracted/reflected off the atoms in a crystalline material. The constructive interference causes an increase of X-ray intensity, picked up by the detector and plotted against 2θ to produce an X-ray spectrum.

It is clear from Figure 3.5 that for Bragg's law to be satisfied for situations other than that shown (i.e. if the orientation of the planes in this sample was not that shown in the figure), it is necessary to change the angle of the incident beam and detector. The X-ray diffractometer in the GeoSciences department of the UoE is a theta-theta instrument: this means the sample is kept stationary while the incident X-ray beam and the detector rotate around the sample at the same, but opposite, rate (i.e. $-\theta$ °/min for the incident beam and θ °/min for the detector). This setup, which avoids the powdered sample falling out of its holder, is shown in Figure 3.6.

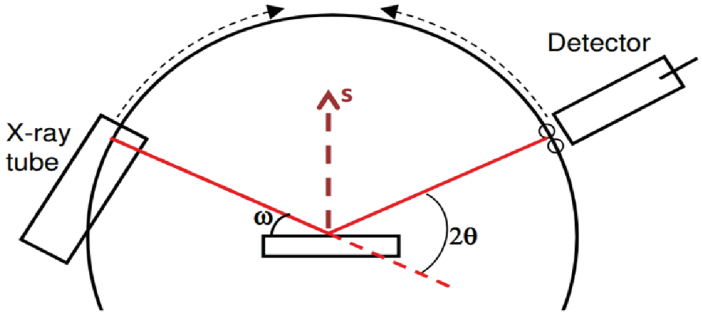

Figure 3.6: Schematic of the theta:theta X-ray diffractometer in the School of GeoSciences, UoE. The X-ray source and detector rotate at the same rate but in opposite directions while the sample remains stationary.

As the angle is changed, Bragg's law may be satisfied and an intense X-ray beam produced, which is recorded as a function of degrees 2θ. These data can then be plotted as an XRD trace or spectra. An example is shown in Figure 3.7. If the material is amorphous (i.e. do not have a long-range repeating structure) the repeating planes required for constructive interference are not present, and the PXRD trace will have no peaks. This is also shown in Figure 3.7. In the current investigation the majority of PXRD spectra were collected from 2° to 65° 2θ at intervals of 0.025° for 1.5 seconds each. These values were chosen because they offered the best acquisition time to resolution, and because the additional information obtained beyond 65° did not significantly affect the interpretation of the samples.

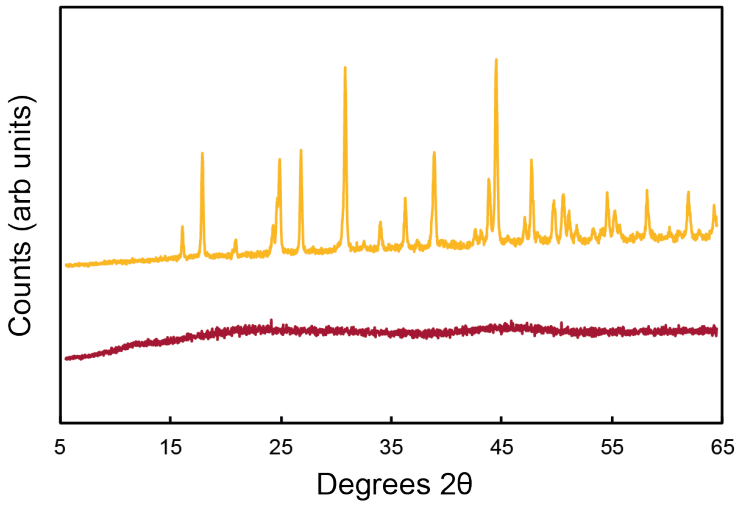

Figure 3.7: Example of an X-ray spectrum for a highly crystalline material (yellow line) and an X-ray amorphous material (red line). Note the lack of strong, narrow peaks for the amorphous material. The top trace is a kozoite-(Nd) ($NdCO_3OH$).

Once an X-ray trace is produced, computer software is used to assign the reflections (based on their intensities and degrees 2θ values) to the mineral from which they were produced. This is achieved by comparison with a database containing the reflections of thousands of inorganic phases (including minerals). During this investigation, EVA X-ray diffraction software (produced by Bruker) and the International Centre for Diffraction Data (ICDD) database were used. Because the solutions used in these experiments were fairly simple (i.e. few elements), multi-phase products were encountered on only a few occasions. When this occurred, the percentage of each phase was quantified using the Rietveld technique with the software TOPAS (also produced by Bruker). This technique compares the experimental (observed) and theoretical (calculated) patterns for the phases in the sample, with the user-selected parameters refined until the difference between the two is minimised.

3.3.3.5 Fourier transform infrared spectroscopy (FTIR)

The following is adapted from Stuart (2004).

Many of the materials produced in this study were X-ray amorphous. These samples were further characterised using Fourier transform infrared spectroscopy (FTIR). This technique is useful for determining the constituent molecules/functional groups of a sample, because they absorb infrared radiation at different, characteristic, wavelengths. As molecules absorb the IR radiation they experience a change in dipole moment which causes them to vibrate or rotate. These absorptions can be used as a 'fingerprint' for the contents of a sample.

A modern variety of IR spectroscopy, which utilises the phenomenon of total internal reflection, is attenuated total reflectance (ATR). The IR radiation will be totally reflected when the angle of the incident beam between the crystal and the sample is greater than the critical angle. ATR measures the changes that occur in a totally reflected beam as it comes into contact with the sample. This is shown in Figure 3.8.

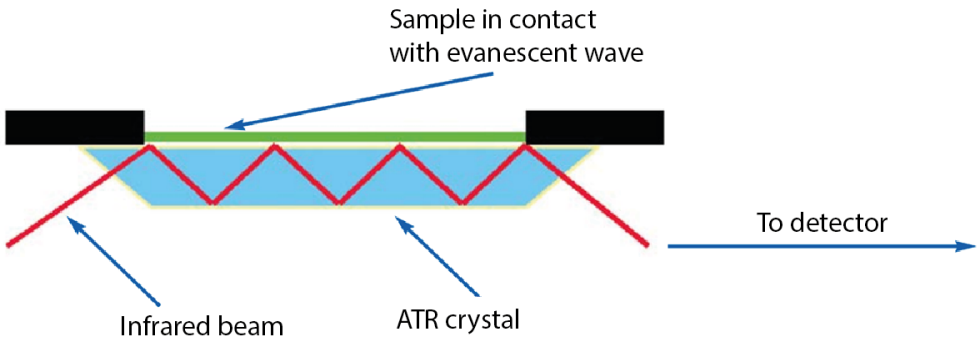

Figure 3.8: Schematic showing the path a beam of IR radiation takes as it is totally reflected off the diamond crystal and is attenuated during interaction with the sample. Image taken from PerkinElmer (2005).

An evanescent wave is produced by the internal reflection, which protrudes beyond the surface of the crystal and into the sample, where it will be attenuated when the infrared beam energy is the same as the resonant energy of the molecules in the sample. The attenuated energy then exits the reflecting crystal and into the detector, where an IR spectrum is produced. This variation of IR is useful because it does not require the sample to be prepared other than size homogenisation, achieved by crushing. The IR spectra is presented as transmittance vs. wavelength (cm^{-1}), an example of which is shown in Figure 3.9.

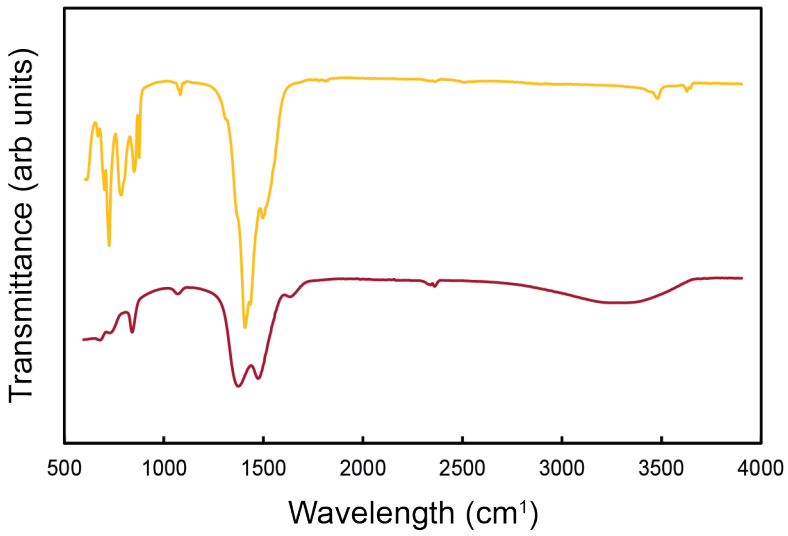

Figure 3.9: Example FTIR spectra showing the transmittance of the IR beam with respect to its wavelength, when interacting with the same two phases presented in the example PXRD traces in Figure 3.7 (X-ray amorphous Nd-bearing material and kozoite-(Nd)).

In the School of GeoSciences, the IR instrument is a Bruker Vertex 70 spectrometer equipped with a diamond internal reflection cell. Data were collected from 500 to 3900 cm^{-1} at a resolution of 4 cm^{-1}, with a total of 500 analyses merged to produce each spectrum. The beam source was a MIR source (SiC glo-bar), with a range of 8000 - 350 cm^{-1}, the splitter was an MIR-KBr beamsplitter, and the detector a room temperature DLaTGS. This setup was chosen because it is the IR region at which the functional groups of interest are IR active, and it gave a good resolution-to-time ratio. The software used to transform the raw data into the IR spectra (*via* Fourier transform) was OPUS 7.0, produced by Bruker.

3.3.3.6 X-ray absorption spectroscopy (XAS)

X-ray absorption spectroscopy is a technique commonly used for the identification of atomic local structure and electronic states of elements within both crystalline and amorphous materials. During this investigation, XAS was used to probe the local structure of precipitates formed during titrations (the frozen solutions), the 'fresh' precipitates filtered immediately afterwards, and the aged products, including those found to be amorphous when analysed by PXRD. Testing at these different stages meant evolution of the local structure could followed: therefore it could be determined whether the solution precipitates had the same/similar local structure as that of the bulk, crystalline material (e.g. Meldrum and Cölfen, 2008). All XAS (XANES - X-ray absorption near-edge structures, and EXAFS - extended X-ray absorption fine structures) data were collected in September 2014 at the Diamond Light Source, Oxfordshire, UK, on the core EXAFS beamline B18.

The following information on XAS theory is modified from Anderson et al. (2002), Newville (2014) and Henderson et al. (2014). Synchrotron radiation is produced when electrons are accelerated in a circular path, which is achieved using bending magnets in a large ring structure (Figure 3.10). The electron beam is first produced with an electron gun, and then accelerated to nearly the speed of light in a booster ring. The energy of these electrons at Diamond is 3 GeV. Once at this speed they are transferred to the storage ring, where they are held in place with bending magnets. The emitted synchrotron radiation, which contains light with energies spanning the electromagnetic spectrum, is channelled into 'beamlines' where the experiment takes place. Diamond Light Source is shown in Figure 3.10

The high brilliance (i.e. a large number of photons, narrow beams, low angular divergence of photons) X-ray beam is polychromatic, so a monochromator is used to select and then scan through the energy range required during an experiment. XAS is the measurement of the X-ray absorption coefficient of an atom as a function of energy, with the energy range incremented using the monochromator. The absorption coefficient gives the probability that X-rays will be absorbed, as described by Beer's law:

$$I = I_0 e^{-\mu t}$$

where I = intensity of the X-ray transmitted through the samples, I_0 the intensity of the incident X-ray, μ = the absorption coefficient and t = the sample thickness. The absorption coefficient is, at most energies, a smooth function of energy. However, as the X-ray energy approaches that of the binding energy of a core electron in an atom of the sample, there is a dramatic rise in absorption, known as an absorption edge. At this energy an inner core electron is either promoted to a higher shell or ejected from the atom altogether, leaving a 'core hole'. This process is the photoelectric effect (and the ejected electron is known as a 'photoelectron'). After the absorption event, the core hole will be filled by a higher shell, higher energy electron 'falling' into place, with the energy difference given off as a fluorescent X-ray. The energies of these X-rays are element (and shell-transition, e.g. K, L_1, L_2, L_3) specific, as are the energies of absorption edges. The energy range available on beamline B18 is 2 – 35 KeV, but the K edges of the REEs are significantly higher than this (La and Yb K edge energies are 38 and 61 KeV, respectively). Therefore, during this investigation, the L_3 edges were used. The edge energies of the REEs are given in Table 3.2.

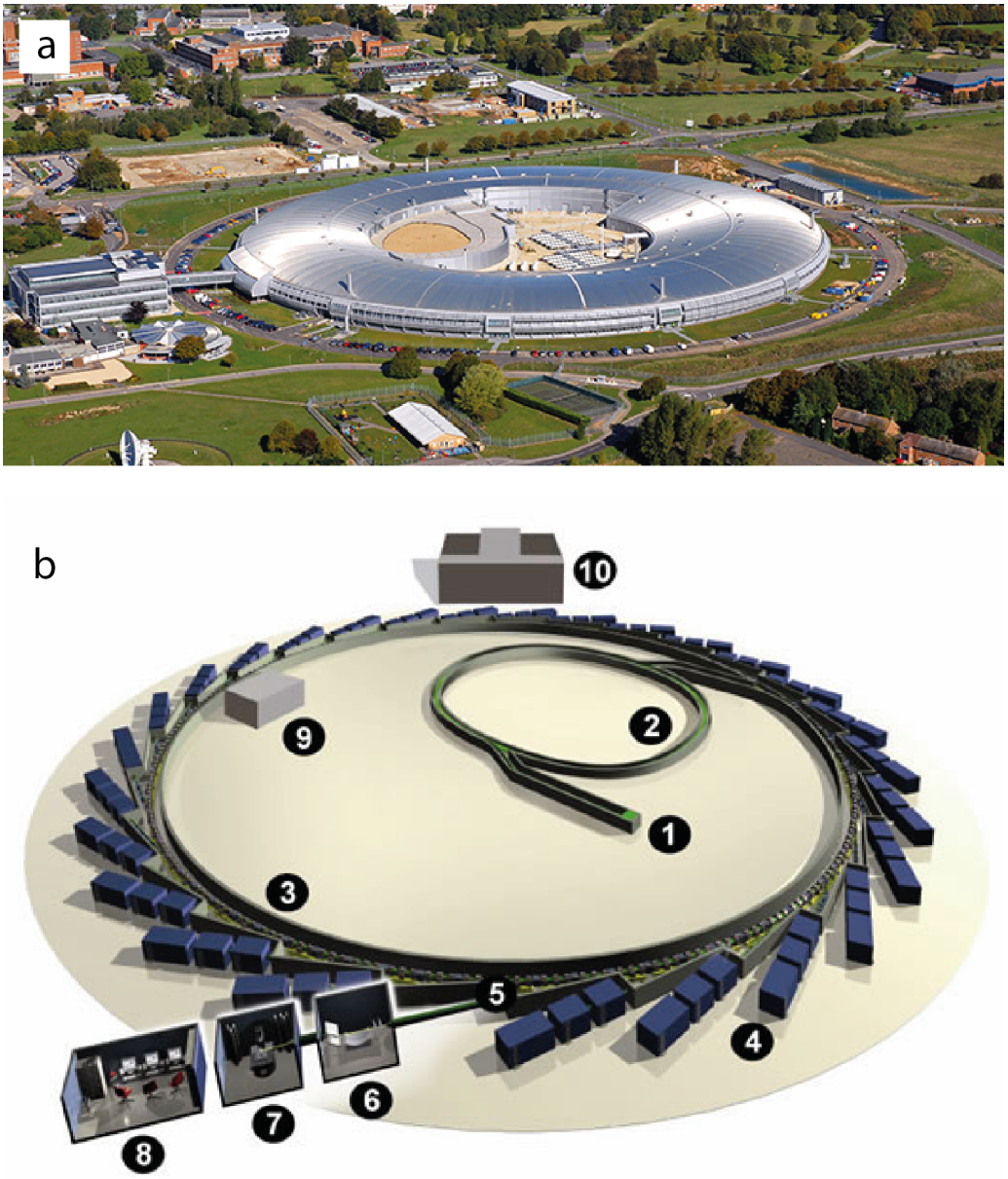

Figure 3.10: a) aerial photograph of the Diamond Light Source synchrotron, Oxfordshire, UK. The large donut-shaped structure, which is 560 m in diameter, is the storage ring where the synchrotron radiation is produced; b) schematic of the synchrotron setup: 1. Electron gun; 2. Booster ring; 3. Storage ring; 4. Beamline; 5. Frontend (connection between synchrotron light and beamline; 6, 7, 8. Beamline (optics hutch, experimental hutch, control hutch). Both images taken from www.diamond.ac.uk.

	K	L_1	L_2	L_3
La	38,894	6,235	5,860	5,452
Nd	43,538	7,095	6,691	6,177
Er	57,464	9,725	9,243	8,336
Yb	61,322	10,479	9,968	8,933

Table 3.2: X-ray absorption edge energies (eV) for the REEs analysed by XAS.

XAS can be measured in either transmission or fluorescence modes:

$$Transmission : \mu(E) = log(I_0/I)$$
$$Fluorescence : \mu(E) = \alpha I_f/I_0$$

Where I_f = the intensity of the fluorescence beam. In transmission mode the number of photons are measured before (the incident beam, I) and after (I_0) the beam has passed through the sample, while in fluorescence mode the incident and fluorescent X -rays are measured. In general, fluorescence mode is used when the concentration of the element(s) of interest is low (ppm level or lower), or when the sample is thick. Transmission mode is more commonly used in the opposite situation (transmission mode is dependent on sample thickness, μt).

The frozen samples (pre-pH stat and pH stat) were measured in fluorescence mode (they were 6 mm thick) in a specialist cryostat. The cryostat was cooled with LN_2 such that the chamber in which the sample sat was about 80 K. When measuring in fluorescence mode the detector was set at 90° to the incident beam, with the sample sitting at 45° to both. This setup avoids self-absorption of the fluorescent X-rays and maximises the count rate. The transmission and fluorescence setups are shown in Figures 3.11 and 3.12, respectively.

When absorption is plotted against energy, the absorption edge is clearly visible as a large jump, and is followed by a number of oscillations (Figure 3.13). The oscillations in the region about + 30 eV beyond the edge contain the X-ray absorption near edge structures (XANES), and beyond this are the extended X-ray absorption fine structures (EXAFS). XANES is sensitive to the oxidation state and coordination number of the absorbing atom, while EXAFS is used for the determination of coordination number, and identity of, and bond lengths between, the absorber and its nearest neighbour atoms. In this study the EXAFS were used for determining changes in bond lengths and coordination number of the REEs during their precipitation from solution.

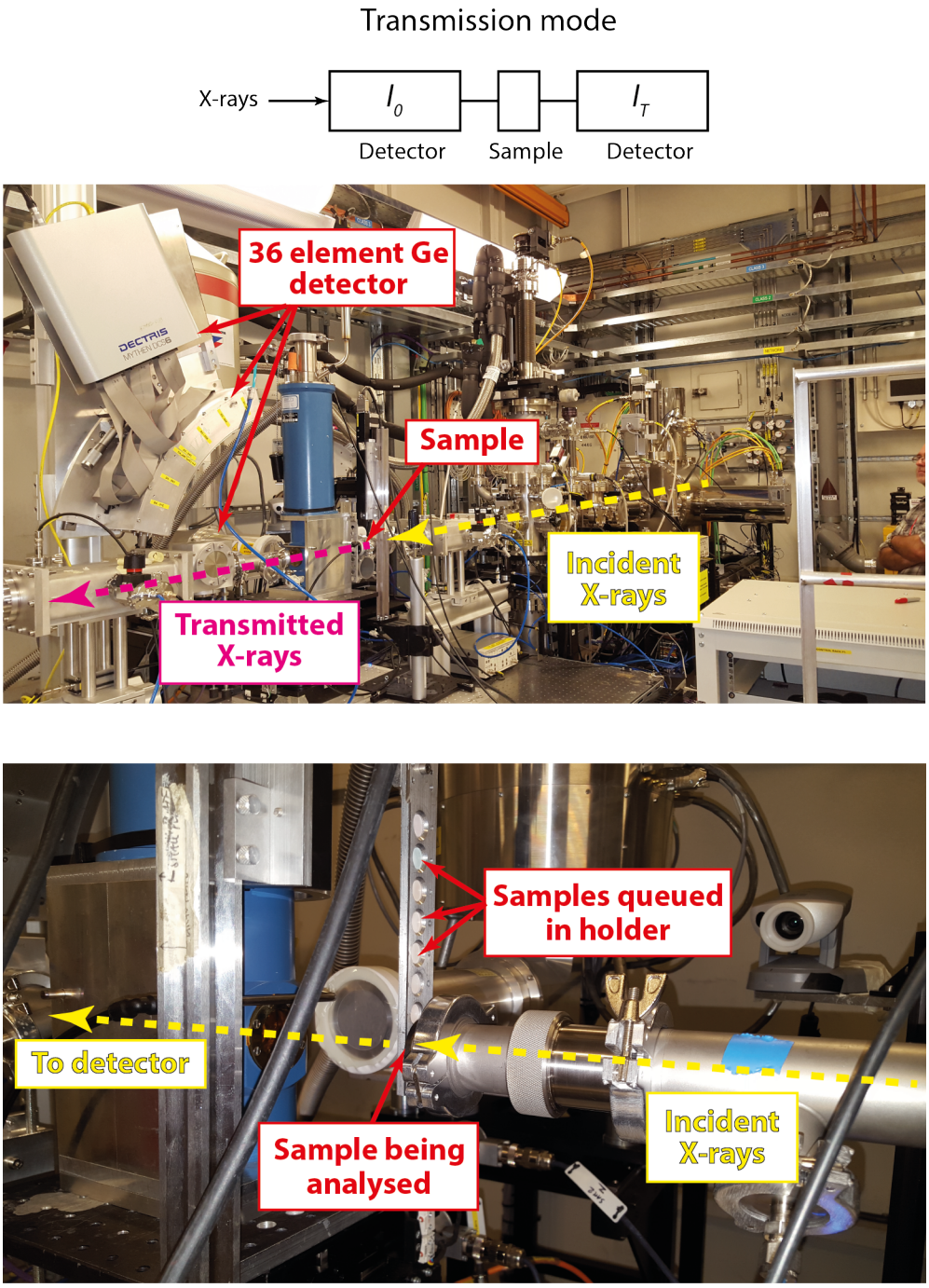

Figure 3.11: Schematic of the XAS in transmission mode and photographs of the setup at beamline B18 on which the XAS spectra were measured. The lower photograph is a close up of the sample holder (with the pellets). The blue cylinder in the top photo is the cryostat used for collecting spectra in fluorescence mode. Photos taken by M. Holloway.

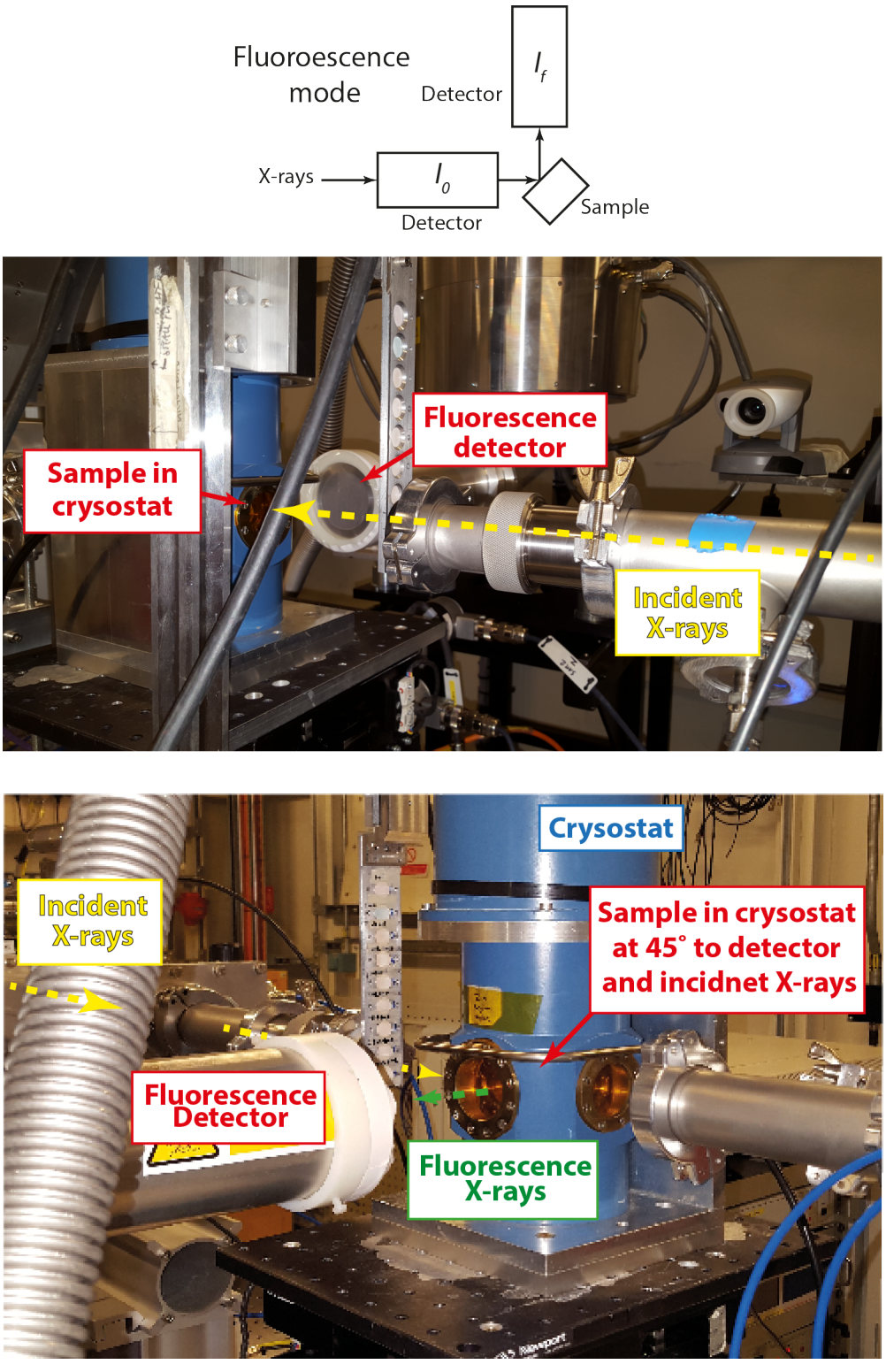

Figure 3.12: Schematic of the XAS in fluorescence mode and photographs of the setup at beamline B18. During the measurements made in fluorescence mode the sample (one at a time) was held in the cryostat. The holder with the pellets (pictured) was removed. The two images are taken either side of the cryostat, showing the fluorescent X-rays' path to the detector (at 90 ° to the incident X-rays). Photos taken by M. Holloway.

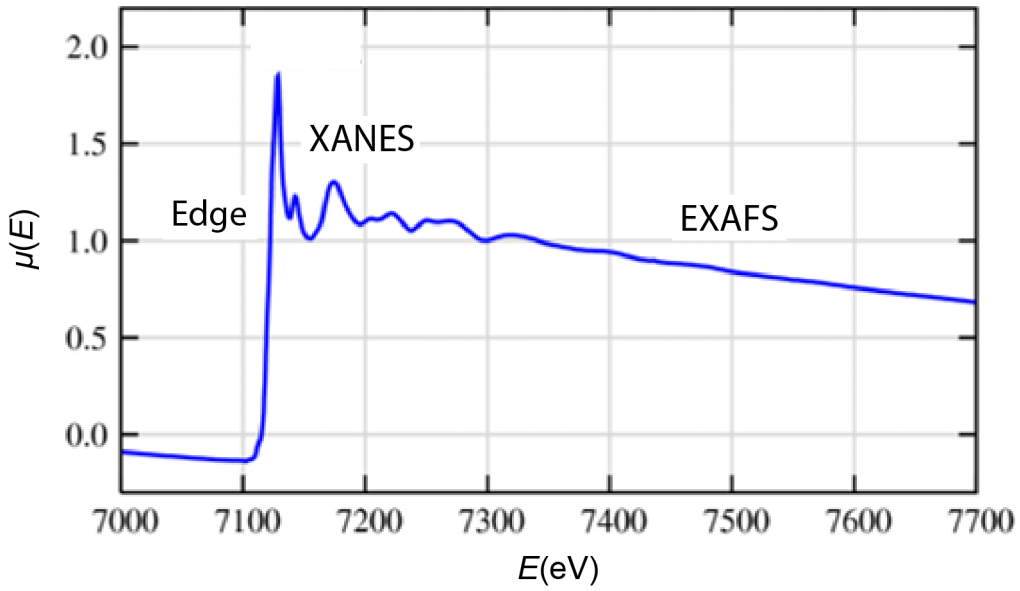

Figure 3.13: XAS spectra of FeO showing the absorption edge, and the XANES and EXAFS regions. Image taken from Newville (2014).

The oscillations in the XANES and EXAFS regions are a product of the interaction ('scattering') of the ejected photoelectron wavefunction and the electrons of the neighbouring atoms. If the backscattered wavefunction is in phase with those propagating from the absorber, then an increase in the absorption coefficient is seen as a result of constructive interference. The constructive and destructive interference form the oscillations seen in Figure 3.13 as the wavelength of the X-rays (and therefore the photoelectron) is decreased as the energy of the incident X-rays is increased.

Data processing and analysis

The theory and data processing/analysis of EXAFS data is well documented in the literature. The following was therefore collated from a handful of sources (Roy and Gurman, 1999; Allen et al., 2000; Mayanovic et al., 2002; Ha et al., 2011; Frenkel et al., 2011; Newville, 2014; Louvel et al., 2015).

A typical workflow for XAS data processing and analysis followed the steps:

1. Conversion of raw data into $\mu(E)$ (the X-ray coefficient, explained below);

2. Removal of unwanted data in $\mu(E)$ - i.e. defining the final energy range to be included in the further stages (avoiding other edges, etc.);

3. Background removal and normalisation, and defining a value for the threshold energy, E_0;

4. Conversion of $\mu(E)$ data into k-space to produce data as $\chi(k)$ (the EXAFS data), accompanied by the necessary k-weighting (depending on signal strength);

5. Defining the useful data range of k (Å);

6. Fourier transform $\chi(k)$ to produce $\chi(R)$ (i.e. k- to R-space), which isolates the oscillations in the data attributable to different shells.

These steps are shown in Figure 3.14.

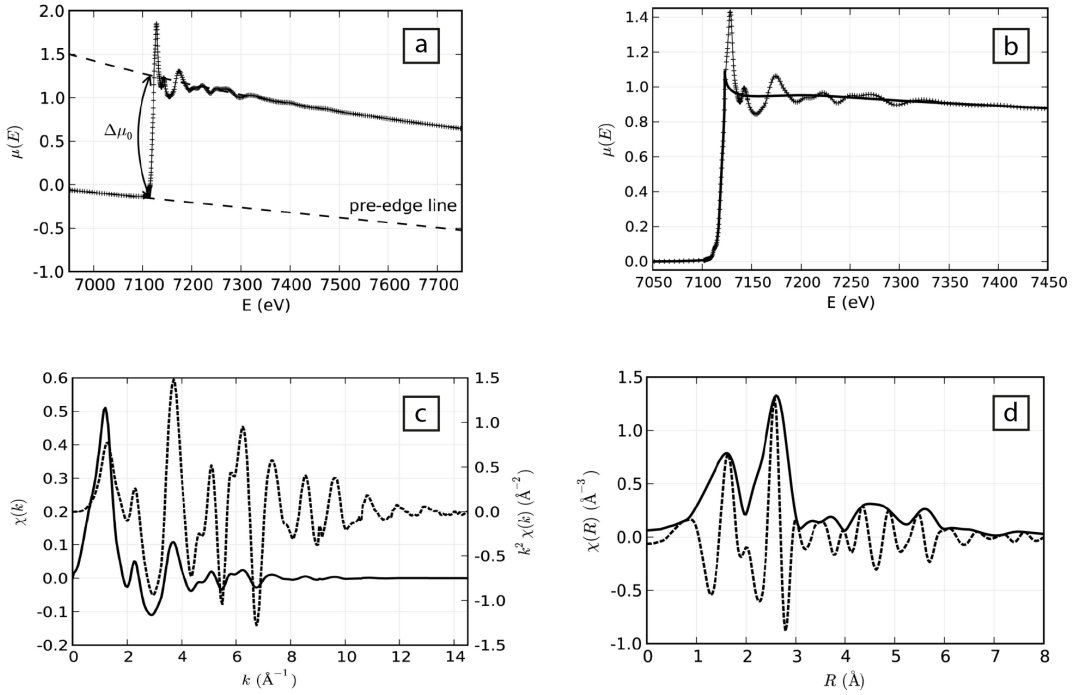

Figure 3.14: Examples of the data processing steps mentioned in text. a) pre-edge subtraction and normalisation; b) post-edge subtraction; c) isolated $\chi(k)$ (bold line) and the same data K^2-weighted (dashed line); d) Fourier transforemd data, $\chi(R)$, with the magnitude (bold line) and real (dashed line) parts. Images taken from Newville (2014).

Once the data is reduced/processed, the following steps are taken:

7. Modelling of the $\chi(R)$ (and $\chi(k)$) data to individual scattering paths, which are calculated from the structural information in .cif files. Progressively more distant shells are included in the fit (by defining and then increasing the fitting window in R-space), which is limited by the useful data in k-space.

Reduction of the raw data included the XANES and EXAFS regions (steps 1 to 6), and was performed using the Athena programme, and modelling to structural information files (step 7) was performed in the Artemis programme, both of which are part of the Demeter package version 0.9.25 (Ravel and Newville, 2005).

Raw XAS data collected from the beamline are converted to $\mu(E)$, the X-ray absorption coefficient, which for transmission mode is the natural log of the incident beam intensity over the transmitted beam intensity:

$$\mu(E) = log(I_0/I)$$

where I = intensity of the X-ray transmitted through the samples, and I_0 = the intensity of the incident X-ray. In fluorescence mode, $\mu(E)$ is proportional to the fluorescence beam intensity over the incident beam intensity:

$$\mu(E) \alpha I_f/I_0$$

where I_f = the intensity of the fluorescence X-rays. The EXAFS signal contained within the oscillatory region of $\mu(E)$ is then extracted by normalising the $\mu(E)$ data by the edge step and subtraction of the background:

$$\chi(E) = \frac{\mu(E) - \mu_0(E)}{\Delta\mu_0(E)}$$

where $\mu_0(E)$ is a smooth background function, as shown in Figure 3.14. Background removal was done in the pre- and post-edge regions, which in most instances was based on automatically-chosen values in Athena; where unsuitable, manual values were input. The edge value, E_0, was determined as the inflection point of the derivative of the spectra, also automated by the software but again adjusted where necessary. The X-ray energy is then converted into wave number, k:

$$k = \sqrt{\frac{2m(E - E_0)}{\hbar^2}}$$

Where m is the electron mass. In this way, the EXAFS signal is presented as $\chi(k)$. Because the amplitude of the signal in k decays quickly, it can be amplified by k^2 or k^3. In this investigation, k^2-weighting was used in all cases for plotting.

The EXAFS equation describes the oscillations in the $\chi(k)$ data in terms of the number of neighbouring atoms, the scattering properties of those atoms and their disorder:

$$\chi(k) = \sum_j \frac{S_0^2 N_j f_j(k) e^{-2Rj/\lambda(k)} e^{-2k^2\sigma_j^2}}{kR_j^2} sin2kR_j + \delta_j(k)$$

where $f(k)$ is the amplitude; $\delta(k)$ is the phase shift; j is the individual coordination shell of identical atoms at the same distance from the absorbing atoms; N is the coordination number; R is the distance to the neighbouring atom; and σ^2 is the mean-square displacement in the bond distance (or disorder of the neighbouring atoms, also referred to as the Debye-Waller factor). The final signal is the sum of the contributions of every

possible path the photoelectron can take from the neighbouring atoms. The contribution to the measured spectrum of a scattering path is related to the coordination number, which is calculated by multiplication of the amplitude and a correction factor of the amplitude, known as the passive electron reduction factor, S_0^2. Elemental values for S_0^2 are well approximated, and generally fall between 0.7 and 1.0. The EXAFS equation is used for determining N, R and σ^2.

The final data processing step is to Fourier transform the data into R-space, which isolates the different frequencies within the oscillations of k-space that are related to different coordination shells. The measured data is then fit, using the EXAFS equation and its variable parameters, in both the magnitude and real part of the Fourier transform.

During the modelling stage, structural information files (.cif) containing atomic coordinates are input (using the programme ATOMS) and used to generate all possible paths (using the programme FEFF) the photoelectron can take when scattering off nearest neighbours. These include both single- (SS) and multiple-scattering (MS) paths, the former of which dominate the total signal EXAFS signal (i.e. the most intense). The .cif files used in this investigation were downloaded from the Inorganic Crystal Structure Database (ICSD).

When FEFF is run, the phase shift and amplitude are calculated for each path, leaving the parameters of interest to be guessed or refined during the modelling of experimental data to the theoretical fit of that structure. During fitting these parameters were:

1. coordination number, N;
2. the effective half-path length, R (interatomic distance in single scattering paths), or technically ΔR (i.e. the difference in R between measured and calculated bond length);
3. atomic/structural disorder, or Debye-Waller factor, σ^2;
4. passive electron reduction factor, S_0^2;
5. ΔE_0, the difference between the user-defined E_0 value in Athena and that calculated by FEFF.

However, when modelling, the number of free parameters being calculated should not exceed the number of independent data points available from the data, which is determined from the available data range in k- and R-space:

$$N_i np = 2\Delta k \Delta R/\pi$$

The number of parameters is restricted, and the quality of the final fit is judged partly on the number of parameters used/guessed; during the analysis of the samples in this investigation the values of S_0^2 and E_0 were treated as a 'global parameter' – i.e. the same value was used for each path in a single fit. The value for S_0^2 was determined by collecting XAS data on standard materials. Data for REE carbonate and REE fluoride samples were modelled using their respective .cif files; knowing the structure, and therefore the REE coordination number, means the value for CN can be fixed and the value for S_0^2 set as a guess parameter. As the S_0^2 value for an element, e.g. Nd, can be approximated as being the same for different materials in which that element is the absorbing atom, the value calculated from the standards was used (i.e. set, not guessed) when modelling unknown samples. The values used for S_0^2 in this investigation were: La = 0.9, Nd = 0.85, Er = 0.95, Yb = 1.0

Additional steps taken to reduce the number of 'guess' parameters were:

1. grouping of atoms (of the same element) at distances closer than $\pi/(2 * k\text{-range})$ Å of each other (i.e. assignment of the same guess value for σ^2 and ΔR). This is the physical limit of determining bond length with EXAFS;

2. using the same 'guess' parameter of σ^2 for atoms (of the same element) within about 0.5 Å of each other. These were applied on a fit-by-fit basis.

A final parameter fixed during most fits was coordination number. In the case of known structures (i.e. from PXRD), this is easily and obviously justified. In the case of X-ray amorphous material and the unknown phases in solutions, which are the focus of the XAS work in this thesis (Chapter 5), the experimental data was fit to a structural file thought most likely to represent the crystalline phase it would transform into – i.e. potentially show similar short-range order as the crystalline material. These assumptions were based on the results of previously published works (Wakita and Nagashima, 1972; Liu and Ma, 1997b, 2007), where the elements found to produce X-ray amorphous material in the current study (most notably Er) have been shown to form crystalline material (probably a result of slight variations in preparation method as discussed in the previous chapter). However, to justify further this action, first shell-only fitting was undertaken on each of these phases, fixing S_0^2 to the values stated above, and guessing coordination number. In all cases the returned values were within error to those expected. CN values of distant shells were also manually-refined to assess the influence on the fit quality, with the idea that X-ray amorphous material should not have longer-range structure the same as the structural file used in modelling; smaller CN values for more distant shells suggests lower order.

Reasonable values for the other guessed parameters, when CN was fixed, were used as an additional tentative check to a fit's quality. These are flagged by the software if exceeded:

1. σ^2 values be positive definite (values initially guessed at 0.003 Å^2);

2. ΔR values should not exceed 0.5 Å ($<$ 0.3 Å used here);

3. E_0 values should not exceed $\pm$ 10 eV;

4. An R-factor of < 0.02 (explained below).

When fitting in Artemis, a 'window' was used to restrict the R-space range over which the data was fit, effectively isolating different shells. Guess values for the unknown parameters of interest were assigned and the fit assessed. Fitting was iterated by inclusion of different SS and MS paths over the data range of interest until the returned value for chi-square and reduced chi-square were at their minimum, assuming the other checks noted above were met. In the X-ray amorphous materials the inclusion of more distant paths to the absorbing atom often reduced the determined quality of the fit. Chi-square and reduced chi-square measure the misfit relative to the estimated uncertainty, with the latter used to compare fit quality as it takes into account the number of variables used relative to the number of independent points. Here, chi-square is defined as:

$$\chi^2 = \sum_{i}^{N_{data}} \frac{[y_i^{data} - y_i^{model}(x)]^2}{\epsilon^2}$$

where N_{data} = the number of points being fit, y_i^{data} = the experimental data, $y_i^{model}(x)$ = the model, which depends on the variable fitting parameters, x, and ϵ = the measurement uncertainty. Reduced chi-square is defined as:

$$\chi_v^2 = \frac{\chi^2}{N_{data} - N_{var}}$$

where N_{var} = the number of variable parameters in the fit. During EXAFS analyses, values for reduced chi-square are commonly up to several orders of magnitude worse than 1, which in principal is the value for a good fit when the uncertainty is well known.

An additional statistic, known as the $\mathcal{R}$-factor, is used as a measure of the 'closeness of fit' (or misfit) between modelled and experimental data, and is defined as:

$$\mathcal{R} = \frac{\sum_i^{N_{data}} [y_i^{data} - y_i^{model}(x)]}{\sum_i^{N_{data}} [y_i^{data}]^2}$$

Values are measured as a percentage of misfit, with a value of 0.02 (i.e. 2 %) chosen as the upper limit in the current investigation.

Ultimately the fits were deemed acceptable when the above criteria were met, and when the addition of more scattering paths did not improve the fit.

During XAS analyses, a two-REE (Nd and Er) solution was used to precipitate a carbonate, although in this instance only the aged samples were analysed. Despite the initial solution being equimolar, it was unknown what the relative amounts of Nd and Er were in the precipitates, and how this would affect its behaviour. Using the XAS spectra, it is possible to calculate the former because the amount of the absorbing element is proportional to the edge step (i.e. the jump from the pre-edge energy to that just at the post edge), as this is related to the X-ray cross-section and the density and thickness of the sample. The procedure, explained in a personal communication by Fred Mosselmans (2017), is as follows:

1. Extract the edge step values from Athena (they were calculated during the background removal steps);
2. Calculate the log of the change in transmission over the edge (at both the Nd and Er edge), i.e. ln (% transmitted pre edge / % transmitted post edge) for each sample (i.e. four values – NdEr 40 A and NdEr 90 A);
3. Use the calculator at http://henke.lbl.gov/optical_constants/filter2.html to equal the values found in step 2. This requires guessing the thickness of the sample until the calculated edge step value matches those in step 2 – i.e. working out the thickness of the sample;
4. Using the calculated thickness of the sample, calculate the volume;
5. Using this volume and the density of the material of interest, calculate its mass;
6. Using the mass of the material calculate the number of moles of Nd and Er in each sample, and hence the relative amounts.

This procedure was only used for the Nd+Er precipitates, and the results can be found in Chapter 5.

Chapter 4

Structural and morphological variations of synthetic REE carbonates with respect to atomic number: implications for HREE crystallinity in low temperature environments

4.1 Introduction

Rare earth elements (REEs) are essential components in a multitude of modern industrial and digital applications but their supply is marred by volatility issues, and as such they are included in the list of critical metals (Chakhmouradian and Wall, 2012; USGS, 2016). Their predominant source is the fluorocarbonate bastnäsite ($REECO_3F$), and a number of other REE-carbonates are becoming increasingly important for materials science purposes. Such minerals include the carbonate hydrates ('normal type') lanthanite ($REE_2(CO_3)_3 \cdot 8\,H_2O$) and tengerite ($REE_2(CO_3)_3 \cdot 2{-}3\,H_2O$), and hydroxyl carbonates ('basic-type') hydroxylbastnäsite ($REECO_3OH$) and its polymorph kozoite (Wickleder, 2002). With the exception of tengerite-(Y), natural specimens of these minerals are enriched in light REEs (LREE - Dal Negro et al., 1977; Bevins et al., 1985; Maksimovic, 1985; Miyawaki et al., 1993, 2000; Yang et al., 2008; Morrison et al., 2013).

Despite the importance of REE carbonates and fluorocarbonates, the conditions at which these minerals form, their crystallisation pathways, and the reason why HREE enriched versions are so uncommon in nature remains unclear. Synthetic crystallisation of simple REE carbonate phases, under controlled conditions, can shed light on

these processes, and accordingly has been the focus of research over the past 60 years, with numerous methods employed (e.g. Salutsky and Quill, 1950; Charles, 1965; Sastry et al., 1966; Nagashima et al., 1973; Christensen, 1973a; Foger et al., 1992; Refat, 2004; Liu and Ma, 2007; Rodriguez-Blanco et al., 2014). The most common methods are simple mixing experiments followed by ageing at various (commonly low, i.e. < 200 °C) temperatures, with other variables including the precipitant, solution concentration, start and finish pH, use of a CO_2 atmosphere, length of ageing, and agitation/stirring of the solutions. Although a significant amount of data has been collected, the results are inconsistent, with some authors observing micro (and nano?) crystals, while others produce only X-ray amorphous material when working with the same REE. These discrepancies are attributed to (often very) subtle differences in preparation technique. However, a general pattern appears to be that, even with these variations in preparation, X-ray crystalline materials are more commonly produced when working the lighter REEs and the behaviour of the heavier REEs is less predictable. Although crystalline material for the heaviest REEs (Ho, Er, Tm, Yb and Lu) has been synthesised previously (e.g. Caro et al., 1972; Foger et al., 1992; Liu and Ma, 1997b), the methods employed are in some cases very similar to those in which only X-ray amorphous material was formed.

Recent work has shown that LREE carbonates crystallise *via* the transformation of an X-ray amorphous, highly hydrated precursor phase, and that the structure and morphology of the crystalline material is dependent on the temperature at which the solutions are heated (e.g. Shang et al., 2009; Vallina et al., 2014). Results suggest that the lifetime of this precursor phase is controlled by the energy required to dehydrate it, which, for the elements La, Ce, Pr, Nd and Dy, is seen to increase linearly with Z (e.g. Vallina et al., 2013, 2014). This trend has therefore been postulated to extend to the heavier REEs, however, data for these elements are lacking and few studies have investigated the crystallinity of representatives from across the REE series as a function of temperature (e.g. Nagashima et al., 1973).

Although a large number of studies utilising various preparation techniques have been undertaken, there has been a surprising lack dedicated to preparation of carbonates from solutions containing more than one REE (e.g. Lechevallier et al., 2010; Zhou et al., 2015), and even fewer have studied solutions with more than two REEs. Such an observation is important given that natural systems and minerals always contain multiple REEs, and many modern applications require the use of numerous REEs (particularly doping of materials with REEs to exploit their luminescent and magnetic properties - e.g. Kaczmarek et al., 2015). Identifying cross-series trends, as well as behavioural differences in the presence or absence of others REEs, is important for synthesis of multi-REE carbonates.

This chapter is dedicated to the synthesis of REE carbonates using a consistent, simple and common solution mixing technique, followed by ageing at temperatures up to 200 °C. It includes representatives from across the REE group, used in individual and multi-REE systems, to identify any differences in crystallisation characteristics as a function of *Z*. The behaviour of individual REEs when precipitated from multi-REE solutions is also assessed.

4.2 Methods

4.2.1 REE carbonate synthesis

To produce the material for this study, REE-bearing chloride solutions were titrated with sodium carbonate at room temperature (RT). Some were filtered immediately after cessation of carbonate addition (approximately 10 mins, termed 'fresh' precipitates - FP), while in other experiments the precipitates were aged in their mother solutions at various temperatures and for different lengths of time (termed 'aged' precipitates - Table 4.1).

The concentrations of individual REEs was between 0.1 and 0.066 M, which were made by mixing the stock 0.2 M REE chloride with HCl (single REE solutions) or other REE chloride solutions (multi-REEs), as described in Chapter 3. Each of the REE-bearing solutions was titrated quickly (approx. 10 mins) with 0.15 M Na_2CO_3 at room temperature (21 °C), while stirring continuously. In all cases the pH was monitored throughout carbonate addition with a Radiometer Analytical PHM 220 pH meter and REFEX glass AgAgCl combination electrode. Starting pH values for REE chloride solutions were around 0.8 – 0.9, and titrations were terminated at approximately pH 8.5. All the solutions were completely opaque at the cessation of carbonate addition. The final pH of 8.5 was chosen because above this the rate of pH change with addition of Na_2CO_3 solution rapidly increased.

A total of 47 experiments were completed for single- and multi-REE-bearing systems. Table 4.1 outlines the experimental matrix, including the temperatures and ageing durations.

The solutions heated at < 100 °C were placed in 15 ml serum bottles that were stoppered shut with butyl rubber, crimp sealed and placed in a preheated oven at 40 or 90 °C, and left for six weeks. The experiments run at > 100 °C were heated in custom made, sealed PTFE vessels (10 ml volume), which were themselves placed into a larger vessel equipped with a pressure release valve, and placed into an oven. The larger vessel was half-filled with deionised water to balance the pressure between the two sets of vessels. At the end of each experiment the products were quenched, vacuum filtered

on 0.45 μm mixed cellulose ester membrane filters, washed with deionised water and left to air dry.

REE	FP	40 °C	90 °C	130 °C	170 °C	200 °C	Conc (M)
La	0	42	42	-	-	-	0.1
Nd	0	42	42	4	2	1	0.1
Er	0	42, 84	42	4, 14	2	1	0.1
Yb	0	42	42	14	2	1	0.1
La+Nd	0	42	42	-	-	-	0.1
La+Gd	-	42	42	-	-	-	0.1
La+Er	-	42	42	-	-	-	0.1
La+Yb	0	42	42	-	-	-	0.1
Nd+Er	-	42	42	4	2	1	0.1
Er+Yb	-	42	42	-	-	-	0.1
La+Nd+Er	-	42	42	-	-	-	0.66
La+Nd+Gd+Er+Yb	-	42	42	4	2	1	0.044

Table 4.1: Experimental matrix for the titrations showing the time (days) and temperatures at which each of the solutions and their precipitates were treated. FP = fresh precipitates formed at room temperature. Two 40 °C and two 130 °C Er samples were run. The concentrations quoted in the final column refer to each individual REE, not the total concentration. Hyphens denote no sample.

4.2.2 Characterisation

All products were characterised by powder X-ray diffraction (PXRD). Most samples were also characterised using attenuated total reflectance Fourier transform infrared spectroscopy (ATR-FTIR), and most were imaged by scanning electron microscopy (SEM).

FTIR spectra were collected using a Bruker Vertex 70 spectrometer equipped with a diamond internal reflection cell and running OPUS 7.0 spectroscopy software. Spectra were collected from 500 to 3900 cm^{-1} at steps of 4 cm^{-1}, with a total of 500 measurements merged to produce each spectrum.

Powder PXRD patterns were collected on a Bruker D8 Advance X-ray spectrometer, using CuKα radiation, from 2 to 65 2θ at intervals of 0.025° and for 1.5 seconds per step. Phase identification was performed using EVA X-ray diffraction software utilising the international centre for diffraction data (ICDD) database, and Rietveld analyses for quantitative mineral identification in multi-phase systems was performed using TOPAS, both of which are made by Bruker.

SEM imaging was performed on a Carl Zeiss SIGMA HD VP field emission gun scanning electron microscope operating at an accelerating voltage of 20 kV. Qualitative chemical analyses were obtained using energy-dispersive X-ray spectrometry (EDS) using an Oxford Instruments Aztec analysis system, which required the samples to be carbon-coated before analysis.

4.3 Results

4.3.1 Fresh precipitates

The behaviour of the fresh precipitates (i.e. those filtered immediately after the termination of the titrations) of the elements investigated varied systematically. The PXRD and FTIR spectra for these products are presented in Figure 4.1a and b, respectively.

In the La system, PXRD analysis identified the structure lanthanite ($La_2(CO_3)_3 \cdot 8\,H_2O$ - PDF 04-010-3609) as having formed within the first 10 minutes of reaction (i.e. before the precipitates were filtered). The FTIR spectra of this sample contains characteristic bands for carbonate ions between approximately 670 and 1500 cm^{-1} (e.g. Zhao et al., 2008; Shang et al., 2009; Frost et al., 2013), and large, broad bands for symmetrical O-H stretching (between 2500 and 3700 cm^{-1}) and in-plane O-H scissoring (approximately 1645 cm^{-1}, Chukanov and Chervonnyi, 2014), consistent with a highly hydrated lanthanite phase (Dal Negro et al., 1977).

In the Nd, Er and Yb experiments, the fresh product was in all cases found to be X-ray amorphous. In the case of Nd, two broad humps centred approximately on 23 and 45 degrees 2θ were observed. Similar humps were seen in the Er and Yb spectra, this time at approximately 32 and 48 degrees 2θ.

FTIR analyses of the Nd, Er and Yb phases again reveals vibrations characteristic of carbonates between 670 and 1500 cm-1, although the spectra are more simple than that of lanthanite-(La). The most intense of these occur at approximately 1506, 1384 and 844 cm^{-1} (values stated for Er), which are attributed to C-O υ_3 asymmetrical stretching of carbonate (Adler et al., 1963). The same O-H stretching of structural water as seen in the La sample is present. Bands corresponding to O-H stretching (around 3475 cm^{-1}) and bending (around 3625 cm^{-1}) of hydroxyl groups are absent, indicating these products are likely hydrated normal carbonates. The bands between approximately 2320 cm^{-1} and 2430 cm^{-1} in some of the Nd, Er and Yb spectra are attributed to C-O stretching of atmospheric CO_2 (Hartman and Hisatsune, 1966).

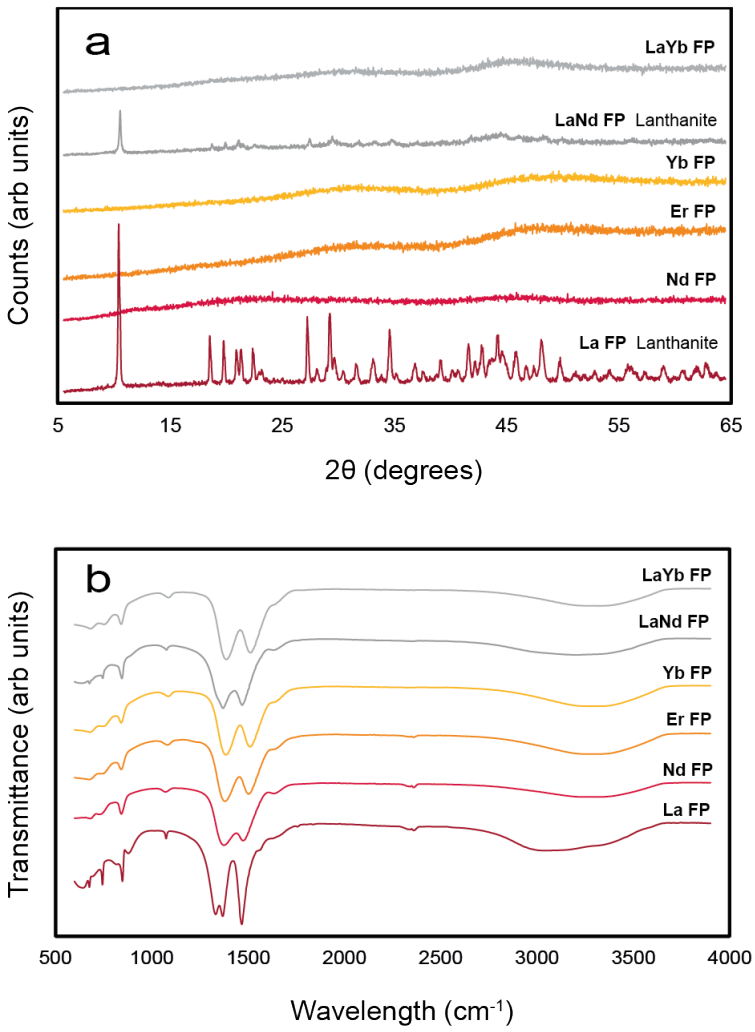

Figure 4.1: a) PXRD traces for the fresh precipitates; b) FTIR data for the same samples. FP = fresh precipitate.

The mixed La and Nd solution behave in an intermediate way when compared to the individual elements, with the PXRD analysis again detecting lanthanite, but this time of lower intensity than in the La-only sample. This could indicate the presence of pure La-bearing lanthanite mixed with an X-ray amorphous phase (Nd or mixed La+Nd?) or a mixed La- and Nd-bearing lanthanite (Nd can accommodate into the lanthanite structure, e.g. Graham et al., 2007). Evidence for a mixture of crystalline and X-ray amorphous material is provided by the FTIR spectrum for this sample, which most resembles that of the X-ray amorphous Nd, Er and Yb precipitates (Figure 4.1b).

In the mixed La+Yb experiment, the first-formed precipitates behave in a similar way to that of the individual Yb precipitates outlined above. There is no crystallisation observed when analysing the sample by PXRD, with an identical trace to that of the single Yb run observed. The same is true of the FTIR spectra.

In all cases above where the materials are X-ray amorphous but produce FTIR absorption bands for carbonate, it is likely these are nano-particulate materials. These phases are the focus of further investigation in Chapter 5.

4.3.2 Aged precipitates

4.3.2.1 Lanthanum

Under all experimental conditions of this study, the La solutions produced crystalline material, as shown in Figure 4.2a.

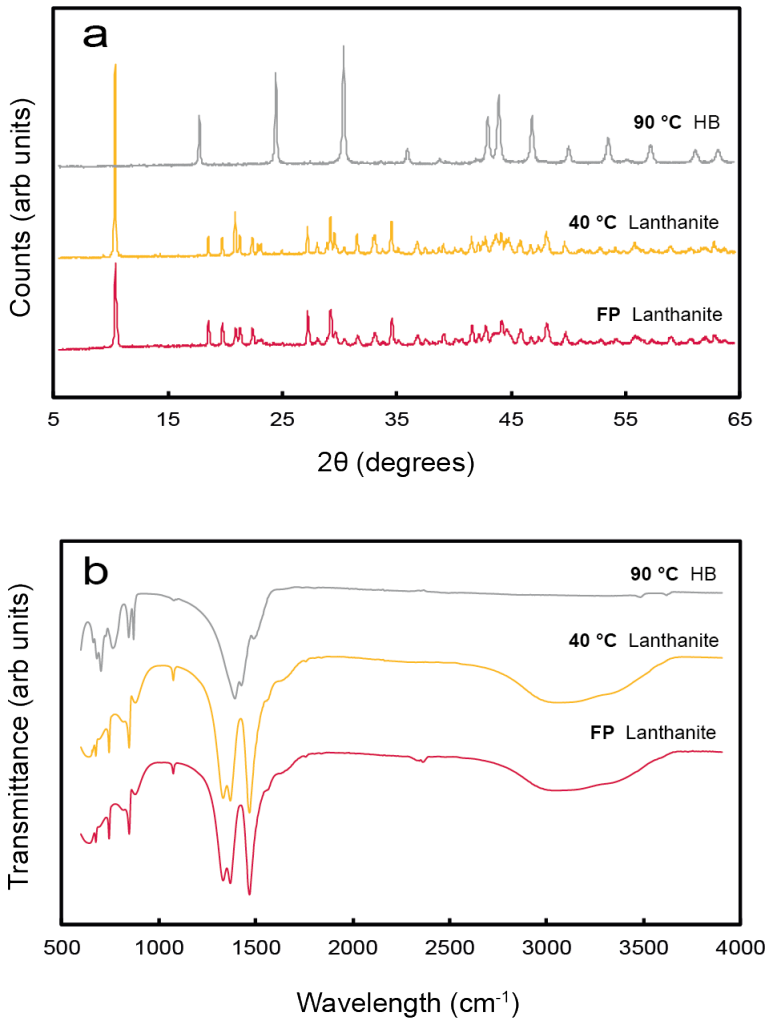

Figure 4.2: a) PXRD traces for the La precipitates; b) FTIR data for the same samples. FP = fresh precipitate; HB = hydroxylbastnäsite.

After six weeks at 40 °C lanthanite-(La) was the sole phase detected, as identified by PXRD, which was identical to that for the fresh precipitate (Figure 4.1a). At 90 °C and after the same length of time, the only phase identified was hexagonal hydroxylbastnäsite-(La) ($LaCo_3OH$ - PDF 00-026-0815).

As might be expected form the PXRD traces, the FTIR spectra for the six week, 40 °C run is identical to that of the FP sample. However, in the 90 °C sample the structural water has been replaced by an hydroxyl group, as evident by the loss of the broad band between 2500 and 3700 cm^{-1} and the appearance of OH bands at 3475 and 3625 cm^{-1} (Figure 4.2b). The trace is also notably different in the region between 600 and 1700 cm^{-1} as a result of the change in structure from lanthanite to hydroxylbastnäsite.

SEM images of the lanthanite-(La) formed after six weeks of ageing at 40 °C reveal the characteristic platey morphology of this mineral (e.g. Dal Negro et al., 1977), with crystals up to 10 μm in length and commonly exhibiting an intergrown habit (Figure 4.3a and b). The hydroxylbastnäsite-(La) is composed entirely of spherules of between 2 and 5 μm in diameter (Figures 4.3c and d), with no other morphologies observed.

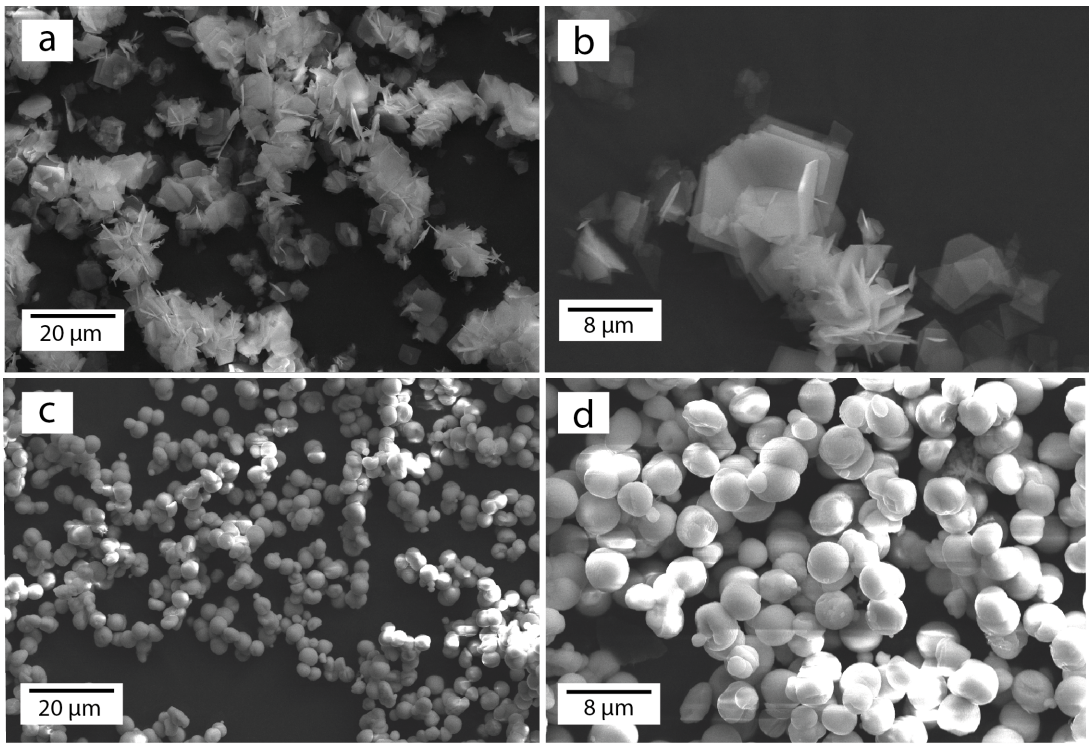

Figure 4.3: SEM images for products of La titrations. a - b) lanthanite formed at 40 °C; c - d) hydroxylbastnäsite-(La) formed at 90 °C.

Experiments were not run at temperatures higher than 90 °C because previous studies have shown that hydroxylbastnäsite-(La) is stable under hydrothermal conditions beyond the upper working limit of the oven used (Vallina et al., 2015).

4.3.2.2 Neodymium

As in the La system, all products of hydrothermal ageing were crystalline, as shown in Figure 4.4a.

At 40 °C the majority of the product was identified as lanthanite-(Nd) (PDF 00-029-0918), with a minor, unquantified amount of tengerite-(Nd) (PDF 00-033-0932). At higher temperatures only mixtures of kozoite-(Nd) (PDF 04-014-7918) and hydroxylbastnäsite-(Nd) (PDF 00-027-1295) were observed. The percentage of each phase, as identified *via* Rietveld analyses, is included in Figure 4.4.

The loss of structural water with increasing temperature is evident from the FTIR spectra. The O-H vibrational bands of H_2O between 2500 and 3700 cm^{-1} are strong in the FP and 40 °C samples but disappear at higher temperatures. O-H stretching of a hydroxyl group is seen in the 90 °C sample, and both stretching and bending bands are present in the samples formed at higher temperatures (the small bands under the labels in Figure 4.4b).

The SEM images reveal the same platey morphology for lanthanite-(Nd) (e.g. Graham et al., 2007) as was seen for lanthanite-(La), but in this case having produced significantly larger crystals up to 500 μm (Figure 4.5a). Also in this sample are radial crystals, possibly the minor tengerite detected by PXRD, that appear to be forming from the lanthanite (Figure 4.5b). A few examples of ball-shaped masses transforming into more crystalline-looking plate-like material composed of elongate crystals are observed (Figure 4.5c), which are also thought to be tengerite (they were sparsely distributed throughout the sample). These images suggest that lanthanite is dissolving and then reprecipitating as tengerite.

The kozoite-(Nd) crystals formed after six weeks at 90 °C exhibit a floret (or sometimes dumbbell) morphology (Figure 4.5d), with some crystals up to 100 μm in length. Figures 4.5e - h show mixtures of a needle-like morphology and a more amorphous looking material at 130 °C (4.5e - f), 170 °C (4.5g) and 200 °C (4.5h). It is unclear which phase is the hydroxylbastnäsite and which is kozoite, particularly at the highest temperature where the majority of material is very fine-grained, even at this magnification.

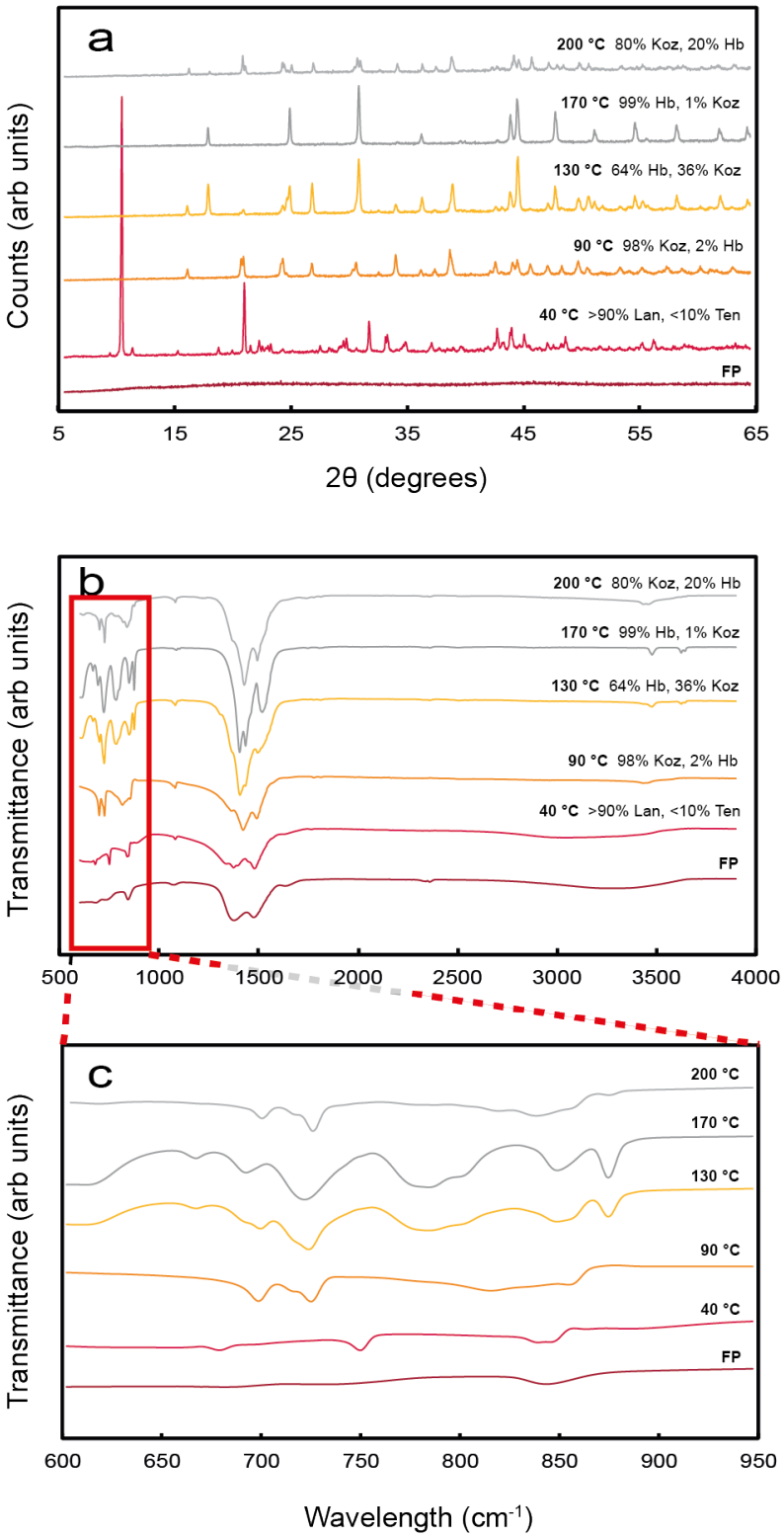

Figure 4.4: a) PXRD traces for the Nd precipitates, including the results of the Rietveld analyses for quantitative phase identification; b) FTIR data for the same samples; c) enlarged view of the 'fingerprint' region of the FTIR spectra. FP = fresh precipitate. Lan = lanthanite; Teng = tengerite; Koz = kozoite; Hb = hydroxylbastnäsite. The exact amount of lanthanite-(Nd) and neodymium carbonate hydrate (i.e. kozoite-(Nd) is unknown in the 40 °C sample because an appropriate structural file necessary for the Rietveld analyses could not be found in the database. Estimate is based made on SEM imaging of this sample in Figure 4.5.

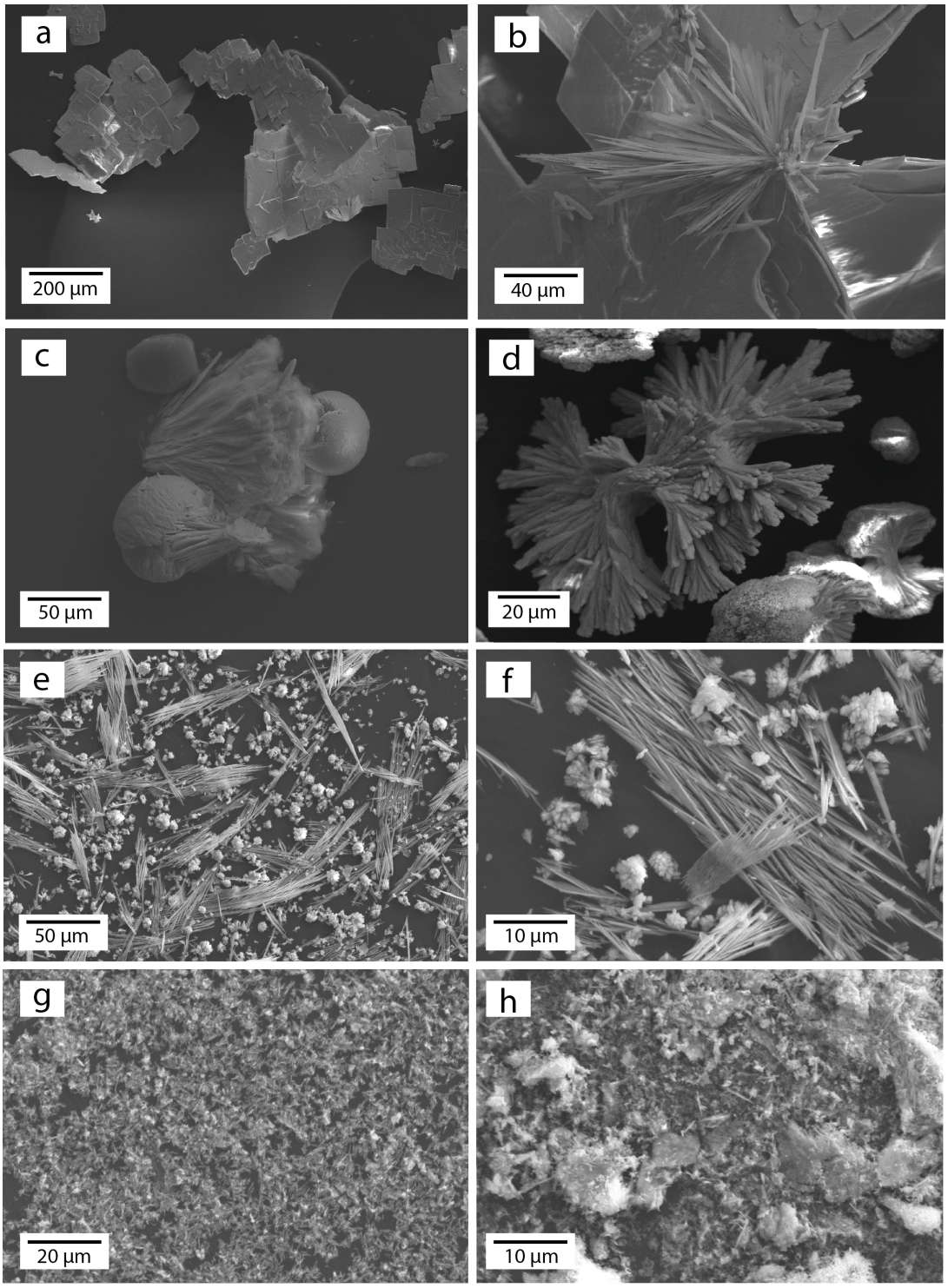

Figure 4.5: SEM images for products of Nd titrations. a - b) lanthanite formed at 40 °C, with minor radial tengerite crystals forming from the former; c) unidentified, but probable tengerite forming at 40 °C; d) kozoite formed at 90 °C; e - f) mixtures of hydroxylbastnäsite and kozoite formed at 130 °C; g) mixture of hydroxylbastnäsite and kozoite formed at 170 °C; h) mixture of hydroxylbastnäsite and kozoite formed at 200 °C.

4.3.2.3 Erbium

The behaviour of erbium was significantly different to that of the LREEs studied. Under all experimental conditions but one, the products remained X-ray amorphous, with two broad humps centred approximately on 32 and 48 degrees 2θ (Figure 4.6a), as described for the FP sample. The only exception is the sample aged for 84 days, which had crystallised into tengerite. Apart from that example, the FTIR spectra were all identical (Figure 4.6b), containing bands characteristic of carbonates, O-H vibrations from structural water, and no hydroxyl groups. The only difference was a decrease in the intensity of the water-related bands (2500 – 3700 cm^{-1} and 1645 cm^{-1}) with increasing temperature. This might suggest a decrease in the number of structural water molecules.

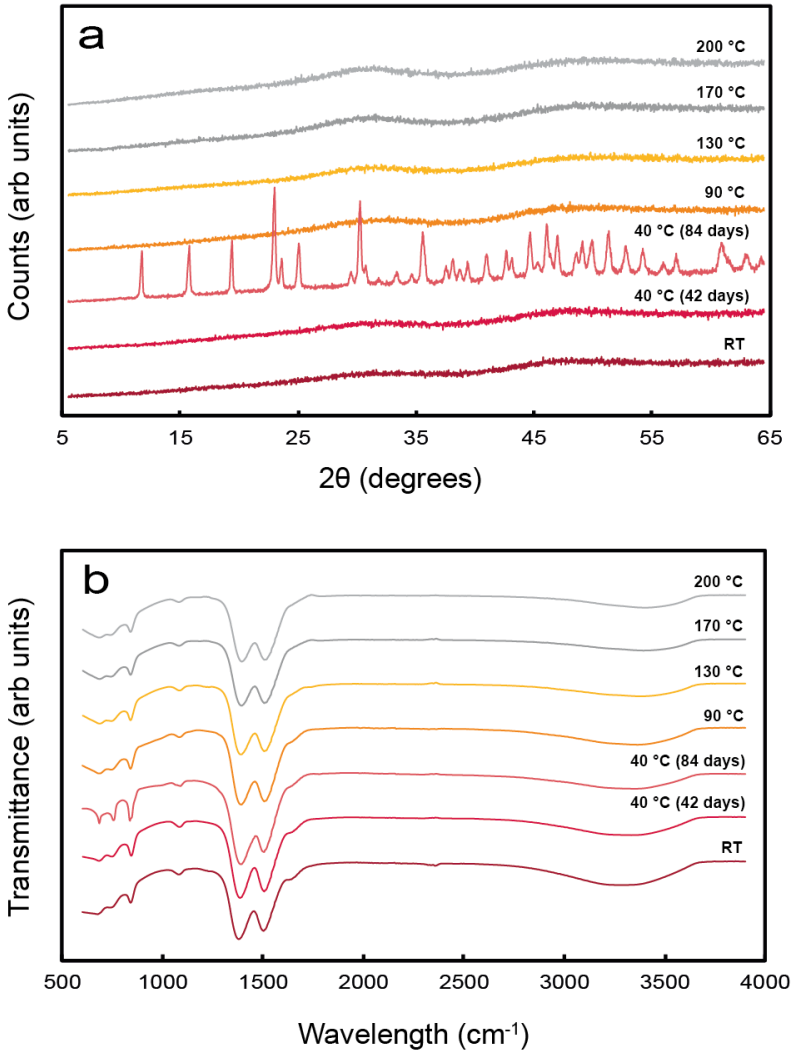

Figure 4.6: a) PXRD traces for the Er samples, all of which are X-ray amorphous except for the 84 day aged, 40 °C sample, which was found to be Er-tengerite; b) FTIR spectra of the same samples, demonstrating their hydrated nature (broad bands below/to the left of the sample labels).

As expected from the PXRD traces, the SEM images of the X-ray amorphous samples revealed no crystal morphologies. Only masses of 'fluffy' textured material were observed (Figure 4.7). Unfortunately there are no SEM images for the crystalline material. Results here suggest that the crystallisation of Er from the X-ray amorphous starting material takes significantly longer than in the lighter REEs studied presently. Interestingly, two experiments were conducted at 130 °C - one for four days and another for 14 - that both produced identical results to the other X-ray amorphous material.

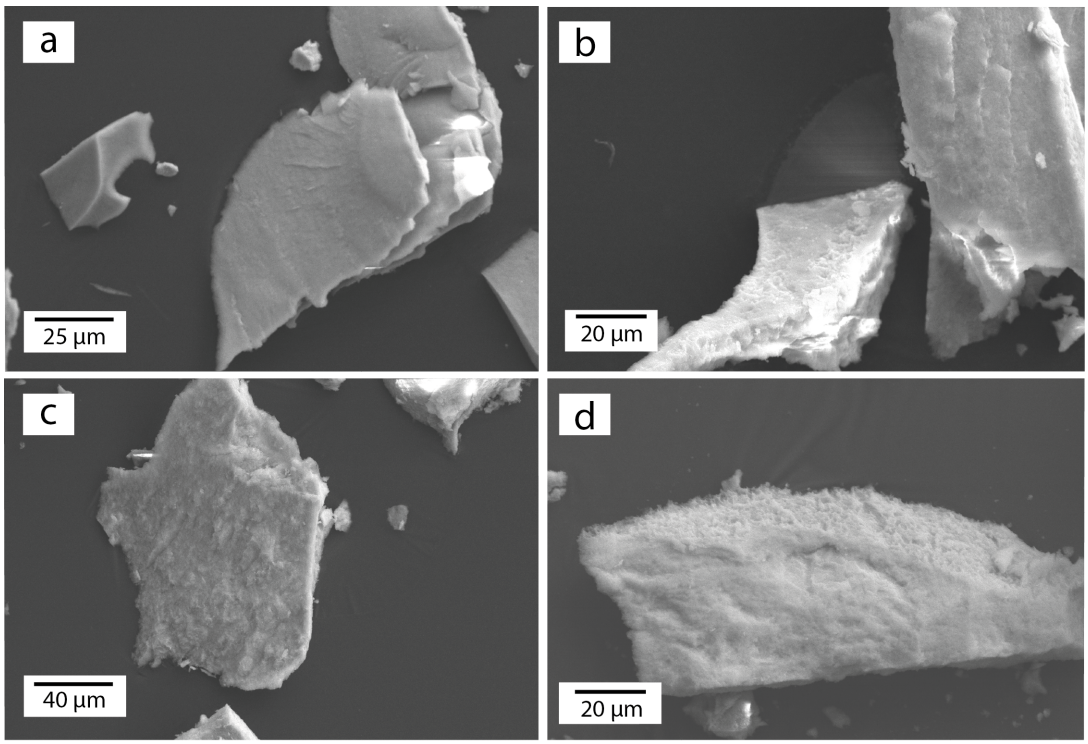

Figure 4.7: SEM images for the products of Er titrations heated at a) 40 °C; b) 90 °C; c) 170 °C; d) 200 °C.

4.3.2.4 Ytterbium

The data for Yb show intermediate behaviour between the LREEs studied and Er. At the lowest temperatures (40 and 90 °C) only an X-ray amorphous material was produced, but at higher temperatures this material started to crystallise (Figure 4.8).

The XRD spectra of the amorphous Yb material was identical to those of the Er samples, with the broad humps centred on the same 2θ values. Their FTIR traces (Figure 4.8) were the same as Er samples at these temperatures (Figure 4.6). At 130 °C the X-ray amorphous material became sufficiently crystalline to produce Bragg peaks (Figure 4.8), although none could be indexed to the reflections of any Yb carbonate phase in the database. It is interesting to note the low intensity of these Bragg peaks given

the crystals observed during SEM analysis (Figure 4.9), which could be explained by dilution of the signal by the X-ray amorphous material; automated background subtraction was performed for all samples, and as such any broader features resulting from amorphous material may have been removed.

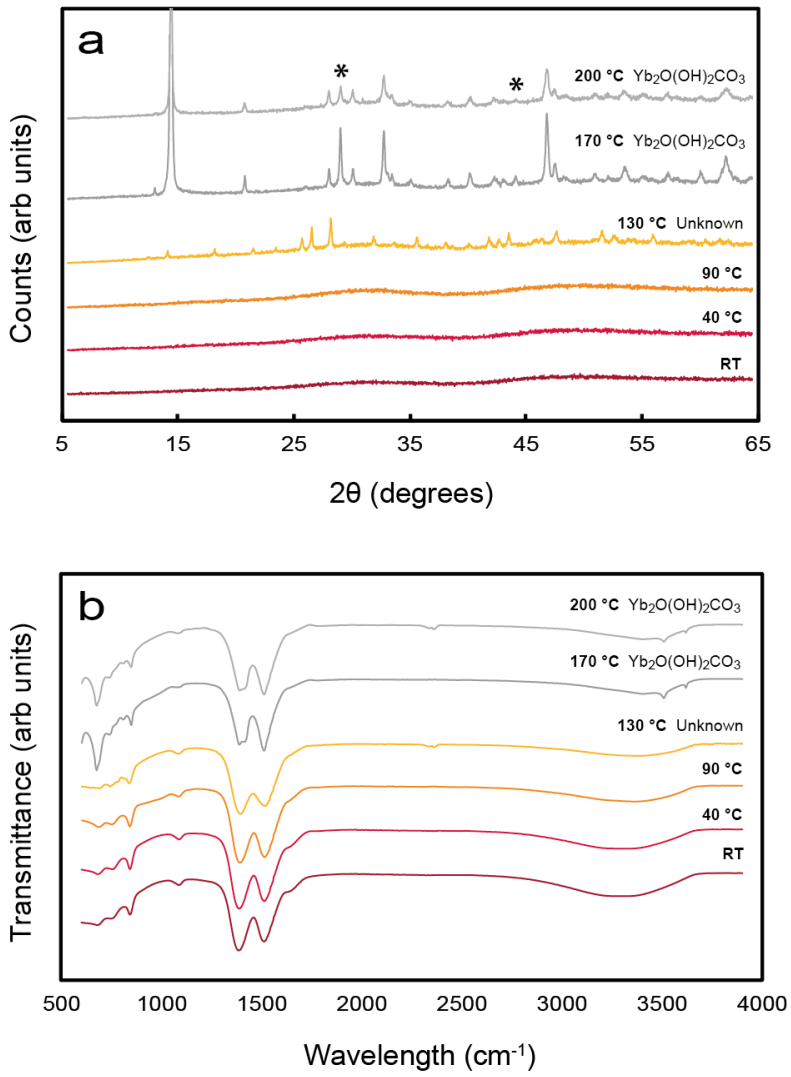

Figure 4.8: PXRD traces of the products from Yb titrations. Asterisks represent peaks in the 170 and 200 °C samples that could not be indexed to any known structure, and that are also not included in the trace of the unknown structure formed at 130 °C. b) FTIR data for the same samples.

The same 'fluffy' texture was observed for the 40 and 90 °C samples, but at 130 °C the X-ray amorphous material was seen to crystallise into spherules composed of plates. The transformation is clearly demonstrated in Figures 4.9b into c. These spherules were quite common, although the remainder of the sample was composed of the same fluffy textured material, presumably the amorphous Yb carbonate. The FTIR trace for

this sample was similar to those at lower temperatures, although the band at approximately 761 cm^{-1} was absent and instead three weak bands at 744, 781 and 811 cm^{-1} were observed, which were presumably from the unidentified crystalline Yb phase. In addition, the absorption bands for H_2O were weaker, but still present; this band was probably from the 'fluffy' material. None of the samples obtained up to 130 °C contained hydroxyl group ions.

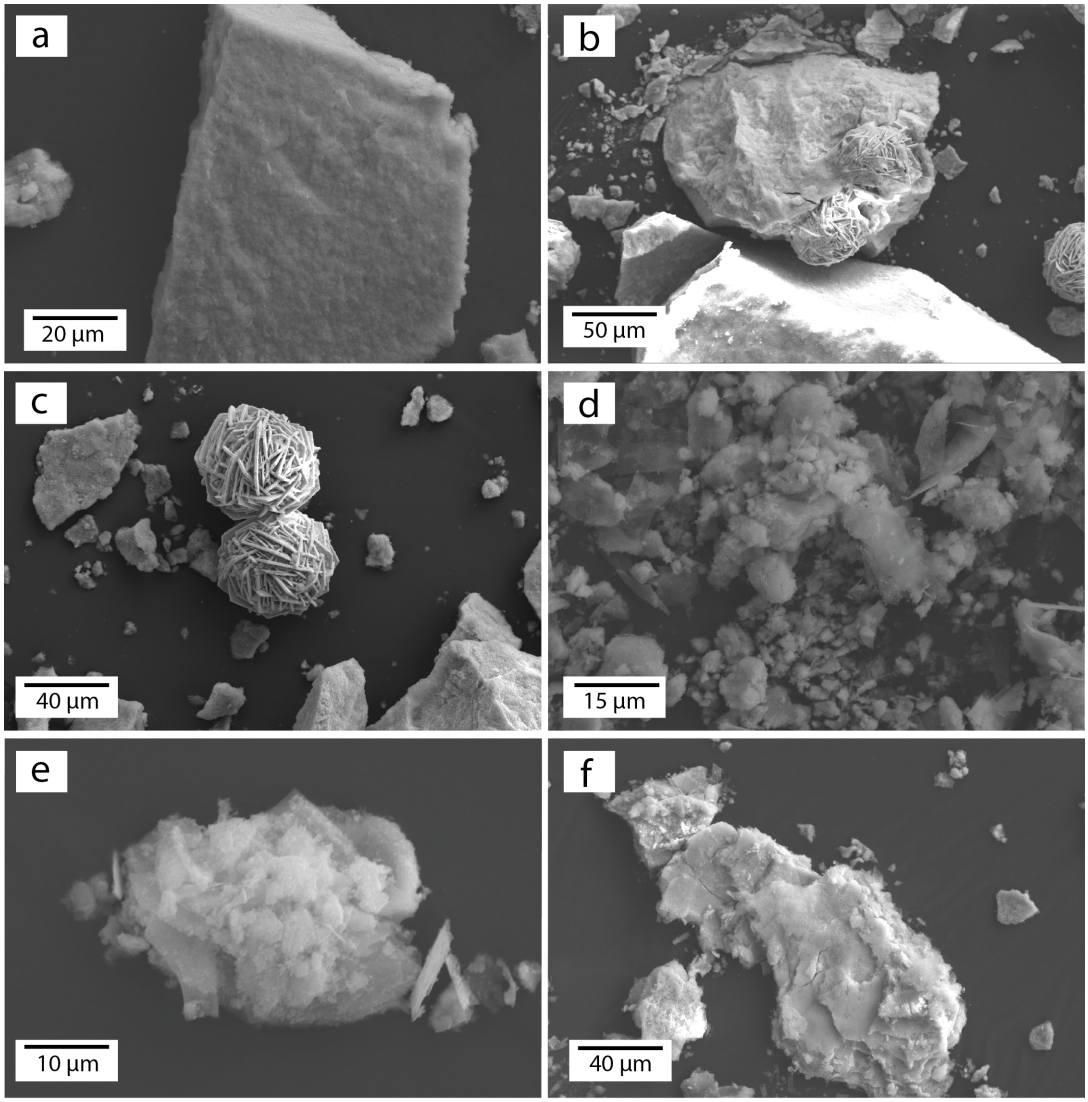

Figure 4.9: SEM images for the products of Yb titrations. a) was heated at 40 °C, and is representative of the material formed at 90 °C (not shown); b - c) shows the unknown crystalline phase apparently forming from the presumed X-ray amorphous material at 130 °C; e) mostly amorphous-looking 'fluffy' phase plus a few crude platey features formed at 170 °C($Yb_2O(OH)_2CO_3$); f) 'fluffy' material from the 200 °C run ($Yb_2O(OH)_2CO_3$).

When the temperature was increased to beyond 130 °C, the material becomes highly crystalline, particularly after two days at 170 °C. All but two of the peaks (asterisked) were indexed to the phase ytterbium oxide carbonate hydroxide ($Yb_2O(OH)_2CO_3$ - PDF 00-039-0500); neither of the unknown peaks matched those of the 130 °C sample, suggesting at least two additional phases. FTIR analyses of these two samples revealed the same characteristic bands for carbonates at 1517, 1390, 1090, 842 and 690 cm^{-1} as seen in every Yb sample, and also contained those at 744 and 811 cm^{-1} seen in the 130 °C run. Additional bands not seen in the other Yb samples occurred at 673, 769 and 1415 cm-1. These higher temperature samples also contained the absorption bands for hydroxyl-group bending and stretching, as well as retaining weak bands for structural water. This may indicate the presence of an additional, hydrous phase, possibly the amorphous Yb carbonate; SEM images confirmed this (Figure 4.9d - f). Very small (< 5 μm) and thin plate-like material was observed in both the 170 and 200 °C samples, although were easier to find in the former. This material was assumed to be $Yb_2O(OH)_2CO_3$ as no other crystalline phases were observed in either sample. None of the spherules in the 130 °C sample were found at the higher temperatures.

4.3.2.5 Multi-REE mixes

To further assess the influence of atomic number on the crystallinity and morphology of the precipitates, a number of experiments containing multiple-REEs in solution were completed. These include mixed LREEs+LREEs, LREEs+HREEs and HREEs+HREEs. More focus (in terms of temperatures investigated) was given to the solutions containing Nd+Er and a five-REE mix, while all the others were heated only up to 90 °C.

La+Nd

When equal concentrations of La and Nd were titrated and heated, the products were crystalline at both temperatures investigated (Figure 4.10). At 40 °C the sole product was lanthanite - i.e. the same as in the La-only solution (Figure 4.2); this mineral was also the most abundant product in the Nd-only example (Figure 4.4). However, the SEM images revealed a slightly different morphology (Figure 4.11); qualitative EDS spectra showed this phase contained both REEs . The crystals retained their platey morphology, as expected from the structure of lanthanite, but this time formed flat, elongate crystals that in many places exhibited intergrown cruciform habit up to 300 μm in length.

When heated at 90 °C, the precipitates did not form either hydroxylbastnäsite (as with La) or kozoite (like Nd), but instead the commonly-occurring natural mineral ancylite (PDF 01-070-1774 - Figure 4.10). However, this phase is isostructural with kozoite (e.g.

Miyawaki et al., 2000) - i.e. the product of Nd-only experiments. The only difference in PXRD spectra between the ancylite and kozoite is a very small (approx. 0.1 degree 2θ) shift in the latter, which is presumably from the incorporation of the larger La ions.

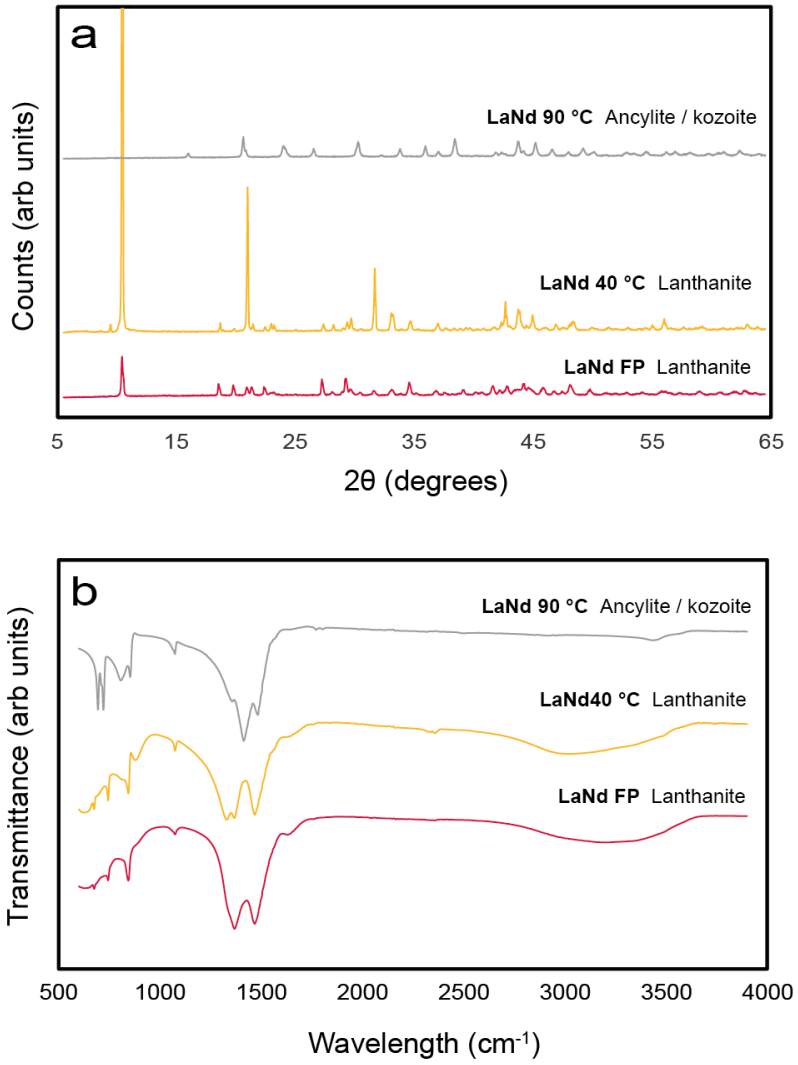

Figure 4.10: a) PXRD trace for the mixed La+Nd precipitates; b) FTIR spectra of the same samples. The FP sample has been included for reference.

SEM analyses (Figure 4.11) reveal the same dumbbell-shaped morphology as was seen for the kozoite-(Nd), and the EDS spectra confirm the presence of both La and Nd (not shown).

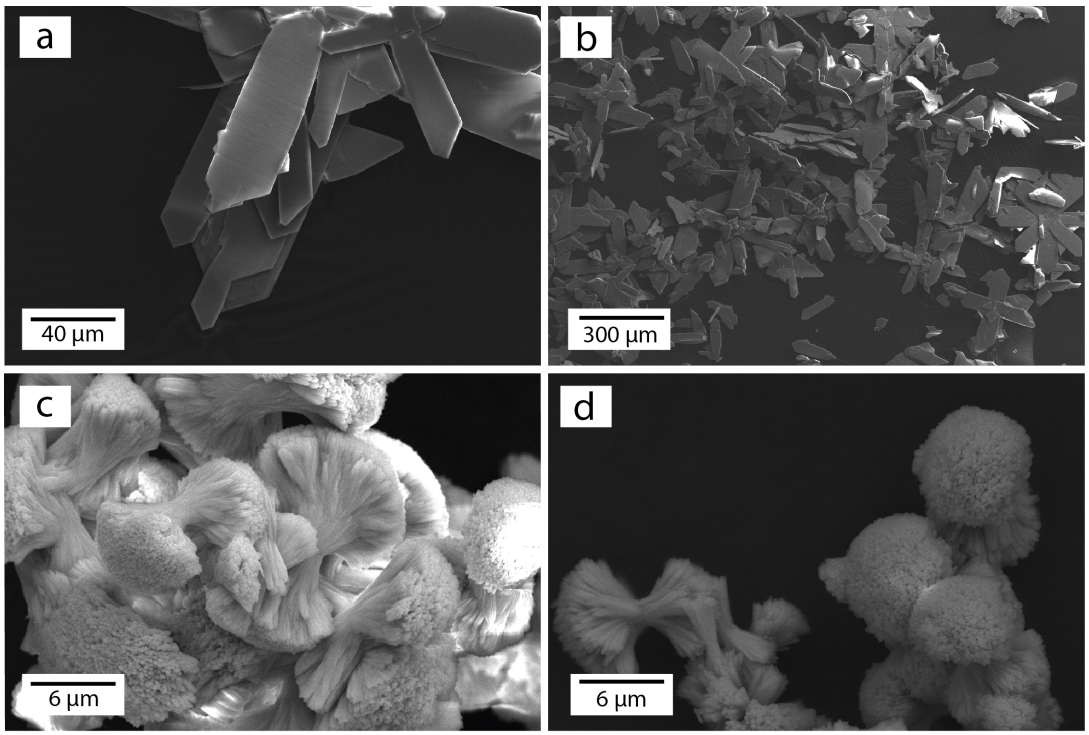

Figure 4.11: SEM images of the precipitates formed from mixed La+Nd solutions. a - b) lanthanite formed at 40 °C; c - d) ancylite formed at 90 °C.

Nd+Er

When equimolar concentrations of Nd and Er chloride were titrated and the products heated, the results were most similar to those of the individual Er experiments. The PXRD traces from 40 to 200 °C were identical, indicating an X-ray amorphous material in all cases; the two broad humps were located at the same 2θ positions as in the Er only samples (4.12). The FTIR spectra were also all identical, except that the bands in the 40 °C sample were stronger than the other samples (Figure 4.12).

The fluffy, amorphous texture of these samples is demonstrated in an SEM image in a few pages, along with those of other mixed REE precipitates (Figure 4.14).

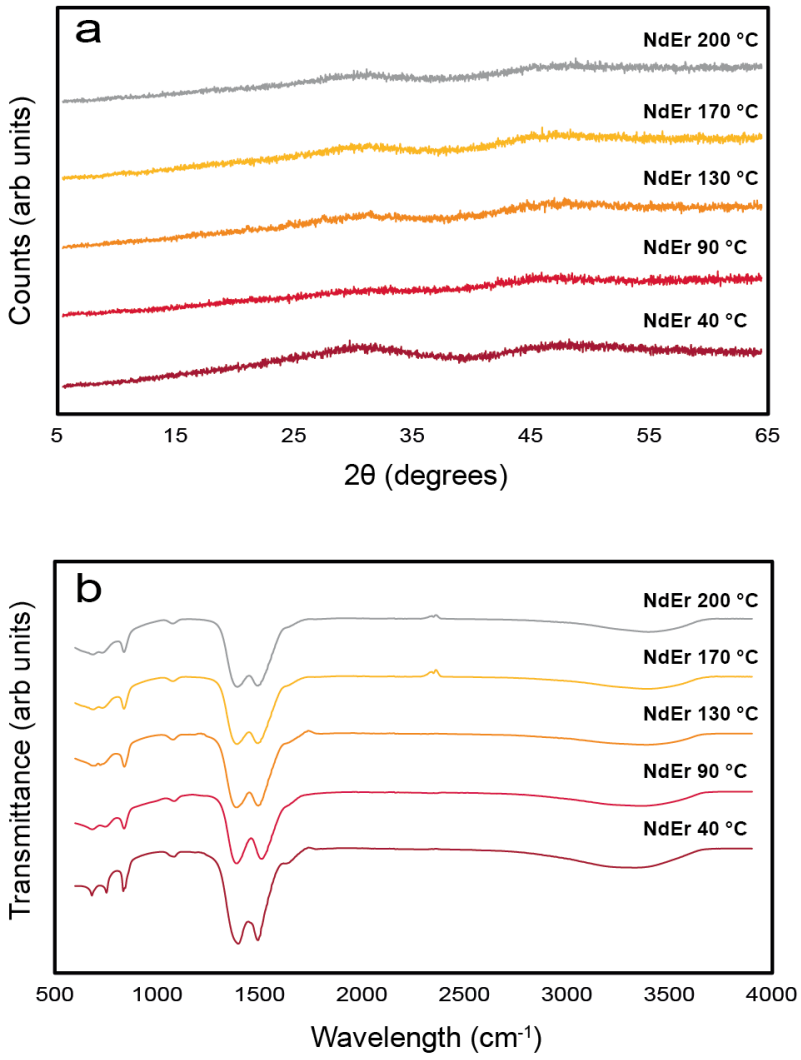

Figure 4.12: a) PXRD traces for the mixed Nd+Er precipitates; b) FTIR spectra of the same samples.

Additional two-REE mixes

Four additional two-REE mixes were chosen to cover more of the REE series. The PXRD and FTIR results (Figure 4.13) further demonstrated the amorphous nature of products when precipitated in the presence of HREEs, as just shown for Nd+Er. Although these solutions were only heated up to 90 °C, the PXRD spectra showed that incorporation of Er or Yb into a mix, even in the presence of the most-easily crystallised REE, (La), produced only X-ray amorphous material. However, when mixing a LREE and MREE, i.e. La+Gd, a number of Bragg peaks were detected that most closely matched kozoite. Because this material was not well crystalline (weak Bragg peaks and noisy spectra), it was difficult to determine whether the reflections were related to Gd or La kozoite (suggesting two discrete phases), or whether they were slightly shifted from ideal values of either (suggesting a mixed La-Gd kozoite). SEM analysis of this sample (Figure 4.14b) did not reveal discrete phases, but instead the familiar 'fluffy' texture seen in other X-ray amorphous materials. Again this is suggestive of nano-particulate material.

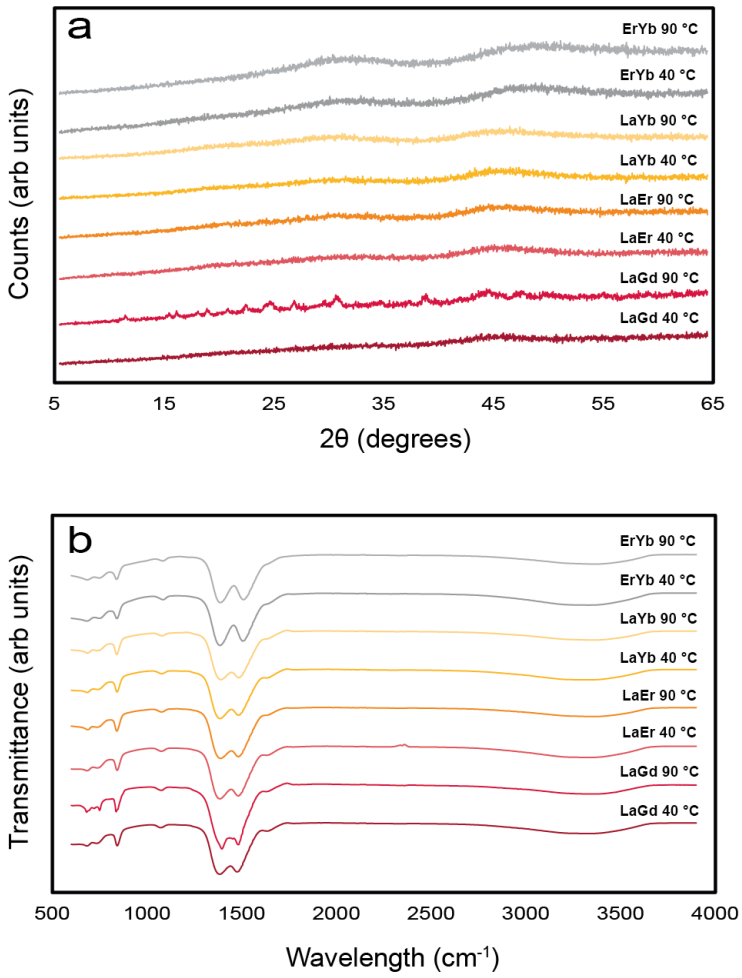

Figure 4.13: a) PXRD traces for the other two-REE mixed precipitates; b) FTIR spectra of the same samples.

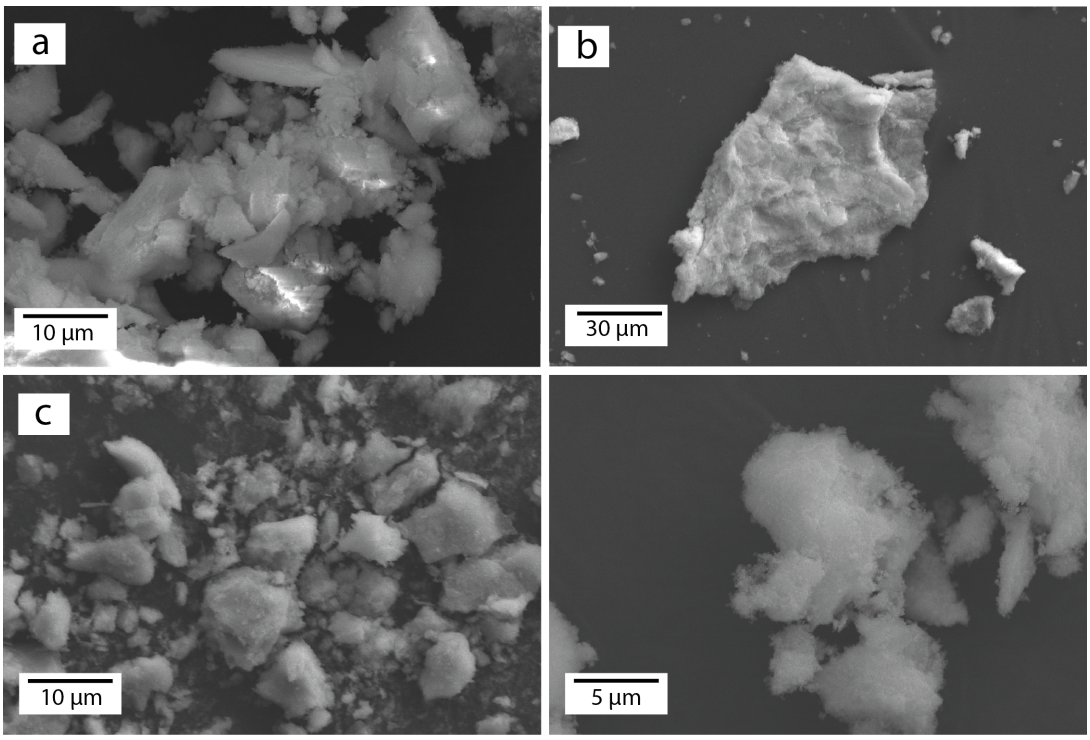

Figure 4.14: SEM images for some of the two-REE mixed precipitates whose PXRD spectra suggested X-ray amorphous material a) La+Yb at 90 °C; b) La+Gd at 90 °C; c) Nd+Er at 130 °C and representative of all other temperatures; d) Er+Yb at 90 °C.

Three- and five-REE mixes

The PXRD and FTIR spectra for the three- and five-REE mixed precipitates are shown in Figure 4.15. Both the 90 °C samples contained weak Bragg peaks, although they were stronger in the five-REE mix. In the case of the three-REE mix, the weak peaks were at 21, 31 and 34 degrees 2θ, which were most closely indexed to kozoite or ancylite, whereas in the five-REE mix the peaks were suggestive of tengerite. The FTIR revealed little additional information; all contained bands for water, indicating hydrated phases as seen for the other X-ray amorphous material.

SEM analyses revealed the same 'fluffy' texture in all cases. The only exception was the 90 °C La+Nd+Er experiment, where a few 'radiating micro-flower'-shaped plates were seen growing among the X-ray amorphous material (Figure 4.16). These plates reached 20 μm in length, and the EDS spectra taken on and around them suggested the they were depleted in Er relative to La and Nd; the opposite was true of the bulk 'fluffy' phase. Precipitates from the five-REE solutions were found to be 'fluffy' at all temperatures investigated, and despite the weak Bragg peaks of a tengerite phase detected, no candidates for this phase were identified.

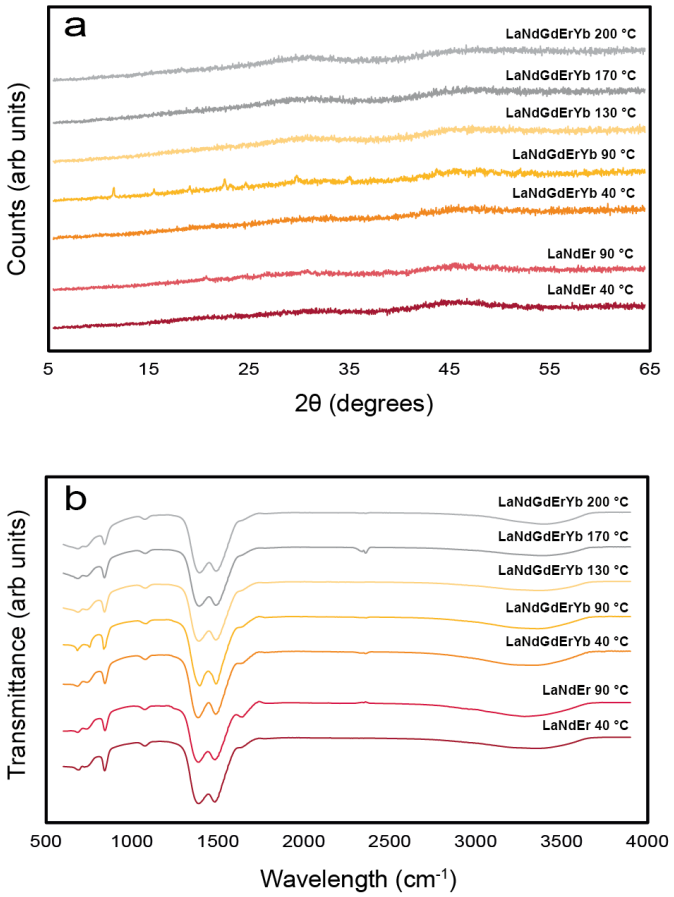

Figure 4.15: a) PXRD traces for the three- and five-REE mixed precipitates; b) FTIR spectra of the same samples.

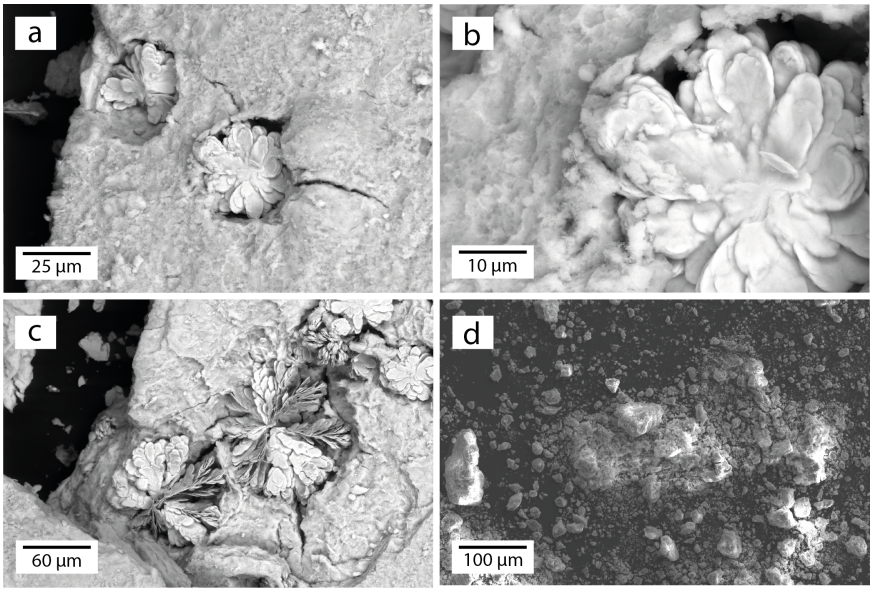

Figure 4.16: SEM images for some of the three- and five-REE mixed precipitates. a - c) La+Nd+Er at 90 °C showing the 'micro-flower'-shaped crystal forming out the more amorphous looking material; d) Five-REE mix at 90 °C, which is representative of all other temperatures.

4.3.3 Results summary

Given the large number of experiments and results presented above, a summary table detailing the product(s) at each temperature is presented (Table 4.2).

In summary, the lighter REEs crystallise more easily than their HREE counterparts. La precipitated as the highly-hydrated mineral lanthanite within 10 minutes (i.e. the length of titrations), whereas the other single-REE systems were X-ray amorphous after the same length of time. When aged, La went on to form the basic carbonate hydroxylbasntnäsite (i.e. $LaCO_3OH$) at temperatures < 100 °C. Nd also formed lanthanite, but only when aged at 40 °C; at higher temperatures it formed first kozoite (i.e. orthorhombic $NdCO_3OH$), then the hexagonal dimorph hydroxylbastnäsite. Er was more consistently X-ray amorphous, even at temperatures up to 200 °C; the exception was an Er sample left for 84 days at 40 °C, which possessed tengerite-type structure. Yb formed crystalline material only at 130 °C and higher; the identity(ies?) of phase(es) formed at 130 °C is currently unknown.

Multi-REE-bearing experiments highlighted the X-ray amorphous nature of precipitates formed in the presence of HREEs. Mixed LREE (La+Nd) precipitates behaved in an intermediate manner to the results of single REE experiments containing the individual elements: lanthanite was formed within 10 minutes, but was either less crystalline or produced smaller crystals (weaker Bragg peaks) than the La-only example. At 90 °C ancylite/kozoite (isostructural) was observed, but no hydroxylbastnäsite, which was more in-line with Nd-only results. When La+Gd solutions were used, the material only crystallised at 90 °C (no higher temperatures were tested); the product was kozoite.

When mixed HREEs (Er+Yb) or LREE+HREE (e.g. La+Yb) solutions were used, all products were X-ray amorphous, even up to 200 °C in the case of Nd+Er. In the precipitates from three-REE solutions there is tentative evidence for discrete LREE- and HREE-enriched phases forming that possessed kozoite structures (only at 90 °C); in five-REE mixes there was no crystallisation observed *via* SEM, although PXRD contained very weak reflections for a tengerite-type phase.

REE	**RT**	**40 °C**	**90 °C**	**130 °C**	**170 °C**	**200 °C**
La	Lan (*no image*)	Lan (*plates*)	HB (*spheres*)	-	-	-
Nd	A	Lan (*plates + radiating needles*)	Koz (*dumbbells + spheres*)	Koz+Hb (*needles + ?*)	Hb (*needles + ?*)	Hb + Koz (*needles + ?*)
Er	A	A; Teng - (*unknown*)	A	A; A	A	A
Yb	A	A	A	Unknown (*spheres made of plates*)	Yb-oxcarb (*unknown*)	Yb-oxcarb - (*unknown*)
La + Nd	Lan (*no image*)	Lan (*cruciform*)	Koz (*dumbbells*)	-	-	-
La + Gd	-	A	Teng+koz (*unknown*)	-	-	-
La + Er	-	A	A	-	-	-
La + Yb	A	A	A	-	-	-
Nd + Er	-	A	A	A	A	A
Er + Yb	-	A	A	-	-	-
La + Nd + Er	-	A	Koz (*'micro-flower'*)	-	-	-
All	-	A	Teng (*unknown*)	A	A	A

Table 4.2: Summary of results for the products of titration experiments, with morphologies in parenthesis. 'All' in column one denotes the five REE mix. A = X-ray amorphous; Lan = lanthanite ($REE_2(CO_3)_3 \cdot 9\,H_2O$); Koz = kozoite and ($REECO_3OH$); Hb = hydroxylbastnäsite ($REECO_3OH$); Teng = tengerite structures ($REE_2(CO_3)_3 \cdot 2{-}3\,H_2O$); Yboxycarb = $Yb_2O(OH)_2CO_3$. The two 'A' at Er 130 °C represent the two different ageing durations. The Yb 130 °C sample was crystalline but could not be identified. RT = room temperature. A hyphen denotes no experiment.

4.4 Discussion

The results of this study demonstrate differences in the crystallisation behaviour of the precipitates as a function of atomic number and ageing temperature, which will be discussed separately below.

4.4.1 Differences in crystallinity and crystallisation pathways as a function of atomic number

There is a clear distinction between the behaviour of LREE and HREE in both the single- and multi-REE-bearing systems.

FTIR data for all precipitates formed at RT and filtered immediately at the end of titrations (fresh-precipitates) displayed intense bands resulting from structural water, and did not contain bands for hydroxyl groups, suggesting they were hydrated 'normal type' carbonates (e.g. Wickleder, 2002). Except for precipitates from the La and mixed La+Nd solutions, all these materials were X-ray amorphous. Although an X-ray amorphous La phase was not observed in this investigation, it has been noted previously (e.g. Rodriguez-Blanco et al., 2014; Vallina et al., 2015). The reason for this was based on the subtle differences between the experimental procedure: the current investigation used a titration method, which, although rapid (i.e. $<$ 10 minutes), was sufficiently long enough for lanthanite-(La) crystallisation (large enough to produce intense Bragg peaks). In contrast, solutions in the experiments of (e.g.) Vallina et al. (2015) were directly mixed and filtered immediately, producing X-ray amorphous material (termed 'amorphous lanthanum carbonate', ALC). The detection of ALC immediately after solution mixing, crystalline lanthanite-(La) after 10 minutes, but X-ray amorphous fresh precipitates when using the other REEs (Nd, Er, Yb), confirms the transformation of ALC to lanthanite-(La) is more rapid than for equivalent reactions of the other REEs (at least those investigated here).

An X-ray amorphous phase has also been previously identified for Ce, Pr, Nd and Dy (Vallina et al., 2014; Rodriguez-Blanco et al., 2014). In those studies, the X-ray amorphous phases were left in their mother liquids at 21 °C, whereupon they were seen to crystallise to lanthanite-(Ce) after 10 minutes, lanthanite-(Pr) after one hour, lanthanite-(Nd) after 15 hours, and tengerite-(Dy) after 48 hours, respectively. These results, combined with those mentioned in the previous paragraphs, demonstrate a correlation between the lifetime of X-ray amorphous material and Z of the REE. The data presented in the current work for Er and Yb supports this conclusion, insofar as the X-ray amorphous material stays as such for longer than 15 hours (i.e. longer than 'amorphous Dy carbonate' - Vallina et al., 2013). However, data on the length of time required to crystallise Er and Yb at ambient temperature, which was not obtained

presently, is necessary to confirm whether the correlation is linear (i.e. time increases with Z).

It is clear from the results of the current investigation, and those published previously, that crystallisation occurs *via* the formation of an X-ray amorphous, hydrated precursor phase, as described by the non-classical nucleation theory (e.g. Meldrum and Cölfen, 2008). Such phases have been described previously for other systems, the most studied of which is calcium carbonate (e.g. Gebauer et al., 2008; Raiteri and Gale, 2010; Trushina et al., 2015; Dietzsch et al., 2017), but also calcium phosphate (e.g. Dey et al., 2010), zinc phosphate (e.g. Bach et al., 2015) and metal sulfides (e.g. Rickard and Luther, 2006), among others. Characterisation of amorphous calcium carbonate (ACC) has suggested it may contain short-range order similar to the bulk phase into which it eventually crystallises, termed proto-calcite-ACC and proto-vaterite-ACC, the structures of which are thought to be based on the distinct structures of the prenucleation cluster (PNC), which are themselves controlled by the conditions of the fluid (notably pH and temperature – e.g. Gebauer et al., 2008; Gebauer and Cölfen, 2011; Dietzsch et al., 2017). In the current investigation, the structure of the amorphous phase is unknown – hence its being termed 'X-ray amorphous' throughout this thesis. It is unknown whether this material is truly amorphous or nano-particulate, or it possesses short-range structure similar to or distinct from the bulk phase into which it is known to form (i.e. Nd), or thought to form (e.g. Er). The structure of these X-ray amorphous phases is probed in more detail using X-ray absorption spectroscopy (XAS) in Chapter 5.

The lifetime of the REE carbonate X-ray amorphous precursor phases – which are shown to be highly hydrated (as shown in the FTIR data) – has been suggested previously to be controlled by the energy required to dehydrate them (e.g. Vallina et al., 2015), which is itself a function of the ionic potential (charge/radius) of the cation. As the REEs decrease in size systematically across the series, but the charge remains constant at +3 (except Ce and Eu under certain conditions), the ionic potential increases with Z. In the current investigation, the La and Nd materials followed the same pathways as reported previously (e.g. Vallina et al., 2015) and conform to the pattern above, but the results for Er and Yb do not. If the pattern was linear, it would be expected that either Er would crystallise first when treated at the same temperature and ageing duration as Yb, or that both would behave the same (i.e. both are crystalline, or not). However, under the same experimental conditions (130 °C and higher), Er remained X-ray amorphous but Yb was crystalline, demonstrating that the breakdown of X-ray amorphous Yb was more rapid than Er.

The reason for the difference in behaviour of X-ray amorphous Er compared to the other REEs discussed is currently unknown. Higher dehydration energies with increas-

ing Z would suggest reducing solubility across the series, but unfortunately there exists no solubility data for any of these phases. There are no immediately-obvious anomalies or features in the trends of thermodynamic data, including the hydration energies or structural parameters of lanthanide hydration (see review in e.g. D'Angelo and Spezia, 2012) that can be used to account for the behaviour of Er. Nevertheless, the results demonstrate the deviation from the linear trend observed previously for La, Ce, Pr, Nd and Dy X-ray amorphous precursor material.

The crystallisation of tengerite from the Er-only solution at 40 °C after 84 days demonstrates the influence of kinetic factors to these reactions. Er X-ray amorphous material to tengerite is clearly thermodynamically-favoured, but the time taken for this to occur is significantly longer than the other REEs studied. The lack of crystallisation at higher temperatures, even after two weeks at 130 °C, highlights further this point. Unfortunately, there was no 40 °C Yb experiment run for 84 days, but it would certainly be interesting to see how this element (and Tm and Lu) behaves under these conditions.

Crystalline Er carbonate has been synthesised previously at room temperature after one week (Liu and Ma, 2007), and 40 °C – 120 °C after one week (Nagashima et al., 1973). Both studies started with 0.1 M REE chloride solutions, but the former used ammonium bicarbonate (0.3 M) as precipitant while, the other used sodium carbonate and adjusted the total solution volume to 100 ml (with deionised water). Solutions were directly mixed in both experiments. Interestingly, when Yb was used the product was crystalline ($Yb_2O_3 \cdot 2.17CO_2 \cdot 6.17H_2O$ - Liu and Ma, 1997b) and 'amorphous' (Nagashima et al., 1973), which highlights, even from these two studies, the influence that preparation technique has on the precipitants. The Yb PXRD trace from Liu and Ma (1997b) does not match either of those produced in the current investigation (Figure 4.8a).

At higher temperatures, there is a crystallisation sequence for La and Nd indicating dehydration from the first crystalline phase, lanthanite (La and Nd), to tengerite (Nd), then kozoite (Nd) and finally hydroxylbastnäsite (La and Nd). Tengerite does not form in the La only solutions because its structure can only accommodate REEs smaller (i.e. heavier) than Pr (Wakita and Nagashima, 1972; Miyawaki et al., 1993). Recent solubility studies have shown hydroxylbastnäsite-(La) and hydroxylbastnäsite-(Nd) to be almost more stable than kozoite-(Nd) (Voigt et al., 2016), which explains the lack of the former mineral at lower temperatures and its dominance at the higher ones.

Although the behaviour of Er is unexpected, it is at least consistent between the precipitates from the single and mixed REE solutions. In all cases including Er, the material was found to be X-ray amorphous, even when mixed with La or Nd. In addition, the two, two-REE experiments in which Yb was included (La+Yb, La+Er – both < 100

°C) were again X-ray amorphous, even when mixed with La. This behaviour indicated that in the presence of the harder-to-crystallise HREEs, the LREEs are inhibited from crystallisation, at least at the conditions studied. The same was not true in materials precipitated from three- or five-REE mixed solutions, although the crystallites were either very sparse or small (i.e. weak Bragg peaks Figure 4.15a). The only difference between the ≤ 2 and ≥ 2 REE experiments was the concentration of the individual REE (0.1 in the one and two mixes; 0.04 and 0.06 in the three and five mixes, respectively). The concentration of REE and precipitant has been shown exert major influence on the morphology of REE carbonates (Shang et al., 2009; Zhang et al., 2015). In the five-REE mixed results, a kinetic control to crystallisation is again observed as the experiments conducted at 130 °C (five days), 170 °C (two days) and 200 °C (one day) are all X-ray amorphous, yet minor Bragg peaks were detected at 90 °C (six weeks).

4.4.2 Influence of temperature on the structure and morphology of REE carbonates

The influence of temperature on the morphology of the products is striking. Examples of spherical, acicular, 'micro-flower', cruciform, dumbbell and plate morphologies are observed for the crystalline materials, in addition to the widespread 'fluffy' texture of the X-ray amorphous phases.

The X-ray amorphous precursor phase when directly mixing solutions is composed of very homogenous, monodispersed particles (20 nm spheres) with a narrow size distribution (Vallina et al., 2013, 2015), indicating extensive nucleation and little growth, as would be expected during the massive, solution-wide supersaturation experienced after the introduction of dissolved carbonate (Karthika et al., 2016). Although the current investigation added dissolved carbonate at a slower rate, the X-ray amorphous material is assumed to be the same as in those other studies.

The breakdown of this metastable X-ray amorphous phase is, in the case of La, Nd and Yb (the latter at > 90 °C) followed by recrystallisation. In the case of La and Nd, the first phase to form is lanthanite, which in both cases exhibits plate-like morphology, interpreted as forming *via* Ostwald ripening in the non-equilibrium solutions followed by growth along the [100] and [121] planes (Bevins et al., 1985). In the La examples, it is unclear whether the lanthanite-(La) is transforming to the spherical hydroxylbastnäsite-(La) observed at 90 °C, or whether the latter is forming directly from the X-ray amorphous material (not observed in this investigation). Previous works on carbonate mineral precipitation and morphologies have suggested that particles with spherulitic morphologies form by randomly orientated attachment of particles, which occurs at high supersaturation conditions (e.g. Beck and Andreassen, 2010). In the case of the La hydroxylbastnäsite formed at 90 °C, a possible suggestion for its spherical

morphology is the rapid breakdown of either the X-ray amorphous phase or lanthanite-(La), leading to supersaturation (with respect to hydroxylbastnäsite) quick enough to promote the growth of nuclei rather than crystal growth. This would then lead to many mono-dispersed crystals with a narrow size distribution, as shown in Figure 4.3.

In the Nd sample, tengerite-(Nd) is seen forming at the expense of lanthanite-(Nd) at 40 °C (Figure 4.5), but at 90 °C it is again unclear if the observed kozoite-(Nd) is forming from either of these two phases or directly from the breakdown of X-ray amorphous Nd. The morphology of this kozoite-(Nd) is almost identical to kozoite-(La) and kozoite-(Nd) of Vallina et al. (2015), and to YCO_3OH of Zhang et al. (2009). However, there are significant differences in the methods used in those two studies: the first has been discussed already, but the latter involved the mixing of $Y(NO_3)_3 \cdot 6\,H_2O$ with urea in deionised water, followed by heating in an autoclave at 150 °C for up to 22 hours. The authors in the former study explained this morphology as 'category 2' spherical growth, which is a classification taken from Granasy et al. (2005). Category 2 growth is described as an initial growth of threadlike fibres that experience unilateral growth followed by branching to form the 'weights' at the end of the dumbbells; this growth is experienced in lower supersaturation conditions as compared with the spherical growth described above. The YCO_3OH dumbbells of Zhang et al. (2009) were described as growing via 'orientated attachment assisted self-assembly of the particles', which follows that 'primary particles' share common crystallographic orientation that 'dock' together at a planar face. Similar morphologies have been reported for aragonite (e.g. Sand et al., 2012). The formation of dumbbells in the Nd and mixed La+Nd experiments of the current investigation conform to the 'category 2' spherulitic growth mechanisms of Granasy et al. (2005).

In the higher temperature (130, 170 and 200 °C) Nd experiments, there is clear evidence of two distinct morphologies (Figure 4.5). At 130 °C, the needle/dendritic-like morphology (up to 50 μm length) is thought to be the hydroxylbastnäsite, meaning the smaller material with less defined shape is tengerite. The former is thought to be forming at the expense of the latter *via* dissolution-reprecipitation. The needles of hydroxylbastnäsite form by non-equilibrium anisotropic growth, i.e. one face growing more quickly than the others (Meekes et al., 2003). The same is true of dendritic morphologies, examples of which have been published previously for Nd carbonates (Shang et al., 2009; Vallina et al., 2014). At the 170 °C (Figure 4.5g) the needles are smaller (5 μm) are more uniform in size than at 130 °C, which may point to the more uniform breakdown of tengerite (only 1 % of the sample). This would increase the rate of Nd^{3+} and $CO_3{}^{2-}$ supply, as compared with the slower dissolution of tengerite at 130 °C, resulting in a more uniform size distribution. The same is observed at 200 °C, however, a larger proportion of tengerite remains present, suggesting the ageing length was not sufficient for complete transformation to hydroxylbasnäsite at this temperature.

No crystalline material was observed for Er, but at 130 °C in the Yb experiment there is clear evidence for the transformation of the X-ray amorphous material into the unknown Yb carbonate phase (Figure 4.9). The morphology of the crystalline material consists of small (20 μm length) plates aggregated into spherical masses, which are forming directly from the X-ray amorphous material. Despite strong Bragg peaks, no obvious candidates for the crystalline $Yb_2O(OH)_2CO_3$ were identified at 170 or 200 °C, although a few crude plates were (possibly) observed.

Although not investigated as a variable here, the molar ratios of the starting reagents is known to control the morphology of REE carbonate precipitates (e.g. Nagashima et al., 1973; Zhang et al., 2007; Shang et al., 2009; Zhang et al., 2009; Qian et al., 2012), $CaCO_3$ (e.g. Sand et al., 2012; Trushina et al., 2015 and many other carbonates, oxides, phosphates etc. (e.g. Wang and Muhammed, 1999; Wickleder, 2002; Colfen, 2003; Lv et al., 2004; Meldrum and Cölfen, 2008).

4.4.3 Implications

The results presented in this chapter have implications for the synthesis of crystalline material containing different REEs, particularly those containing HREEs.

Controlled synthesis and growth of known morphologies is important for materials sciences applications, and in recent years there has been renewed interest in nano- and micro-particles of REE carbonates (Kaczmarek et al., 2015). Depending on their size and morphology, REE carbonates of different types (e.g. basic or normal) have numerous applications, for example in pharmaceuticals (e.g. targeted anti-cancer drug delivery, Yang et al., 2013) and as MRI contrast agents (e.g. Jin et al., 2013), although by far the most common is the exploitation of their luminescent properties (e.g. Lechevallier et al., 2010; Kaczmarek et al., 2015). The concentration of lanthanide dopant and the crystal structure determine the luminescence efficiency: REE may be doped into normal ($REE_2(CO_3)_3$), basic ($REECO_3OH$) or oxycarbonates ($REE_2O(CO_3)_2$ or $REE_2O_2CO_3$) carbonates. Although Tb and Eu are the REEs used as dopants, the REE used to make the host carbonate can affect their luminescent properties.

Neither Tb nor Eu were investigated presently, but the results show that normal, basic and oxycarbonates can be synthesised from different REEs and at different conditions. Use of Er does not result in a crystalline material, and as such is unsuitable for use in any application requiring an ordered structure (at least under the conditions of this investigation). Yb may be an applicable host for doping, but only at temperatures $>$ 90 °C. The mixed La+Nd precipitates formed cruciform (40 °C) or dumbbell (90 °C) morphologies, however, when mixed with a further REE (Er), the crystallinity was

hindered. Most commonly for materials used for luminescence applications, the REE dopant is Eu or Tb and the most frequently reported morphology for the nano- and micro-technologies is spherical, but there are examples of dendrites (Qian et al., 2012). In the present work, dendrites were formed for $NdCO_3OH$ at 130 °C, and spheres for $LaCO_3OH$ at 90 °C, but neither were present in the other experiments.

The results presented here show that HREEs are more difficult to crystallise under the conditions of this study as compared with the LREEs. This is attributed to the increased dehydration energy moving across the series (from lower to higher Z), but that this is not a linear trend as previously suggested. The morphologies identified are highly variable and are dependent on the temperature and duration of ageing the initially X-ray amorphous precursor phase. The addition of HREEs to a LREE results in behaviour more like that of the former (i.e. crystallisation is inhibited by the presence of a HREE). The morphologies presented are not suitable for use in most reported nano- and micro-technologies. Under the conditions employed, Er and Yb have been shown to be unsuitable elements for applications requiring crystalline material with corresponding properties.

Chapter 5

Determining the local structure of fresh and aged REE carbonate precipitates *via* X-ray absorption spectroscopy

5.1 Introduction

The previous chapter highlighted the different characteristics of REE carbonates when precipitated from solutions containing different REEs. Precipitates become increasingly X-ray amorphous with increasing Z, suggested to result from the increased energy required to dehydrate the initial highly-hydrated precipitates (shown in Chapter 4, and e.g. Vallina et al., 2013; Rodriguez-Blanco et al., 2014). However, the X-ray amorphous nature of most the first-formed precipitates, and many of their aged products, makes determining the crystallisation pathways difficult using only the characterisation techniques used thus far. Therefore, in an attempt to address those difficulties, X-ray absorption spectroscopy (XAS) is employed in this chapter to follow the evolution of structures from precipitation through ageing.

There is a growing body of evidence suggesting that the crystallisation of certain phases proceeds *via* the aggregation of X-ray amorphous nano-scale precursor phases, or clusters, that may or may not have the same short-range structures to that of the bulk material into which they grow (e.g. Gebauer et al., 2008; Meldrum and Cölfen, 2008; Gebauer and Cölfen, 2011). One of the most studied systems is that of $CaCO_3$, for which it has been suggested that pre-critical clusters aggregate to form amorphous calcium carbonate (ACC), that then goes on to form crystalline $CaCO_3$ (e.g. Rieger et al., 2007; Gebauer et al., 2008; Rodriguez-Blanco et al., 2011; Bots et al., 2012; Dietzsch et al., 2017). The polymorph of $CaCO_3$ that forms may be controlled by the short-

range order of these clusters, which itself can be controlled by precipitation conditions (temperature, pH, ageing duration etc.). Amorphous precursors have also been identified for numerous other systems, including crystallisation of calcium phosphate (Dey et al., 2010), cobalt phosphate (Bach et al., 2016), zinc phosphate (Bach et al., 2015), transition metal sulfides (Rickard and Luther, 2006) and REE carbonates (Ce, Pr, Nd and Dy - e.g. Vallina et al., 2013, 2015). The short-range structures of most of these materials have not been determined, in some cases because their lifetimes are too short.

In the case of REE carbonates, previous studies (Vallina et al., 2013; Rodriguez-Blanco et al., 2014) have used thermogravimetric and standard-less EDS analyses to estimate the formulae of first formed X-ray amorphous precipitates, with suggested hydration numbers of 4-5 for normal carbonates (i.e. $REE_2(CO_3)_3 \cdot 4{-}5\,H_2O$). These go on to crystallise when heated, with the structure controlled by the temperature and length of ageing, and the REE investigated. What is unknown, however, is whether these amorphous precursor phases possess the same short- or intermediate-range order as the bulk crystalline phases. Additionally, it was shown in the previous chapter that for heavier REEs, the aged products of titrations remain X-ray amorphous at temperatures below 130 °C (Yb) and 200 °C (Er). The identity – i.e. the local structure – of the precipitates in solution (La, Nd, Er and Yb), the fresh precipitates (Nd, Er and Yb) and the aged products (Er and Yb) therefore remain uncertain. Detailed knowledge of the precursors' characteristics is required for a fuller understanding of the crystallisation pathways of REE carbonates, which is vital during the controlled preparation of materials used in various nano-technologies in fields such as medicine, electronics, catalysis and even cosmetics (Tan, 2012; Malathi et al., 2013; Katz et al., 2015).

Another result from Chapter 4 requiring further investigation is the different characteristics of single and multi-REE-bearing carbonates. It was shown that individual LREEs did, and HREEs did not, crystallise at temperatures up to 90 °C, but that when LREE and HREE were mixed the precipitate formed only an X-ray amorphous material. It is unclear from the results of the previous chapter whether the REEs form discrete admixed phases, or a single phase into which multiple REEs have substituted. The doping of materials with REEs is common in the literature, particularly for exploiting their photo-luminescent properties during which the quality is reported to be dependent on the size and morphology of the crystallites (Tu et al., 2006; Van et al., 2006; Mao et al., 2008). However, a common occurrence during doping is the clustering or irregular distribution of the REE ions, which decreases the efficiency of the characteristic being exploited (e.g. Van et al., 2006). Investigation of the local structure of the mixed REE precipitates from the previous chapter may therefore help to identify the location of the REEs in these systems and hone preparation techniques.

This chapter presents the results of X-ray absorption spectroscopy (XANES - X-ray absorption near edge structures, and EXAFS - extended X-ray absorption fine structures) analyses of REE carbonate precipitates. Samples analysed included precipitates collected during the first period of rapid pH rise (pre-stat), and the period of prolonged static pH maintained despite considerable dissolved carbonate addition (pH stat), observed during titration experiments; the X-ray amorphous solid precipitates (fresh and aged) of those titrations, and; the solid precipitates of two aged, mixed REE samples. The objectives of this chapter were:

1. Identify the evolution of their local structures from solution to solid precipitates;
2. Comparison of the local structure of material in solution to that of the crystalline phases into which they eventually evolved (La and Nd);
3. Comparison of the local structure in solution to the local structure of X-ray amorphous solids (Er and Yb);
4. Attempt to identify the X-ray amorphous material (Nd, Er and Yb);
5. Determine if mixed NdEr aged precipitates form well-mixed material or experience clustering.

5.2 Materials and methods

A detailed description of the materials and characterisation methods are given in Chapter 3. In summary, titration experiments like those presented in the previous chapter were conducted, but this time at temperatures of 40 and 90 °C for Nd, and 90 °C for all others. The samples analysed and details of the XAS acquisition conditions - including the standard reference materials - are presented in Table 5.1. The idea of conducting the titrations at temperature was to assess whether this influenced the local structure of the first precipitates/solution clusters, and see how this compared with the aged products (crystalline or not).

The REE chloride and sodium carbonate solutions used were 0.1 and 0.15 M, respectively (same as Chapter 4). REE chloride solutions were heated in a glass beaker on a hot plate, while the sodium carbonate was heated in bunged serum bottles to slightly above the desired temperature before being transferred to the burette. Titrations were completed in around 5 minutes to minimise heat loss from the sodium carbonate. The temperature of the REE solution was monitored with a glass thermometer and found to be 40 ± 3 °C (Nd) and 90 ± 6 °C (all others). Solution pH was monitored with a pre-calibrated Radiometer Analytical PHM 220 pH meter and REFEX glass Ag/AgCl sensor. The start pH of all solutions was around 0.8.

Sample	No. scans	Mode	Edge energy (eV)	Scan range (eV)	E_0
La 90 pre stat	15	F	5483 (L_3)	5283 - 5881	5487.6
La 90 stat	20	F	5483 (L_3)	5283 - 5881	5487.6
La 90 fresh	3	T	5483 (L_3)	5283 - 5881	5487.6
La 40 aged	3	T	5483 (L_3)	5283 - 5881	5487.6
La 90 aged	3	T	5483 (L_3)	5283 - 5881	5487.0
La carbonate std	3	T	5483 (L_3)	5283 - 5881	5487.6
La fluoride std	3	T	5483 (L_3)	5283 - 5881	5487.6
La oxide std	3	T	5483 (L_3)	5283 - 5881	5485.3
Nd 40 pre stat	10	F	6208 (L_3)	6008 - 6712	6212.4
Nd 40 stat	20	F	6208 (L_3)	6008 - 6712	6211.7
Nd 40 fresh	3	T	6208 (L_3)	6008 - 6712	6211.7
Nd 40 aged	3	T	6208 (L_3)	6008 - 6712	6211.7
Nd 90 pre stat	15	F	6208 (L_3)	6008 - 6712	6212.0
Nd 90 stat	20	F	6208 (L_3)	6008 - 6712	6211.7
Nd 90 fresh	3	T	6208 (L_3)	6008 - 6712	6211.7
Nd 90 aged	3	T	6208 (L_3)	6008 - 6712	6211.0
Nd carbonate std	6	T	6208 (L_3)	6008 - 6712	6211.7
Nd fluoride std	3	T	6208 (L_3)	6008 - 6712	6212.1
Nd oxide std	3	T	6208 (L_3)	6008 - 6712	6210.3
Er 90 pre stat	20	F	8358 (L_3)	8158 - 9254	8358.8
Er 90 stat	20	F	8358 (L_3)	8158 - 9254	8358.8
Er 90 fresh	5	T	8358 (L_3)	8158 - 9254	8358.8
Er 40 aged	5	T	8358 (L_3)	8158 - 9254	8358.8
Er 90 aged	5	T	8358 (L_3)	8158 - 9254	8358.8
Er carbonate std	5	T	8358 (L_3)	8158 - 9254	8358.9
Er fluoride std	5	T	8358 (L_3)	8158 - 9254	8358.9
Er oxide std	5	T	8358 (L_3)	8158 - 9254	8357.3
Yb 90 pre stat	15	F	8943 (L_3)	8779 - 9829	8944.7
Yb 90 stat	15	F	8943 (L_3)	8779 - 9829	8945.0
Yb 90 fresh	3	T	8943 (L_3)	8779 - 9829	8945.3
Yb 40 aged	3	T	8943 (L_3)	8779 - 9829	8945.3
Yb 90 aged	3	T	8943 (L_3)	8779 - 9829	8944.4
Yb carbonate std	3	T	8943 (L_3)	8779 - 9829	8944.8
Yb fluoride std	3	T	8943 (L_3)	8779 - 9829	8945.4
Yb oxide std	3	T	8943 (L_3)	8779 - 9829	8944.1
NdEr 40 aged	3	T	6208 Nd (L_3)	6008 - 6712	6212.1
NdEr 40 aged	3	T	8358 Er (L_3)	8158 - 9254	8358.9
NdEr 90 aged	3	T	6208 Nd (L_3)	6008 - 6712	6211.7
NdEr 90 aged	3	T	8358 Er (L_3)	8158 - 9254	8358.9

Table 5.1: Samples analysed by XAS in this study. Mode = the mode of data collection, where F = fluorescence and T = transmission. Std = standard reference materials: carbonate = $REE_2(CO_3)_3 \cdot xH_2O$; fluoride = $REEF_3$; oxide = REE_2O_3. The value for E_0 is explained in Chapter 3.

Each experimental solution was sub-sampled several times, the idea for which was borne from the observation that pH increase was not linear with carbonate addition. By sub-sampling at several points the evolution of the local structure could be assessed. Samples were collected:

1. During the period of rapid pH increase (**pre-pH stat**), early in the titration;
2. During prolonged periods of static pH (**pH stat**);
3. At the cessation of carbonate addition, around pH 8.5, ('fresh precipitates').

Subsamples 1 and 2 were pipetted into specially-made aluminium cells with holes covered in Kapton (polymide) tape, as described in Chapter 3. The whole cell, once watertight, was submerged into liquid nitrogen to preserve the speciation, oxidation and crystallinity of the solutions/precipitates. The time from solution extraction to preservation was around 10 seconds. The 'fresh' precipitates were also pipetted from the mother liquid, this time at the end of the experiment, and immediately vacuum filtered on 0.45 μm mixed cellulose ester membrane filters, repeatedly washed with deionised water and left to air dry. In addition to these solution samples, several aged precipitates were analysed, including those containing single and multi-REEs.

Standard reference materials (REE carbonate, REE fluoride and REE oxide) were analysed for each of the four REEs studied, facilitating comparison between the local structures of these known samples and those of the unknowns.

5.3 Data acquisition and processing

5.3.1 Data acquisition

XAS data were collected in both transmission and fluorescence mode, which required different sample preparation. The solution samples were frozen in the cells described above, and all solid samples (fresh and aged precipitates, plus standards) were made into pellets by mixing with cellulose (used to bind the sample together).

All XAS (XANES and EXAFS) data were collected in September 2014 at the Diamond Light Source, Oxfordshire, UK, on the core EXAFS beamline B18. Storage ring energy was 3 GeV. Data were collected in fluorescence mode for the frozen solutions (i.e. all pre-pH stat and pH stat samples) and transmission mode for precipitates. The fluorescence data were collected at around 85 K, with the aluminium cell (containing a frozen solution sample) housed in a cryostat and orientated at 45 ° to a 32 element Ge solid-state detector, which was itself at 90 ° to the incident beam. Transmission measurements were made at ambient temperature, with several pellets held in a vertically-orientated sample holder allowing for automated data acquisition. Pellets

were made by mixing approximately 0.01 g of crushed sample with 0.08 g cellulose, and then pressing them using a pin press and hydraulic press. Pellets were about 1 mm thick. The photon energy was calibrated using a Cu foil at 8979.1 eV (for the Cu K-edge).

Spectra were collected at the L_3 edge over an energy range from approximately -175 to between 430 and 1000 eV below and above the absorption edge, respectively, depending on the REE. Energy scans were made using an Si (111) monochromator. The difference in energy range collected beyond the edge (i.e. higher eV) for each REE is a consequence of the energies at which their L_2 edges are located. Several scans (between 2 and 20) were collected and averaged (merged) for each sample, which helped improve the signal-to-noise ratio. Details of all samples, including the number of spectra collected, the mode in which, the energy range over which, and the absorption edge at which data was collected are outlined in Table 5.1.

5.3.2 Data processing and analysis

A detailed explanation of the data processing and analysis procedure was described in Chapter 3, including the checks required for determining the quality of a fit. In brief, during data processing the signal in terms of energy, $\mu(E)$, is converted to wavenumber of the photoelectron, (k), such that the oscillations are plotted as a function of wavenumber $\chi(k)$. The different frequencies apparent in $\chi(k)$ corresponds to the shells of different near neighbours. The data is then Fourier transformed into 'R' space, which presents the oscillations as a peaked function of distance.

A typical workflow for XAS data processing and analysis followed the steps:

1. conversion of raw data into $\mu(E)$ (the X-ray coefficient);

2. removal of unwanted data in $\mu(E)$ - i.e. defining the final energy range to be included in the further stages (avoiding other edges, etc.);

3. background removal and normalisation, and defining a value for the threshold energy, E_0;

4. conversion of $\mu(E)$ data into k-space to produce data as $\chi(k)$ (the EXAFS data), accompanied by the necessary k-weighting (depending on signal strength);

5. defining the useful data range of k (Å);

6. Fourier transform $\chi(k)$ to produce $\chi(R)$ (i.e. k- to R-space), which isolates the oscillations in the data attributable to different shells.

5.4 Results and discussion

5.4.1 XANES of REE standards

XANES spectra for the carbonate, fluoride and oxide standard materials of La, Nd, Er and Yb are shown in Figure 5.1.

The spectra all contain similar features, including intense white lines (main peak at the absorption edge) and a single larger oscillation beyond this, but differ in their details, including the number of smaller oscillations. These dissimilarities indicate differences in local structures.

The most obvious observation to be made from comparison of the samples is that the spectra for carbonate, fluoride and oxide are different to each other. This is true for the La and Nd examples, where the spectra are clearly not the same, but not so in the case for Er and Yb. In the latter examples, very similar spectra are produced for fluorides and oxides of both Er and Yb, indicating they possess similar local structure.

The other major observation is the similarity in spectra for the same compound of the lighter (La and Nd) and heavier REEs (Er and Yb), e.g. the La fluoride and Nd fluoride spectra are the same, the Er fluoride and Yb fluoride spectra are the same, but these two groups are not the same. This indicates a change in the local structure of materials possessing the same formula but composed of lighter or heavier REEs, something already shown in the results of Chapter 4. Based on the spectra in Figure 5.1, this is least prominent for the carbonates (i.e. most similar spectra between light and heavy REEs). The change in local structure between compounds containing light and heavy REEs is a consequence of different coordination numbers resulting from the lanthanide contraction, as mentioned in Chapter 2. This has also been shown experimentally for REE fluorides, which, when synthesised under identical conditions, produce hexagonal crystal structures for REEs from La to Eu, and orthorhombic structure from Gd to Lu (e.g. Wang et al., 2006).

The XANES data for each of the REE standards presented in Figure 5.1 are also included with the relevant experimental results of the same element, as presented in section 5.4.3 below.

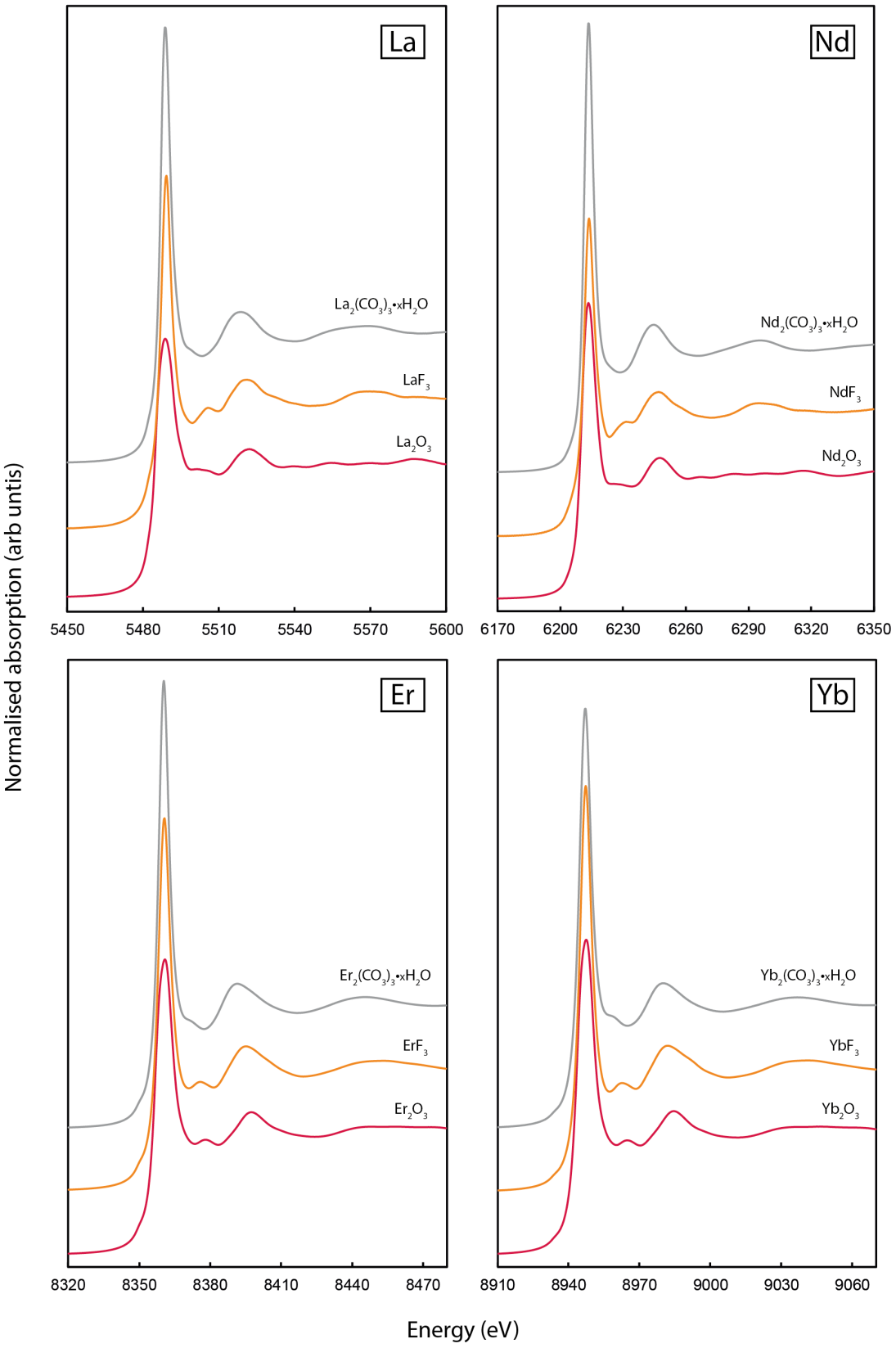

Figure 5.1: XANES spectra of the REE carbonate, fluoride and oxide standards used in this study. All were collected at the respective REE L_3-edge.

5.4.2 PXRD of REE standards

The four REE carbonate standards used in this XAS investigation, which were bought from Alfa Aesar, had reported formulae of $REE_2(CO_3)_3 \cdot xH_2O$. Given the results of the previous chapter - i.e. that different REEs produced different structures at various formation conditions - it was decided to subject these materials to PXRD analyses in order to determine their structures. Based on the supplier's formula and the literature presented in this thesis, the standards were expected to be: La = Lanthanite; Nd = either lanthanite or tengerite; Er = tengerite. There are no reported naturally-occurring minerals with the formula $Yb_2(CO_3)_3 \cdot xH_2O$, and so the precise structure of this phase was unknown.

PXRD results are presented in Figure 5.2. The results were as expected for the La and Nd material, however, the Er was found not to be tengerite, and in fact couldn't be matched to any known structure in the database. Interestingly, the Yb sample is crystalline, but the Bragg peaks are weak and broad, suggesting a less crystalline material or one in which the particles were very small. It also appears to have a small fraction of X-ray amorphous material admixed, as evidenced by the broad hump at > 35 degrees 2θ.

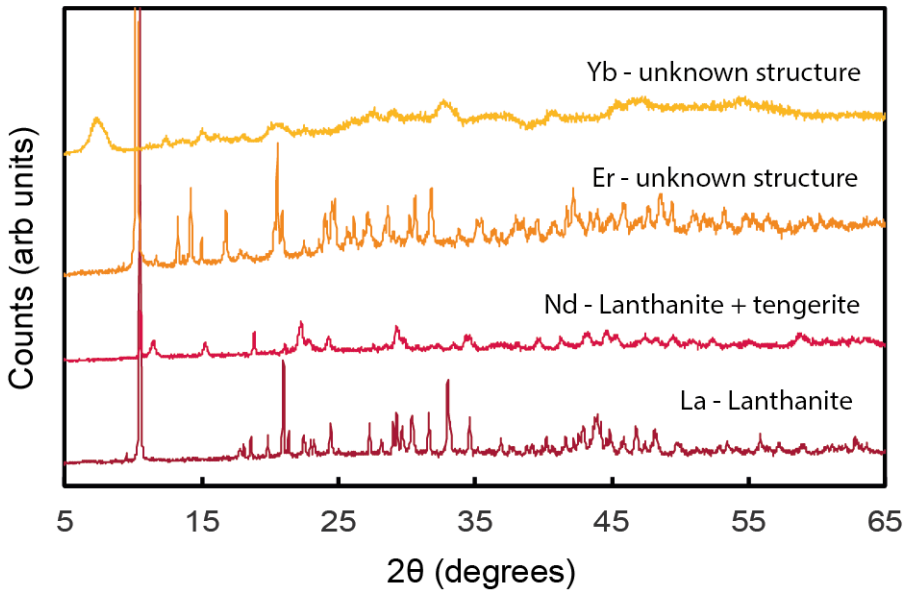

Figure 5.2: PXRD results of the REE carbonate standards used in this study.

5.4.3 XANES of experimental samples

The XANES spectra for all experimental samples, including the mixed-REE precipitates, are shown in Figures 5.3, 5.4, 5.5 and 5.6. All spectra of the experimental samples share common features, including intense white lines, a prominent single oscillation roughly 30 eV above the white line, no pre-edge features, and a strong similarity to their respective REE carbonate standard (i.e. $REE_2(CO_3)_3 \cdot xH_2O$). Given this similarity to the carbonate standards, it is pertinent to include the XANES spectra of the other standards along with the experimental results, as the differences between them can immediately rule out certain local structures. Of all the experimental spectra presented in Figures 5.3, 5.4, 5.5 and 5.6, only one shares the same spectrum as either the fluoride or oxide standard - this is sample La 90 A, identified as hexagonal hydroxylbastnäsite-(La), whose spectra is the same as that of the La oxide reference (Figure 5.3). This indicates that all the other experimental samples do not possess local structures akin to those of hexagonal REE oxides or fluorides.

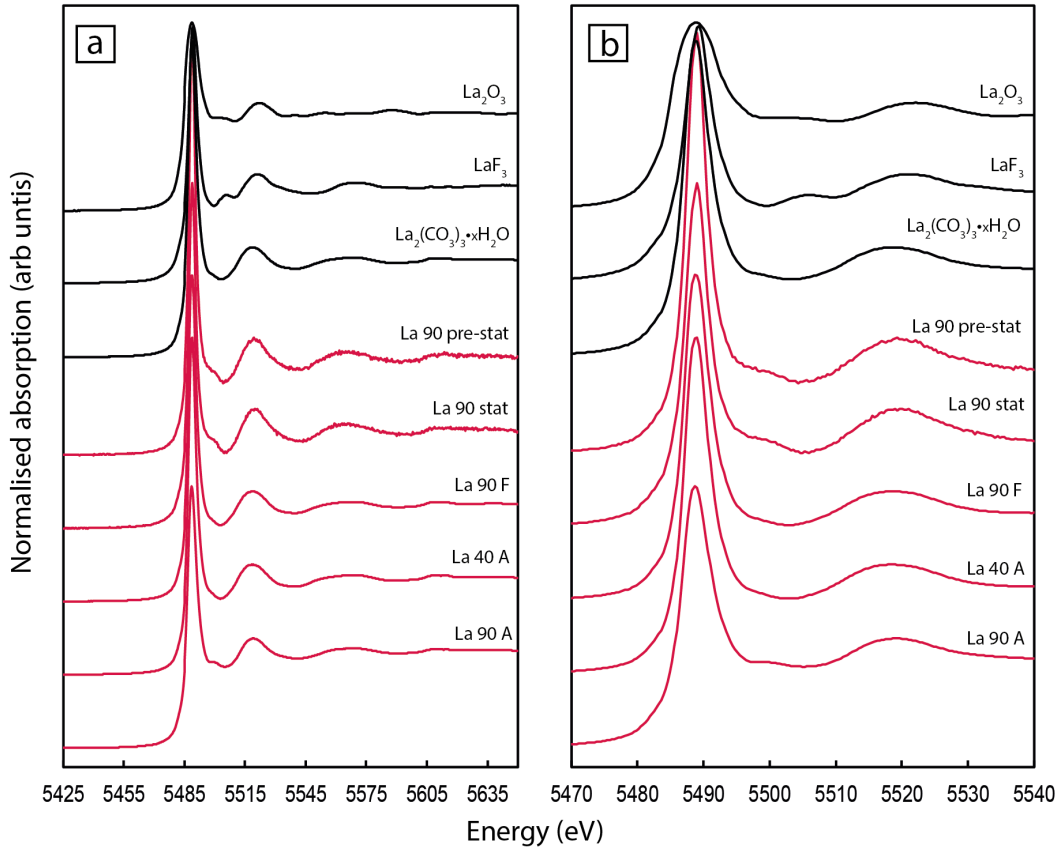

Figure 5.3: a) Comparison of the normalised La L_3-edge XAS spectra for the La samples (red lines). The spectra of standards are shown for reference (black lines); b) enlarged area of a) showing the XANES region. A = aged, F = fresh; number = the temperature at which titrations were conducted and/or the solutions were aged. Standards and all A and F samples measured at ambient temperature; pre-stat and stat samples were measured at about 85 K.

Although the REEs most commonly occur in the +3 oxidation state, of the four investigated here by XAS, Yb is also known to exist in the divalent state, for example during the synthesis of Yb-doped calcite from solutions (Tsuno et al., 2003). In that study, a small pre-edge feature was observed in Yb L_3-edge that was attributed to Yb^{2+}, an observation also made for Sm (Elzinga et al., 2002). No such features were observed in the current investigation. It is therefore concluded that Yb exists in the trivalent state in all samples. Comparison of the XANES spectra of the three other REEs investigated with those in the literature also confirms this oxidation state (e.g. Asakura et al., 2014a,b, 2015).

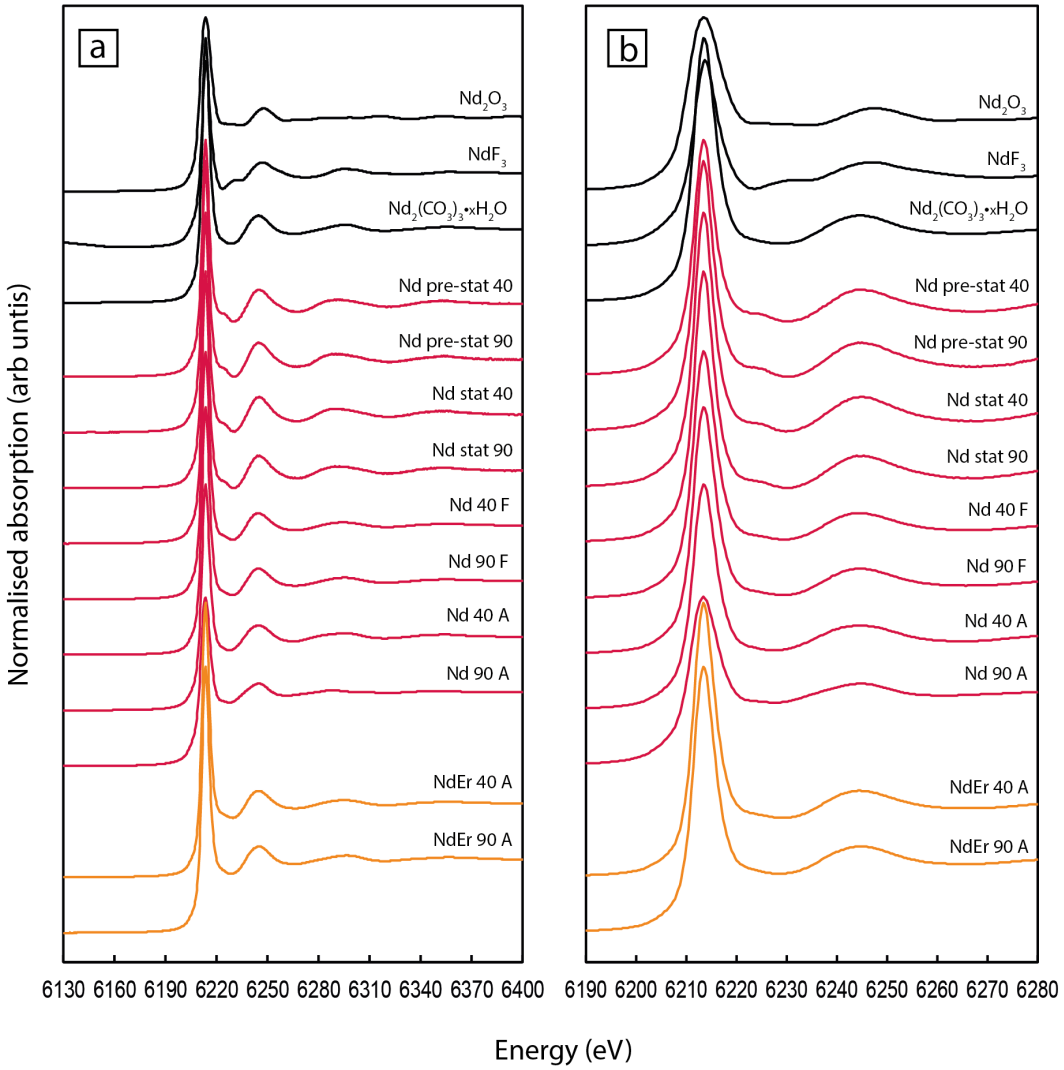

Figure 5.4: a) Comparison of the normalised Nd L_3-edge XAS spectra for the Nd samples (red lines) and mixed NdEr samples (orange lines). The spectra of standards are shown for reference (black lines); b) enlarged area of a) showing the XANES region. A = aged, F = fresh; number = the temperature at which titrations were conducted and/or the solutions were aged. Standards and all A and F samples measured at ambient temperature; pre-stat and stat samples were measured at about 85 K.

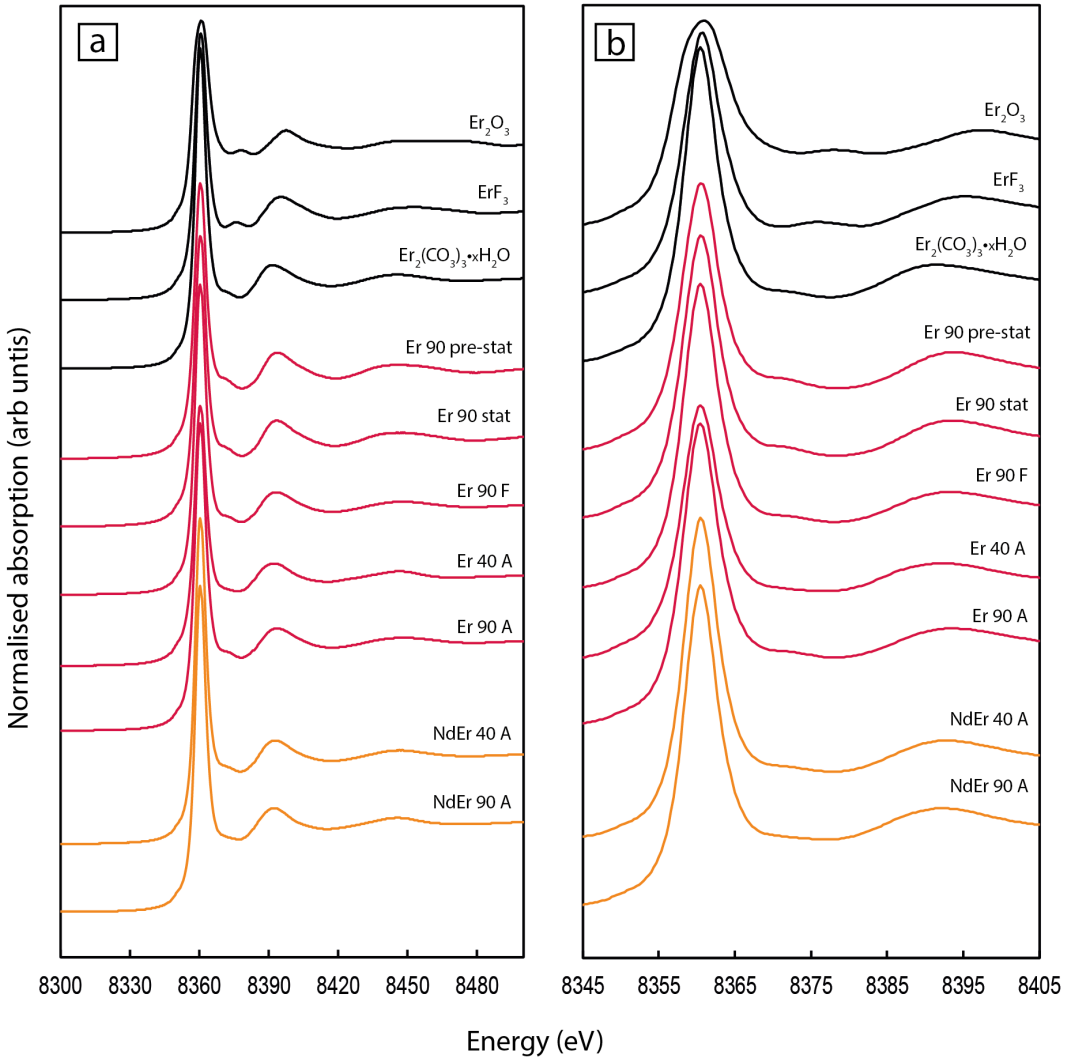

Figure 5.5: a) Comparison of the normalised Er L_3-edge XAS spectra for the Er samples (red lines) and mixed NdEr samples (orange lines). The spectra of standards are shown for reference (black lines); b) enlarged area of a) showing the XANES region. A = aged, F = fresh; number = the temperature at which titrations were conducted and/or the solutions were aged. Standards and all A and F samples measured at ambient temperature; pre-stat and stat samples were measured at about 85 K.

Although the XANES spectra appear similar, they differ in their details. The first difference to address is the variable intensity and width of the white line. Several samples exhibit white lines less intense and broader than the other samples, most notably La 90 A, Nd 90 A and Er 40 A. Although not directly measured here, previous authors have noted a correlation between the full width half maximum (FWHM) of the L_3-edge white line and coordination number for many of the REEs, including La, Nd, Er and Yb (e.g. Asakura et al., 2014a,b, 2015). In those studies, the XANES of various complex oxides suggests that the larger the FWHM (i.e. wider), the smaller the coordination number (their samples were from 7 to 12 coordinated). If this rule extends to the carbonates, it may be suggesting a change in local structure/coordination of several samples in the current investigation, although no quantitative conclusions can be made. Two of the

mentioned samples are known to be crystalline (La 90 A and Nd 90 A), whereas the Er 40 A sample was not. However, it was this sample that, when treated for 84 days (rather than the 42 as before), transformed into the mineral tengerite, as shown in Chapter 4. This may provide evidence for a changing local structure/coordination (as compared with the other Er samples) identified before the material acquired long range order.

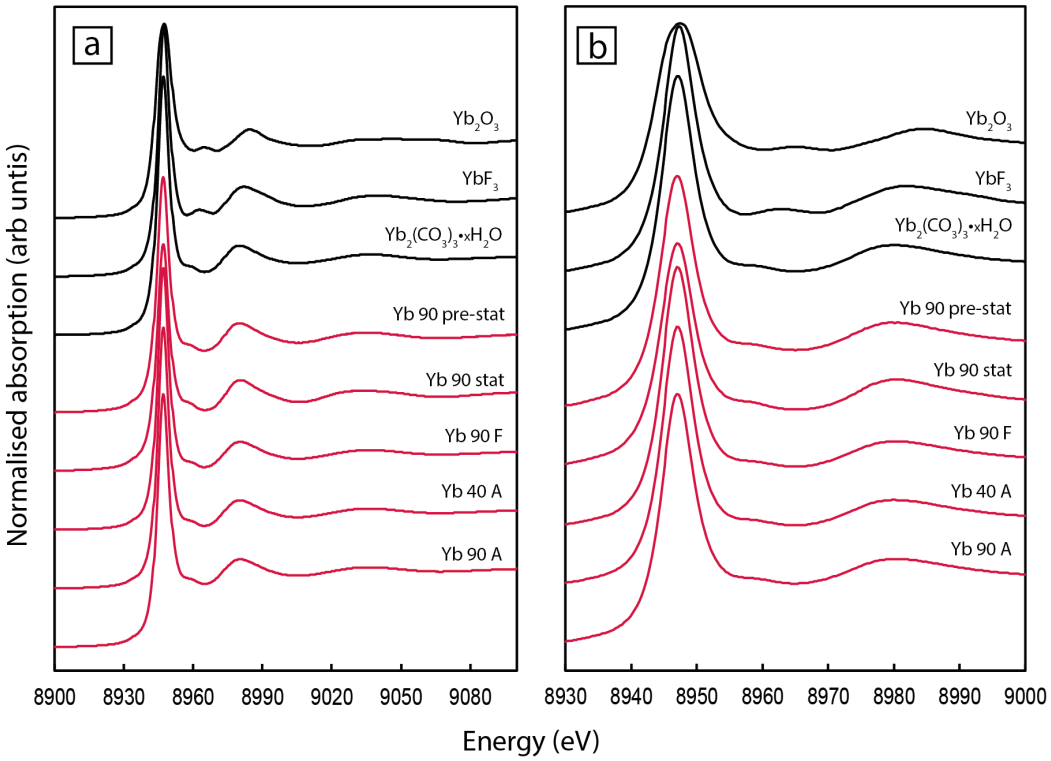

Figure 5.6: a) Comparison of the normalised Yb L_3-edge XAS spectra for the Yb samples (red lines) and standards (black lines); b) enlarged area of a) showing the XANES region. A = aged, F = fresh; number = the temperature at which titrations were conducted and/or the solutions were aged. Standards and all A and F samples measured at ambient temperature; pre-stat and stat samples were measured at about 85 K.

The other notable difference in the XANES spectra is the presence and intensity, or absence of, the shoulder in the first trough about 15 eV higher energy than the white line (on the downward, white line side of the trough). In the La samples, the carbonate standard, La 90 F and La 40 A are identical, which would be expected as they are all the mineral lanthanite. Sample La 90 A, found to be hydroxylbastnäsite in the previous chapter, is different to those just mentioned. The samples with the largest variation from the others, however, are the solutions (pre-stat and stat), which both show more prominent shoulders.

The same large shoulders are observed in the solution samples of the other elements: the Nd examples are most like those of La, while the Er and Yb examples are most similar

to each other. This could reflect changes in local structure resulting from the different rate at which crystallisation is occurring in solution as a function of atomic number, i.e. one of the main conclusions of previous authors (e.g. Rodriguez-Blanco et al., 2014) and the previous chapter. Most Er samples are similar, and all the Yb samples are identical.

The mixed NdEr 40 A and 90 A (both Nd and Er edges) have a less prominent/absent shoulder than in their single REE counterparts, suggesting these elements behave differently when mixed than present as the sole REE.

5.4.4 EXAFS of experimental samples

The results of EXAFS modelling are presented in order of increasing atomic number.

5.4.4.1 Lanthanum

Although EXAFS data were collected for the La samples, modelling them beyond the first shell oxygen atoms was difficult, even for the samples with known structures. Isolated $\chi(k)$ data, including those of the three standards, are shown in Figure 5.7, and the best fit parameters are presented in Table 5.2. When reviewing $\chi(k)$ spectra, it is important to note that data from 0 to about 3 $Å^{-1}$ is associated with the absorption edge structure. When differences in the spectra occur in this region it is necessary to consult the XANES spectra once again: if these are the same, or very similar, the differences in the < 3 $Å^{-1}$ $\chi(k)$ data is a product of the background subtraction procedure (Mosselmans, 2017 – personal communication). In other words, the differences are not real. Comparing the La sample data presented in Figure 5.7, the differences between the two solution samples (90 pre-stat and 90 stat) and the others are thought to be real, while the differences between all the solid samples are not.

Comparison of the $\chi(k)$ data reveals identical spectra for the $LaCO_3$ standard, La 40 A and La 90 F. This is expected because based on the PXRD results from Chapter 4, all three are the mineral lanthanite-(La). The spectrum of La 90 A (identified as hydroxylbastnäsite in Chapter 4) is different to these three, again as would be expected from the structural change. Despite the XANES of sample La 90 A appearing the same as the La oxide standard, the EXAFS spectra are quite different. In fact, the La oxide and La fluoride standards have produced spectra dissimilar to all the experimental results. EXAFS of the two solution samples, La pre-stat and stat, are similar to the other experimental samples, although the lower quality data makes comparison in the higher k regions difficult. These results suggest that the structure of the La-bearing phase in solution is not the same as in the solid precipitates.

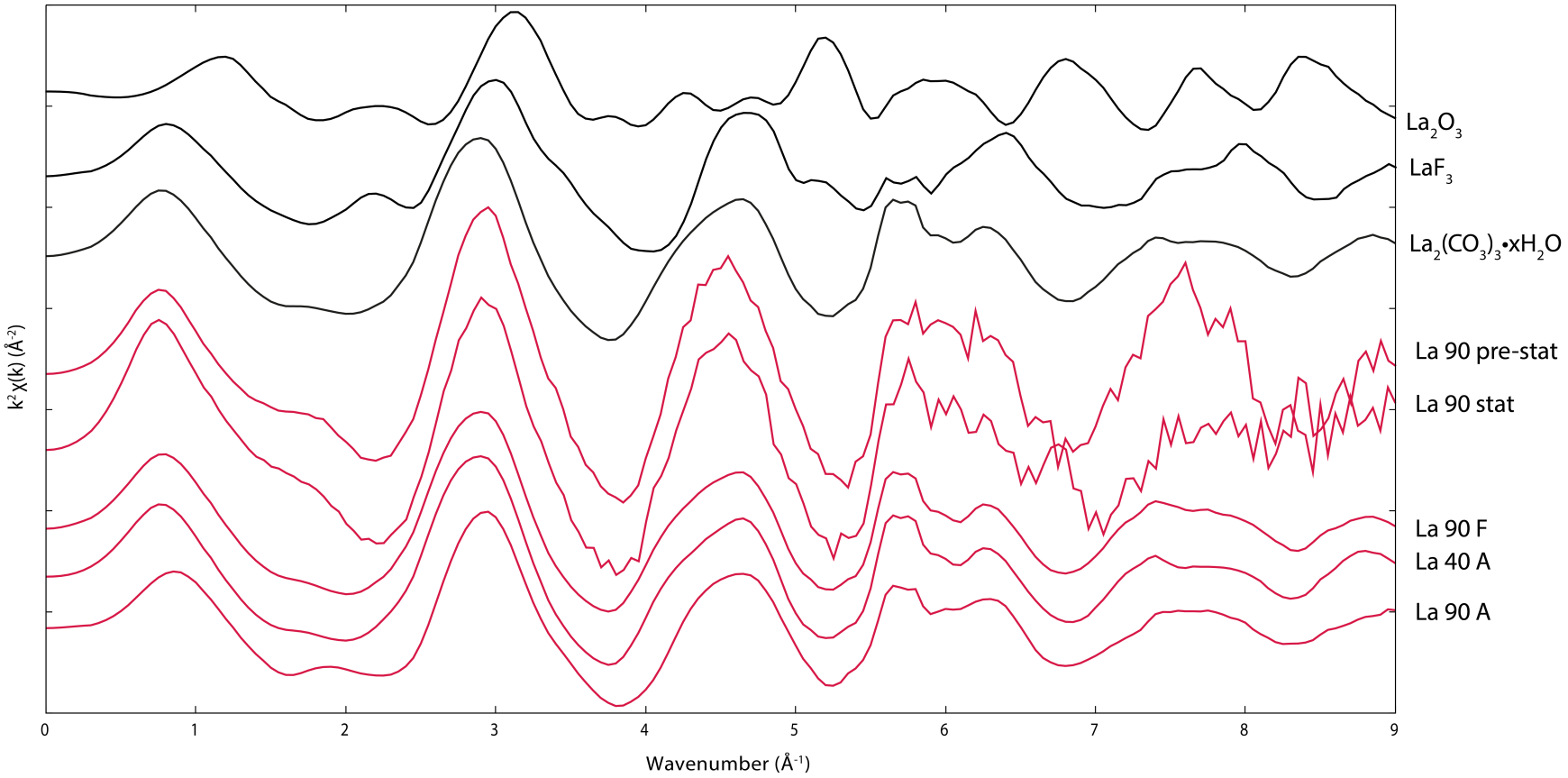

Figure 5.7: Isolated k^2-weighted $\chi(k)$ data for the solution and solid La samples (red lines). The standards have been included for reference (black lines).

Sample	Element	N	R (Å)	σ^2 (Å^2)	$\mathcal{R}$ factor	*k*-range	*R*-range
La 90 pre-stat	O	8.6 ± 1.7	2.58 ± 0.02	0.011 ± 0.003	0.017	3.0 - 7.0	1.3 - 3.0
La 90 stat	O	10.1 ± 3.9	2.57 ± 0.04	0.007 ± 0.005	0.019	3.0 - 7.5	1.5 - 3.0
La 90 F	O	9.1 ± 2.5	2.57 ± 0.03	0.012 ± 0.005	0.009	3.0 - 9.2	1.5 - 2.7
La 40 A	O	9.0 ± 1.6	2.59 ± 0.02	0.012 ± 0.003	0.015	3.0 - 9.4	1.3 - 3.0
La 90 A	O	8.9 ± 1.7	2.57 ± 0.02	0.011 ± 0.003	0.017	3.0 - 9.4	1.4 - 3.0
La carb std	O	8.6 ± 1.7	2.58 ± 0.02	0.011 ± 0.003	0.017	3.0 - 9.4	1.4 - 3.0

Table 5.2: Results of best fit parameters for the La samples. Only the first shell was fit in these examples. N = coordination number; R = distance from the absorbing La atom; σ^2 = Debye-Waller factor. Coordination numbers were determined using an S_0^2 value of 0.9. Values for the La carbonate standard are included for reference (final row). Errors are calculated in Artemis during fitting and are at the 1σ confidence level. La carb std = $La_2(CO_3)_3 \cdot xH_2O$

In all samples the range of average first shell oxygen distances was between 2.57 and 2.59 Å, and the coordination number, which it should be noted commonly has errors of up to 20 %, was around 9. Inclusion of more distant shells, i.e. potential carbon atoms, was unsuccessful in almost every case, producing visually- and statistically-worse fits.

The mineral lanthanite and the synthetic hexagonal phase $LaCO_3OH$ (i.e. the same structure as hydroxylbastnäsite-(La)) have average REE-O bond for first shell oxygen atoms of 2.58 and 2.59 Å, respectively, and coordination numbers of 10 and 9, respectively (e.g. Dal Negro et al., 1977; Michiba et al., 2011). Based on PXRD analyses from the previous chapter, it is known that samples La 90 F and La 40 A are lanthanite, and sample La 90 A is hydroxylbastnäsite. The values returned from modelling for average La-O distances and CN are therefore within error for both phases. However, this information is inadequate for a more detailed determination of these phases. Without the inclusion of additional shells, the comparison of the data for the known and unknowns (i.e. the solutions) cannot be used for phase identification. The only solid conclusion that can be made from these data is that the unknown solution samples are not identical to those with either the lanthanite or hydroxylbastnäsite structures. These may be the short-lived 'amorphous lanthanum carbonate (ALC)' observed by e.g. Vallina et al. (2015). As discussed in the previous chapter, ALC was obtained by those authors after directly mixing REE chloride and sodium carbonate solutions, but its lifetime was only around two or three minutes. It then crystallised into lanthanite-(La). It was for this reason that ALC was not observed in the results of Chapter 4 (i.e. the titrations took approximately 10 minutes). In the current chapter, samples pre-stat and stat were obtained after about one and two minutes, respectively.

5.4.4.2 Neodymium

The isolated k^2-weighted $\chi(k)$ data for all the Nd-bearing phases, including the standard materials, are shown in Figure 5.8. As with the La examples, the differences between solution and solid samples in the < 3 Å region of the EXAFS is thought to be real, but those between the solids are not. The $\chi(k)$ data for all samples are similar, although the solution samples are again noisier in the higher k region. EXAFS of the solutions, regardless of the temperature, are identical beyond 2 Å, suggesting the same local structure/environment. The X-ray amorphous fresh samples (Nd 40 F and Nd 90 F), obtained only a few minutes after the frozen solutions, display different spectra that are phase-shifted to higher k in the region > 4 Å. These spectra are almost identical to those of the Nd carbonate standard (identified as lanthanite with minor tengerite by PXRD) and both X-ray amorphous NdEr samples. Nd 40 A (90 % lanthanite-(Nd) and 10 % tengerite-(Nd) - Chapter 4) is similar. These results suggest that the X-ray amorphous materials may have local structures similar to the 'normal' carbonates lanthanite and tengerite. The only sample significantly different to the others is Nd 90 A, which was identified by PXRD as the carbonate hydroxide mineral kozoite-(Nd). None of the samples share similar spectra to those of the Nd oxide or Nd fluoride standards.

The magnitude of the Fourier transform of the $\chi(k)$ data, including the results of fitting, are shown in Figure 5.9. All samples contain a large peak at 2 Å (not phase shift corrected), attributed to first shell oxygen atoms. Most the spectra have small features on the higher R side of the main peak, the closest of which (up to around 4 Å) are mostly attributed to carbon atoms (see below). The Nd 90 A sample has the most intense features beyond 2 Å, which results from distant Nd atoms in the kozoite structure. The pre-stat samples at both temperatures contain features beyond 2 Å, however, as will be explained below, these were not included during fitting. The features on the lower R side of the main peak are related to the background and were also not included during fitting (fitting windows are presented as dashed green lines in Figure 5.9). Given the dissimilar spectra for the Nd oxide and fluoride standards, these were not modelled in R space.

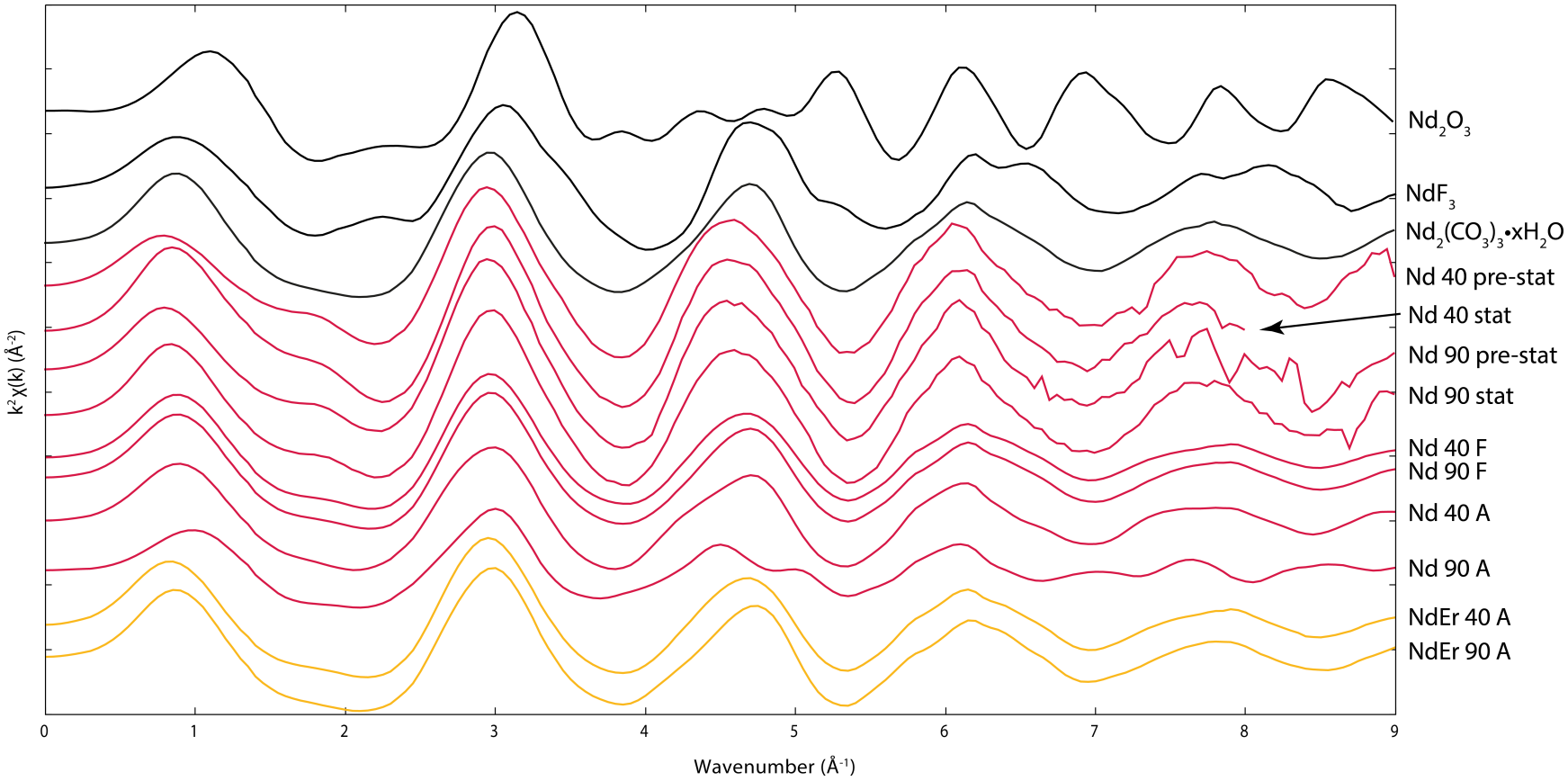

Figure 5.8: Isolated k^2-weighted $\chi(k)$ data for the Nd samples (red lines), mixed NdEr precipitates (orange lines), and Nd standards (black lines).

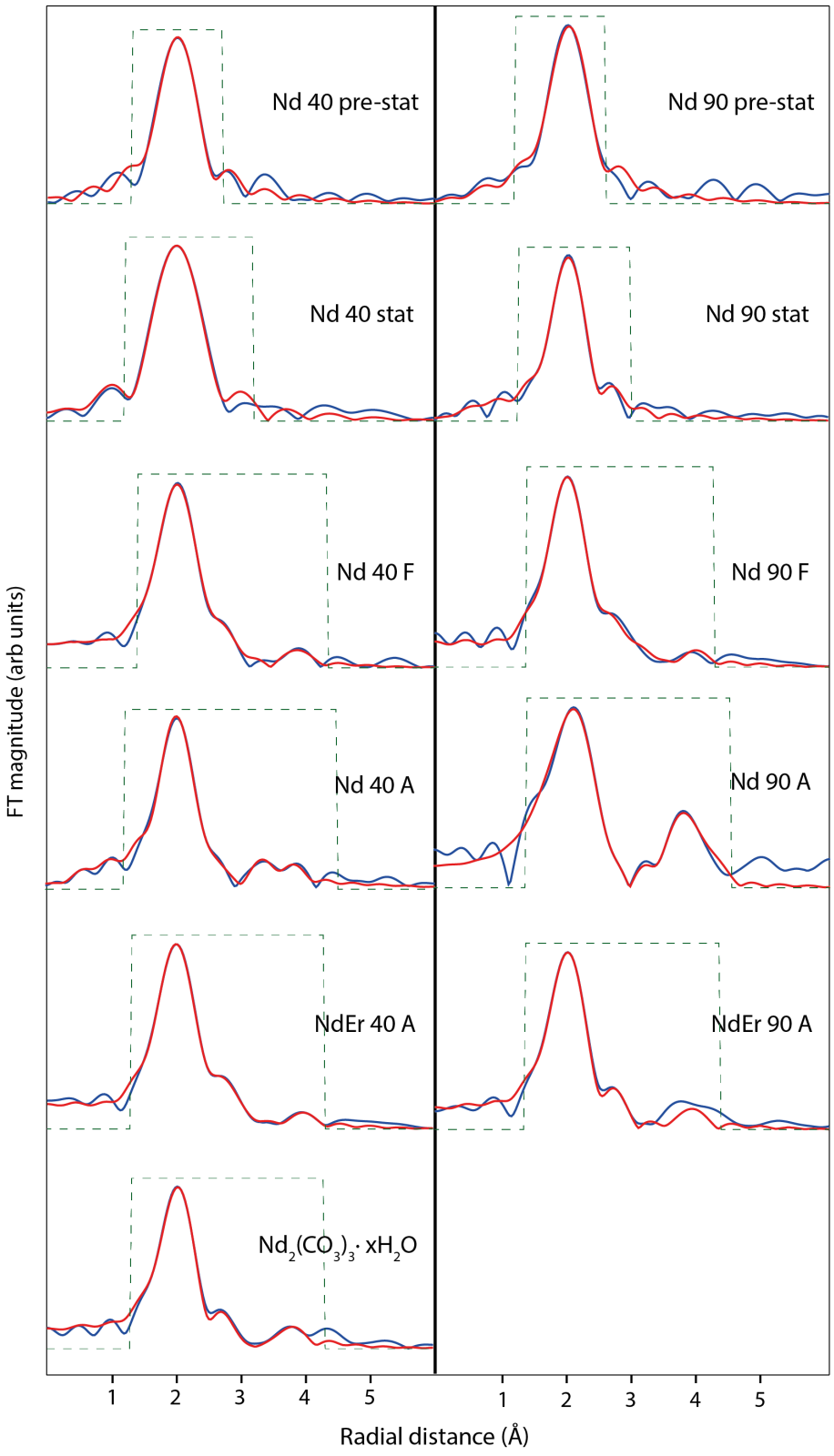

Figure 5.9: Magnitude of the Fourier transform (blue lines) of the k^2-weighted $\chi(k)$ data from Figure 5.8, and the corresponding best fits to the data (red lines). The dashed green line is the window used for fitting in R-space. The k- and R-space ranges used are also indicated in Table 5.3.

The best fit parameters are presented in Table 5.3. During the fitting procedure, numerous combinations of carbon atoms (with fixed CN values) at different distances were iterated until the best fits were returned. In several cases, notably for the pre-stat samples (at both temperatures), the inclusion of these C atoms was visually acceptable, producing low $\mathcal{R}$-factor values (i.e. low miss-match between experimental and modelled data), but did not meet the statistical thresholds mentioned in the data analysis section in Chapter 3. Because the lower Z REEs have shorter data ranges (due to the other nearby absorption edges) than their HREE counterparts, the amount of information available is limited, which makes fitting several paths more difficult to justify statistically. In the case of the pre-stat and stat examples, the inclusion of C atoms probably makes the fit better, but it is impossible to be definitive (Mosselmans, 2017 – personal communication) - hence their omission from Table 5.3.

A large amount of literature has been published on the structural parameters of REEs in solutions, utilising an array of techniques including EXAFS, with most studies agreeing on a CN hydration value for Nd of 9. Nd-O bond lengths (average for first shell) differ across the literature, but mostly fall within 2.48 – 2.53 Å (see reviews in D'Angelo and Spezia, 2012; Smirnov and Trostin, 2012). These bond lengths and CN values are within error to those presented for the Nd pre-stat and stat samples. However, as with the La examples before, without fitting additional shells it is impossible to determine more about their local structures, or, because the presence of C atoms cannot be confirmed definitively, state whether they exist as hydrated ions or have coordinated with carbonate. What can be confirmed, however, is that they do not possess intermediate- or longer-range local structures the same as known, crystalline Nd carbonate materials (i.e. Nd 40 A, Nd 90 A, Nd carbonate standard).

As outlined in the methods, the REE carbonates synthesised throughout this study were done so by precipitation from chloride-rich solutions. Therefore, as an additional side check, the pre-stat and stat samples were modelled using a two-subshell fit with oxygen and chloride. Results showed that in all cases inclusion of the latter was severely detrimental to the fit, indicating no chloro-aqua complex formation. These observations are in agreement with previous works for Nd chloride solutions at similar concentrations and temperatures (e.g. Mayanovic et al., 2009a).

Sample	Element	N	R (Å)	σ^2 (Å^2)	$\mathcal{R}$ factor	*k*-range	*R*-range
Nd 40 pre-stat	O	9.2 ± 1.4	2.50 ± 0.02	0.003 ± 0.002	0.006	3.0 - 8.8	1.3 - 2.7
Nd 90 pre-stat	O	10.5 ± 1.1	2.51 ± 0.01	0.007 ± 0.002	0.003	3.0 - 9.0	1.2 - 2.6
Nd 40 stat	O	11.5 ± 2.1	2.51 ± 0.02	0.007 ± 0.003	0.007	3.0 - 8.0	1.2 - 3.2
Nd 90 stat	O	9.7 ± 0.9	2.50 ± 0.01	0.005 ± 0.001	0.007	3.3 - 10.5	1.3 - 3.0
Nd 40 F	O	9.1 ± 1.0	2.48 ± 0.01	0.010 ± 0.002	0.005	3.2 - 10.0	1.4 - 4.35
	C	2	3.09 ± 0.06	0.011 ± 0.007			
	C	2	3.61 ± 0.07	0.011 ± 0.007			
	Nd	2	4.04 ± 0.04	0.017 ± 0.006			
Nd 90 F	O	8.0 ± 0.8	2.48 ± 0.01	0.009 ± 0.001	0.004	3.5 - 10.5	1.4 - 4.25
	C	2	3.09 ± 0.05	0.009 ± 0.007			
	C	2	3.41 ± 0.06	0.009 ± 0.006			
	Nd	2	4.03 ± 0.04	0.014 ± 0.005			
Nd 40 A	O	8.4 ± 1.2	2.51 ± 0.01	0.006 ± 0.001	0.010	3.0 - 10.4	1.2 - 4.5
	O	2	2.70 ± 0.03	0.006 ± 0.001			
	C	2	2.99 ± 0.06	0.006 ± 0.005			
	C	2	3.64 ± 0.08	0.006 ± 0.005			
	O	2	4.01 ± 0.07	0.005 ± 0.008			
	O	8	4.24 ± 0.06	0.020 ± 0.009			
Nd 90 A	O	8.7 ± 1.5	2.57 ± 0.01	0.018 ± 0.003	0.004	3.5 - 10.5	1.4 - 4.5
	C	3	3.04 ± 0.01	0.010 ± 0.006			
	C	2	3.43 ± 0.03	0.010 ± 0.006			
	Nd	2	3.88 ± 0.02	0.009 ± 0.008			
	Nd	2	4.30 ± 0.02	0.009 ± 0.008			
NdEr 40 A	O	8.8 ± 0.5	2.48 ± 0.01	0.009 ± 0.001	0.002	3.5 - 10.2	1.3 - 4.3
	C	1	3.11 ± 0.04	0.005 ± 0.002			
	C	3	3.63 ± 0.02	0.005 ± 0.002			
	Nd	2	4.03 ± 0.03	0.014 ± 0.003			
NdEr 90 A	O	9.9 ± 2.4	2.50 ± 0.02	0.010 ± 0.003	0.017	3.25 - 10.1	1.37 - 4.33
	C	2	2.88 ± 0.06	0.008 ± 0.007			
	C	2	3.66 ± 0.10	0.008 ± 0.007			
Nd carb std	O	10.4 ± 1.5	2.50 ± 0.01	0.009 ± 0.002	0.008	3.25 - 10.5	1.3 - 4.3
	C	2	2.88 ± 0.04	0.005 ± 0.005			
	C	2	3.69 ± 0.06	0.005 ± 0.005			
	O	6	4.23 ± 0.04	0.009 ± 0.004			

Table 5.3: Results of best fit parameters for the individual Nd and mixed NdEr samples. N = coordination number; R = distance from the absorbing Nd atom; σ^2 = Debye-Waller factor. Coordination numbers were determined using an S_0^2 value of 0.85. Values for the Nd carbonate standard are included for reference (final rows). CN values presented without errors were fixed during fitting. Several more shells were fit in the Nd 40 A and 90 A samples because their identities were already known from PXRD. Errors are calculated in Artemis during fitting and are at the 1σ confidence level. Nd carb std = $Nd_2(CO_3)_3 \cdot xH_2O$

In Table 5.4, distances from the absorbing Nd atom to the O, C and Nd atoms (up to about 4.5 Å) of various natural and synthetic Nd-bearing minerals mentioned throughout this thesis (e.g. kozoite, tengerite, hydroxylbastnäsite) are presented. This is to aid comparison between modelling results and known structures in the following discussion. The two samples with known structures (Nd 40 A and Nd 90 A) were successfully modelled to their respective .cif files (structural information files). Because the structures were known, they were modelled with more shells than the unknowns, which meant the number of variables used approached the maximum number permitted by the k-range used. Although this decreases the statistical confidence and is generally to be avoided, it was deemed not an issue here because the thresholds mentioned earlier were not exceeded (except one σ^2 value in Nd 40 A), and their inclusion was useful for comparative purposes.

Sample Nd 90 A (kozoite) has average Nd-O (first-shell) of 2.60 Å, which is in excellent agreement with natural kozoite-(Nd) (2.62 Å - Miyawaki et al., 2000) and synthetic orthorhombic $NdCO_3OH$ (2.57 Å - Tahara et al., 2007). The slightly larger value for the natural kozoite is attributed to the incorporation of the larger (lighter) REEs, particularly La (approx. 21 wt.% in their example). In Nd 40 A (90 % lanthanite), the average distance to oxygen atoms is 2.55 Å. This value is in good agreement with natural lanthanite-(La) (2.58 Å - Dal Negro et al. 1977), in which the bond lengths are slightly longer than pure lanthanite-(Nd) for the same reason as before; atomic coordinates for the latter were not found in the literature, although there have been several studies of natural occurrences of this mineral (e.g. Graham et al. 2007; Morrison et al. 2013). The additional REE-C, REE-O and REE-Nd distances in both Nd 40 A and Nd 90 A are in excellent agreement with the structural files (Table 5.4).

In the unknown precipitates, including the mixed NdEr, the average first shell REE-O bond length is approximately 2.50 Å, and CN values are (within error) around 9 or 10, except Nd 90 F (8.0 ± 0.8). These bond lengths are shorter than those reported for the natural or synthetic versions of the commonly-mentioned minerals in this Table 5.4, which may suggest that these bond lengths increase as the structure of the material becomes more regular and extended. Similar average Nd-O bond lengths have been reported previously, however, for several materials including: aqueous hydrated complexes (as mentioned above); high order tri- or tetra-carbonate complexes produced in very high carbonate concentration (> 2.5 M) environments, and the crystals obtained from them, e.g. $[C(NH_2)_3]_5[Nd(CO_3)_4(H_2O)]\cdot H_2O$ (range from 2.452 – 2.544 Å - Runde et al., 2000); and the phase $KNd(CO_3)_3OH$ (2.50 Å - Kutlu et al., 1997). In addition, various molecular dynamics simulations of carbonate complexes suggest similar bond lengths, e.g. $[Nd(CO3)4]^{5-}$ (e.g. 2.49 Å - Sinha et al., 2010).

	Lanthanite-(La)		**Tengerite-(Y)**		**$NdCO_3OH$** (orth)		**$NdCO_3OH$** (hex)	
	Element	*R (Å)*	*Element*	*R (Å)*	*Element*	*R (Å)*	*Element*	*R(Å)*
	O 9.1	2.520	O 6.1	2.335	O 1.1	2.352	O 6.1	2.428
	O 9.1	2.520	O 3.1	2.360	O 1.2	2.369	O 16.1	2.434
	O 7.1	2.543	O 2.1	2.377	O 2.1	2.535	O 13.1	2.474
	O 7.1	2.543	O 4.1	2.392	O 2.1	2.535	O 3.1	2.486
	O 2.1	2.625	O 5.1	2.411	O 3.1	2.583	O 17.1	2.490
	O 2.1	2.625	O 1.1	2.414	O 3.1	2.583	O 12.1	2.501
	O 1.1	2.660	O 2.2	2.435	O 3.2	2.620	O 4.1	2.518
	O 1.1	2.660	O 3.2	2.452	O 3.2	2.620	O 11.1	2.685
	O 8.1	2.733	O 1.2	2.529	O 3.3	2.748	O 10.1	2.713
	O 8.1	2.733			O 3.3	2.748	O 4.2	2.985
Mean		2.616		2.411		2.569		2.610
	C 2.1	3.053	C 1.1	2.770	C 1.1	2.958	C 6.1	2.996
	C 2.1	3.053	C 2.1	2.803	C 1.2	3.035	C 2.1	3.162
	C 2.2	3.626	C 1.2	2.884	C 1.2	3.035	C 2.2	3.389
	C 2.2	3.626	C 1.3	3.476	C 1.3	3.497	O 12.2	3.569
	O 8.2	4.094	C 1.4	3.552	C 1.3	3.497	C 3.1	3.577
	O 8.2	4.094	O 3.3	4.001	Nd 1.1	3.886	C 5.1	3.653
	O 7.2	4.318	O 1.3	4.001	Nd 1.1	3.886	Nd 2.1	3.963
	O 7.2	4.318	O 1.4	4.057	O 2.2	3.989	Nd 3.1	3.972
	O 5.1	4.321	O 6.2	4.060	O 2.3	4.134	O 6.2	4.019
	O 5.1	4.321	O 3.4	4.070	O 2.4	4.191	O 4.3	4.083
	O 5.2	4.339	Y 1.1	4.124	O 2.4	4.191	O 3.2	4.106
	O 5.2	4.339	Y 1.1	4.124	O 3.4	4.213	Nd 2.2	4.151
	O 3.1	4.399	O 5.2	4.147	O 3.4	4.213	Nd 3.2	4.167
	O 3.1	4.399	O 5.3	4.233	Nd 1.2	4.301	C 6.2	4.189
	O 4.1	4.495	O 6.3	4.276	Nd 1.2	4.301	Nd 1.1	4.229
	O 4.1	4.495	O 1.5	4.323	O 3.5	4.316	Nd 1.1	4.229
	La 2.1	4.527	O 5.4	4.326	O 3.5	4.316	O 12.3	4.249
	La 2.1	4.527	O 6.4	4.342	O 1.3	4.410	O 2.1	4.265

Table 5.4: Distances (Å) from the absorbing atom to first shell oxygen atoms (O; mean also shown), bidentate and monodentate carbons (C; shorter and more distant, respectively), and more distant oxygen or metal atoms (O, La, Nd, Y) in some relevant carbonate minerals. The mean value is the mean of the first shell metal-coordinated O atoms; note the smaller value for tengerite-(Y), resulting from the lanthanide contraction. $NdCO_3OH$ orth and hex are kozoite and hydroxylbastnäsite, respectively. Numbers after the element symbols are the atomic labels. Structural files taken from the ICSD database, with original sources: Dal Negro et al., 1977 (Lanthanite-(La); Miyawaki et al., 1993 (Tengerite-(Y); Tahara et al., 2007 ($NdCO_3OH$ – orth); Michiba et al., 2011 ($NdCO_3OH$ – hex).

Despite the similarity in bond length between the modelling results of the X-ray amorphous material in this study and the high-order complexes mentioned above, it is unlikely the two are same because the conditions at which they were formed are quite different. Those experiments and MD simulations were conducted using very high carbonate concentrations, low concentrations of REEs (orders of magnitude lower than the current experiments), and high pH (> 10). These conditions are used to promote REE-carbonate complex formation and stability, whereas the conditions employed in the current investigation were designed to precipitate REE carbonates.

To probe further the two unknown solid Nd-only samples (Nd 40 F and 90 F), it is necessary to look at the atoms beyond the first shell. Given the similarities in their EXAFS (Figure 5.8) to those of samples Nd 40 A and the Nd carbonate standard (lanthanite/tengerite), models including C atoms in the second shell were tested. Consultation of the literature suggests that in high-order REE carbonate complexes and their single crystals, the most stable form involves fully-bidentate carbonate ions; the final (ninth) coordination site is filled by a water molecule in the larger REEs (La, Ce, Nd) (e.g. Sinha et al., 2010; Martelli et al., 2014). In contrast, in all the crystalline REE carbonates mentioned in Table 5.4, and many more that are not, the C atoms are broadly grouped at two distances, which results from mixed mono and bidentate coordinated carbonates; the remaining sites are occupied by water molecules.

Although the X-ray amorphous samples were not believed to be high-order carbonates, without long-range structures it was deemed not wise to simply *assume* they contained mixed mono and bidentate carbonates. This was doubly true given that the features seen in the FTs at around 3.5 Å could be attributed to the non-REE bound O atom(s) of carbonate ions, especially as C and O have similar EXAFS scattering properties (given their proximity in the periodic table). Therefore, to understand more fully the type of carbonate coordination, the FTIR data of the X-ray amorphous samples in this chapter/Chapter 4 were re-examined, specifically the fingerprint region from 2000 to 600 $cm^{-}1$ (Figure 5.10). As they are almost identical, all samples (i.e. all REEs investigated) are treated together, and the discussion holds true for them all.

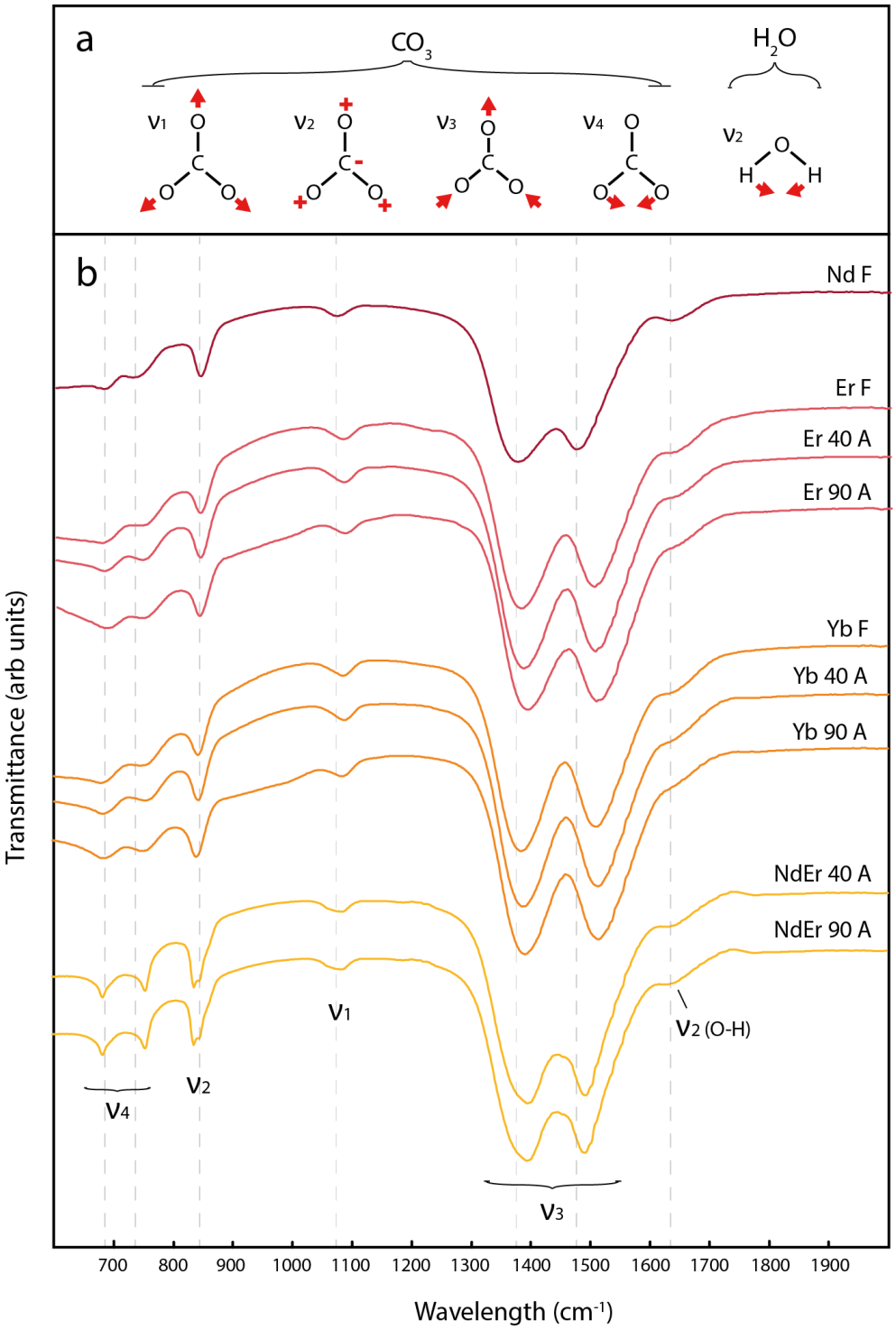

Figure 5.10: FTIR spectra of the X-ray amorphous samples studied in the current and previous chapter. The faint dashed lines in b) are aligned to the bands of the Nd sample (top) so that frequency changes in the spectra of different REEs can be observed. The modes $\upsilon_1 - \upsilon_3$ are stretching bands, and υ_4 is a bending band, of carbonate ions, and the υ_2 (O-H) mode is in-plane bending of H_2O molecules, which are demonstrated in a). The Nd 40 F and Nd 90 F samples are represented by the single Nd F spectra. F = fresh, A = aged.

All the FTIR spectra are characterised by two intense bands between 1300 and 1550 cm^{-1}, which are assigned to the asymmetric stretching of carbonate (υ_3); splitting of this band indicates metal-carbonate complexation, as does splitting of the υ_4 bending mode. The extent of the υ_3 split provides evidence for mono or bidentate carbonate complexation: in the former, the split is typically less than 100 cm^{-1} and the higher frequency part of the split is at < 1500 cm^{-1}, whereas in bidentate complexation the opposite is true (e.g. Nakamoto et al., 1957; Bond et al., 2000, 2001; Janicki et al., 2011). The splitting of υ_3 in Figure 5.10, which ranges from 103 cm^{-1} (Nd) to 120 cm^{-1} (Yb), indicates bidentate coordination. However, it is noted that the identification of bidentate does not preclude the presence of monodentate carbonates, as the splitting of the υ_3 mode can also result from two different carbonate groups (equatorial vs axial bridging, e.g. Bond et al., 2000). The additional modes in Figure 5.10 are symmetric (υ_1) and asymmetric (υ_2) stretching of carbonate. It is worth quickly noting that the shift of the υ_1 and υ_3 bands to higher energy (roughly 20 $cm^{-}1$ shift from Nd to Yb) results from the decrease in the REE-O(CO_3) bond length and coordination number caused by the lanthanide contraction (Janicki et al., 2011), as will be shown in the coming subsections. This confirms further the REE-carbonate coordination.

Using this information, the modelling best fits resulted in the carbon atom CN and bond length values that were presented in Table 5.3. The CN values were varied during fitting, but always fixed (i.e. not guessed), until the best fits were returned. Attempts to guess their CN numbers were made difficult/impossible, as doing so exceeded the number of independent points available from the data. Also, as found in an EXAFS study by Heberling et al. (2008) on the co-precipitation of Np with calcite, guessing CN values of C atoms (in that case at about 3.1 Å) was associated with errors of up to almost 100 % (e.g. 3.0 ± 2.9). Therefore, although the results presented in Table 5.3 for the CN values of C do meet all the statistical thresholds and improve the fits, the exact number comes with errors probably in the region of $\pm$ 1. This then has implications for the number of water molecules (i.e. fewer C atoms, or more mono than bidentate carbonate ions, means more uncoordinated sites, which are likely filled by water - see next paragraph).

The results of fitting suggest that samples Nd 40 F and 90 F contain two C atoms at 3.1 Å and a further two at 3.6 Å (40 F) and 3.4 Å (90 F). The values for both C distances in the 40 F sample are identical (within error) to natural lanthanite-(La) and seem to strongly suggest a similar short-range carbonate structure between the two. In the 90 F sample the more distant of the C atoms are approximately 0.2 Å closer to the absorbing Nd, which is more closely matched to the monodentate C atoms in tengerite (Table 5.4). In both cases, the remaining coordinating sites around the Nd atom are assumed, given the lack of additional elements in the experiments and the absence of absorption bands from OH groups in the FTIR spectra, to be filled by water

molecules. This would also account for the large, broad water-associated bands in the FTIR spectra, as was shown in Chapter 4.

Modelling further than these C atoms becomes very difficult in unknown samples and the results are certainly not conclusive. However, inclusion of two Nd atoms did improve both the Nd 40 F and 90 F fits, with identical distances returned for both samples. Although it is unclear whether the features around this distance in the FTs are attributed to Nd or O atoms, the latter being expected from the lanthanite structure, fitting O instead of Nd was unsuccessful/worse in all cases. Therefore, the results of EXAFS modelling of the X-ray amorphous Nd samples suggests that the metal is coordinated with both mono and bidentate carbonate at distances similar to lanthanite when titrations are performed at 40 °C, and perhaps slightly mixed lanthanite/tengerite distances when precipitated at 90 °C. It is suggested that the longer Nd-O (first shell) bond lengths in crystalline materials as compared with those in the amorphous materials reflects a lengthening of bonds as the structure becomes extended. This suggests that in the results presented here for the X-ray amorphous 'fresh precipitates', the material is made up of nanoscale or smaller REE carbonate units larger than simple complexes but smaller than material identifiable from PXRD analysis. These conclusions add to the results from Chapter 4 (X-ray amorphous but with FTIR bands for carbonate), and also the findings of studies such as Vallina et al. (2015) in which the 'amorphous Nd carbonate (ANC)' was postulated to have the chemical formula $Nd_2(CO_3)_3 \cdot xH_2O$ ($x < 5$), calculated based on standard-less EDS and thermogravimetric analyses.

In Figure 5.11, simple ball and stick models are presented to visually demonstrate the difference in coordination around the Nd atom resulting from the different number of monodentate and bidentate carbonate ions. Although the results presented in Table 5.3 included distant Nd atoms for some samples, these have not been included in the ball and stick models because the location/bonding of these atoms is unknown. Additionally, the non-REE-bonded oxygen atoms of the carbonate groups have been included, despite their absence from Table 5.3, simply because they must be present. Although the carbon atom distances from the absorbing Nd atom are not the same between samples, the two ball and stick models presented in Figure 5.11 represent the two broad groups of carbonate coordination around the Nd atom (i.e. two monodentate and two bidentate, and two monodentate and three bidentate - see Table 5.3).

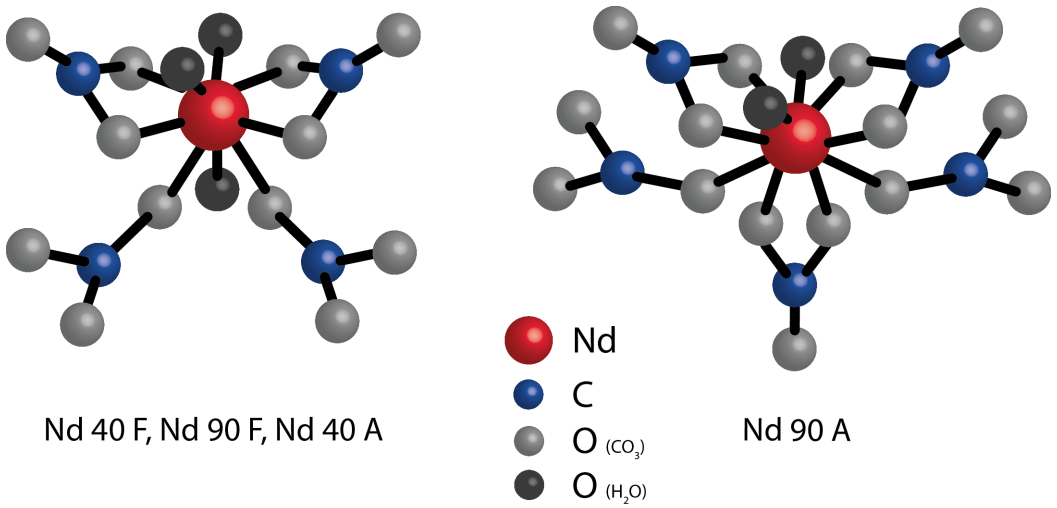

Figure 5.11: Simple ball and stick models showing the possible coordination of Nd atoms with carbonate groups and water molecules, based on the results from Table 5.3. The geometries are unknown. Non-REE-coordinated oxygen atoms of the carbonate groups have been included, despite their absence from Table 5.3.

These results, when combined with the other studies in which 'amorphous Nd carbonate' has been observed, raise a question as to the crystallisation pathway from X-ray amorphous material to crystalline lanthanite-(Nd). If the X-ray amorphous material is indeed hydrated with 5 water molecules (Vallina et al., 2015), but possesses short-range structure analogous to lanthanite, is the crystalline lanthanite forming by dissolution of X-ray amorphous material, followed by reprecipitation (rendering the structure of the amorphous phase irrelevant), or is the X-ray amorphous phase actually *hydrated* further? At the moment this latter suggestion is purely speculation, and would require further evidence to confirm. An alternative interpretation could be that the X-ray amorphous material is lanthanite, and therefore perhaps more hydrated than previously suggested (Vallina et al., 2015).

Nd+Er precipitates - Nd-edge

In the mixed NdEr precipitates, the material aged at 40 and 90 °C for 42 days was found to be X-ray amorphous. As previously discussed, this was interesting because the materials on their own were crystalline (Nd) and X-ray amorphous (Er), respectively. The FTIR of these samples, which were shown along with the Nd-only examples in Figure 5.10, again indicate bidentate carbonate coordination. It is also worth noting from these spectra the intermediate shift of the υ_1 and split υ_3 bands compared with the Nd- and Er-only materials. What is also interesting from the FTIR is the width of the υ_4 bands in comparison to the other samples. It has been shown previously (using density functional theory - DFT) that the υ_4 broadens more than the υ_2 band (in calcite at least) when going from crystalline to amorphous, which was suggested as being consistent with a lack of long-range periodicity (Gueta et al., 2007). In Figure

5.10 the width of υ_4 in the mixed NdEr samples compared with the other elements is smaller and the intensity greater, both of which suggests a relatively more crystalline material (although this was not picked up during PXRD analyses). This then raises the question of whether a mixed NdEr material is forming, or in fact there are discrete Nd- and Er-rich clusters in which the Nd is starting to crystallise and the Er not. To address this question, the mixed NdEr samples were analysed via XAS at both the Nd and Er edges. The following is related to the Nd edge only; the Er edge will follow in the next section.

Despite the initial solution being equimolar, it was unknown what the relative amounts of Nd and Er were in the precipitates, and how this would affect its behaviour. Using the XAS spectra, it is possible to calculate the former because the amount of the absorbing element is proportional to the edge step (i.e. the jump from the pre-edge energy to that just at the post edge), as this is related to the X-ray cross-section and the density and thickness of the sample. The procedure, explained in a personal communication by Fred Mosselmans (2017) and outlined in the methods chapter, produced the results in Table 5.5.

Sample	**Edge**	**Step**	**T**	**D**	**V**	**M**	**Moles**	**%**
NdEr 40	Nd	0.595	6.60	7.24	165.0	1194.6	3.6	49
NdEr 40	Er	0.437	6.50	8.62	162.5	1400.8	3.7	51
NdEr 90	Nd	0.614	6.70	7.24	167.5	1212.7	3.6	49
NdEr 90	Er	0.478	6.75	8.62	168.8	1454.6	3.8	51

Table 5.5: Procedure for calculating the relative amounts of Nd and Er in the mixed samples using the edge step. Step = the edge step as described in text; T = the calculated thickness of the sample using the website provided in text - this values is then used, along with two arbitrary values for the length and width, so that volume can be calculated; V = volume - this value is then used to calculate the mass of the sample using the density value of Nd_2O_3 or Er_2O_3; D = density; M = mass - this value is then used to calculate the number of moles in the sample using the molecular mass of either Nd_2O_3 or Er_2O_3.

The results suggest an almost 50/50 share of Nd and Er at both the 40 A and 90 A samples.

The results of EXAFS modelling, as were shown in Table 5.3, do not suggest a change in the Nd-O (first shell) bond lengths when compared to the Nd-only X-ray amorphous materials, and the CN value is the same within error (although the NdEr 90 A sample is associated with a significantly larger error). In fact, modelling of this sample was difficult and the results should be treated with caution; modelling further than the C atoms was not possible. The reason for this difficulty is unknown, but may be related to the increased disorder associated with having both the REEs in the material. In

contrast, the NdEr 40 A sample was more confidently modelled, with the C atoms found to have CN values and distances from the Nd atoms within error of the Nd 40 F sample (i.e. possibly like lanthanite). To test whether there was well mixed Nd and Er, or localised Nd- or Er-rich clusters, the REE atoms at about 4 Å were fit using either Nd, Er or a mix of one atom each. If well mixed, the results would be expected to show Er near Nd and (at the Er edge, next section) Nd near Er; clusters would have the Nd near Nd and Er near Er. The results showed that changing the Nd:Er ratio from 2:0 to 1:1 decreases the value of reduced chi square by about 10 - 15 %, although the other parameters (bond lengths, CN) are not affected beyond errors. This would suggest a fairly well mixed precipitate, although slight clustering may be occurring. Because of the difficulty in fitting the 90 °C example, the same conclusion cannot be made as confidently. The results of both mixed samples measured at the Er edge are required to make a more informed conclusion on clustering. These will be presented in the following subsection. As with the Nd-only samples, the inclusion of distant O atoms was not possible, in all cases worsening the fit.

Simple ball and stick models for these two samples are shown in Figure 5.12. As with the Nd-only models, these are over simplified, contain the non-REE-coordinated oxygen atoms of the carbonate ions, and do not include the distant REE atoms (see Table 5.3).

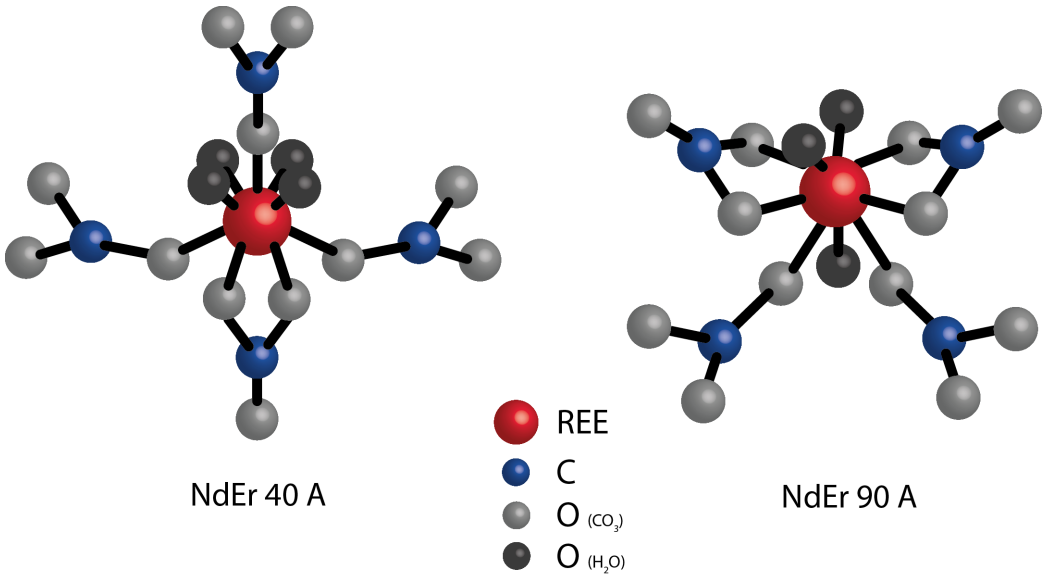

Figure 5.12: Simple ball and stick models showing the possible coordination of Nd atoms with carbonate groups and water molecules in the NdEr samples measured at the Nd edge, based on the results from Table 5.3. The geometries are unknown. Non-REE-coordinated oxygen atoms of the carbonate groups have been included, despite their absence from Table 5.3.

In conclusion, the results of modelling Nd-only samples indicates a difference between the solution precipitates and the 'fresh' and 'aged' examples. The X-ray amorphous material contains mixed mono and bidentate carbonate ions, and possibly Nd atoms beyond those. The local structures of the 40 °C 'fresh precipitate' is similar to lan-

thanite, while that at 90 °C is perhaps more like that of tengerite. Lanthanite has been shown (Chapter 4) as the first crystalline phase in the Nd system, which dehydrates to form tengerite. Perhaps then, the results here suggest the X-ray amorphous 'fresh precipitates' have short-range structures akin to the crystalline phase into which it forms, which is itself controlled by temperature. The mixed NdEr samples suggested a well-mixed precipitate, perhaps with some evidence for slight clustering.

5.4.4.3 Erbium

The isolated k^2-weighted $\chi(k)$ data for all the Er-bearing phases, including the NdEr samples (measured at the Er edge) are shown in Figure 5.13, and the magnitude of the Fourier transform of the $\chi(k)$ data, including the results of fitting, are shown in Figure 5.14.

The EXAFS are again comparable to each other but differ in their details. None share the exact spectra of the erbium carbonate standard, although most of the solid samples are similar; Er 40 A is the most different, suggesting some local structural changes as compared with the others. This is the sample that went on to crystallise into tengerite after a longer ageing period (Chapter 4). Unlike in the La and Nd samples, here there is some similarity between the Er fluoride standard and the experimental samples. As mentioned earlier, REE fluorides form two different crystal structures when synthesised under the same conditions, depending on the REE (e.g. Wang et al., 2006). When the fluoride is composed of a REE from La to Eu, the material will take on the hexagonal crystal structure, whereas using a REE from Gd to Lu results in an orthorhombic structure. The spectra in Figure 5.13 would suggest the unknown materials possess a local structure similar to that of both the REE carbonate and fluoride standards, i.e. they are orthorhombic.

Based on the XANES presented in Figure 5.5, the differences in the spectra below about 3 Å are thought to result from the background removal procedure and not represent real changes in the local structures of these samples. The two solutions are identical to each other and, like La and Nd, are subtly different to the EXAFS of the solids.

The Fourier transform data all exhibit a large peak, this time at 1.9 Å (not phase-shift corrected), attributed to first shell oxygen atoms. The solutions have a few small features at < 3.5 Å. All others contain features out to around 4 Å, particularly Er 40 A and NdEr 90 A, and the only crystalline material, the Er carbonate standard. The identities of these features are discussed below.

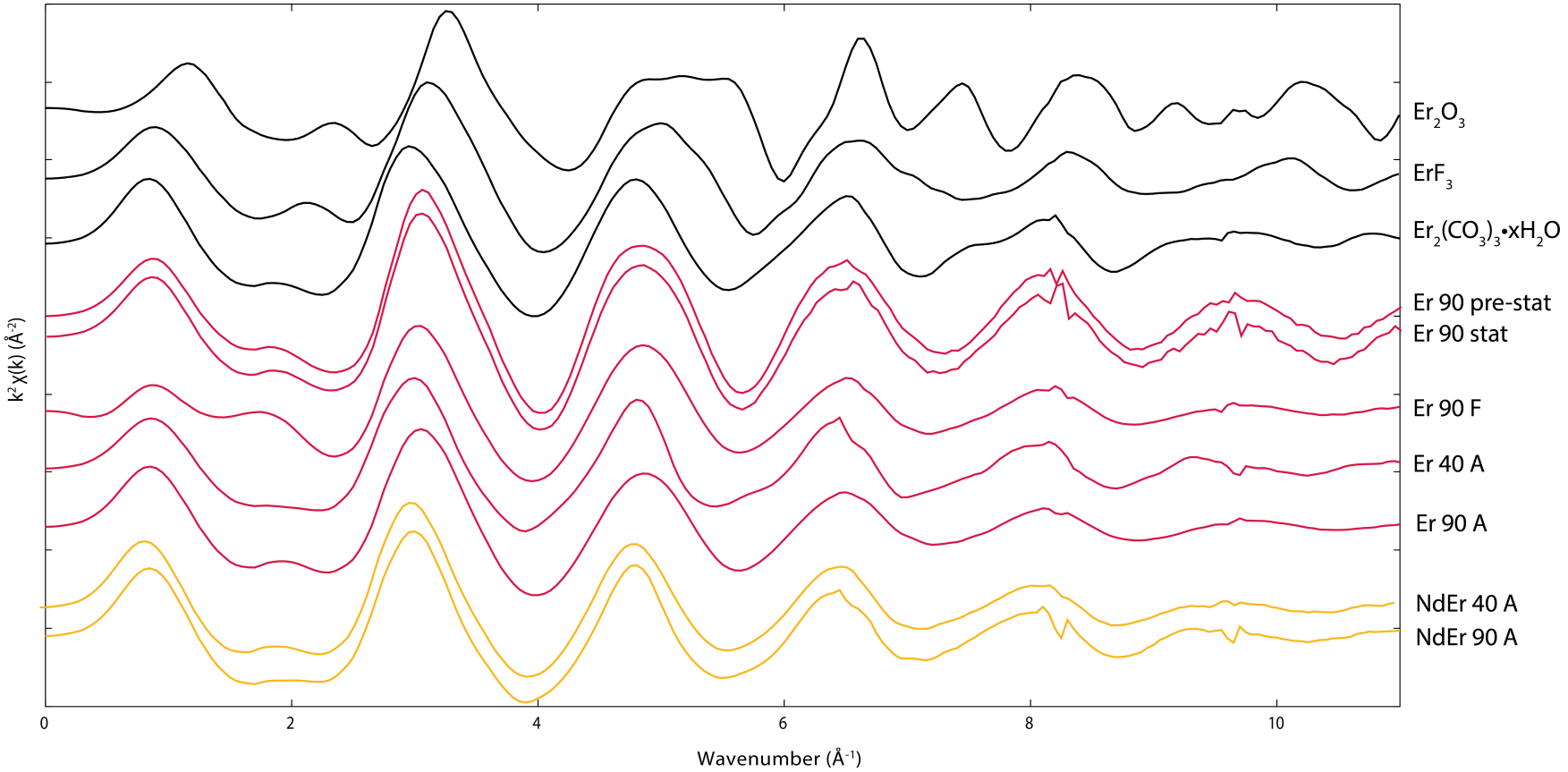

Figure 5.13: Isolated k^2-weighted $\chi(k)$ data for the Er samples (red lines), mixed NdEr precipitates (orange lines), and Er standards (black lines).

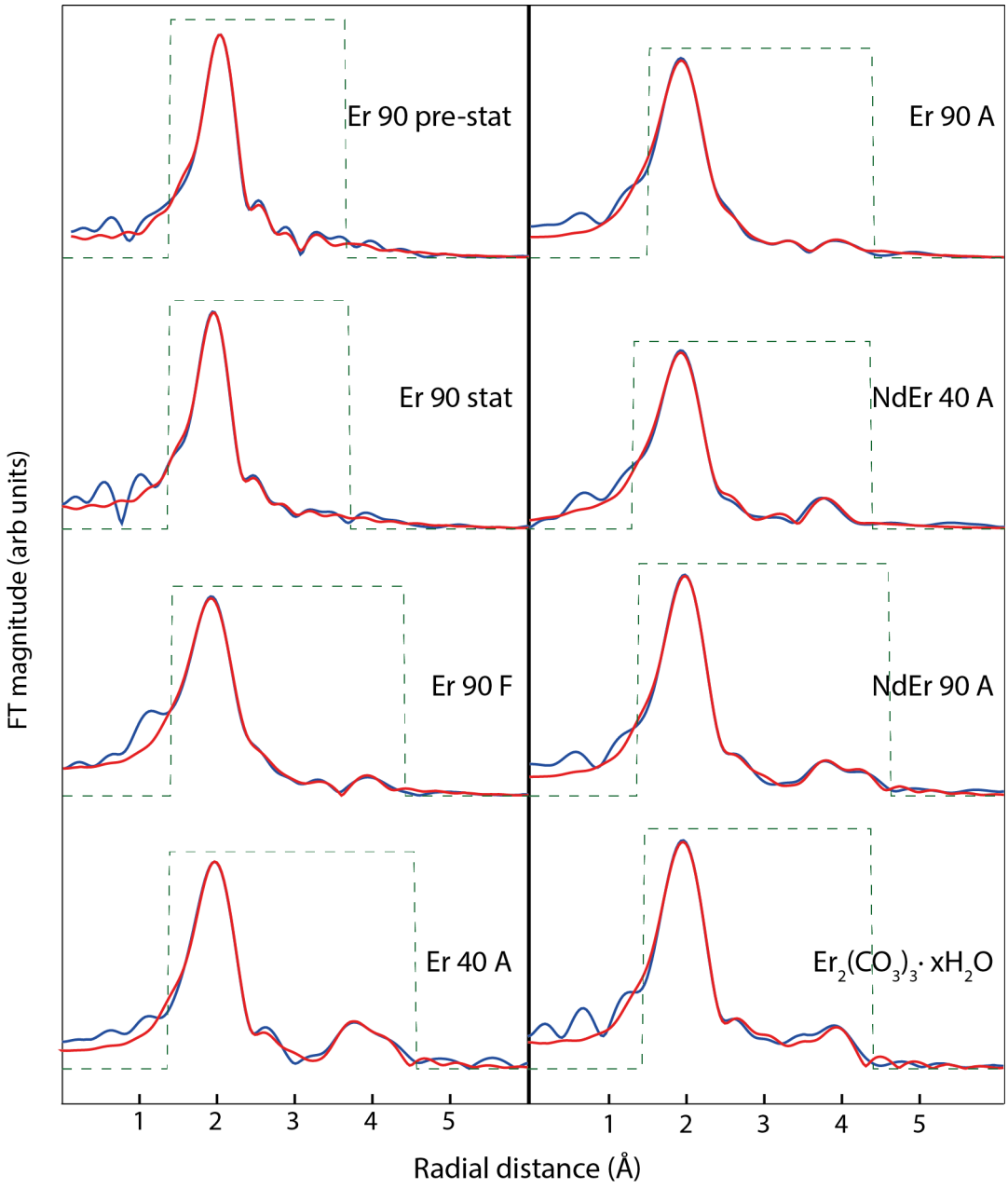

Figure 5.14: Magnitude of the Fourier transform (blue lines) of the k^2-weighted $\chi(k)$ data from Figure 5.13, and the corresponding best fits to the data (red lines). The dashed green line is the window used for fitting in R-space. The k- and R-space ranges use are also indicated in Table 5.6.

The best fit parameters from the fitting procedure are shown in Table 5.6, and the atomic distances of elements in some relevant Er carbonate minerals are given in Table 5.7. The Er-O (first shell) distance is more variable between the Er samples than was seen for La and Nd, but one clear observation is they are shorter, as is expected from the lanthanide contraction.

The two solution samples have identical bond lengths (2.35 Å) and CN values (8). The literature on lanthanide hydration is less consistent for Er (and many of the HREEs) than it is for La and Nd, which is itself interesting in the context of results from Chapter 4 (i.e. different behaviour of LREE, HREE and mixed LREE+HREE precipitates). In reviews by D'Angelo and Spezia (2012) and Smirnov and Trostin (2012) (which include EXAFS and computer simulations), the values for hydration number vary from 8 to 9 and the average Er-O bond length is between 2.34 – 2.41 Å, although 2.35 Å is the most common. The values obtained in the current investigation are also in excellent agreement with the average Ho-O (2.35 Å) and Y-O (2.37 Å) bond lengths of aqua ions, determined in a study of REE incorporation into calcite, both of which were calculated with a fixed CN of 8 (Tanaka et al., 2008). (These comparisons are made with the current Er data because of the similar ionic radii of Y, Ho and Er.) However, in that same study the authors took XAS analyses on two REE carbonate standards, $Ho_2(CO_3)_3 \cdot xH_2O$ and $Y_2(CO_3)_3 \cdot xH_2O$, resulting in average REE-O distances of 2.35 and 2.36 Å, respectively – i.e. the same (within error) as the aqua-ions. They also assumed the yttrium carbonate standard possessed the same structure as tengerite-(Y), without presenting results to confirm those assumptions. This is noted because in the current investigation the REE carbonate standards *were* analysed *via* PXRD, and although the Er sample was highly crystalline, its structure could not be determined from the database: i.e. it was not tengerite. When this standard was fit, the best fit parameters returned a CN of around 9 and an average Er-O bond length of 2.38 Å (Table 5.6), i.e. slightly longer than the solution samples and the REE standards analysed by Tanaka et al. (2008). These overlapping values make it very difficult to determine whether the Er pre-stat and stat samples of the current investigation are aqueous ions or have coordinated with carbonate.

Fitting further than the first shell O atoms was possible, but proved difficult. Inclusion of C atoms did improve the fit for Er pre-stat and stat samples, although only when fitting 2 C atoms at a single distance from the central Er atom. A variety of other combinations did not meet the statistical thresholds. In both examples the C atoms are at approximately 3.5 Å from the absorbing Er, which based on previous discussion in this investigation would suggest monodentate coordination. That in turn would imply 6 to 7 water molecules coordinating the remaining sites. The lack of features at higher R in their FTs does not support any short- or intermediate-range structure. FTIR of the solutions would be required to confirm the type of carbonate coordination.

Sample	Element	N	R (Å)	σ^2 (Å^2)	$\mathcal{R}$ factor	*k*-range	*R*-range
Er 90 pre-stat	O	8.3 ± 0.3	2.35 ± 0.04	0.005 ± 0.001	0.004	3.5 - 12.5	1.38 - 3.6
	C	2	3.49 ± 0.02	0.003 ± 0.003			
Er 90 stat	O	8.2 ± 0.3	2.35 ± 0.01	0.005 ± 0.001	0.002	3.5 - 12.5	1.35 - 3.7
	C	2	3.50 ± 0.04	0.014 ± 0.007			
Er 90 F	O	9.1 ± 0.5	2.35 ± 0.01	0.011 ± 0.001	0.003	3.5 - 11.5	1.4 - 4.4
	C	1	2.81 ± 0.07	0.012 ± 0.005			
	C	3	3.54 ± 0.03	0.012 ± 0.005			
	Er	2	3.97 ± 0.02	0.011 ± 0.003			
Er 40 A	O	8.2 ± 0.8	2.40 ± 0.01	0.009 ± 0.001	0.005	3.3 - 11.0	1.35 - 4.55
	C	3	2.85 ± 0.02	0.010 ± 0.004			
	C	2	3.75 ± 0.05	0.010 ± 0.004			
	Er	2	4.15 ± 0.02	0.008 ± 0.003			
	O	5	4.22 ± 0.02	0.011 ± 0.002			
Er 90 A	O	8.6 ± 0.4	2.35 ± 0.01	0.012 ± 0.001	0.002	3.38 - 11.3	1.5 - 4.35
	C	1	2.82 ± 0.05	0.005 ± 0.004			
	C	3	3.54 ± 0.03	0.005 ± 0.004			
	Er	2	3.98 ± 0.03	0.015 ± 0.004			
NdEr 40 A	O	8.8 ± 0.7	2.37 ± 0.01	0.011 ± 0.001	0.004	3.5 - 11.0	1.3 - 4.3
	C	2	2.83 ± 0.04	0.011 ± 0.006			
	C	2	3.58 ± 0.06	0.011 ± 0.006			
	Nd	1	3.99 ± 0.03	0.010 ± 0.003			
	Er	1	3.99 ± 0.03	0.010 ± 0.003			
NdEr 90 A	O	9.0 ± 0.7	2.40 ± 0.01	0.010 ± 0.001	0.003	3.3 - 11.0	1.35 - 4.55
	C	3	2.85 ± 0.05	0.012 ± 0.005			
	C	2	3.69 ± 0.05	0.012 ± 0.005			
	Nd	2	4.15 ± 0.02	0.006 ± 0.002			
	O	5	4.23 ± 0.02	0.010 ± 0.002			
Er carb std	O	8.8 ± 0.8	2.38 ± 0.01	0.009 ± 0.001	0.004	3.5 - 11.0	1.45 - 4.35
	C	3	2.87 ± 0.03	0.008 ± 0.004			
	C	2	3.18 ± 0.07	0.008 ± 0.004			
	Er	2	3.97 ± 0.02	0.004 ± 0.002			
	O	5	4.02 ± 0.22	0.028 ± 0.017			

Table 5.6: Results of best fit parameters for the individual Er and mixed NdEr samples. Only the first shell was fit in these examples. N = coordination number; R = distance from the absorbing Er atom; σ^2 = Debye-Waller factor. Coordination numbers were determined using an S_0^2 value of 0.95. Values for the Er carbonate standard are included for reference (final rows). CN values presented without errors were fixed during fitting. Errors are calculated in Artemis during fitting and are at the 1σ confidence level. Er carb std = $Er_2(CO_3)_3 \cdot xH_2O$.

	Tengerite-(Y)		**$ErCO_3OH$** (orth)		**$ErCO_3OH$** (hex)	
	Element	*R (Å)*	*Element*	*R (Å)*	*Element*	*R (Å)*
	O 6.1	2.335	O 1.1	2.254	O 6.1	2.341
	O 3.1	2.360	O 1.2	2.255	O 17.2	2.370
	O 2.1	2.377	O 4.1	2.408	O 16.1	2.372
	O 4.1	2.392	O 4.2	2.412	O 13.1	2.396
	O 5.1	2.411	O 2.1	2.443	O 12.1	2.402
	O 1.1	2.414	O 3.1	2.477	O 3.1	2.420
	O 2.2	2.435	O 2.2	2.495	O 4.1	2.430
	O 3.2	2.452	O 3.2	2.604	O 10.1	2.576
	O 1.2	2.529	O 3.3	2.620	O 11.1	2.626
Mean		2.411		2.441		2.437
	C 1.1	2.770	C 1.1	2.864	C 6.1	2.958
	C 2.1	2.803	C 1.2	2.933	O 4.2	3.035
	C 1.2	2.884	O 4.3	2.988	C 2.1	3.035
	C 1.3	3.476	C 1.3	3.091	C 2.2	3.497
	C 1.4	3.552	C 1.5	3.373	C 3.1	3.886
	O 1.3	4.001	Er 1.1	3.770	C 5.1	3.886
	O 1.4	4.057	Er 1.1	3.770	Er 2.1	3.989
	O 6.2	4.060	O 2.3	3.894	Er 3.1	4.134
	O 3.4	4.070	O 2.4	3.910	O 6.2	4.191
	Y 1.1	4.124	O 4.4	4.000	Er 3.2	4.191
	Y 1.1	4.124	O 2.5	4.049	O 4.3	4.213
	O 5.2	4.147	Er 1.2	4.104	Er 2.2	4.213
	O 5.3	4.233	Er 1.2	4.104	O 3.2	4.301
	O 6.3	4.276	O 2.6	4.108	C 6.2	4.301
	O 1.5	4.323	O 3.4	4.110	O 2.1	4.316
	O 5.4	4.326	O 4.5	4.219	Er 1.1	4.316
	O 5.4	4.342	O 4.6	4.315	Er 1.1	4.410

Table 5.7: Distances (Å) from the absorbing atom to first shell oxygen atoms (O; mean also shown), bidentate and monodentate carbons (C; shorter and more distant, respectively), and more distant oxygen or metal atoms (O, Er, Y) in some relevant carbonate minerals. $ErCO_3OH$ orth is essentially a distorted kozoite-(Nd) structure, and $ErCO_3OH$ hex is thought to be isostructural with hydroxylbastnäsite. Structural files taken from the ICSD database, with original sources: Miyawaki et al., 1993 (Tengerite-(Y); Tahara et al., 2007 ($ErCO_3OH$ – orth); Michiba et al., 2011 ($ErCO_3OH$ – hex).

In contrast, samples Er 90 F and Er 90 A, despite having the same average Er-O bond lengths as the solutions, have more C atoms located at two distances, and first shell CN values nearer to 9. The best fit for these two samples resulted in 1 close and 3 distant C atoms, at around 2.80 and 3.50 Å, respectively. This is interpreted as mixed bidentate and monodentate coordination, which is supported by the FTIR spectra presented earlier (Figure 5.10). The distances (but not the CN values) match those of the mineral tengerite-(Y) (Table 5.7); they do not match the other Er carbonate phases in Table 5.7. Given the neighbouring positions of Er and Y in terms of ionic radii, the bond lengths would not be expected to change by more than a few hundredths of an angstrom by the substitution of the Er for Y, and as such tengerite is a likely Er mineral to form at < 100 °C (something already shown by other authors under different conditions, e.g. Liu and Ma, 2007).

As in the Nd samples, the features at approximately 4 Å were best fit with REE atoms (Er) and not additional oxygen – however, as before, such modelling is difficult to prove conclusively. The improved reduced chi square value was deemed significant enough to justify their inclusion. The identical Er-O (first shell) values to those determined for the solution samples is again suggested to result from a lack of longer-range order in which carbonate ligands may form bridges between REE atoms, which likely increases the bond length of Er-O (e.g. Goff et al., 2010). These results suggest additional carbonate coordination between the period of static pH (Er 90 stat) and the cessation of carbonate titration (Er 90 F), but no significant change in the local structure as the solution is aged for 42 days at 90 °C.

In clear contrast to this story are the intense features at around 4 Å in sample Er 40 A (Figure 5.14), and the results of its fit (Table 5.6). The Er-O average bond length was significantly larger than the other samples mentioned, at 2.40 Å, with a CN of around 8 but possibly 9 – this average bond length and CN value are within error of tengerite-(Y), as are the bidentate C atoms, although the monodentate C refine to 0.2 Å longer. The features at 4 Åwere not satisfactorily fit with Er atoms alone, and instead required – and was improved by – the addition of 5 oxygens. This value returned the best fit (numerous other combinations were attempted), and matches the number of O atoms in this region in natural tengerite; as with the monodentate C atoms, the O also refined to values different (+ 1.1 Å) than the crystalline material. This sample is suggested as having a local structure most resembling that of a known mineral (i.e. tengerite), but the mismatched monodentate C and distant O atom bond lengths means the structure does not completely mirror that of tengerite. As noted on several occasions previously, this sample did crystallise into tengerite after an additional 42 days (total 84 days) in the oven.

Simple ball and stick models of the experimental samples are shown in Figure 5.15. As with the Nd examples, the distant Er atoms are not included as their location/bonding in relation to the absorbing Er atom is unknown. The non-REE-coordinated oxygen atoms of the carbonate groups are also included. It is once again stressed that these models are simplified and not necessarily accurate in their geometries. What is clear from these models is the loss of water molecules moving from the solution samples into the fresh and aged samples, and finally the Er 40 A example (that was most similar to the mineral tengerite).

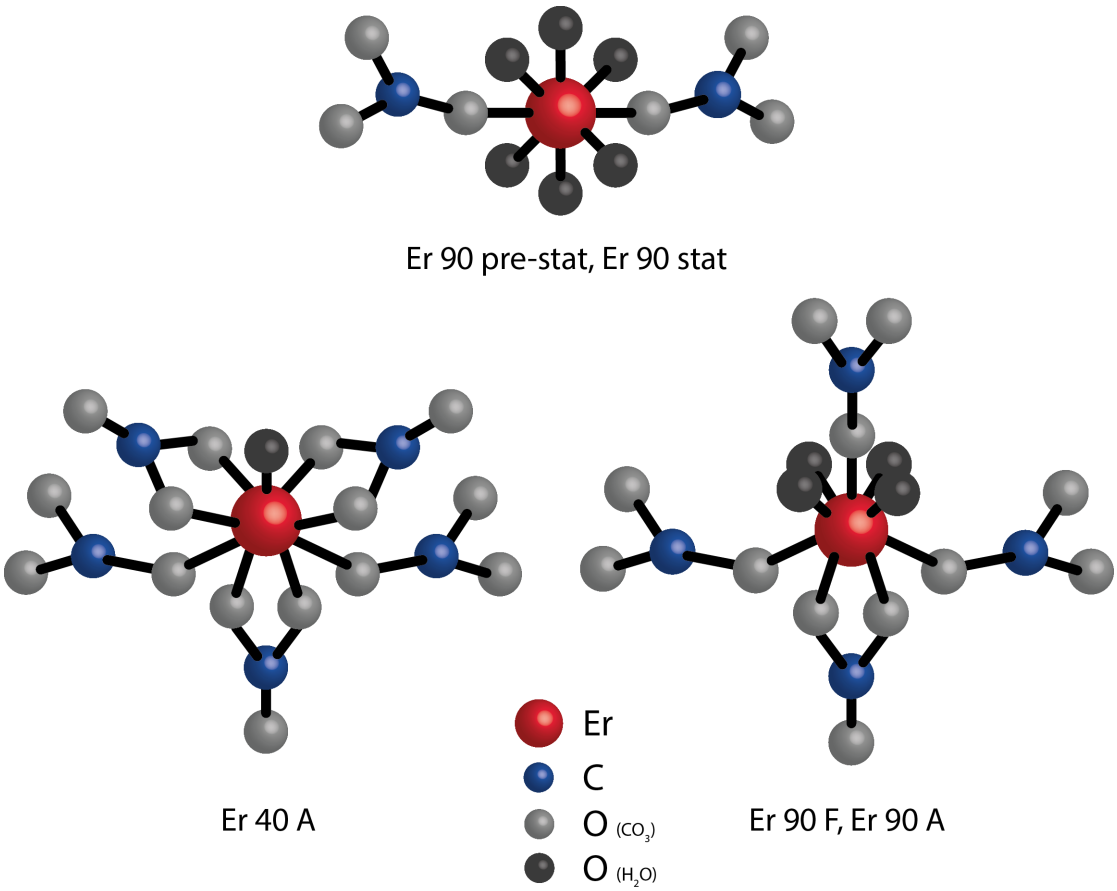

Figure 5.15: Simple ball and stick models showing the possible coordination of Er atoms with carbonate groups and water molecules, based on the results from Table 5.6. The exact geometries are unknown.

Nd+Er precipitates - Er-edge

Fitting of the mixed NdEr precipitates was more successful than at the Nd edge. The CN values of the first shell O atoms at 40 °C is the same as at the Nd edge, but the bond lengths are not (2.37 compared with 2.48 Å). These values are longer (Er) and shorter (Nd) than the average in X-ray amorphous samples of the same element (i.e. average for Nd was 2.50 and average for Er is 2.35 Å) – this supports a fairly-mixed sample (as opposed to Nd- and Er-rich clusters), as the difference in ionic radius for

Nd and Er would result in distortions to these bond lengths (given they have the same coordination number – e.g. Shannon, 1976). However, the location of C atoms around the Er atom are more comparable to those in tengerite (they are identical within error), although the CN values are slightly off. It is worth restating that the errors in C atom CN values can be large. Further support to a well-mixed precipitate is the fact that inclusion of Nd and Er (ratio of 1:1) at the ca. 4 Å distance improves the fit by approximately 40 % as compared with Er atoms only.

In the 90 °C mixed precipitate, the first shell CN value (9 – 10) and average bond length (2.40 Å) are larger than the other Er-only X-ray amorphous material, both being within error of tengerite. The bidentate C atoms also have CN and bond lengths that match that mineral, although as with some of the other Er samples, the monodentate C are slightly longer (3.69 Å) than in the ideal structure (ca. 3.5 Å). The C atoms are at almost the same distance from the Er atoms as they were from the Nd atom – this suggests a similar local structure around both REEs, probably resulting from an even distribution of Nd and Er. The distant REE atom in this sample was best fit with 2 Nd atoms as compared with only Er (55 % decrease/improvement in reduced chi square), further supporting mixing and not clustering. Interestingly, the feature at around 4 Å was more satisfactorily fit with an additional 5 oxygen atoms (as in the suspected tengerite sample, Er 40 A), which also seems to lend weight to this sample having a short-range structure of tengerite with well mixed Nd and Er atoms.

Simplified ball and stick models of these two samples are shown in Figure 5.16, which demonstrate the coordination around the Er atom, based on the results presented in Table 5.6.

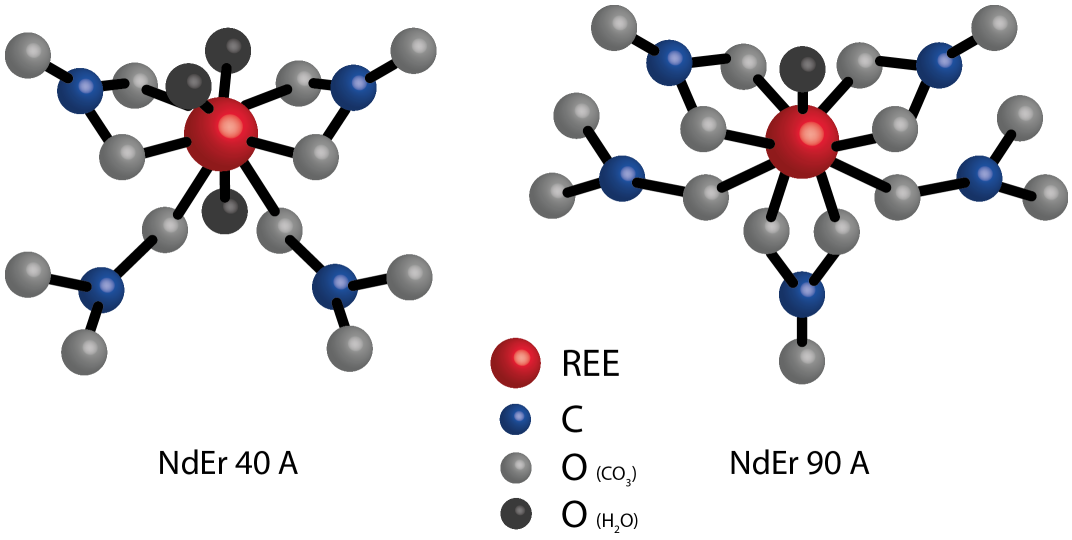

Figure 5.16: Simple ball and stick models showing the possible coordination of Er atoms with carbonate groups and water molecules in the NdEr samples measured at the Er edge, based on the results from Table 5.6. The exact geometries are unknown.

5.4.4.4 Ytterbium

The isolated k^2-weighted $\chi(k)$ data for all the Yb-bearing samples are shown in Figure 5.17, and the magnitude of the Fourier transform of the $\chi(k)$ data, including the results of fitting, are shown in Figure 5.18. Unlike the previously discussed elements, the EXAFS for all the solids (including the carbonate standard) and one of the solution samples (Yb 90 pre-stat) are identical, with only the 90 stat differing slightly. This is also apparent from the FTs: all have a large peak at approximately 1.8 Å (not phase shift-corrected), and small features around 4 Å, while the 90 stat sample has additional features around 3 Å. As before, the first peak is attributed to O atoms.

As was the case for the Er samples, the $\chi(k)$ spectra for the Yb fluoride standard is similar to that of the Yb carbonate standard and the experimental samples. As previously mentioned, HREE fluorides crystallise in the orthorhombic system, and as such it is likely the experimental samples precipitated in the present study also share this property.

The results of fitting are presented in Table 5.8. As expected from the lanthanide contraction, the first shell Yb-O distances are shorter than in Er samples. They are all identical, at 2.32 Å (within error); CN values are also consistent, at 8 (within error). These are the same as previously-reported results for the hydrated Yb ion (e.g. Allen et al., 2000; Mayanovic et al., 2002; D'Angelo and Spezia, 2012; Smirnov and Trostin, 2012), however, the material in the current investigation is clearly not the hydrated ion. The FTIR data presented earlier (Figure 5.10) demonstrated the metal-carbonate bonding for samples Yb 90 F, 40 A and 90 A, and seeing as the EXAFS and their FTs are almost identical, all the Yb phases must be carbonates. Although a few previous studies have synthesised Yb carbonates (e.g. Liu and Ma, 1997b; Tahara et al., 2007; Rahimi-Nasrabadi et al., 2017), none were found in which XAS was used to elucidate structural details, except those related to Yb incorporation into calcite and garnet (e.g. Quartieri et al., 1999; Elzinga et al., 2002; Tsuno et al., 2003, 2005), thus making comparisons with this work impossible.

When fitting C atoms, their inclusion improved the quality of all fits. Although multiple combinations were tried, the best results suggest 3 mono and 1 bidentate C at around 3.5 and 2.8 Å, respectively. Such a configuration would imply 3 coordinated water molecules. The C atom distances are within error of each other between all samples expect Yb 90 stat, in which the shorter C bond is > 0.2 Å longer (3.05 Å) and the longer bonds are approximately 0.1 Å shorter (3.40 Å). The reason for changes in this sample alone is currently unknown.

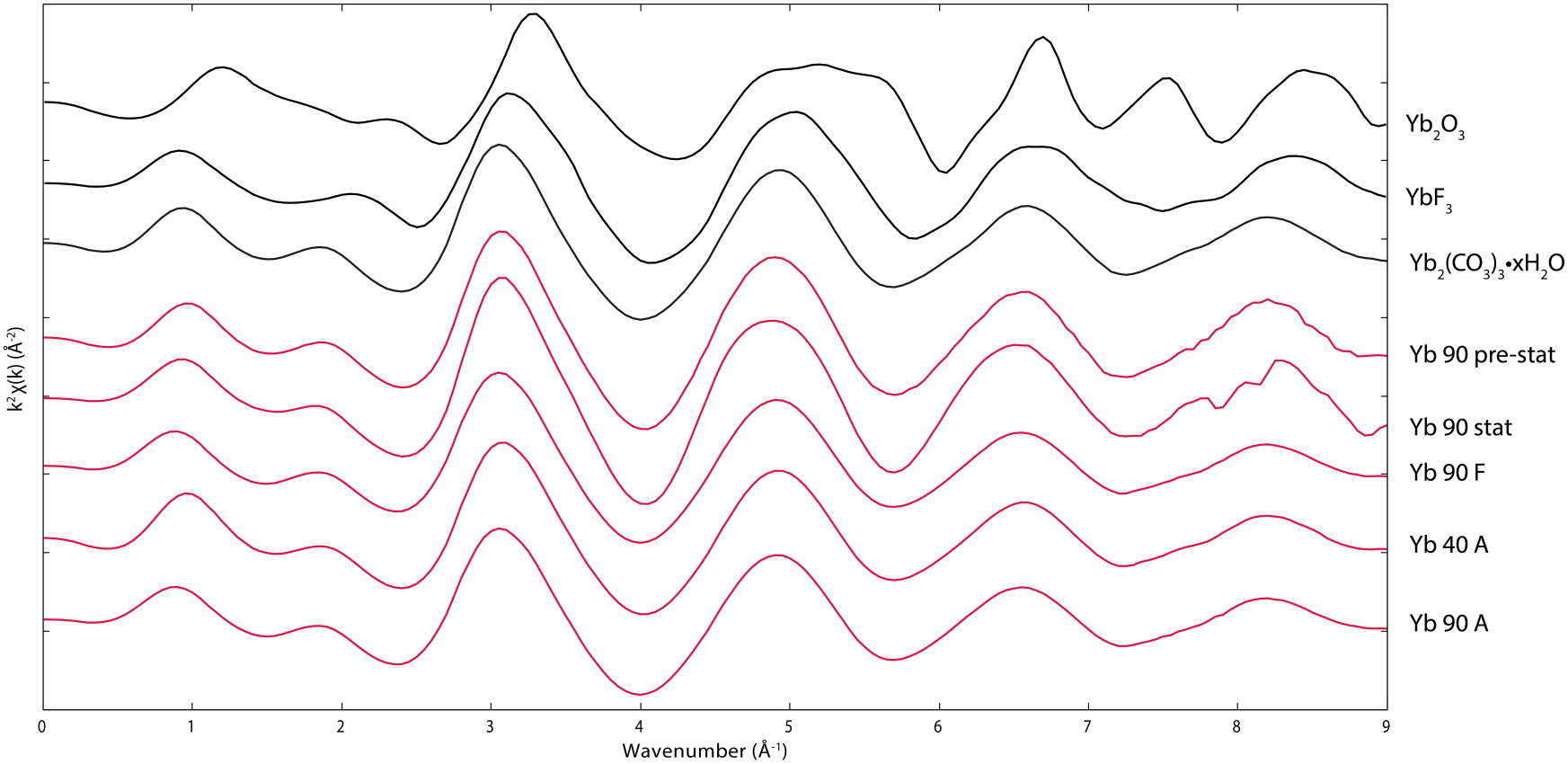

Figure 5.17: Isolated k^2-weighted $\chi(k)$ data for the Yb samples (red lines) and Yb standards (black lines).

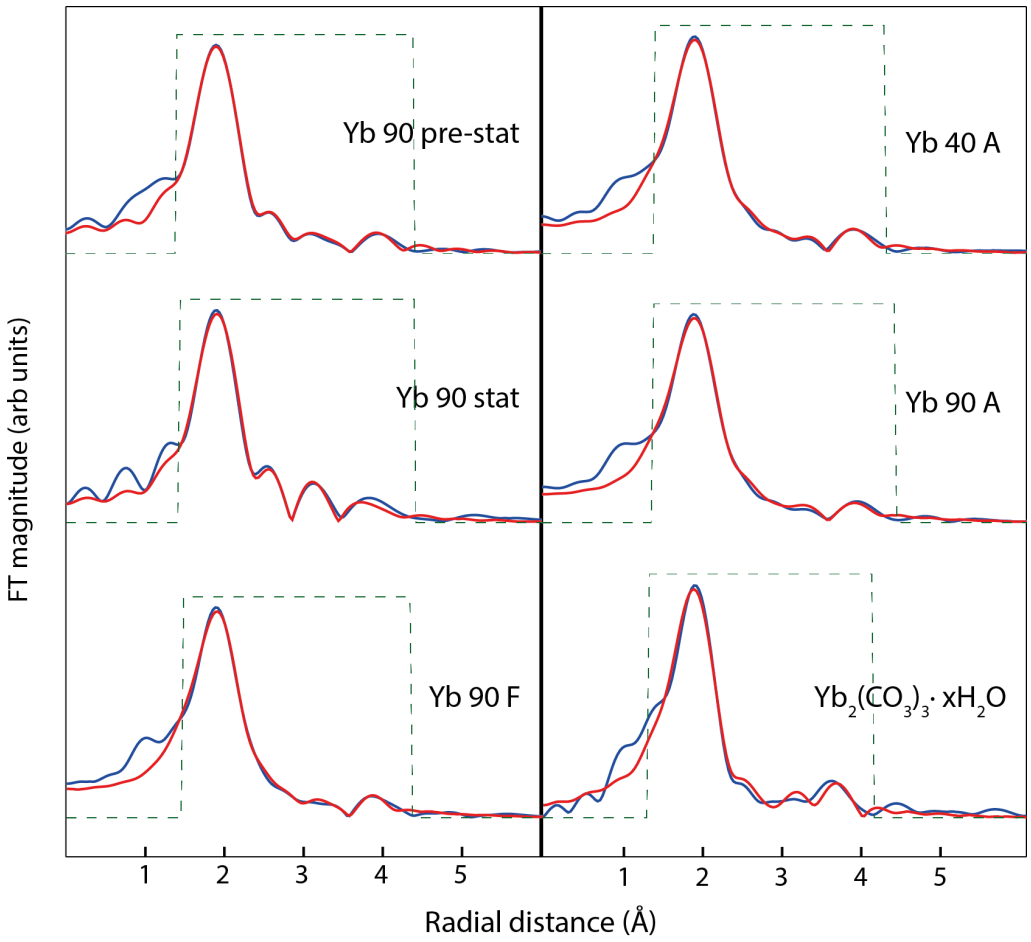

Figure 5.18: Magnitude of the Fourier transform (blue lines) of the k^2-weighted $\chi(k)$ data from Figure 5.17, and the corresponding best fits to the data (red lines). The dashed green line is the window used for fitting in R-space. The k- and R-space ranges use are also indicated in Table 5.8.

The Yb carbonate standard was best fit with 2 mono and 2 bidentate carbonates, as opposed to 3 and 1 in the experimental samples, which would mean one fewer water molecule. This may be a consequence of the material becoming more crystalline (weak Bragg peaks were observed *via* PXRD - Figure 5.2). In all the samples the feature at about 4 Å was fit with either Yb or O atoms, and although both were successful, the former returned reduced chi square values about 20 % lower. Therefore, the final fits included Yb atoms at this distance.

The similarity between the Yb samples is in contrast with the other elements studied. The results suggest formation of Yb carbonate units that remain unchanged when treated at up to 90 °C for 42 days. This implies a more stable phase and supports the broad observations/conclusions of the previous chapter in that HREEs remain X-ray amorphous for longer than their LREE counterparts, at least at $<$ 100 °C. A contrasting conclusion could be that these Yb results are the only ones that show the solution cluster/complexes determine the structure of the amorphous precursor.

Sample	Element	N	R (Å)	σ^2 (Å^2)	$\mathcal{R}$ factor	*k*-range	*R*-range
Yb 90 pre-stat	O	8.3 ± 0.7	2.33 ± 0.01	0.007 ± 0.001	0.002	3.5 - 10.2	1.4 - 4.4
	C	1	2.75 ± 0.11	0.012 ± 0.008			
	C	3	3.49 ± 0.05	0.012 ± 0.008			
	Yb	2	3.95 ± 0.03	0.008 ± 0.004			
Yb 90 stat	O	8.6 ± 1.1	2.32 ± 0.01	0.007 ± 0.002	0.009	3.45 - 10.2	1.42 - 4.4
	C	1	3.05 ± 0.07	0.008 ± 0.003			
	C	3	3.40 ± 0.03	0.008 ± 0.003			
	Yb	2	3.91 ± 0.06	0.008 ± 0.008			
Yb 90 F	O	8.6 ± 0.5	2.32 ± 0.01	0.012 ± 0.001	0.004	3.5 - 12.5	1.47 - 4.35
	C	1	2.81 ± 0.03	0.013 ± 0.003			
	C	3	3.47 ± 0.03	0.013 ± 0.003			
	Yb	2	3.92 ± 0.03	0.012 ± 0.002			
Yb 40 A	O	8.3 ± 0.5	2.32 ± 0.01	0.011 ± 0.001	0.003	3.5 - 11.2	1.4 - 4.25
	C	1	2.82 ± 0.08	0.012 ± 0.004			
	C	3	3.49 ± 0.04	0.012 ± 0.004			
	Yb	2	3.92 ± 0.02	0.010 ± 0.003			
Yb 90 A	O	8.4 ± 0.6	2.32 ± 0.01	0.012 ± 0.001	0.004	3.5 - 11.5	1.35 - 4.36
	C	1	2.80 ± 0.09	0.014 ± 0.004			
	C	3	3.47 ± 0.04	0.014 ± 0.004			
	Yb	2	3.93 ± 0.04	0.013 ± 0.004			
Yb carb std	O	8.2 ± 1.0	2.32 ± 0.01	0.009 ± 0.002	0.014	3.45 - 11.5	1.35 - 4.4
	C	2	2.77 ± 0.05	0.010 ± 0.008			
	C	2	3.52 ± 0.08	0.010 ± 0.008			
	Yb	2	3.89 ± 0.04	0.011 ± 0.006			

Table 5.8: Results of best fit parameters for the individual Yb samples. N = coordination number; R = distance from the absorbing Yb atom; σ^2 = Debye-Waller factor. Coordination numbers were determined using an S_0^2 value of 1.0. Values for the Nd carbonate standard are included for reference (final row). CN values presented without errors were fixed during fitting. Errors are calculated in Artemis during fitting and are at the 1σ confidence level. Yb carb std = $Yb_2(CO_3)_3 \cdot xH_2O$.

As the experimental samples all returned the best results when modelled with one bidentate and three monodentate carbonates, only one ball and stick model has been produced, which is shown in Figure 5.19. As before, the distant Yb atoms have been omitted and the non-REE-coordinated oxygen atoms of the carbonate ions have been included. The remaining oxygen atoms not attributed to carbonate are assumed to be water molecules.

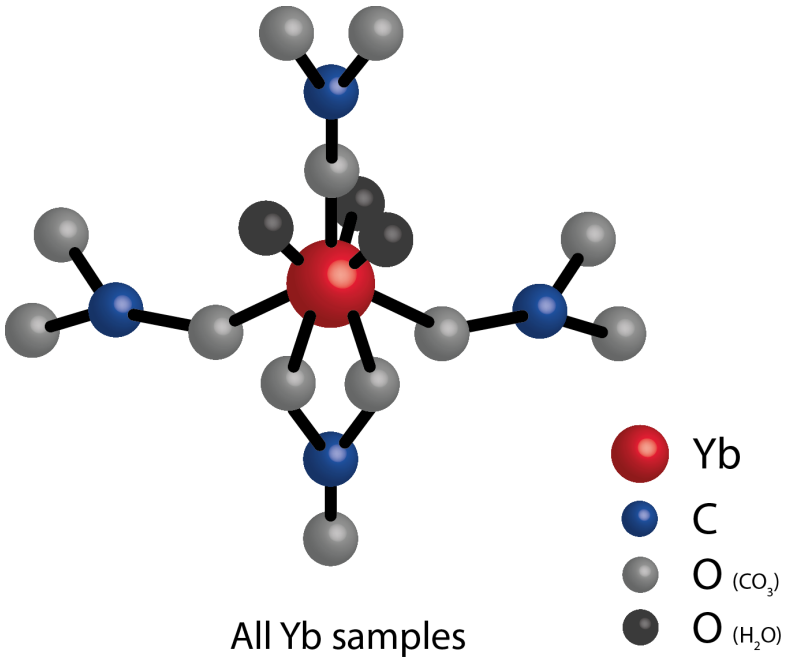

Figure 5.19: Simple ball and stick model showing the possible coordination of Yb atoms with carbonate groups and water molecules in the Yb samples, based on the results from Table 5.8. The exact geometry is unknown.

5.5 Synthesis

The results presented in this chapter further highlight the different behaviour of the L- and HREEs, and has provided some general information on the behaviour of REEs as they go from solution, to amorphous precursor, to crystalline solid.

The formation of many crystalline phases follows a non-classical nucleation pathway, as evidenced by the formation of X-ray amorphous precursor phases (e.g. Gebauer et al., 2008; Raiteri and Gale, 2010; Cho et al., 2011; Bach et al., 2015; Vallina et al., 2013). This has been shown applicable to REE carbonates. There is growing evidence that in some systems, the clusters making up these X-ray amorphous phases possess short-range structure analogous to that of the bulk phase into which it crystallises. Results from the current chapter indicate that, for the REE carbonates, this may be the correct in some cases but not in others.

Modelling of the La and Nd solution samples tentatively pointed to coordinated carbonate, however, this could not be confirmed definitively. The La material in solution might be the X-ray amorphous La phase observed by Vallina et al. (2015), however, without improved spectra or other characterisation techniques, this cannot be confirmed. The Nd solutions were also not definitely carbonates, but the fresh precipitates were, and found to possess short-range structures similar to the first crystalline phase observed for this sequence in Chapter 4 (lanthanite).

In the Er experiments, inclusion of C atoms was successful when modelling the data, indicating the material formed at pre-stat and stat conditions was indeed a REE carbonate. However, the results suggested a different local structure for this as compared to the fresh precipitates, manifested as a change in carbonate coordination from solely monodentate (2 ions), to mixed bidentate (1) and monodentate (3). Given no evidence for chloro-aqua ions, the remaining coordination sites must be occupied by water (or OH^-). The CN values of these solution precipitates was 8, which implies 6 coordinated water molecules, while the CN of the fresh precipitate was 9, suggesting 4 water molecules. The fresh precipitate had a local structure less similar to a known crystalline phase than the Nd counterpart, although when heated the Er 40 A sample did have local structure like tengerite, despite the sample being X-ray amorphous. The results did not support the solution precipitates having the same structure as a crystalline phase.

The Yb samples were more consistent. Solution, fresh and aged materials were almost identical, which indicated the formation of REE carbonate units in solution that did not significantly change when aged at 90 °C for six weeks. It is noted that none of this material was crystalline enough to produce Bragg peaks, meaning it is not possible to determine whether the solution precipitates exhibit the same local structure as bulk Yb carbonate. The only sample slightly different was that of the Yb carbonate standard, however, the conditions of synthesis for this material are unknown (e.g. temperature), and so it cannot be compared directly.

Figure 5.20 compares the ball and stick models presented in the earlier sections of the current chapter. Although the geometries of these materials are unknown, they can still be used to observe general trends as a function of both atomic number of the absorbing REE atom and temperature. Increasing the temperature from 40 to 90 °C in the Nd samples sees a change from lanthanite to kozoite, which is a dehydration reaction accompanied by an additional bidentate carbonate coordination. A dehydration pattern can also be observed for the Er samples as the material transforms from the pre-stat material into the fresh and aged precipitates (at 90 °C). The exception to this is the aged Er 40 °C sample, which, as mentioned numerous times in this chapter, was not crystalline enough to produce Bragg peaks, but did so when left for an additional 42 days in the oven (forming tengerite). This demonstrates further that crystallisation from the fresh and non-crystalline aged products proceeds *via* dehydration (and additional carbonate coordination). The Yb samples, as mentioned in the previous section, all returned modelling results suggesting the same local structure.

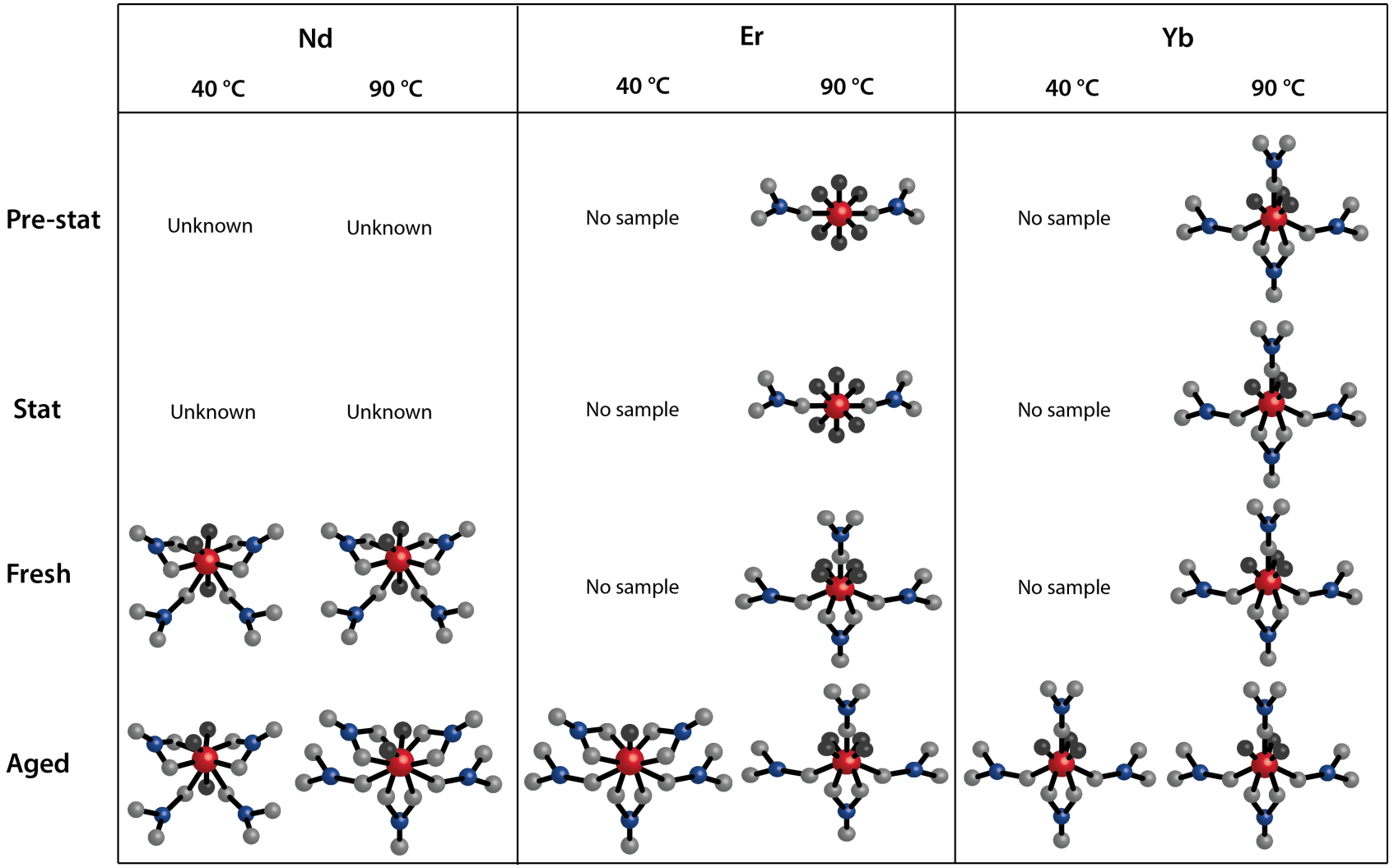

Figure 5.20: Comparative figure showing the same ball and stick models presented in the earlier sections. The figure demonstrates the possible changes in coordination around the absorbing REE atom as a function of both REE and temperature. Colours are as in the previous figures (red = REE; blue = carbon; light grey = oxygen (of carbonate ions); dark grey = oxygen (of water or hydroxyl molecules).

In the literature, the (generally accepted) change in coordination number from 9 to 8 when moving across the REE series has implications for the hydration number and therefore the kinetics of water exchange. The current investigation supports the reduction in CN from LREE to HREE. Numerous experimental (Anderson et al., 2002; D'Angelo et al., 2008; Ohta et al., 2008; D'Angelo et al., 2011; D'Angelo and Spezia, 2012) and theoretical investigations (e.g. Hughes et al., 2005; Hofer et al., 2006; Buzko et al., 2009; Villa et al., 2009; Duvail et al., 2010; Louvel et al., 2015; Smirnov and Grechin, 2015) have studied the coordination environment of REE ions in solution and shown the water exchange rate decreases systematically from MREEs to LREEs, and from MREEs to HREEs, but that the REE-water bonds are weaker for the LREEs than HREEs. This results from the shorter REE-O bond lengths and steric hindrance (from the tighter packing around the smaller HREEs). This in turn may lead to a higher activation energy for these reactions with the HREEs, which may account for their greater stability, particularly at low temperatures (i.e. < 100 °C).

In high order REE carbonate complexes (e.g. $REE(CO_3)_3^{3-}{}_{(aq)}$ or $REE(CO_3)_4^{5-}{}_{(aq)}$), the most stable form was shown to be fully a bidentate structure for all REEs, meaning there was room for up to four (LREEs) or two (HREEs) water molecules in the first shell (Martelli et al., 2014). These data do not reflect those of the current investigation - at least for Er and Yb where data on the solutions were obtained - possibly resulting from lower order carbonates (i.e. $REECO_3^{+}{}_{(aq)}$ or $REE(CO_3)_2^{-}{}_{(aq)}$). However, the general trend seems to hold, in that the La and Nd fresh precipitates were similar to bulk crystalline phases, Er was less similar to the bulk phase, and Yb remained unchanged under all conditions. This is only applicable, however, if the behaviour of complexes is the same/similar to the X-ray amorphous material - something that would require more data than presently available.

Another potentially important observation from this study is that the Nd X-ray amorphous material (at 40 °C) is similar to the mineral lanthanite. Tying all the information together, the following crystallisation pathway can be tentatively proposed:

1. An X-ray amorphous precipitate is formed in all systems investigated;

2. In the case of La, Nd and Er, this may not be the same as the solution precipitates - i.e. the solution clusters are not analogues of the bulk crystalline material. The Yb solution material appears to be the same as the X-ray amorphous and aged precipitates;

3. La and Nd form X-ray amorphous material with a local structure similar to lanthanite, which *may* undergo additional hydration as it crystallises. The same could be true of Ce and Pr (heavier REEs than Nd cannot form the lanthanite structure). These go on to form tengerite (Nd-only), kozoite then hydroxyl-

bastnäsite *via* dehydration, as previously proposed;

4. Er cannot form lanthanite, so instead forms tengerite *via* dehydration of the initial X-ray amorphous material;

5. Yb is not able to form the tengerite structure, so remains X-ray amorphous under the conditions of this investigation. The Er and Yb phases are more difficult to dehydrate as discussed in Chapter 4.

Although no direct evidence has been collected for the hydration of La and Nd precursor material, the morphologies in the previous chapter may support this. The idea that spherulitic morphologies formed for hydroxylbastnäsite-(La) as a consequence of rapid precursor breakdown (which occurred more slowly than for Nd, which experienced 'category 2' spherulitic growth) at 90 °C is still valid, but does not satisfactorily explain the non-spherulitic morphologies of lanthanite in the La, Nd and mixed La+Nd systems at 40 °C. Perhaps the large (100s μm) plates, sheets and cruciform morphologies can be explained not by the breakdown of X-ray amorphous precursors and their subsequent recrystallisation, but instead by its slow(er) growth. At higher temperatures the X-ray amorphous material would likely breakdown more rapidly before these morphologies appear.

5.6 Chapter conclusions

Despite minimal information from the La samples, the ease with which La-carbonates crystallise (shown in Chapter 4), combined with the variable results from the Nd samples in this chapter, suggests an increase in stability of the precipitates composed of the HREEs compared with LREEs. In La, Nd and Er samples, the analysed solutions cannot be definitively confirmed as containing REE carbonate complexes or larger precipitates, however, the Yb samples can.

The LREE materials are transforming from the initial precipitates formed during the titrations into materials that appear to possess short range structures like those of stable crystalline minerals. The Er samples mostly behave in the same way, but possibly require more time, with potential REE carbonate formation early on and further carbonate coordination by the time end of titrations. The local structure of the fresh material remains the same even when heated at 90 °C for 42 days, although the same is not true when heated at 40 °C. The reason for this is currently unknown. The Yb material, in contrast to the other three elements, exhibits REE carbonate coordination in solution precipitates that match those in the solid samples, including the (unidentified) carbonate standard. The Yb material therefore appears the most stable from the point of initial precipitation.

The almost identical behaviour of the Yb, but differing behaviour of Er, suggests the latter material is, despite appearing X-ray amorphous, in fact more dynamic. This is interesting based on the results of the previous chapter, in which the Er material did not crystallise at temperatures > 90 °C, but Yb did. Although the reason for this remains unknown, the results presented in this chapter show the differences in behaviour (i.e. amorphous vs crystalline) seems most relevant at temperatures > 90 °C.

In the mixed REE system, XAS measurements taken at both the Nd and Er edges has revealed well-mixed precipitates at 40 °C, as might be expected given that both tengerite-(Nd) and tengerite-(Er) have been previously identified (e.g. Wakita and Nagashima, 1972; Liu et al., 1999a; Vallina et al., 2014). However, at the higher temperature (90 °C), there appears to be more evidence for clustering, although data from one of the edges was less conclusive. These results highlight the importance of temperature when synthesising well-mixed REE precipitates.

Although the carbon atom CN values are presented with potentially large errors, the suggested CN values for mono and bidentate carbonates in the Er and Yb fresh precipitates and the other X-ray amorphous materials would imply a larger number of water molecules than in crystalline material. This, then, would support the previously suggested theory that an increase in energy is required to dehydrate the heavier REEs than their lighter counterparts.

Chapter 6

The role of wall rocks and reaction temperature on REE carbonate mineralisation: an experimental study

6.1 Introduction

Many REE deposits are hydrothermal in origin, formed by late-stage hydrothermal fluids reworking primary magmatic deposits (e.g. Williams-Jones et al., 2012; Nadeau et al., 2015). Transport/remobilisation of REEs during reworking, and efficient depositional mechanisms, are essential if these elements are to concentrate to levels worthy of economic exploitation. REE transport is facilitated by complexation with inorganic ligands, e.g. chloride, fluoride, sulphate and carbonate (e.g. Migdisov et al., 2016), and as such the availability of these ligands and the strength of the complexes they form dictates the REEs' mobility. However, equally important is the solubility of REE minerals that contain those ligands, for example REE fluorides or fluorocarbonates, because a low solubility will remove the REEs from solution. Changes in the fluid's chemistry and pH, for example brought on by dissolution of the wall rocks through which the fluid is passing (commonly carbonates), or by mixing with another fluid, may cause REE complex destabilisation and mineral precipitation.

Some of the most important REE ore minerals are fluorocarbonates, and to a lesser extent carbonates (e.g. bastnäsite $REECO_3F$; parisite $Ca(REE)_2(CO_3)_3F_2$; synchysite $CaREE(CO_3)_2F$; hydroxylbastnäsite $REECO_3OH$; kozoite $REECO_3OH$ - e.g. Walters and Lusty, 2011; USGS, 2016). All of these minerals are light REE (LREE) enriched (e.g. Maksimovic, 1985; Miyawaki et al., 2000; Chakhmouradian and Wall, 2012). Descriptions of these minerals in the literature highlights their common association with

carbonate-bearing wall/host rocks, including at the world's largest REE deposit, Bayan Obo, China (e.g. Smith et al., 2015), the Wicheeda carbonatite, British Columbia (Trofanenko et al., 2016), the Kangankunde and Tundulu carbonatites, Malawi (e.g. Duraiswami and Shaikh, 2014; Ngwenya, 1994; Broom-Fendley et al., 2016), the Barra do Itapirapuã carbonatites, southern Brazil (Ruberti et al., 2008) and carbonatite veins of the Sokli complex, north east Finland (Sarapaa et al., 2013). These authors have documented dissolution-replacement reactions between host rocks (often dolomitic) and REE mineralisation, highlighting the importance of understanding the processes occurring at the fluid-rock interface.

Ngwenya (1994) studied in detail these processes for the REE mineralisation at the Tundulu carbonatite, Malawi. Based on textural relationships, it was argued that the chemistry of the wall rock - through which the presumed REE- and F-bearing hydrothermal fluid had flowed - controlled the supply of CO_3^{2-} and Ca^{2+} during their dissolution, thereby determining which of parisite, synchysite or bastnäsite was the dominant fluorocarbonate to precipitate. The supply of CO_3^{2-} and Ca^{2+} has also been suggested as the major control to REE fluorocarbonate mineralisation at the Gallinas Mountain fluorite-bastnäsite deposit, New Mexico (e.g. Williams-Jones et al., 2000). Many other authors have also noted the common association of fluorite with REE mineralisation (e.g. Chao et al., 1992; Smith and Campbell, 2000; Pingitore et al., 2014; Graupner et al., 2015; Mondillo et al., 2016). Predicted high T and P data on REE-fluoride complexes – extrapolated from room temperature experiments (e.g. Wood, 1990a; Haas et al., 1995) – were frequently used as evidence that these complexes were the principal transport ligand for REE in hydrothermal fluids, which was further justified by the common occurrence of fluorite at these deposits. However, recent data suggest that, contrary to previous conclusions, REEs are most likely transported as complexes with chloride under hydrothermal conditions (e.g. Migdisov and Williams-Jones, 2014) because REE fluoride and fluorocarbonate solids have very low solubilities (e.g. Migdisov et al., 2009; Gysi and Williams-Jones, 2015; Shivaramaiah et al., 2016). Although no data exist on the stability of REE-carbonate complexes at hydrothermal conditions, it has been suggested that carbonate ions may also act as efficient depositional ligands, and therefore that dissolution of carbonate wall rocks may be an efficient depositional mechanism.

The combination of field observations, textural relationships and theoretical results highlights further the importance of understanding fluid-rock interactions during REE mineralisation, particularly as this can also lead to fractionation between the lower-value light-, and higher-value heavy-REEs (L/HREEs) (e.g. Smith and Campbell, 2000; Forster, 2001; Broom-Fendley et al., 2016; Benaouda et al., 2017). While the aforementioned observations and results help to understand REE behaviour in hydrothermal fluids and predict the product(s) of fluid-rock processes, experiments conducted under

controlled conditions are essential to provide empirical data on crystallisation pathways and mechanisms, and to confirm theoretical predictions.

Although fluid-rock reaction experiments are common in the literature (e.g. Hövelmann et al., 2010; Okamoto et al., 2010; Wolterbeek et al., 2016), there are few focussed on the systems applicable to REE carbonate or fluorocarbonate mineralisation. This is due mostly to the difficulties of working with fluoride solutions, both because of their corrosive properties and the tendency of REE fluorides to precipitate.

In this chapter, the results of reactions between REE-bearing solutions (single and multiple REEs) and dolomite are presented. These experiments were designed to test the hypothesis that interaction of an acidic, REE-bearing solution with a carbonate rock would result in the precipitation of a REE carbonate, and therefore that carbonate acts as a precipitation ligand under these conditions. The influence of temperature on the characteristics of the products was assessed by conducting experiments at various temperatures (between 90 and 200 °C). Single-REE-bearing solutions of LREE and HREE representatives were investigated to assess whether there are any changes in mineralisation across the series, and multi-REE-bearing solutions tested whether mixed or separate LREE- and/or HREE-enriched phases formed.

Results showed that under almost all conditions tested, excellent secondary mineralisation of REE carbonates was observed. In multi-REE-bearing solutions both mixed LREE + HREE and discrete LREE- and HREE-enriched phases were observed, depending on the experimental conditions.

6.2 Methods

6.2.1 REE carbonate synthesis

The synthesis of REE carbonates was achieved *via* the interaction of REE-bearing, acidic solutions with a carbonate rock at different temperatures and reaction durations. During this investigation, the focus was on comparing LREE and HREE, so Nd and Er were chosen as representatives and are the focus of these experiments. However, a few Yb runs were also completed to compare with the results from Chapter 4. Solutions containing mixed Nd+Er, and the same five REE mix as in Chapter 4 were also used, to assess if this would have any influence on mineralisation.

The stock solutions of 0.2 M $REECl_3$ (REE = La, Nd, Gd, Er and Yb) were used to prepare solutions with REE concentrations of 0.1 M or 0.02 M, achieved by dilution with the stock HCl, as outlined in the methods chapter. The higher concentration was used in the experiments conducted at < 100 °C, and the lower concentration was used

for all others (explained below). The starting pH of all the REE chloride solutions was around 0.8 – 0.9, as measured using a pre-calibrated Radiometer Analytical PHM 220 pH meter with a REFEX glass AgAgCl sensor.

A preliminary 'batch' style experiment was run to establish whether the proposed reaction of REE chloride with a carbonate would result in REE carbonate deposition. This involved 15 ml 0.1 M Nd chloride and 1 g calcite, reacted in a 20 ml bunged and crimp-sealed serum bottle at 90 °C. This method provided a fast and low cost way to test the reaction. The result was complete calcite dissolution and no obvious new mineralisation. This indicated either that the reaction between dissolved REE and the released carbonate ions does not produce a REE carbonate solid, or that the dissolution of calcite was too rapid, and the reaction between carbonate and REE too slow, for the precipitation to occur. When the crimped bung was removed from the bottle there was an audible pop and gas release, presumably CO_2. Based on its lower reactivity and common association with natural mineralisation, including carbonatite-hosted REE (and HFSE) deposits (e.g. Smith et al., 2015), dolomite was chosen as an alternative carbonate source. The pure-white dolomite, sourced from a builders' merchant, came as small (10 mm) chips that were further crushed to approximately 3 mm. This step was required so they could fit into the experimental cell (described below and in Chapter 3). No mineral impurities were detected when analysed by PXRD. In each experiment the initial mass of dolomite was 0.5 g (typically four to six chips).

A total of 20 experiments were completed at temperatures ranging from 90 to 200 °C, which included two blank runs. The experimental matrix is presented in Table 6.1.

	Temperature (°C)				
REE	**90**	**130**	**170**	**200**	**REE conc (M)**
Blank	14	-	2	-	-
Nd	14	4	2	1	0.1, 0.02
Er	14	4	2	1	0.1, 0.02
Yb	14	-	2	1	0.1, 0.02
Nd+Er	14	4	2	1	0.1, 0.02
La+Nd+Gd+Er+Yb	-	4	2	1	0.02

Table 6.1: Experimental matrix showing the length of time (days) and temperature at which each of the experiments were conducted. The individual REE concentrations were 0.1 M in experiments conducted at 90 °C in the 'batch' reactions (serum bottles). At > 100 °C, the individual REE concentrations were 0.02 M, and the experiments completed in the PEEK reaction vessel using the 'continual batch' method (see text).

In experiments at < 100 °C, a 1 g dolomite chip and 10 ml of 0.1 M REE-bearing solution were placed into a serum bottle (20 ml volume), which was stoppered with butyl rubber, crimped shut and placed into a preheated oven at 90 °C. These were aged for

two weeks. Most of these experiments had visible crystals in the bottles (i.e. separate from the dolomite), and all but three (blanks plus one REE-run) had crystallisation on the dolomite surface. The contents of each bottle were vacuum filtered on 0.45 μm mixed cellulose membrane filters using a vacuum pump, washed repeatedly with deionised water and left to air-dry.

The experiments conducted at > 100 °C involved pumping a 0.02 M REE-bearing solution through a heated cell containing 0.5 g dolomite. The difference in dolomite mass and the lower REE concentration as compared with the batch reactions was based on the observation that in the latter, the conditions produced sufficient material without exhausting the dolomite. The reaction cell consisted of a 10 cm long PEEK cylinder, down the centre of which a 4.5 mm diameter bore was drilled. This gave a volume capable of holding 1.5 ml of solution. PEEK was chosen for its chemical inertness to the reagents and conditions of the study, and its superior machinability in comparison to other inert polymers (e.g. PTFE). At each end of the cylinder was a 20 mm thick cap, into the outwards facing edges of which threads had been milled that could accommodate Upchurch 10/32 UNF HPLC finger-tight PEEK fittings. PEEK HPLC tubing (1/16" OD) was connected and tightened into these fittings. Between the inward-facing ends of the caps and the outwards facing ends of the cell's main body were Viton O-rings, which ensured a watertight face seal once the cell was assembled. Two steel plates, situated at each end of the cell, were held together with six threaded steel rods running parallel to the cell, tightened towards each other with steel nuts. This held the whole cell together.

Before each experiment the cell was loaded with dolomite and the HPLC tubing was connected to each end (inlet and outlet). The cell was then placed into a preheated oven and the inlet tubing was connected to a HPLC pump and the outlet tubing fed to waste. A 500 psi back-pressure regulator (BPR) was fitted before the waste (vapour pressure of water at 200 °C is 225 psi, i.e. well below that of the BPR), and before the BPR were two filters (10 μm and 2 μm), which prevented the BPR from being jammed open by any particulate material. The pump was connected to a reservoir of the appropriate REE-bearing experimental solution; during the blank run a 0.1 M HCl solution was used. A schematic of the flow-through system and PEEK reaction cell is shown in Figure 6.1.

A preliminary experiment using a fully continuous flow-through system (at 0.01 ml min^{-1} - the minimum flow rate of the pump) was found to dissolve all the dolomite within about six hours. Therefore, a hybrid 'continual batch' system was employed instead. This involved the equivalent of two cell volumes (i.e. about 3 ml) being 'flushed through' the cell once every 24 hours (achieved by leaving the pump on at a known flow rate). This ensured a fresh supply of solution to the system but did not result in

complete dissolution of the dolomite. This method was successful even for the longest experiments (five days).

At the end of each run the cell was quenched and the dolomite chips removed, washed with deionised water and air-dried ready for characterisation.

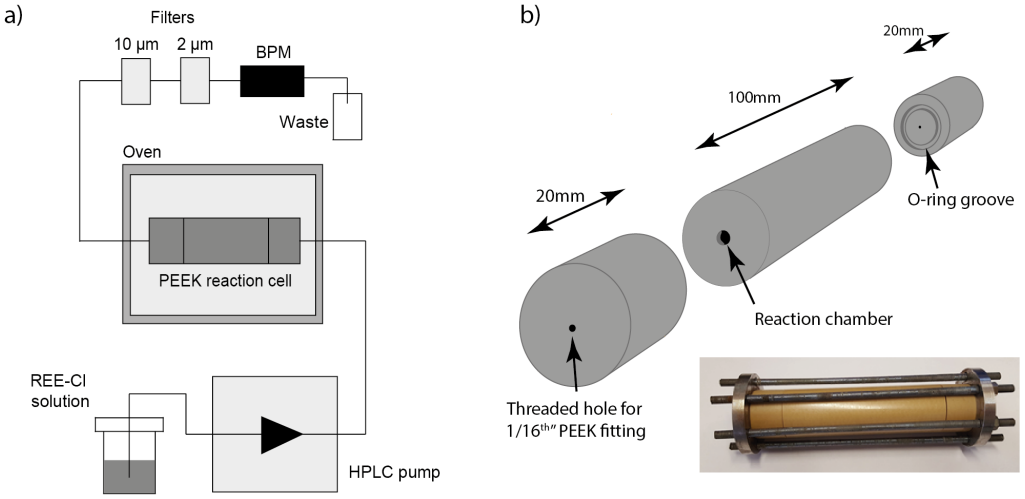

Figure 6.1: a) schematic of the setup for the 'continual batch' experiments (not to scale); b) detail of the PEEK reaction cell. Insert photograph is the cell, including the steel rods and plates used to hold it together.

6.2.2 Characterisation

A few samples had crystallisation large and extensive enough to be seen without the aid of a microscope. In these cases, images were collected using a Leica DFC 420C camera attached to a Nikon SMZ800 Stereo microscope., which helped reveal some of their crystal morphologies.

More detailed imaging of all samples was undertaken on an electron microscope (SEM – Carl Zeiss SIGMA HD VP field emission gun) operating at an accelerating voltage of 20 kV, and qualitative chemical analyses were achieved by energy-dispersive X-ray spectrometry (EDS) with an Oxford Instruments Aztec analysis system. The samples were carbon-coated prior to analyses. The results of EDS analyses were only qualitative/semi-quantitative, but were sufficient to determine the presence/absence of elements from a sample. This was particularly useful for investigating the chemistry of precipitates formed from solutions containing more than one REE.

SEM results revealed material with good crystal shapes for almost all samples, although the amount of crystallisation was small in comparison with the dolomite (only forming

surface coatings). Structural data from PXRD was desired, but because the dolomite-to-product ratio was so large, crushing the dolomite was avoided to prevent dilution of REE precipitates beyond the detection limits of the X-ray diffractometer (about 1 % by volume). Instead the products were filed off the dolomite faces using a stainless-steel file, which, although inevitably including dolomite contamination, was very effective. The filings were crushed in a mortar and pestle and PXRD spectra collected on a Bruker D2 PHASER desktop X-ray spectrometer (Department of Chemistry, UoE), with Cu$K\alpha$ radiation (λ = 0.154 nm) from 2 to 65 2θ at intervals of 0.08° and for 1.5 seconds per step at 8 rpm. Phase identification was performed with EVA X-ray diffraction software and the international centre for diffraction data (ICDD) database.

FTIR analyses were performed on several samples but the signal from dolomite contamination was too dominant in all cases to allow for the identification of peaks attributable to the REE precipitates.

6.3 Results

The PXRD spectrum of the dolomite used in this investigation (before any fluid interaction) is presented with PXRD analyses of all samples (e.g. Figure 6.4), for reference.

6.3.1 Blank

SEM images of the dolomite used in blank runs conducted at 90 and 170 °C are presented in Figure 6.2. The dolomite chips showed heavily-pitted surfaces, but no additional phases or crystallisation. The PXRD analyses (not shown) were identical to that of the dolomite before reaction with HCl.

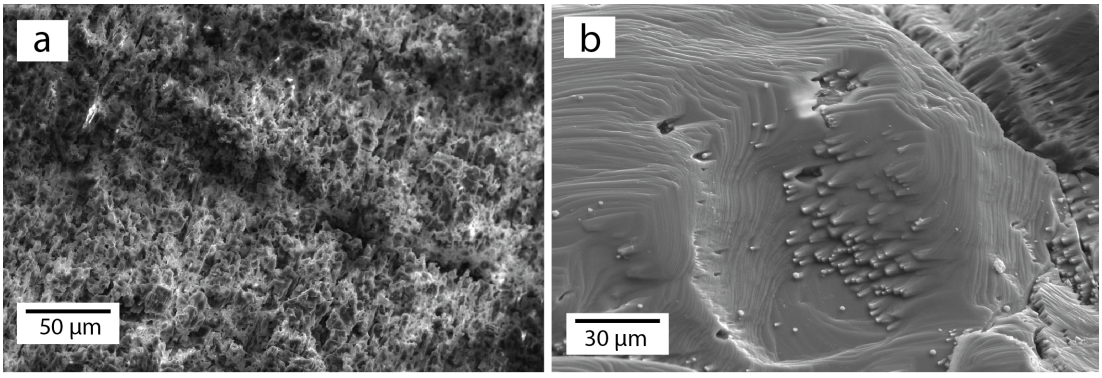

Figure 6.2: SEM images of dolomite surface after reaction with HCl (i.e. devoid of REEs) at a) 90 °C for 14 days, and; b) 170 °C for two days.

6.3.2 Single REEs

6.3.2.1 Neodymium

An optical microscope image shows the extent of neo-formed mineralisation on the faces of dolomite chips reacted with neodymium chloride at 90 °C (Figure 6.3a), while SEM imaging revealed its morphology in greater detail (Figure 6.3b). Elongate bipyramids about 50 μm in length were present in abundance throughout both the 90 °C and 130 °C samples (Figures 6.3b - d). The crystallisation at 130 °C was concentrated along, and clearly picked out, the rhombohedral cleavage of the dolomite. In a closer view of the 130 °C sample many of the crystals radiate out to form fan shapes (Figure 6.3c). PXRD revealed these crystals to be kozoite (Figure 6.4). No additional peaks (other than dolomite) were identified. Due to the difference in experimental setup between the 90 °C sample and those conducted at higher temperatures, the PXRD spectrum for the former was collected from excess crystals obtained during filtering (i.e. not scraped off the dolomite surface). It is for this reason its PXRD spectrum contains no peaks for dolomite.

At 170 °C the crystals were shorter and stubby (lengths around 10 to 20 μm) but still often followed surface traces of cleavage planes in the dolomite (Figure 6.3e - f). A significant number of very small (approximately 1 – 2 μm) spheres were found all over the dolomite. The PXRD spectrum contains reflections for both kozoite (although weaker than at the lower temperatures) and hydroxylbastnäsite-(Nd), which are suggested to represent the stubby crystals and spheres, respectively.

At the highest temperature (200 °C), most crystallisation was in the form of thin, flat plates stacked together (resembling clams), about 30 μm across (Figure 6.3g - h). The strongest reflections in this sample are for hydroxylbastnäsite-(Nd). A few weak reflections for kozoite remain, and were attributed to the small number of bi-pyramidal prisms (e.g. at the top of Figure 6.4h). The mineralisation almost completely covered the dolomite.

As the sample volumes used for XRD analyses were so low, a small signal from the glass slides onto which they were mounted was observed (as the broad humps centred around 22 2θ).

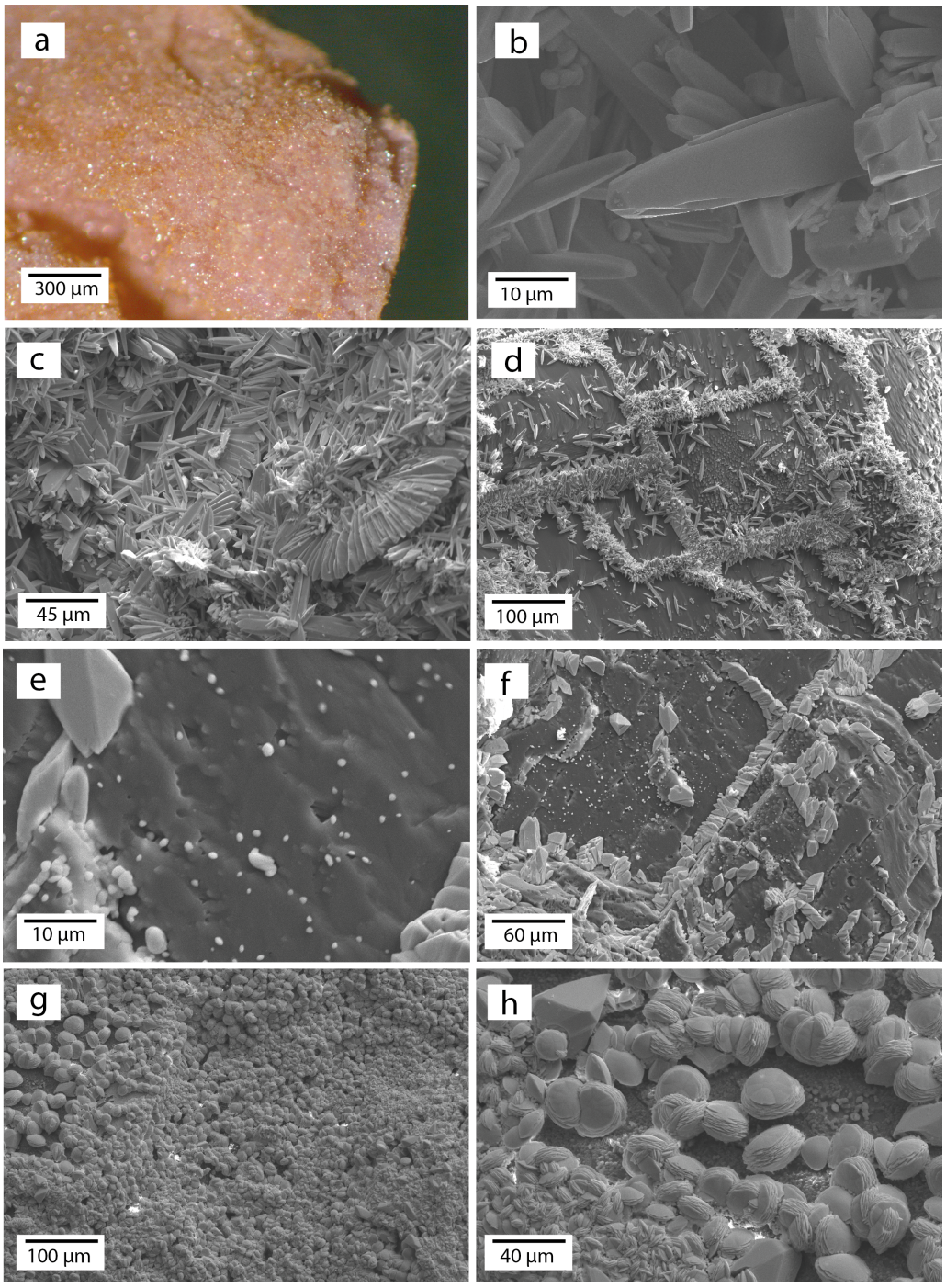

Figure 6.3: Optical microscope (a) and SEM images (b – h) of the products of reactions between dolomite and the Nd-bearing solution. a - b) kozoite formed at 90 °C; c – d) kozoite formed at 130 °C; e - f) a mixture of kozoite and hydroxylbastnäsite formed at 170 °C; g – h) hydroxylbastnäsite with minor kozoite formed at 200 °C.

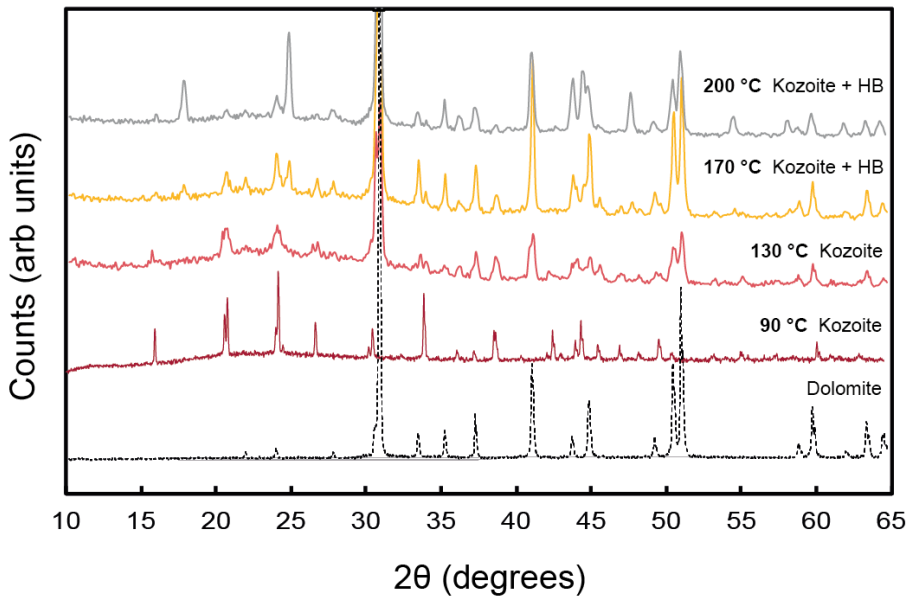

Figure 6.4: Spectra for the PXRD analyses of dolomite filings from the Nd experiments. A PXRD spectra of the unaltered dolomite is also included, which highlights the contamination of this mineral in the samples. The 90 °C spectrum contains no dolomite peaks because of its sampling technique (explained in text). HB = hydroxylbastnäsite.

6.3.2.2 Erbium

Figure 6.5a is an optical microscope image of the reaction product between dolomite and erbium chloride, formed at 90 °C. Figures 6.5b and 6.5c are SEM images of the same sample. In contrast to the extensive Nd mineralisation formed at this temperature, here it was more localised, with about 20 'bow tie'-shaped masses. Closer inspection reveals the acicular morphology of constituent crystals of these clusters/aggregations, with individual crystals up to 600 μm in length. The surface of the dolomite is heavily pitted. A similar morphology formed at 130 °C (Figure 6.5d) but was far more abundant. The crystals grown at 90 °C were large enough to knock off the dolomite, and a few large crystals were recovered from the filter. Combined, these provided enough material for PXRD analysis (Figure 6.6), the results of which matched the structure of synthetic tengerite-(Y) (PDF 00-024-1419). This was also the case for the 130 °C sample.

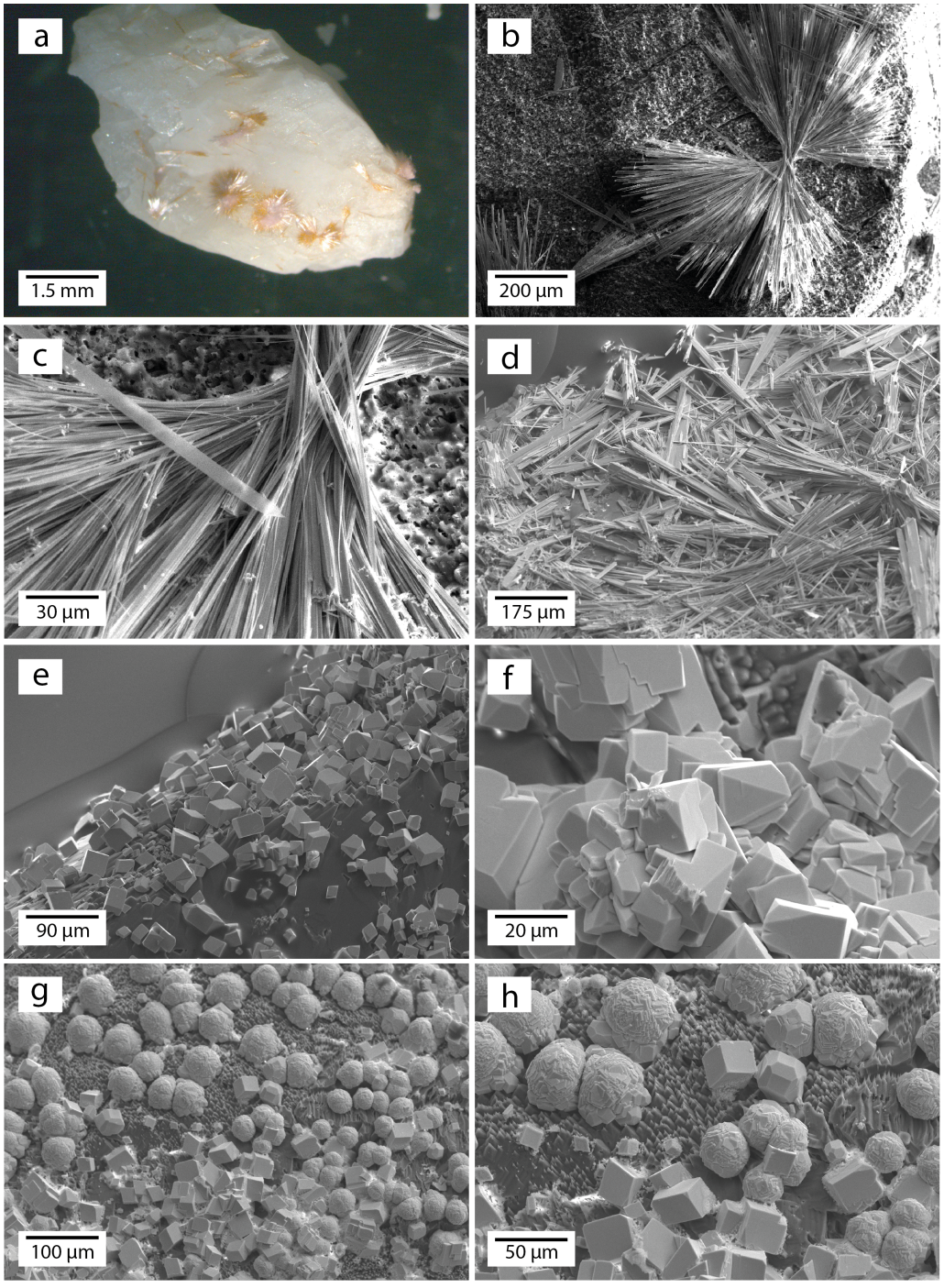

Figure 6.5: Optical microscope (a) and SEM images (b – h) of the Er-bearing minerals formed on the dolomite surfaces. a) mineral with tengerite structure formed at 90 °C; b – c) SEM images of a); d) tengerite formed at 130 °C; e and f) a mineral with the structure of orthorhombic $ErCO_3OH$ formed at 170 °C, and; g and h) unidentified minerals formed at 200 °C.

At higher temperatures (170 and 200 °C), the morphology changes significantly, with distorted cubes, rhombs, pyramid-shaped prisms (similar to the Nd samples at 170 °C) and other more complex multi-faced polyhedra, most of which were 30 to 60 μm in length. These complex morphologies were found, through EDS analyses, to contain minor amounts of chlorine (as chloride - maximum of $<$ 5 wt. %), an element not detected at any other temperature or morphology. The reason for this is currently unexplained. The products of the 200 °C run also contained minor Ca. The cubes and rhombs at 170 °C were indexed to orthorhombic $ErCO_3OH$, a synthetic version of which has been described previously (Tahara et al., 2007). It is similar to kozoite but with lower symmetry, essentially a distorted kozoite structure. Unfortunately, the material recovered from the 200 °C sample was too diluted with dolomite to be identified by PXRD. The only Bragg peak of high enough intensity not indexed to dolomite is at 17.4 2θ (asterisked). A match was not found in the database.

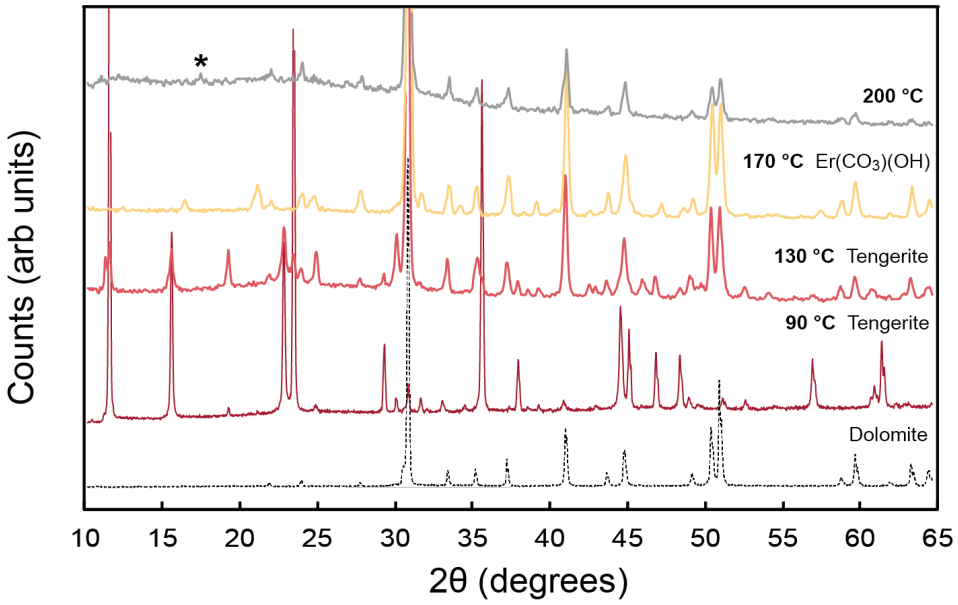

Figure 6.6: PXRD traces of the dolomite filings from the Er experiments. The sample at 200 °C could not be identified due to excess dolomite contamination.

6.3.2.3 Ytterbium

The 90 °C experiment did not produce any new material, and was the only REE-run to do so. However, at 170 and 200 °C there was extensive mineralisation (Figure 6.7). No 130 °C experiment was run. At 170 °C, the crystals were pseudo-cubes, which on closer inspection were actually made up of many more faces (Figure 6.7a - c). At 200 °C there were at least three morphologies, one of which displayed perfect hexagonal faces that were often intergrown. There were also crystals with square faces, and some

examples of complex multi-faced polyhedra. When analysed by PXRD these phases produced strong reflections, but unfortunately they could not be indexed to any known phase. None matched any reflections of the unknown Yb sample from Chapter 4.

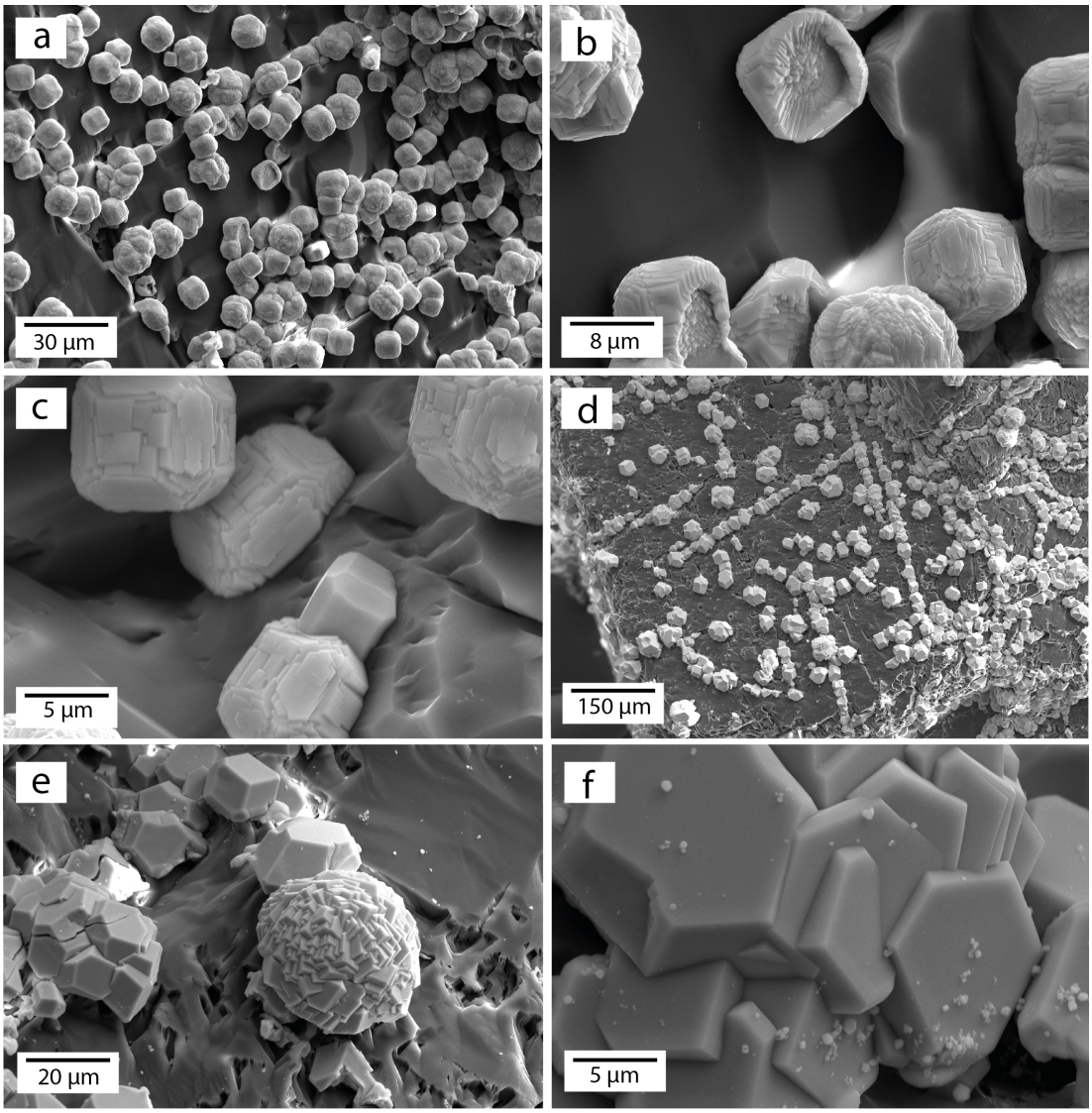

Figure 6.7: SEM images of the products of reaction between dolomite and Yb chloride solutions at 170 °C (a - c) and 200 °C (d - f). None of these phases were identified. The 90 °C experiment did not produce any REE minerals. No 130 °C experiment was run for Yb.

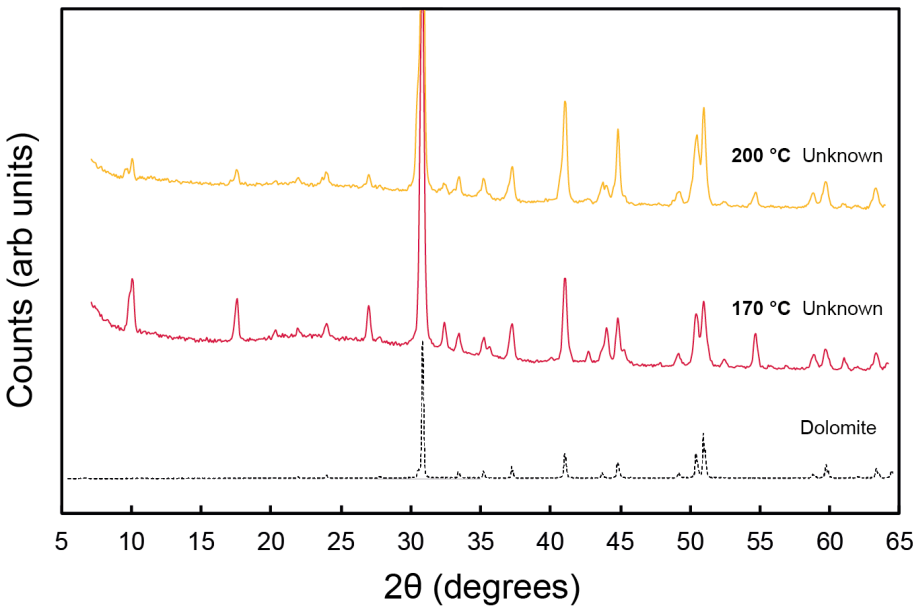

Figure 6.8: PXRD traces of the dolomite filings from the Yb experiments. The experiment at 90 °C did not produce any REE products.

6.3.3 Multi-REEs

6.3.3.1 Nd+Er

When a mixture of equimolar Nd and Er chloride was reacted with dolomite, the results were quite different to those of the individual elements. At the lowest temperature (90 °C), crystallisation was very abundant and its morphology was similar to that of the Nd-only runs at 90 and 130 °C (i.e. elongate bipyramids, Figure 6.9a). Unlike the Nd-only run, however, these crystals were commonly clustered together into larger ball-shaped masses. At 130 °C the morphologies most resembled those of the individual Nd crystals formed at 170 °C, forming elongate triangular prisms terminated by pyramids between 20 and 70 μm in length (Figure 6.3b). EDS analyses indicated the presence of both Nd and Er in all material.

At 170 and 200 °C, most the crystallisation was in the form of rhombohedra or cubes (Figures 6.9c - d). About 10 EDS analyses were made on examples of each, with the results suggesting relative Er-enrichment in the more rhombic examples (EDS spots 3, 4, 5 and 6). At 200 °C the morphologies were similar, although a very fine-grained material covered much of the dolomite chips, including the larger crystals (Figures 6.9e – g). No separate Nd- or Er-only-bearing phases were observed.

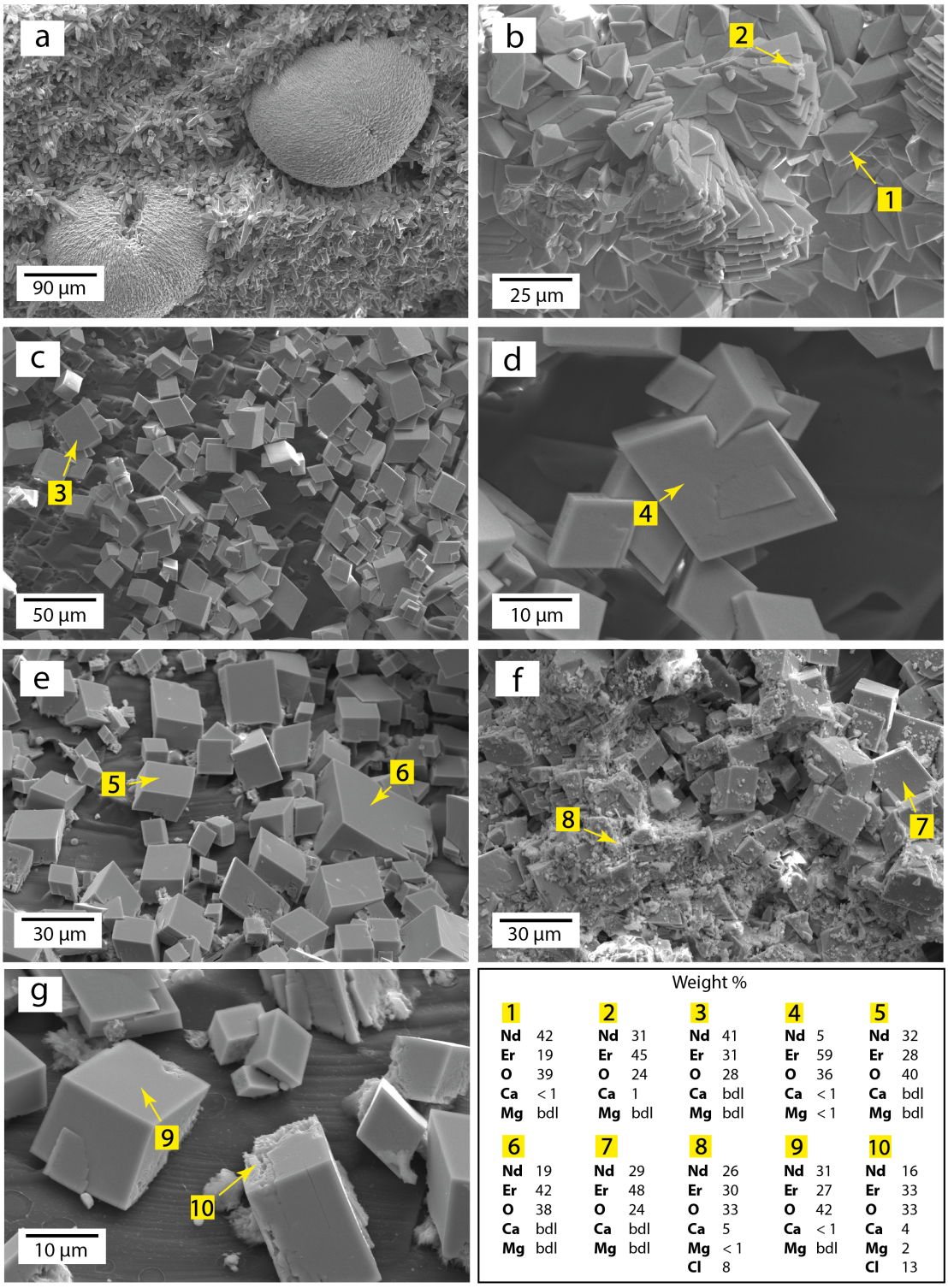

Figure 6.9: SEM images of the products from reactions between dolomite and a mixed Nd+Er solution. Images taken for samples treated at: a) 90 °C; b) 130 °C; c – d) 170 °C, and; e – g) 200 °C. Insert in the bottom right shows some of the EDS results. 'bdl' = below detection limit.

PXRD patterns (Figure 6.10) for all samples were very similar; no analysis was performed on the 90 °C material. The peaks not associated with dolomite were indexed most closely to orthorhombic kozoite at 130 and 170 °C. A few reflections might be attributed to the orthorhombic mineral $ErCO_3OH$ (as seen in the Er-only solution experiments at 170 °C), although they were weak and it is not clear if they were real or part of the background. Unfortunately, the strongest peaks for $ErCO_3OH$ overlapped with those of dolomite, of which there was significant contamination. The 200 °C sample was also heavily diluted with dolomite, although the strongest peaks for kozoite were still visible. This sample also contained a number of peaks (asterisked) not indexed to either kozoite or dolomite, and for which no other match could be found. Based on the SEM images it is unclear which phase was responsible for these additional peaks. A possible candidate is the fine-grained material.

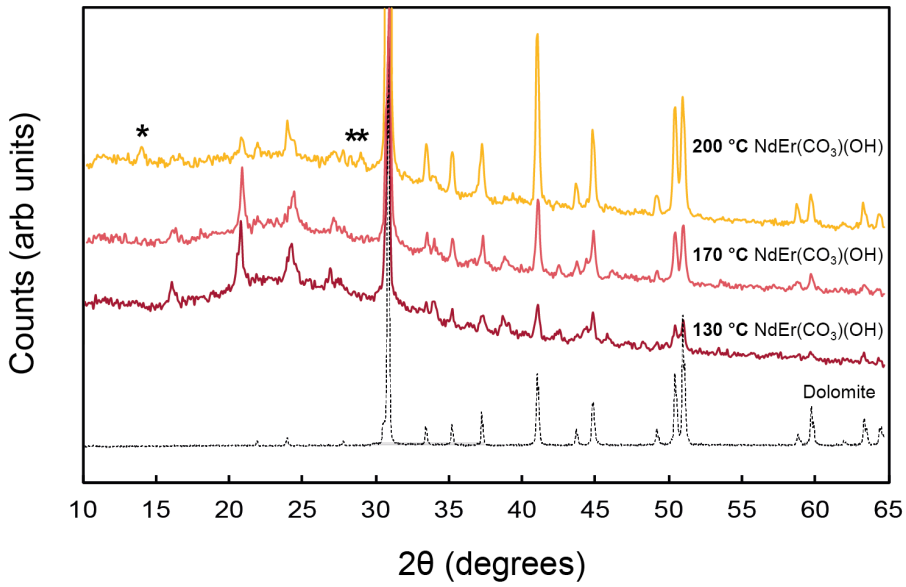

Figure 6.10: PXRD traces of the dolomite filings from the products of reaction between dolomite and mixed Nd+Er solutions. The peaks not indexed to dolomite in were in all cases most closely matched to the orthorhombic mineral kozoite. The three asterisked peaks in the 200 °C sample were unidentified.

6.3.3.2 Five-REE mix

There was no experiment with the five-REE solution at 90 °C. Crystallisation at 130 °C was extensive and very similar in its morphology to that of the 90 and 130 °C Nd experiments, consisting of elongate triangular bipyramids about 20 μm in length (Figure 6.11a – b). The crystals almost completely covered the dolomite surfaces and in places were grouped together forming large ball shaped features (Figure 6.11a), similar to the 90 °C Nd+Er sample. Qualitative EDS analyses confirmed the presence of all five REEs in these crystals, with a suggestion they were more enriched in the light and middle REEs.

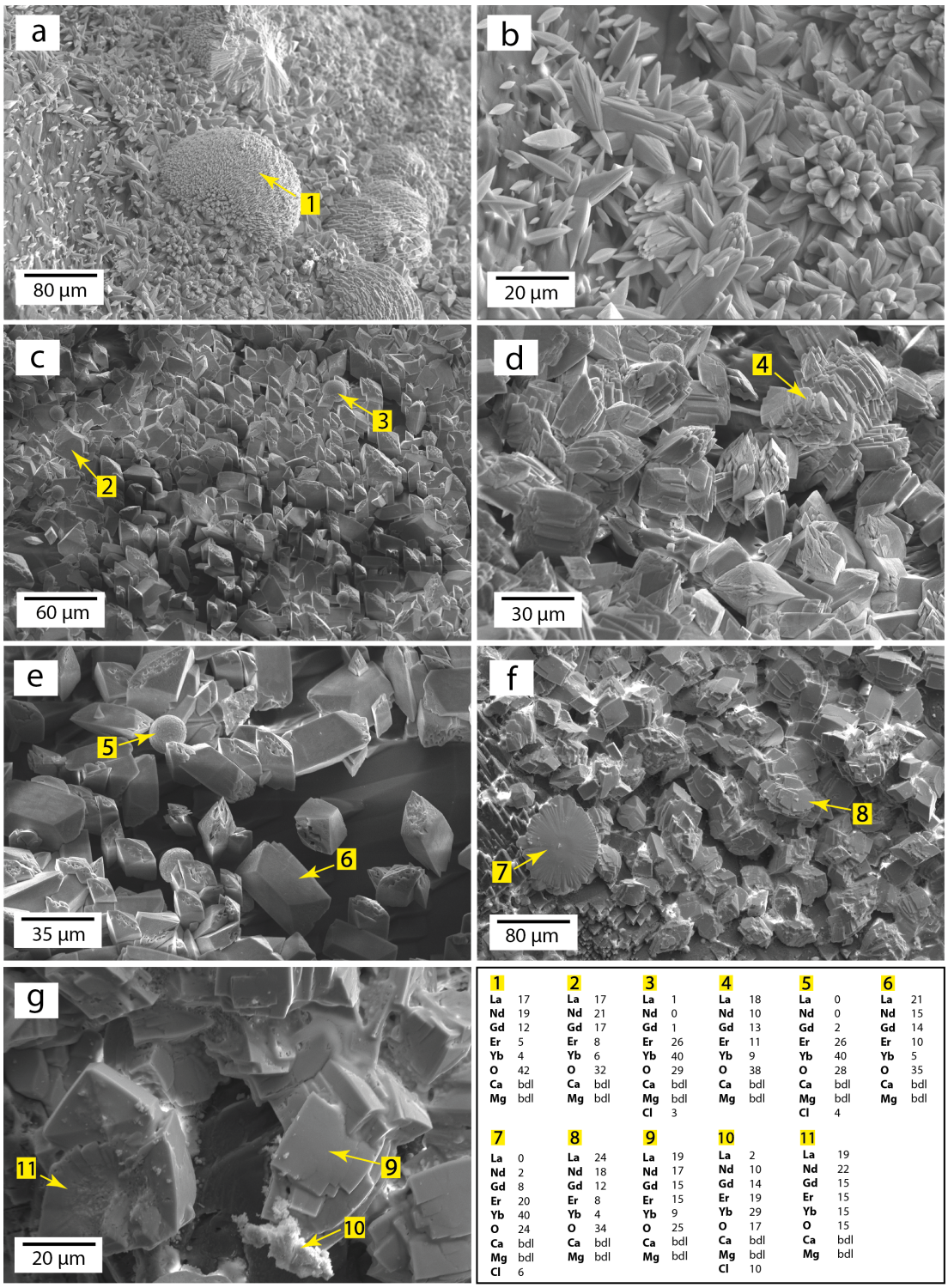

Figure 6.11: SEM images of the products of reaction between dolomite and solutions containing all five REEs investigated in this project (La+Nd+Gd+Er+Yb). Reactions at: a – b) 130 °C; c – e) 170 °C, and; f and g) 200 °C. EDS analyses are shown in the bottom right. Note the spheres in e), which are discussed more in text. 'bdl' = below detection limit.

At 170 °C there were three distinct morphologies: 1) small (< 10 μm) spheres – (Figure 6.11c, spot 3, and 6.11e, spot 5); 2) elongate rhombic prisms about 30 – 40 μm in length (these resembled hip roofs - Figures 6.11c and e, especially spot 6), and; 3) what could be altered versions of morphology 2 (Figure 6.11d). The elongate rhombic prisms were pitted along common edges in different crystals, as shown in Figures 6.11c and e. The spheres, although not that common, nearly always occurred at these locations. The morphologies in Figure 6.11d may represent more advanced stages of rhombic prism alteration (possibly into the spheres?). EDS analyses indicated a relative enrichment of HREEs in the spheres (in which La and Nd were often not detected, Figure 6.11c, spot 3 and 6.11e, spot 5), while the rhombic prisms appeared to contain relatively more LREEs (EDS spot 2 and 6). The other, more complex morphology, have EDS values somewhere in the middle (EDS spot 4). Interestingly, Cl was detected in the spheres but nowhere else, which based on the potential HREE enrichment of these morphologies, might suggest some currently unknown HREE-Cl-bearing mineral.

At 200 °C the morphologies were slightly different, although separate LREE- and HREE-enriched phases were still present. The relatively LREE-enriched phases consisted of rhombohedra and twinned rhombohedra, often with curved faces (Figure 6.11f, spot 8 and 6.11g, spots 9 and 11), while the HREE-enriched phases included the spheres (not shown in the Figures), the more complex-shaped minerals in Figure 6.11f (EDS spot 8), and what could be flattened versions of the spheres (visible in the bottom left of Figure 6.11f, EDS spot 7). There was an additional material throughout this sample that does not appear to have a good crystal shape (at least at this scale) but is HREE-enriched (Figure 6.11g, spot 10). It commonly occurred as small clumps at the contact with dolomite and the rhombohedra, similar to the higher temperature Nd+Er samples. The dolomite was again heavily pitted throughout these samples.

PXRD analyses of the filings at all three temperatures were similar (Figure 6.12). The 130 and 170 °C samples were most closely indexed to the orthorhombic mineral kozoite. There did not appear to be any additional peaks related to the HREE spheres, possibly because they were not abundant enough. The majority of peaks in the 200 °C phase were indexed to kozoite, although a number (asterisked, Figure 6.12) have not been matched to any known phase.

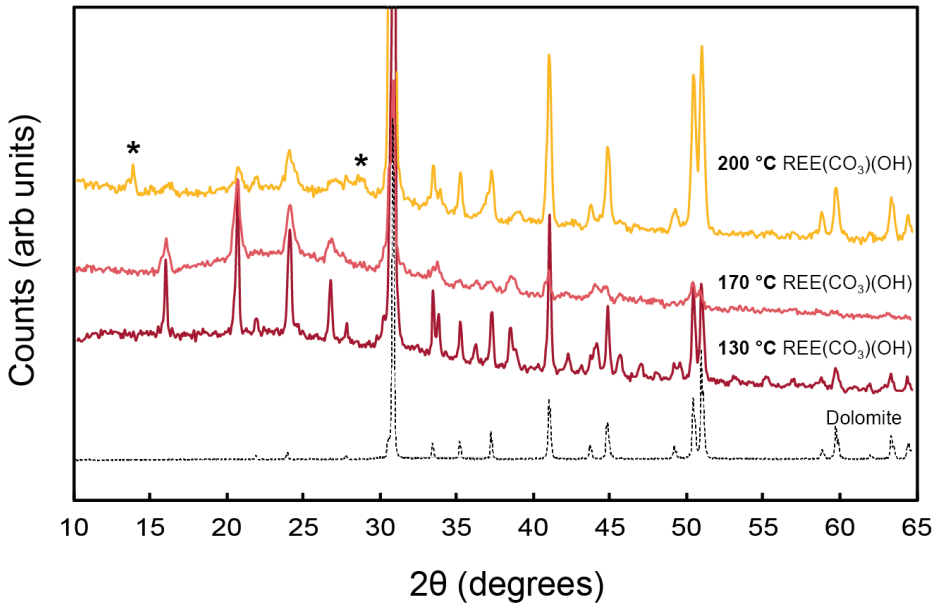

Figure 6.12: Spectra for the PXRD analyses of the samples produced during reaction of dolomite with a five-REE mixed solution. The peaks not indexed to dolomite in were in all cases most closely matched to the orthorhombic mineral kozoite. The two asterisked peaks in the 200 °C sample were unidentified.

6.3.4 Results summary

The results of all wall rock experiments, including mineral names, crystal morphologies and any relevant notes, are summarised in Table 6.2.

In summary, all experiments except the 90 °C Yb run resulted in REE carbonate mineralisation. Neo-formed mineralisation was very abundant in all cases except the 90 °C Er experiment, and in many cases the crystals exhibited complex shapes/twinning/intergrowths. Experiments with two REEs in solutions produced mixed-REE carbonates with almost equal proportions of the respective REE at all investigated temperatures. The five-REE solution also produced carbonates with almost equal proportions of REEs, but only at < 170 °C; at higher temperatures discrete LREE- and HREE-enriched phases started to form.

Element(s)	Temp (°C)	Mineral	Morphology	Notes
Nd	90	Kozoite	Elongate bipyramids	Very abundant
	130	Kozoite	Elongate bipyramids	Commonly grouped as 'fans'
	170	50 % Koz, 50 % HB	Rhombic prisms, micron-sized spheres	Pick out dolomite cleavage
	200	25 % Koz, 75 % HB	Rhombic prisms	Stacked discs, 'clam'-like
Er	90	Tengerite	Acicular	'Bow tie' aggregates
	130	Tengerite	Acicular	Very abundant
	170	$ErCO_3OH$	Cubes, rhombs, stubby bipyramids	
	200	Unknown	Elongate bipyramids, multi-faced polyhedra	Multiple morphologies
Yb	90	No product		
	170	Unknown	Pseudo-cubes	Some 'bowl'-like shapes
	200	Unknown	Multi-faced polyhedra	Rhombic, pentagonal and hexagonal faces
NdEr	130	Kozoite	Rhombic prisms and shapeless	
	170	Kozoite	Rhombohedra, cubes	Commonly twinned and intergrown
	200	Kozoite + unknown	Rhombohedra, cubes, shapeless	Euhedral crystals altered along edges
All	130	Kozoite	Rhombic prisms and shapeless	Commonly grouped in large spheres
	170	Kozoite	Twinned rhombic pyramids, spheres,	HREE spheres; others = LREE enriched
	200	Kozoite	Twinned/intergrown rhombs, discs	Discs = HREE-enriched, lots of twinning

Table 6.2: Summary results table for all the wall rock experiments. 'All' in column one refers to the five-REE mixed solution (i.e. La+Nd+Gd+Er+Yb).

6.4 Discussion

The results presented here confirm for the first time that, at least under the conditions employed in this study, the dissolution of dolomite in the presence of significant soluble REE chlorides leads to the secondary crystallisation of REE-bearing carbonates. It has also been demonstrated that the structure and morphology of these phases are significantly influenced by the temperature at which the reactions take place, although there is limited information to explain why. These observations are consistent with several previous studies in which wall rock dissolution - and subsequent release of 'precipitation ligands' - has been suggested as a mechanism for REE carbonate (and fluorocarbonate) mineralisation (e.g. Ngwenya, 1994; Smith et al., 1999; Mondillo et al., 2016).

6.4.1 Comparison with natural REE carbonate occurrences

Several natural REE carbonate minerals have been described previously, a selection of which are presented in Table 6.3. Many of those minerals are described as crusts or coatings that occur in heavily weathered/supergene zones, and as such are suggested as being alteration products. The REEs are thought to be sourced either from pre-existing REE minerals, or by the circulation of ground/mine waters through country rocks. Pegmatites are also a common host for these minerals, in which they are thought to be either of hydrothermal origin or weathering products (see refences in Table 6.3). A common feature of these minerals, many of which are very rare, is their almost ubiquitous association with dolomite or calcite. They also frequently occur with other, very similar REE carbonates. This intimate association may suggest that host calcite/dolomite dissolution is the trigger for their precipitation, something now shown possible experimentally.

A striking observation from Table 6.3 is the number of additional cations that may be incorporated in these minerals. In the current investigation, the cations available were restricted to the REEs in solution and the constituents of the dolomite, i.e. Ca and Mg. Magnesium-bearing REE carbonates have not been previously reported (and were not seen here), but those containing Ca, e.g. ancylite and lokkaite, have. The results from the current investigation suggest that the most commonly-formed structure was kozoite – an orthorhombic mineral that theoretically contains no Ca. EDS analyses of the kozoites from this study does in some cases suggest the presence of minor Ca, but that this is rare and never exceeds > 5 wt. % (commonly < 1 wt. %). Previously documented natural kozoite-(La) (Miyawaki et al., 2003) and kozoite-(Nd) (Miyawaki et al., 2000) also both contained minor Ca (< 7 wt. % CaO), which agrees with the findings of the current investigation.

Name	Ideal formula	Occurrence (**associated minerals**)	Habit	Refs
Lanthanite-(La), -(Ce), -(Nd)	$REE_2(CO_3)_3 \cdot 8\,H_2O$	Oxidised Cu ore (**malachite, ferric oxyhydroxides, brochanite**); andesite tuff (**calcite**)	Plates (5 x 5 x 0.5 mm); plates and 'blocky' (1mm length)	1, 2, 3
Tengerite-(Y)	$Y_2(CO_3)_3 \cdot 2{-}3\,H_2O$	Granite pegmatites (**lanthanite, bastnäsite-(Ce), gadolinite-(Y), calcite, fluorite**); Cu ores (**decrespignyite-(Y)**)	Radial aggregates of acicular crystals (2 mm)	4
Kozoite-(La), -(Nd)	$REECO_3OH$	Alkali olivine basalt (**kozoite-(Nd), lokkaite-(Y), kimuraite-(Y), calcite**)	Spherical aggregates (< 1 mm) and fine radial crystals	5, 6
Hydroxylbastnäsite-(La), -(Ce), -(Nd)	$REECO_3OH$	Karstic bauxite (**limestone**); pegmatities (**bastnäsite, calcite, ewaldite**)	Aggregates of plates (10 - 100 μm) and fine radial crystals	7, 8
Ancylite-(La), -(Ce)	$(Sr,Ca)REE(CO_3)_2(OH) \cdot H_2O$	Pegmatities, carbonatites		9
Calcioancylite-(Ce), -(Nd)	$CaREE(CO_3)_2(OH) \cdot H_2O$	Syenite pegmatite (**calcite, chlorite, Mn-hydroxides**); granites	1 mm crystals in several cm aggregates; 'pine cone'-like (1 mm)	10, 11
Gysinite-(Nd)	$Pb(Nd,La)(CO_3)_2(OH) \cdot H_2O$	U-Cu ore (**monazite, malachite, cerussite**)	Pseudo-octahedral crystals (1 mm length)	12
Petersenite-(Ce)	$Na_4(REE)_2(CO_3)_5$	Alkaline igneous intrusives (**calcite, fluorite, trona**)	Striated prisms (up to 7 mm), acicular crystals (1 mm)	13
Kimuraite-(Y)	$CaY_2(CO_3)_4 \cdot 6\,H_2O$	Alkali basalt (**lanthanite-(Nd), lokkaite-(Y), calcite**); granite pegmatites (**tengerite-(Y)**)	Aggregates (4 x 2 cm) of tabular crystals (100 x 10 μm)	14
Decrespignyite-(Y)	$(Y,REE)_4Cu(CO_3)_4Cl(OH) \cdot 2.5\,H_2O$	Supergene Cu mine (**dolomite, calcite, malachite, donnayite-(Y), kamphaugite-(Y), bastnäsite-(La), calcioancylite-(Nd), tengerite-(Y)**)	Hexagonal platelets (10 - 50 μm)	15
Kamphaugite-(Y)	$Ca(Y,REE)(CO_3)_2(OH) \cdot 1.5\,H_2O$	Granite (**calcite, kainosite-(Y)**)	Semi-spherical aggregates of radial crystals	16

Table 6.3: A selection of previously-described, naturally-occurring REE carbonate minerals. Minerals in bold text are either REE minerals or those potentially important for REE precipitation (e.g. carbonates). The formulae, associated minerals and crystal habits/morphologies are presented, which have been taken from the following references: 1 - Dal Negro et al. (1977); 2 - Bevins et al. (1985); 3 - Graham et al. (2007); 4 - Miyawaki et al. (1993); 5 - Miyawaki et al. (2003); 6 - Miyawaki et al. (2000); 7 - Maksimovic (1985); 8 - Michiba et al. (2011); 9 - Dal Negro et al. (1975); 10 - Larsen and Gault (2002); 11 - Orlandi et al. (1990); 12 - Sarp and Bertrand (1985); 13 - Grice et al. (1994); 14 - Nagashima et al. (1986) 15 - Wallwork et al. (2002); 16 - del Tanago et al. (2006).

Kozoite and ancylite are isostructural, with the whole ancylite-group of minerals described by the formula $(REE^{3+})_x(M^{2+})_{2-x}(CO_3)_2(OH)_2.(2\text{-}x)H_2O$ (Dal Negro et al., 1975). In the case of kozoite, $x = 2$. The lack of ancylite is probably attributed to low Ca and very high REE in the current study. To date, no kozoite dominated by a REE higher in Z than Nd has been found in nature, but synthetic hydroxyl-carbonates have been produced previously for Eu, Gd, Tb, Dy, Ho, Er, Tm and Y (Tahara et al., 2007). These all exhibit kozoite-type structures but with lower symmetry, caused by a reduction in coordination number resulting from the lanthanide contraction. These results, combined with those of the current investigation, suggest that the lack of natural HREE-bearing carbonates is not restricted by crystal structure but by the relative REE content of the solution. This theoretically means that HREE-rich carbonate minerals could form under the right conditions (i.e. significant HREE in solution).

The natural kozoite-(Nd) described by Miyawaki et al. (2000), which was found associated with (often coating) lanthanite-(Nd) and kimuraite-(Y), exhibits a morphology almost identical to that of the kozoite formed from the Nd-only solution at 170 °C in the current investigation (Figure 6.3e - f). The fact that Miyawaki et al. (2000) did not identify hydroxylbastnäsite-(Nd) suggests, based on the current findings, a formation temperature in the region of 170 °C (although probably lower given the transition to hydroxylbastnäsite seen at this temperature, e.g. Figure 6.3). However, this interpretation assumes a similar fluid composition to that used in the experiments, which cannot be proven. Nevertheless, this temperature range fits with the suggested genesis of this mineral from a 'post-magmatic hydrothermal fluid' (Miyawaki et al., 2000).

The second mineral synthesised in the current investigation that has been previously described in nature is hydroxylbastnäsite-(Nd). Results of experiments showed this phase forms only at the highest temperatures from the Nd-only solutions, where it probably results from the transformation of kozoite-(Nd) (e.g. Chapter 4 and Vallina et al., 2015). Hydroxylbastnäsite is a hexagonal polymorph of kozoite (e.g. Michiba et al., 2011), and naturally occurring species include hydroxylbastnäsite-(La), -(Ce) and -(Nd) (e.g. Michiba et al., 2013; Maksimovic, 1985). There are no natural examples of this mineral being dominated by a REE greater in Z than Nd (although a Y-dominated fluor-bastnäsite is known, e.g. Fleischer, 1972). This is in agreement with the present findings, where only an orthorhombic phase ($ErCO_3OH$) was detected at the higher temperatures, for Er-only solutions. The transformation of the HREE orthorhombic phase to its hexagonal form (which is a valid species, having been synthesised previously, e.g. Michiba et al., 2011), may take longer and/or require higher temperatures than were employed during this study.

The final mineral formed in these experiments that also has a natural analogue is tengerite. The only natural version of this mineral is tengerite-(Y), although the Ca-

bearing kimuraite-(Y) and lokkaite-(Y) (see Table 6.3) can be classified in the same mineral group based on structure (Miyawaki et al., 1993). Tengerite often forms radiating acicular crystals (e.g. Frost et al., 2013), similar to Figures 6.5a - d, although spherulitic aggregates or thin coatings/powders on other REE carbonates (e.g. lokkaite-(Y)) are also documented. The reason for the absence of lokkaite-(Y), Kimuraite-(Y), or any related Ca-bearing HREE carbonate mineral in the current investigation is unknown, particularly as there must be soluble Ca^{2+} as the dolomite dissolves. Perhaps the solubility of Ca-bearing phases is lower than non-Ca examples? Solubility data does not exist for these phases, and is therefore something to be considered in the future.

In the current investigation, tengerite formed only from the Er solutions at temperatures < 170 °C. It has been suggested that only Y-group REEs form (8 coordinated) tengerites and Ce-group REEs form (10 coordinated) lanthanites (i.e. $REE_2(CO_3)_3 \cdot 8\,H_2O$), a consequence of the lanthanide contraction. The present results are in agreement with these suggestions. However, the precipitates formed from Nd+Er and the five REE-bearing solutions behaved most similarly to that of the precipitates formed from the Nd-only solution, i.e. no separate tengerite was identified. The only phase detected from these mixed solutions was of the kozoite-type. At the two highest temperatures (170 and 200 °C) in the five REE solutions, there is evidence for distinct LREE and HREE-enriched phases, although the structures of each is unclear currently (reflections were not indexed to any known mineral). The textures seen in Figures 6.11d - g make it difficult to determine whether HREE-enriched spheres are forming from the dissolution-reprecipitation of other morphologies present (which do have clear dissolution features along some of their faces), or precipitating directly from solution. What is also unclear from these figures is whether the morphologies documented at the higher temperatures formed *via* those seen at lower temperatures, or whether they form directly from the dissolution of dolomite. However, the observation that the HREE-enriched spheres (at 170 °C) always form on the other REE carbonate morphologies suggests dissolution-reprecipitation of the latter (HREE-enriched phases do not occur on their own, distant from other morphologies). This is shown in Figure 6.13, which is an enlarged version of Figures 6.11c and e. Higher resolution sampling, or time-resolved XRD analyses, is required to determine the crystallisation pathways with more confidence.

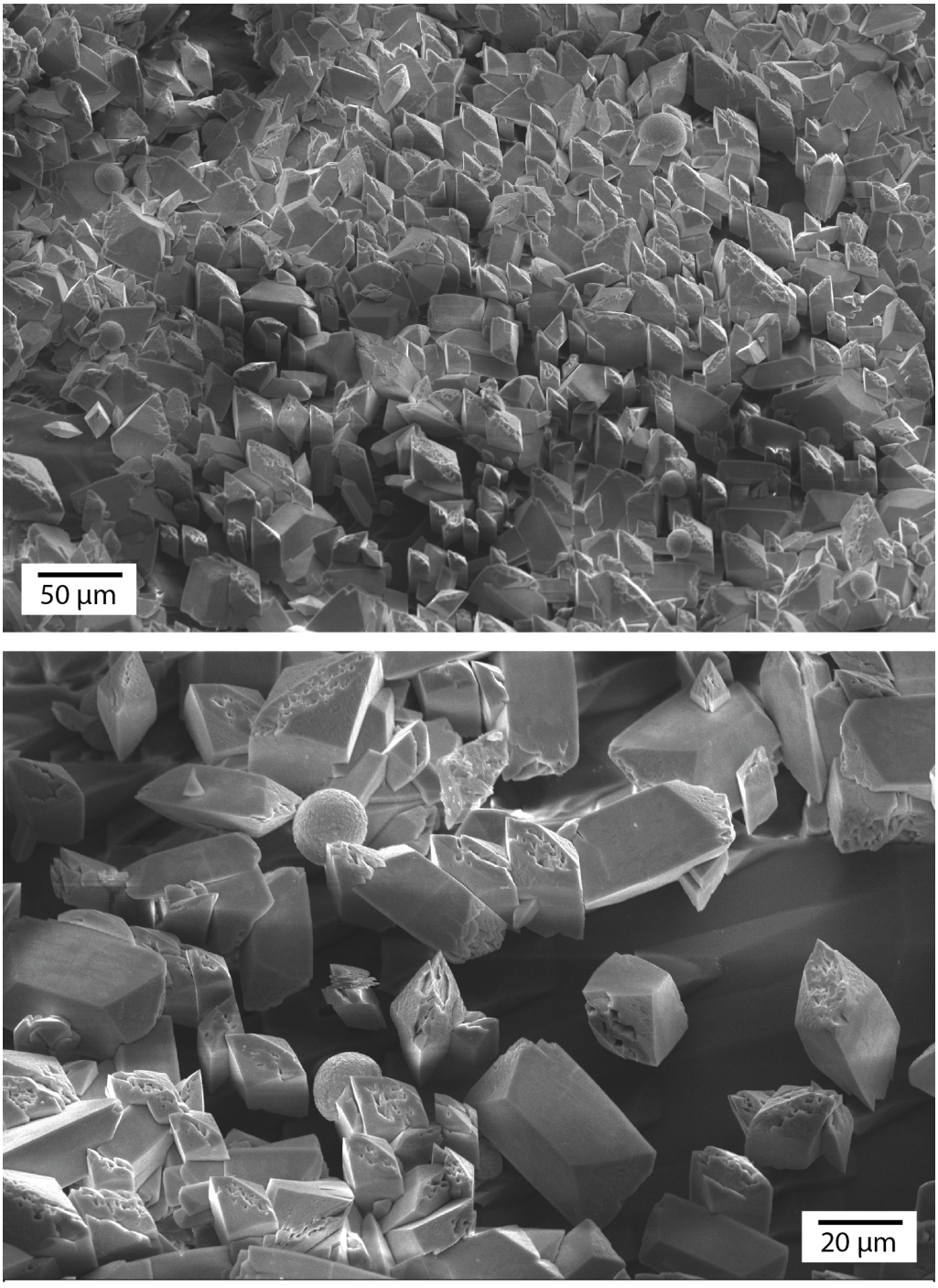

Figure 6.13: Enlarged images of precipitates from the five-REE solutions at 170 °C, highlighting the different morphologies and dissolution features. The spheres are HREE-enriched and the other morphologies contain mostly even proportions of each REE.

Such time-resolved data would be essential in answering the following questions: 1) do the apparent LREE-enriched phases form first, leaving the solution relatively enriched in HREE, which then precipitate as the spheres when the temperature is sufficiently high? Or, 2) does the kozoite-type structured phase form first (containing all REEs), then dissolves-reprecipitates separate LREE and HREE phases? It has been shown that excellent crystallisation of Er occurs at the lower temperatures investigated when precipitated from Er-only solutions (90 °C and 130 °C, Figures 6.5a - d), and that there is a lack of separate Er (or HREE) phases at the lower temperature from the five REE mix solution (130 °C, Figures 6.11a - b). These observations would seem to support the second theory, unless the behaviour of an individual REE in solution is significantly affected by the presence of others. Another line of evidence supporting the second idea is that REE chloride complexes of LREEs have been shown to be stronger than those of HREEs (e.g. Migdisov and Williams-Jones, 2014, also this was shown in Figure 2.2, Chapter 2). This means HREE chloride complexes should destabilise and precipitate before their LREE counterparts, a process that increases with increasing temperature.

The lack (or very low abundance) of separate LREE and HREE phases when precipitated from mixed REE solutions might suggest that natural REE carbonate mineral assemblages at low temperatures (< 170 °C) would contain mixed REE minerals, and at higher temperatures (> 170 °C) separate LREE or HREE minerals. Natural occurrences of tengerite-(Y) with lanthanite-(La) have been described (e.g. Nagashima et al., 1986), although it is more common that tengerite-(Y) is found associated with other Y-bearing carbonates, (e.g. decrespignyite-(Y), donnayite-(Y), caysichite-(Y), Y-rich bastnäsite - e.g. Wallwork et al., 2002). The occurrence of tengerite with lanthanite might, based on the current results, suggest separate mineralisation events from distinct REE-bearing fluids, although it is probably a result of the REE content of the fluids. The composition of the fluids from which these minerals were precipitated is not documented.

6.4.2 Comparison with synthetic REE carbonates

The synthesis of REE carbonates *via* solution mixing experiments was presented in Chapters 4 and 5, and has been well documented in the literature (e.g. Nagashima et al., 1973; Foger et al., 1992; Liu and Ma, 2007; Vallina et al., 2015). The phases produced in the previous chapters/those studies generally follow the rule that larger REE ions form lanthanites, then orthorhombic $REECO_3OH$, and finally hexagonal $REECO_3OH$, while the smaller REE ions form tengerite then orthorhombic kozoite-type phases. This is known to occur *via* the formation then breakdown of an initial X-ray amorphous precursor phase, the lifetime of which appears to be a function of Z. Although the results from the current chapter are consistent with those from Chapters

4 and 5 for the LREEs (i.e. both are well crystalline), those for HREEs and mixed HREE-bearing solutions are not (crystalline here, not there).

The reasons for Er and LREE + HREE mixed precipitates remaining X-ray amorphous in the titration experiments are currently unexplained, but the difference of HREEs (Er and Yb) in the titrations and dolomite experiments may be related to the rate at which CO_3^{2-} is introduced into the system. In the dolomite reactions, the rate of release is slower (i.e. controlled by the rate of dissolution), which would cause only a localised pH rise and supersaturation of the solution in relation to tengerite or orthorhombic $ErCO_3OH$. This process is likely to be more gradual (as the dolomite is relatively slowly dissolved) than the massive, solution-wide supersaturation of the titration experiments. What is unknown in these dolomite reactions, however, is whether the same X-ray amorphous phase forms at the dolomite surface immediately after dissolution - something impossible to prove from either the SEM or PXRD data (e.g. Figures 6.5, 6.7 and 6.9). If it does form, the slower localised supersaturation may provide enough time for this X-ray amorphous phase to breakdown/transform into tengerite before more is formed, allowing the tengerite crystals to grow. The same would apply to the unidentified Yb products.

6.4.3 A model for REE carbonate mineralisation

Combining the results/observations from natural occurrences, synthetic studies and the wall rock dolomite experiments, here a conceptual model for REE carbonate mineralisation as a consequence of wall rock dissolution is presented. Comparisons are made, and combined with, the results of some previous studies.

Until recently it had been thought that REEs were most likely transported as complexes with fluoride in ore-forming environments, which was based on thermodynamic data collected at room temperature and extrapolated to higher temperatures (e.g. Wood, 1990a; Haas et al., 1995). One study using those data was Ngwenya (1994), who invoked both REE-fluoride and hypothetical REE-CO_3-F complexes as transport mechanisms for REEs in hydrothermal fluids at the Tundulu carbonatite complex, Malawi. (The latter complex forming when the former reacted with the CO_3^{2-} released during the dissolution of ankerite, dolomite and/or calcite wall rocks.) This model presumably relies on the pH being low enough for the $REECO_3F$ complex not to precipitate as bastnäsite. The REE fluorocarbonate mineral that formed was suggested to be controlled by the composition of the wall rocks with which the REE-fluid reacted. Ca-bearing REE-fluorocarbonates were thought to form first as the hypothetical $REECO_3F$ complex reacted with dissolved calcium (from ankerite/calcite/dolomite dissolution - reaction 6.1), followed by bastnäsite ($REECO_3F_{(s)}$) formation (reaction 6.2) when Ca^{2+} and

H^+ were consumed (i.e. pH rise) as the fluid/rock ratio increased:

$$2\,\mathrm{REECO_3F_{(aq)}} + \mathrm{CaMg(CO_3)_{2(s)}} + \mathrm{H^+{}_{(aq)}} \longrightarrow \mathrm{REE_2Ca(CO_3)_3F_{2(s)}} + \mathrm{HCO_3^-{}_{(aq)}} + \mathrm{Mg^{2+}{}_{(aq)}} \quad (6.1)$$

$$\mathrm{REEF^{2+}{}_{(aq)}} + \mathrm{HCO_3^-{}_{(aq)}} \longrightarrow \mathrm{REE(CO_3)F_{(s)}} + \mathrm{H^+{}_{(aq)}} \quad (6.2)$$

These reactions highlight the importance of wall rock composition during hydrothermal mobilisation and deposition of REEs.

In the current study the REEs are transported not as complexes of fluoride, but of chloride. However, comparisons can be made because the supply of wall rock carbonate, and associated consumption of protons, is clearly the trigger for REE carbonate precipitation. Although the stability of REE chloride complexes has been shown to be lower than that of those with fluoride (e.g. Migdisov et al., 2009), the low and high solubility of REE fluoride and chloride solids, respectively, means that under a wide range of conditions the latter are more likely to be agents of transport, and the former of deposition. Although there are no measured data on REE carbonate complex stability at elevated temperatures (extrapolations from low temperature have been made, e.g. Haas et al., 1995), the results from the current investigation show that, under the conditions imposed, REE carbonate solids are of low enough solubility to precipitate. The reaction of REE-chloride complexes with the dolomite could be described thus:

First the dolomite is broken down, releasing carbonate:

$$\mathrm{CaMg(CO_3)_{2(s)}} + \mathrm{H^+{}_{(aq)}} \longrightarrow \mathrm{Ca^{2+}{}_{(aq)}} + 2\,\mathrm{HCO_3^-{}_{(aq)}} \quad (6.3)$$

with the soluble REE then reacting with the dissolved carbonate to form a REE carbonate solid:

$$\mathrm{REECl^{2+}{}_{(aq)}} + \mathrm{HCO_3^-{}_{(aq)}} + \mathrm{OH^-{}_{(aq)}} \longrightarrow \mathrm{REECO_3OH_{(s)}} + \mathrm{H^+{}_{(aq)}} + \mathrm{Cl^-{}_{(aq)}} \quad (6.4)$$

Equation 6.4 describes the precipitation of phases identified at all temperatures from solutions containing Nd, mixed Nd+Er, and the five REE mix, and also at > 130 °C from the Er solution. A similar reaction can be written for the products of the reaction between Er-chloride and dolomite at 90 and 130 °C:

$$\mathrm{REECl^{2+}{}_{(aq)}} + 3\,\mathrm{HCO_3^-{}_{(aq)}} + 2\,\mathrm{OH^-{}_{(aq)}} \longrightarrow \mathrm{REE_2(CO_3)_3 \cdot 2\,H_2O_{(s)}} + \mathrm{H^+{}_{(aq)}} + 2\,\mathrm{Cl^-{}_{(aq)}} \quad (6.5)$$

Although reaction 6.3 consumes protons (i.e. the solution is buffered by carbonate),

both reaction 6.4 and 6.5 are proton producing, and therefore promote further dolomite dissolution. The reactions above suggest the local pH of solution is alkaline where precipitation of REE carbonates is occurring, but the production of protons sustains the dolomite dissolution.

The pH of the solutions was not measured after the reaction with dolomite. However, there is clear evidence in the SEM images of extensive dolomite dissolution (heavily pitted surfaces).

Given the release of dissolved Ca^{2+}, Mg^{2+} and CO_3^{2-} into the solution during dolomite dissolution, and the low concentration/absence of Ca in the neo-formed REE carbonates, it might be expected that secondary calcite/dolomite would precipitate once the REEs were consumed, however, the there is no evidence for this in the SEM images. This is probably explained by the low pH and very high REE concentrations in the initial solutions, i.e. that there is insufficient carbonate dissolution to buffer the pH or precipitate all the soluble REEs. It is likely, therefore, the Ca and Mg are in solution as free ions, or possibly as chloride complexes given the high Cl content, further supporting an acidic solution pH.

The results for the Nd and Er samples suggest transformation from one phase to another, a process that appears to be controlled by temperature. In the case of Nd, the identification of both kozoite and hydroxylbastnäsite represents a transformation from the orthorhombic to hexagonal system. A recent solubility study of kozoite-(Nd) and hydroxylbastnäsite-(Nd) (Voigt et al., 2016) has shown, at least at 25 °C, that the former is less stable than the latter. This is likely the reason why, in the Nd-only solutions, kozoite is more abundant at the lower temperatures and hydroxylbastnäsite becomes more important at the highest ones, presuming the data of Voigt et al. (2016) can be accurately extrapolated to higher temperatures (clearly a big 'if').

Natural kozoite has only been described from a few occurrences, while hydroxylbastnäsite is more common but still rare. The results of the wall rock experiments would suggest that, in LREE dominated fluids, kozoite is only stable at temperatures < 170 °C (probably lower), and results from Chapters 4 and 5, and previous works, point to a lower stability limit in the region of 100 °C (i.e. below this lanthanite is more common, e.g. Nagashima et al., 1973; Vallina et al., 2015). Such a small temperature window may account for its scarcity in natural systems. However, it is also important to note that in natural systems there will almost certainly be other cations in solution, which may result in the precipitation of other REE carbonate minerals (ancylite or burbankite) or carbonates (e.g. ankerite). Additionally, the presence of even small concentrations of fluoride will see the LREE precipitating as REE fluorocarbonates, not carbonates (Hsu, 1992). This is explored in more detail in Chapter 7.

In the case of Er, the transition from tengerite to $ErCO_3OH$ represents a dehydration reaction, a process that occurs between 130 and 170 °C under the conditions of this study. Natural tengerite is also a very rare mineral, and natural orthorhombic $ErCO_3OH$ has not been described, nor has its hexagonal form. The results of the current investigation have shown that HREE carbonates other than tengerite are feasible during HREE- and mixed REE-bearing solution reactions with dolomite, but unfortunately there exists no solubility studies on natural or synthetic tengerite, or the synthetic HREE-bearing carbonates.

One observation that can be made from the current work is that the stability of the kozoite-type phase is increased by the presence of more than one REE in solution (i.e. hydroxylbastnäsite forms at the higher temperatures in Nd-only experiments but not in mixed-REE solutions). Although this phenomenon was observed in the current results, it is unlikely to occur in natural systems because of the relatively higher abundances of LREEs in hydrothermal fluids. In most natural settings, particularly those associated with carbonatite deposits, fluids are LREE enriched, and as a result, so are the REE minerals found associated with them (e.g. Chakhmouradian and Wall, 2012). The results in this chapter suggest that, if present in high enough concentrations, REE carbonate minerals with appreciable HREEs could form.

At the highest temperatures in the five REE mixed solution there are discrete LREE and HREE enriched phases. Although not conclusive from the SEM images (Figures 6.11d - g), these may form by the recrystallisation of earlier-formed, five REE-bearing phases. The stability of REE chloride complexes has been shown to vary across the series, with LREEs more stable than HREE at 200 - 250 °C, but similar at 150 °C (e.g. Migdisov et al., 2009). Using this information, the following crystallisation model for these five REE solutions/carbonates may be applicable: a kozoite-type mineral forms first, containing all five REEs, which occurs at temperatures where the stability of REE chloride complexes is roughly equal across the series. Then, as the temperature is increased, the kozoite phase dissolves as it is no longer stable, releasing the REEs back into solution. REE complexes with chloride may then differ in stability, resulting in fractionation of LREEs and HREEs into separate solid phases. However, this model may be contested based on the observation of the amorphous-looking material in Figures 6.11f and g, as this would imply that an amorphous phase is forming after the precipitation of the crystalline phases - something not supported by any previous work on crystallisation pathways. However, the crystallinity of the 'fluffy' looking phase in Figures 6.11f and g cannot be confirmed, and therefore, nor can this potential model. This model would explain the low abundance of HREE phases relative to the LREE ones (especially Figures 6.11d and e) if the levels of original kozoite-type phase dissolution is only in its early stages. However, without data on the solubility of the

mixed-REE carbonate phase(s), or the identity/structure of the HREE-spheres, it is impossible to accurately determine the mobility of REEs under the experimental conditions of this study.

An alternative theory, which is more aligned with the results presented in the previous chapters, is that a kozoite-type phase forms at the lower temperature (130 °C) that contains a higher proportion of LREEs than HREEs. The EDS data for Figure 6.11a does suggest this, as do the additional five analyses taken for the other examples precipitated at this temperature (not shown). This would, therefore, imply that the solution is left enriched in HREEs relative to the early formed precipitates (the elongated rhombic prisms), and that the solubility of HREE-enriched spheres seen at the higher temperatures is greater at lower temperatures (i.e. they possess retrograde solubility). As the temperature is increased the HREE-rich spheres begin to form, possibly *via* the transformation of the HREE-enriched amorphous looking material in Figure 6.11f and g? This model would also explain the low abundance of HREE-enriched phases relative to LREE ones, however, this could only be confirmed if the temperatures used in the current investigation were taken beyond the upper boundary used (i.e. $>$ 200 °C). Again, solubility data on these phases would be required to prove this model, particularly that the HREE-enriched phases do indeed exhibit retrograde solubility.

6.5 Chapter conclusions

It has been shown that, in solutions with significant soluble REEs and high chloride concentrations, reaction of these solutions with dolomite at temperatures from 90 to 200 °C results in the precipitation of REE carbonate solids, mostly low in or devoid of calcium. Most of the minerals precipitated are known from nature, although one has only been documented in the lab, and the products of Yb experiments have not been observed before. Products from mixed REE solutions were found to behave differently to those from single REE-bearing solutions, with a seeming preference for retaining the structure of a naturally LREE phase (i.e. remaining as kozoite type, not the hexagonal equivalent, even at the highest temperatures).

Comparisons of products from dolomite dissolution and direct mixing/titration experiments reveal discrepancies in their crystallinity (at least for the preparation methods covered). These are explained by the differences in the rate at, and extent to which, the solutions are buffered to high(er) pH, and the rate at which supersaturation with respect to the solid phases are reached. The massive, solution wide increase in pH experienced during solution mixing results in immediate precipitation of an X-ray amorphous material, that crystallises easily with LREEs, but is more difficult with HREEs. This is not the case in the dolomite experiments, where excellent crystallisation is observed

under all conditions except at 90 °C for Yb-only solutions. This would suggest that slow addition of dissolved carbonate, which would produce only local supersaturation with respect to the solid, is important in precipitating carbonates containing HREEs (or mixed L- and HREEs).

The current lack of thermodynamic data for end-member and mixed REE carbonates makes evaluation of a REE's mobility in hydrothermal systems impossible, and should be a future research target. However, the data presented here provides empirical evidence for the importance of wall rock dissolution on the precipitation of REE carbonates from high salinity, high REE concentration solutions, and also the influence that mixed-REE solutions have on the properties/behaviour of those solid phases.

Chapter 7

REE fluorocarbonate synthesis *via* wall rock reactions, and a textural and mineralogical study of two natural carbonatites

7.1 Introduction

The hydrothermal origin/upgrading of many large REE deposits requires transport and deposition mechanisms capable of accumulating appreciable quantities of these metals. In the introduction to Chapter 6, the role of wall rocks in providing CO_3^{2-} and Ca^{2+} for the precipitation of soluble REEs – as proposed by previous authors (e.g. Ngwenya, 1994) – was highlighted, and the results showed this to be a plausible mechanism for almost every experimental condition. However, in the study of Ngwenya (1994) and the majority of others focussed on REE deposit genesis, the identified REE minerals are more commonly fluorocarbonates than carbonates (e.g. Benaouda et al., 2017; Broom-Fendley et al., 2017; Giebel et al., 2017; Mikhailova et al., 2017; Duraiswami and Shaikh, 2014; Rasoamalala et al., 2014; Ruberti et al., 2008).

The system therefore obviously requires fluoride, which in most relevant literature was suggested to be in the form of soluble REE fluoride complexes (e.g. Ngwenya, 1994; Salvi and Williams-Jones, 1996; Smith and Campbell, 2000; Ruberti et al., 2008)). As previously discussed in this thesis, these complexes were thought to be the main transport mechanisms for the REEs because of their increased stability as compared to e.g. REE chloride complexes (e.g. Wood, 1990a; Haas et al., 1995). The soluble complexes then become destabilised as the physiochemical conditions of the fluid change, e.g. an increase in pH resulting from fluid mixing or dissolution of carbonate wall rocks, often promoting metal deposition. The REEs, fluoride and carbonate would then precipitate

as fluorocarbonate minerals, leaving the fluid undersaturated with respect to that mineral. However, recent work has called into question the ability of REE fluoride species to transport appreciable concentrations of these metals, as large parts of their stability fields overlap with those of REE fluoride and fluorocarbonate minerals (e.g. Migdisov et al., 2009; Migdisov and Williams-Jones, 2014; Migdisov et al., 2016). Although there is limited data on the solubility of these phases, they are known to be highly insoluble, and some exhibit temperature retrograde solubility (Migdisov et al., 2009; Voigt et al., 2016; Shivaramaiah et al., 2016). This temperature-retrograde solubility is the major impediment to experimental studies of REE transport in the presence of fluoride.

Considering recent complex stability and mineral solubility data, the current understanding for REE transport in hydrothermal fluids is they are mobile primarily as chloride species (Migdisov and Williams-Jones, 2014). REE chloride solids are highly soluble, and as such REE chloride species do not encounter the same deposition issues as fluorides. Ore-forming fluids are thought to contain small amounts of fluoride in the form of HF^0, which dissociates as the pH rises. This then makes fluoride available, moves the chemistry of the fluid into the stability field of the common fluoride and fluorocarbonate minerals, and causes their precipitation. It is therefore envisioned that, for example, the dissolution of a carbonate-rich rock (as previously proposed), may be the trigger for REE fluorocarbonate mineralisation. The uncommon occurrence of REE fluoride minerals (e.g. fluocerite - $REEF_3$) in comparison to fluorocarbonates suggests differences in the stability of complexes in the presence of, or formed with, carbonate, and/or differences in the solubility of the aforementioned minerals. Unfortunately, data on REE carbonate complexes at elevated temperatures do not currently exist, and solubility data are scarce.

The common occurrence of bastnäsite ($REECO_3F$) may suggest it is more stable than fluocerite under ore-forming conditions, and the number of documented cases of REE fluorocarbonates associated with either REE fluorides or REE carbonates is limited (e.g. Savel et al., 2011; Gysi and Williams-Jones, 2013; Graupner et al., 2015). Recent studies have modelled the reaction of a REE-, fluoride- and NaCl-bearing fluid with dolomite at around 300 °C (Trofanenko et al., 2016; Migdisov et al., 2016), with results suggesting immediate precipitation of bastnäsite or parisite, depending on the activities of REE^{3+} (controlled by pH), Ca^{2+} and $CO_3{}^{2+}$ (suggested as being controlled by wall rock dissolution or fluid mixing), and F^- (controlled by pH and the solubility of REE fluoride solids). Under the modelled conditions, REE fluorides were subordinate to fluorocarbonates.

Following the successful precipitation of REE carbonates *via* wall rock experiments in Chapter 6, here the results of a small number of batch reactions between REE chloride solutions and pellets made from dolomite and fluorite, conducted at 90 °C, are

presented. The low (and retrograde) solubility of REE fluoride solids, and the high REE concentrations required for sufficient yield in the experiments, precluded the use of soluble REE fluoride solutions at the temperatures used in this investigation. Therefore, a convenient way of introducing fluoride was to use fluorite as an additional wall rock, and continue using dolomite and the REE chloride solutions to see whether a fluorocarbonate would form. The products from these experiments, combined with those from the previous chapters, were compared to the mineralogy of two natural carbonatites previously described in the literature: Tundulu, Malawi, and Bayan Obo, China. The former is the site at which Ngwenya (1994) made his original observations of REE fluorocarbonate species dependence on the composition of the wall rocks, and at which more recent work has been carried out (Broom-Fendley et al., 2016). The latter site has been the subject of hundreds of studies, but its paragenesis is far more complex, showing evidence for multiple REE mineralisation events and textural relationships indicating reaction between REE fluorocarbonate, REE phosphates, dolomite and apatite (e.g. Smith et al., 1999, 2015).

The textures between REE minerals and their hosts were studied at both sites, with the aim of identifying any evidence for the composition/dissolution of wall rock (especially carbonate) controlling/being linked to the type of REE mineralisation. One of the two deposits, Bayan Obo, China, is also known to have been heavily fluoritised, and although the method of fluorocarbonate formation via dissolution of carbonate and fluorite (as in the experiments) is not a previously suggested model, these thin sections were also studied for this scenario (although it is stressed again the use of fluorite was an experimental necessity).

In this chapter, the results of dolomite + fluorite pellet experiments are presented first, and are followed by the EMPA results of Tundulu and Bayan Obo samples. Background geology on the two deposits will be reviewed in the next section, before the methods and results are presented.

7.2 Background geology and paragenesis of Bayan Obo and Tundulu

Samples form Bayan Obo and Tundulu were chosen for several reasons: both contain REE fluorocarbonate minerals (including Ca- or Ba-bearing species), both are carbonatite deposits and so contain abundant carbonate minerals, and both show evidence of hydrothermal alteration, thereby providing a link to the wall rock experiments in the current and previous chapter.

7.2.1 Bayan Obo

The following information is based upon the findings of Smith and Campbell (2000), Kynicky et al. (2012), Lai and Yang (2013), Ling et al. (2013), Smith et al. (2015) and Yang et al. (2017).

Discovered in 1927, the Bayan Obo deposit is located on the northern edge of the North China craton, in Inner Mongolia, China. With resource estimates of 48 mT at 6 wt.% and 750 mT at 4.1 wt.% REE_2O_3, Bayan Obo is currently the world's largest REE source. It also contains estimated resources of 1500 mT Fe (at 35 wt.%) and 2.2 mT Nb (at 0.13 wt.%). The deposit is contained within the Proterozoic Bayan Obo group, which is made up of low-grade metamorphosed sandstones, siltstones, dolomites and limestones. The Bayan Obo group is split into members H1 to H9, with the H8 dolomite marble playing host to the major REE mineralisation. The orebodies are located in the core of an anticline, which includes several thrust, shear and chevron folds. The orebodies contain numerous large fractures, suggested as possible channels for fluids leading to banding (see below). The genesis of the H8 dolomite marble is disputed, with suggestions of both a sedimentary and igneous origin, although combined data seems to suggest the intrusion of carbonatitic magma (1.3 Ga) into earlier (meta)sedimentary marble (1.6 Ga). A geological map of the area is shown in Figure 7.1.

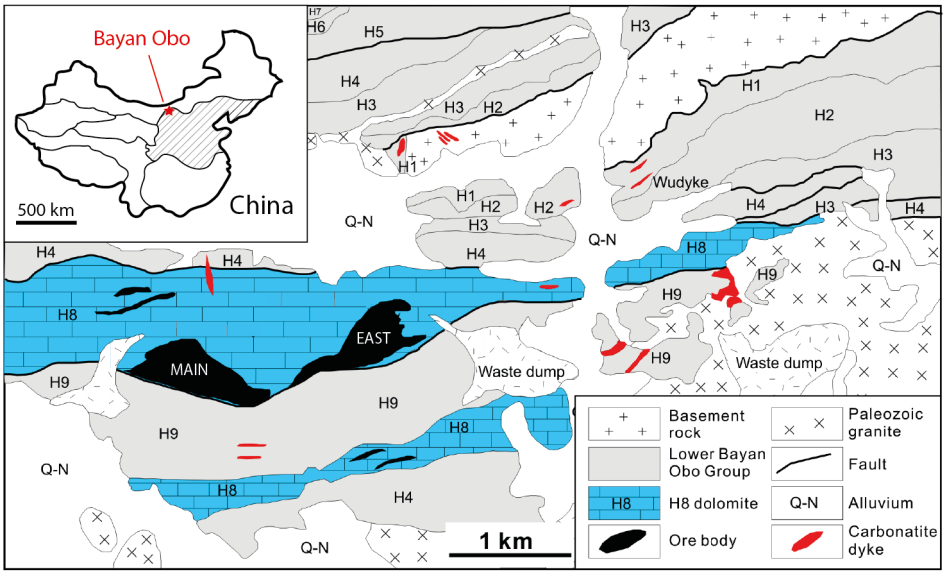

Figure 7.1: Geological map of the Bayan Obo deposit and surrounding area. The H8 dolomite is highlighted in blue, and the ore bodies are in black. The samples analysed in this study were from the Eastern and Main orebodies; the Western orebody is located about 4km to the west of the main orebody, off the map. Map modified from Ling et al. (2013).

The most important mineralisation at Bayan Obo is Fe-REE-Nb dominated, and is concentrated into three main orebodies (Main, Eastern, Western). Much of the Fe mineralisation formed early in the history of the deposit and was metasomatised dur-

ing later REE-Nb mineralisation, which is thought to have formed in two periods (1.3 – 1.0 Ga and 0.5 – 0.4 Ga). REE mineralisation is mostly in the form of REE fluorocarbonates (bastnäsite), REE-Ca fluorocarbonates (e.g. synchysite, parisite), REE-Ba fluorocarbonates (e.g. huanghoite) and monazite, although at least 30 different REE minerals have been described. Dolomite is the main host for REE mineralisation in the Western orebody, while magnetite-hematite is more important in the other two; the highest REE content is found in dolomite ore of the Main orebody. Unfortunately, none of the samples obtained for the current study were from the dolomite-rich Western orebody, but instead sampled the Main and Eastern orebodies (hence omission of the former from the geological map).

Two broad alteration types have been identified: one is F-Na metasomatism, which resulted in widespread fluoritisation (F-metasomatism), and aegirine and riebeckite replacement of dolomite (Na-metasomatism); the second is metasomatic alteration in the form of veins filled with aegirine, riebeckite, apatite and various sulfides (e.g. pyrite, sphalerite, pyrrhotite). The Western orebody is less fluoritised and contains lower overall concentrations of REE and Nb, as compared with the other two, more massive orebodies.

The overall paragenesis of REE mineralisation has been suggested to comprise up to 11 different stages, with examples occurring across the mining region and in different places within each orebody (i.e. some are not exposed at the surface due to faulting and folding). Mineralisation occurs as disseminated, massive and banded ores. A simplified version (Figure 7.2) has the earliest REE minerals occurring as disseminated monazites intergrown with ferroan dolomite that formed in fractures and along grain boundaries of the host marble. The main stage of mineralisation is in the form of massive and strongly banded (mm to decimetre) iron ore (magnetite) and REE mineralisation composed of monazite, bastnäsite, with gangue apatite and aegirine, followed by alkali amphiboles (e.g. riebeckite) and fluorite. Earlier bastnäsite was in places altered to Ca-REE fluorocarbonates by later fluids (presumably Ca-rich - although this is not explicitly stated). Banded ores are then cut by veins of aegirine, calcite, fluorite and bastnäsite. Widespread fluoritisation of the ore is thought to have occurred next, and the final stages of significant mineralisation involved the deposition of barite, alteration of Ca-REE fluorocarbonates to Ba-REE fluorocarbonates (e.g. huanghoite) and Nb mineralisation (e.g. as aeschynite and pyrochlore). The reaction textures between monazite, bastnasite, calcite, fluorite and apatite has been previously studied (Smith et al., 1999), and will be mentioned again later. The multiple stages of hydrothermal fluid influx and metasomatism make the paragenesis of this deposit very difficult to decipher, and are likely the reason for the large REE enrichment of this deposit.

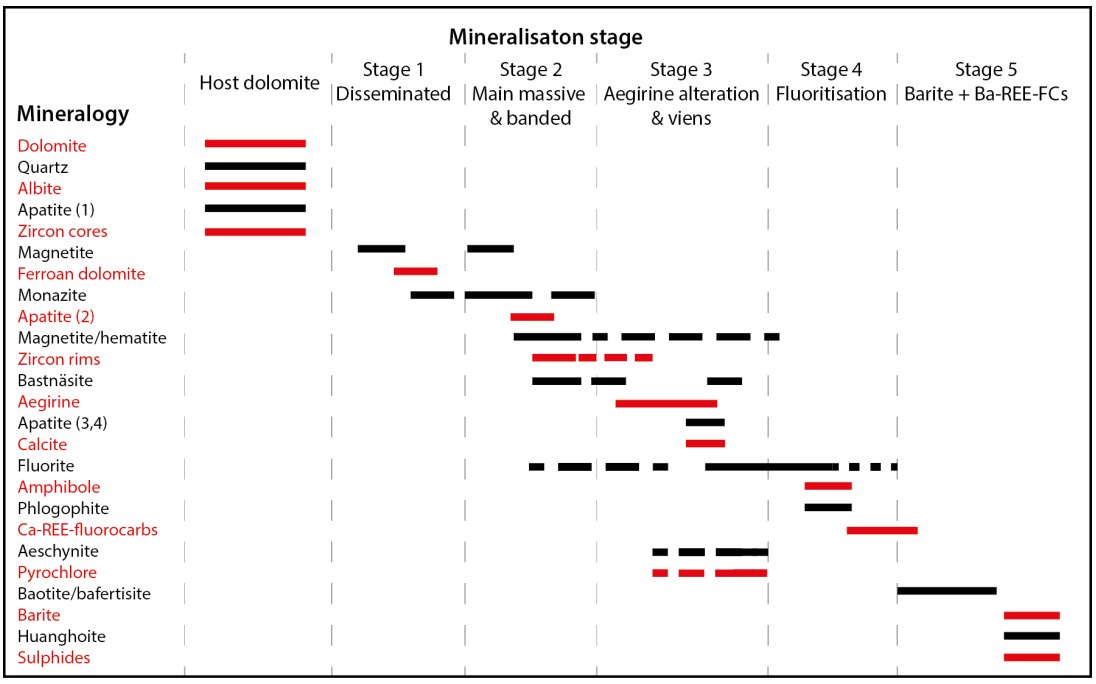

Figure 7.2: Summary paragenetic sequence for the mineralisation at Bayan Obo (redrawn from Smith et al., 2015.

7.2.2 Tundulu

Although the number of published works on Tundulu is far fewer than for Bayan Obo, there are examples in which the textural relationships between REE minerals and their host rocks were studied in detail. The background information for this is based upon the findings of Ngwenya (1994) and Broom-Fendley et al. (2016), and references therein. A geological map and aerial image of the Tundulu deposit are shown in Figure 7.3.

The Tundulu carbonatite is part of the Chilwa Alkaline Province, Malawi, about 1 km east of the border with Mozambique and 2 km south of Lake Chilwa. The deposit is composed of three ring structures, the mineralogy of which varies: calcite carbonatites occur in rings 1 and 2, apatite-rich calcite carbonatites in ring 2, quartz-apatite carbonatites in ring 2, and ankerite carbonatites in rings 2 and 3. Ring 3 also contains alkaline intrusions altered by calcitic and ankeritic fluids.

The REE mineralogy at this deposit is dominated by REE fluorocarbonates and Ca-REE fluorocarbonates, with lesser REE phosphates (e.g. monazite and rhabdophane – $REEPO_4 \cdot H_2O$). Apatite has also been found to be a major host to REEs, with total concentrations reaching up to 20,000 ppm, enhanced through dissolution-precipitation reactions.

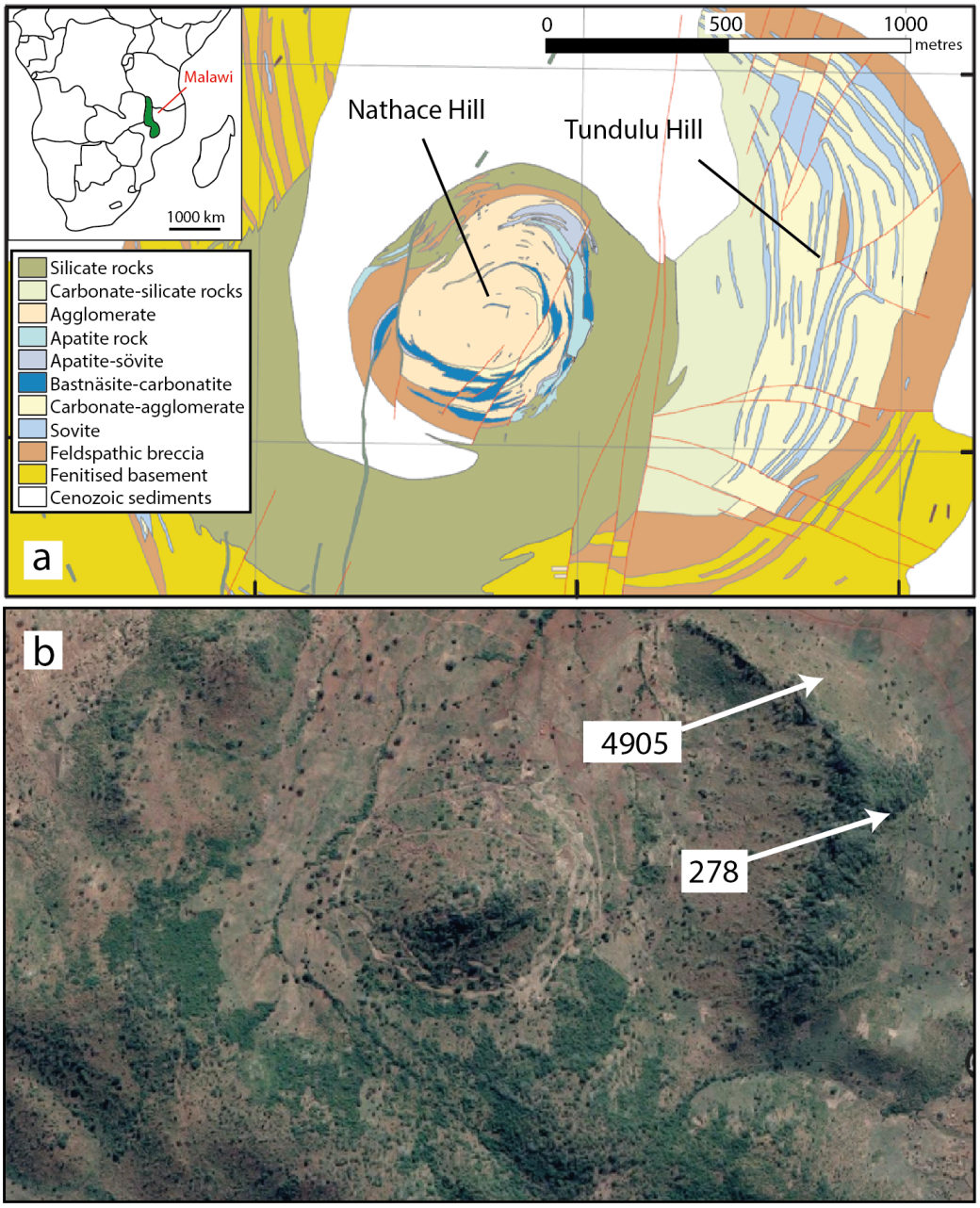

Figure 7.3: a) geological map of the Tundulu deposit (modified from Broom-Fendley et al., 2016); b) aerial image of the same area, including the sites at which the two samples used in the current study were collected (image taken from Google Maps).

Based on textural and compositional evidence, Ngwenya (1994) suggested that the supply of Ca^{2+} and CO_3^{2-} from the dissolution of carbonate wall rock of different composition controlled the species of REE fluorocarbonate that formed. This then led to a general paragenesis of REE fluorocarbonates precipitating before apatite (in the apatite or 'silicified' carbonatites), and terminating with quartz. However, recent work reassessing the textural relationships now points to apatite has having formed prior to REE fluorocarbonates, with quartz and minor calcite groundmass forming the terminating stages of mineralisation (shown in Figure 7.4). This updated paragenesis does not affect the suggestion that wall rock carbonate composition controls the REE fluorocarbonate to form because both models have the REE mineralisation postdating the bulk of carbonates These observations, plus the mineralogy of Bayan Obo (i.e. dolomite and fluorite) provide the framework for experiments on synthesising fluorocarbonates in this chapter, details of which are given below.

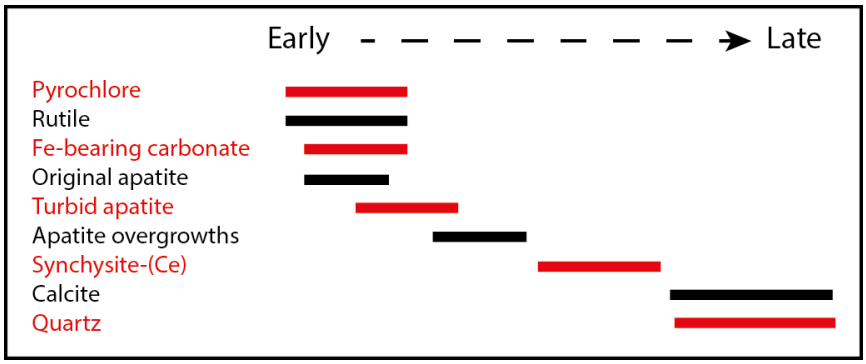

Figure 7.4: Summary paragenetic sequence for the Tundulu deposit (redrawn after Broom-Fendley et al., 2016.

7.3 Materials and methods

This section contains details on the experimental setup used in REE fluorocarbonate synthesis and the techniques used to characterise them, followed by the techniques used to characterise the thin sections.

7.3.1 Experimental studies

Following the theme of the wall rock reactions in Chapter 6, a further set in which the fluoride ion was a component were designed. As highlighted in the introduction, and throughout this thesis, REE fluorides are highly insoluble and therefore working with dissolved REE fluoride complexes, particularly at the temperatures investigated presently, is practically impossible. In response to these difficulties, the idea of using fluorite as the fluoride source was tested with a preliminary experiment involving a small chip each of dolomite and fluorite, reacted with Nd chloride at 90 °C. The results

of this were localised mineralisation of fluorcerite (i.e. NdF_3) on fluorite, and kozoite on dolomite. It was obvious that the dissolution-precipitation reactions were occurring at the surface of the respective chips, and that therefore the two needed to be more intimately associated. To achieve this, 0.15 g each of fluorite and dolomite were crushed together in a mortar and pestle, with the resultant mix made into a pellet by compression in a pin press by a hydraulic press, as described in Chapter 3.

A total of six experiments were run, each at 90 °C for five days (the experimental matrix is shown in Table 7.1). 10 ml of either single or multi-REE bearing solutions were used, and the concentration of each REE chloride was 0.02 M. The solutions and pellets were placed into 20 ml serum bottles that were bunged with butyl rubber stoppers and crimped shut. The experiments were run concurrently in the same oven. After five days the products were filtered on 0.45 μm mixed cellulose filters using a vacuum pump, washed repeatedly with deionised water and left to air-dry, as with all previous experiments.

REE	**Temp (°C)**	**Time (days)**	**REE conc (M)**
La	90	5	0.02
Nd	90	5	0.02
Er	90	5	0.02
Yb	90	5	0.02
La+Er	90	5	0.02
La+Yb	90	5	0.02

Table 7.1: Experimental conditions during the attempted synthesis of REE fluorocarbonates. In the mixed REE solutions, the concentration of each REE was 0.02 M.

An aliquot of each sample was characterised by SEM, and another was crushed in a mortar and pestle and analysed by PXRD. During EDS analyses of these samples on the SEM, the data was unreliable (totals were only around 30 %), and as such EDS data has been omitted from the relevant figures (see results below). The operating conditions of these instruments were the same as reported in the methods section of Chapters 4 and 6.

7.3.2 Natural sample characterisation

Samples from Tundulu were loaned from Dr Sam Broom-Fendley, who had collected them over two field seasons between 2011 and 2012. The 19 samples were a mix of rocks and polished thin sections. After reviewing the enclosed textural and chemical notes and data, several new polished thins were made (at the UoE). Six were studied

using optical microscopy (Nikon SMZ800 Stereo microscope equipped with a DFC 420C camera) as a first pass on mineral identification, and was followed by qualitative identification by secondary electron (SE) and back scattered electron (BSE) SEM, including EDS. The operating conditions were as previously reported in Chapters 4 and 6. Two of these were subsequently chosen for detailed analysis on the EMPA, based primarily on the large quantities of REE fluorocarbonates and carbonate minerals (calcite/dolomite).

The 13 samples from Bayan Obo were borrowed from the Natural History Museum, London. The samples were a mix of rocks and polished thin sections, although the collection of the latter did not represent the full set of the former. Therefore, polished thins for those rocks missing one were made, and all 13 were subsequently reviewed by optical microscopy. Four were then analysed by SEM with EDS. Several of the pre-made thin sections had been previously analysed and their results published (e.g. Smith et al., 1999; Smith and Campbell, 2000), so these were omitted from the current EMPA work; two other samples with high REE contents (from EDS analyses) and large amounts of fluorite (because of the use of this mineral in the experiments) were chosen instead. All polished thin sections used in EMPA analyses were cleaned in an ultrasonic bath before being carbon coated.

Quantitative chemical compositions of bastnäsite, synchysite, huanghoite, monazite, carbonates, fluorite and apatite were determined by EMPA using wavelength-dispersive spectrometer analyses on a Cameca SX1000 electron probe microanalyser (UoE), operating at an accelerating voltage of 20 kV. The beam current was between 1 and 40 nA for major elements and 40 and 100 nA for trace elements, and count times ranged from 20 and 150 seconds depending on the mineral being analysed. Background counting times were typically half that at peak. The beam diameter was between 3 and 5 μm. A range of natural and synthetic samples were used as standards: all the REEs were calibrated using synthetic in-house (UoE) prepared REE phosphates (REEPO4). Other elements were calibrated using the following standards: synthetic fayalite (Fe); synthetic thorium oxide (Th); synthetic Mg-Al spinel (Mg); a pure manganese standard (Mn); natural wollastonite (Ca); Durango apatite (P, F); and natural celestite (Sr). Where measured, fluorine was analysed first to avoid beam-induced element migration. Detection limits for each element varied depending on the mineral being analysed (Table 7.2). When the data was processed there was a systematic Gd spike in all four samples, and as such data for this element has been omitted from the results. Full datasets (including the Gd data) can be found in Appendix A.

The structural formulae of each mineral of interest was calculated by the following procedure (taken from the appendix Deer et al., 2013):

	Synchysite n=21	**Bastnäsite** n=16	**Monazite** n=11	**BaREEFC** n=8	**Apatite** n=29	**Dolomite** n=16	**Fluorite** n=18
F	0.15	0.10	na	0.12	0.42	na	0.31
Mg	0.01	0.01	na	0.01	na	0.08	na
Si	na	na	0.01	na	na	na	0.01
P	na	na	0.02	na	0.10	na	na
Ca	0.05	0.00	0.00	0.00	0.10	0.10	0.12
Mn	na	na	na	na	0.02	0.02	na
Fe	na	na	na	na	0.03	0.02	na
Sr	na	na	na	na	0.02	na	na
Ba	na	na	na	0.34	na	na	na
Y	0.02	0.02	0.02	0.02	0.02	0.01	0.02
La	0.16	0.17	0.06	0.02	0.03	0.02	0.03
Ce	0.17	0.18	0.06	0.56	0.03	0.02	0.03
Pr	0.07	0.07	0.06	na	0.08	0.05	0.08
Nd	0.06	0.06	0.13	0.06	0.08	0.05	0.08
Sm	0.07	0.07	0.06	0.07	0.08	0.05	0.08
Eu	0.06	0.07	0.04	na	na	na	0.07
Gd	0.03	0.03	0.03	0.03	0.04	0.02	0.04
Tb	0.06	0.07	0.04	0.07	na	na	0.09
Dy	0.07	0.07	0.04	0.07	0.07	0.05	0.08
Er	0.06	0.06	0.05	0.06	0.08	0.04	0.08
Yb	0.09	0.09	0.05	0.09	0.10	0.06	0.10
Th	na	na	0.08	na	na	na	na

Table 7.2: Detection limits (weight %) for each element in each of the minerals analysed *via* EMPA. na = not analysed

1. Divide the wt.% of each oxide by the molecular weight of that oxide (if fluorine is present, divide by its atomic weight, 19). This expresses the molecular proportions of each oxide;

2. Multiplying the calculated value from step 1 by the number of oxygen atoms in the oxide (if including fluorine, multiply this by 1);

3. Sum all the values from 3 (i.e. sum of all oxides). If fluorine is present, the value used during summing should be half that calculated from step 2;

4. Divide the value from step 3 by the number of oxygen atoms the structural formula is being calculated to (e.g. 4 O for fayalite, Fe_2SiO_4);

5. Multiply the value for each oxide in step 2 by the value obtained from step 4;

6. Finally, multiply the value from step 5 by the value obtained by dividing the number of cations by the number of oxygen atoms for each of the oxides (e.g. Al_2O_3 = value in step 5 multiplied by 2/3).

In this study, the structural formula of each mineral was calculated to 7 O atoms (synchysite and huanghoite), 4 O (bastnäsite and monazite), 6 O (dolomite), 3 O (calcite) and 12.5 O (apatite).

Backscattered and secondary electron images were also taken at each of the sampling sites, the former for imaging purposes and the latter to clearly identify the position of the spot analysis (i.e. identify any contamination from analyses overlapping other minerals).

The REE concentration values were normalised, as per convention, here using the chondrite values of McDonough and Sun (1995).

7.4 Results and discussion

7.4.1 Batch reactions

PXRD spectra of the products from all six REE fluorocarbonate experiments are presented in Figure 7.5, and the SEM images are split between Figures 7.6 (single-REEs) and 7.7 (multi-REEs).

The PXRD results suggest different behaviour between each REE, and between the single- and mixed-REE solutions, as in previous chapters. A fluorocarbonate (bastnäsite) was only identified in one of the four single-REE solutions (Nd), but interestingly was found in both mixed-REE experiments (La+Er and La+Yb). Although the reflections for the calcium-REE fluorocarbonates (e.g. synchysite and parisite) are similar to bastnäsite, neither of these phases were detected. PXRD of the Er sample showed this element to be the only one for which the sole product was a REE carbonate (tengerite). In the La- and Yb-only experiments, only REE-fluorides were detected. However, in both cases the presence of a Ca-bearing REE fluoride cannot be ruled out because the reflections for Ca-REE fluoride and REE fluoride are the same

Consultation of the SEM (and EDS) data was therefore necessary, however, as the phases of interest contain Ca, C, O and F, and the reactants also contain these elements, it is very difficult to be certain that a phase is, for example, a REE carbonate associated with fluorite, or a REE fluorocarbonate, or even Ca-fluorocarbonate. The interpretation of the EDS data, and therefore the proposed minerals, are subject to caution.

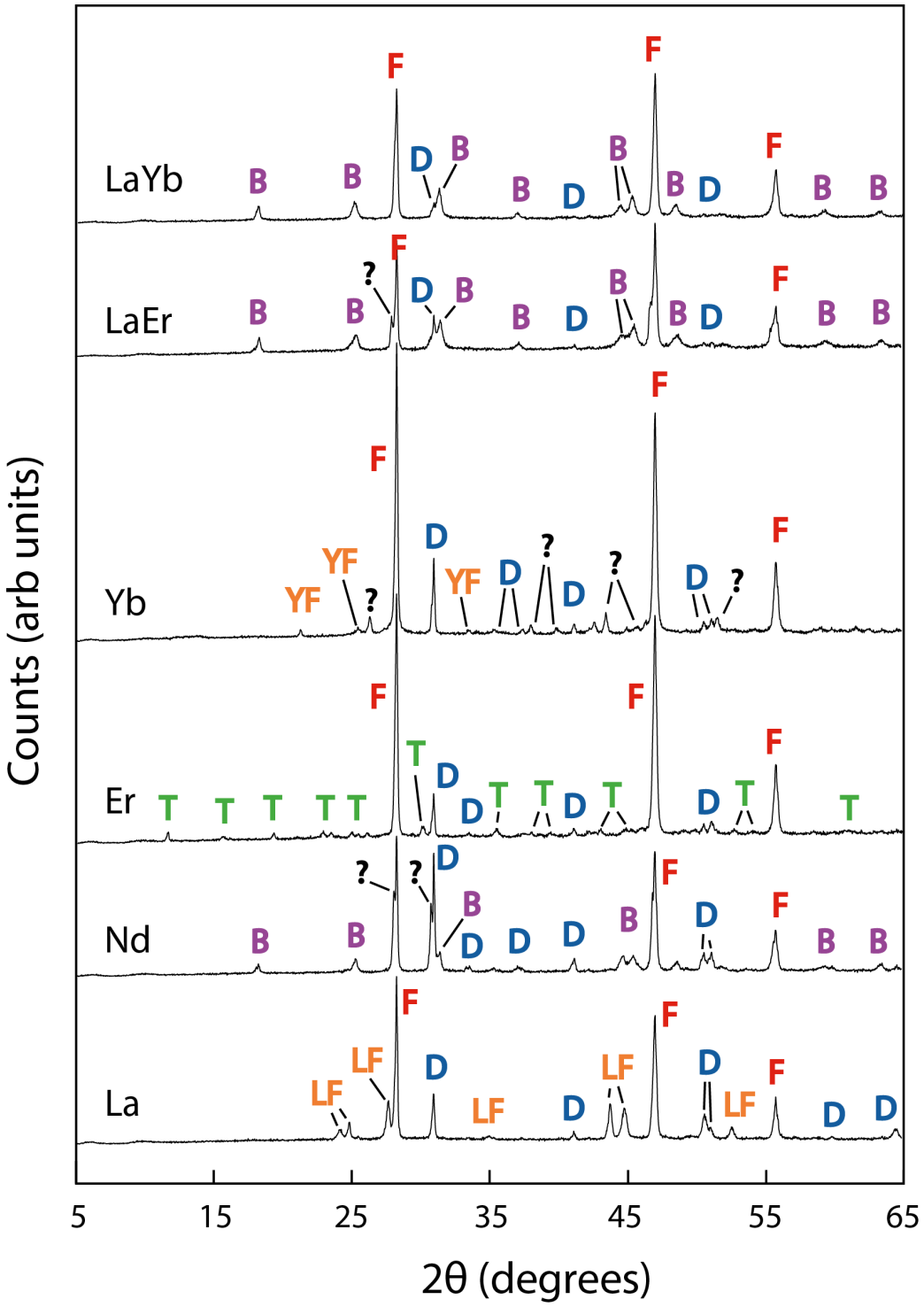

Figure 7.5: PXRD traces for the products of reaction between dolomite + fluorite pellets and REE-bearing chloride solutions. In all samples there is contamination by fluorite (F) and dolomite (D), the main peaks of which were useful for alignment of spectra. LF = lanthanum fluoride; B = bastnäsite; T = tengerite; YF = ytterbium fluoride (potentially also calcium ytterbium fluoride); ? = Bragg peaks not indexed to any phase in the database.

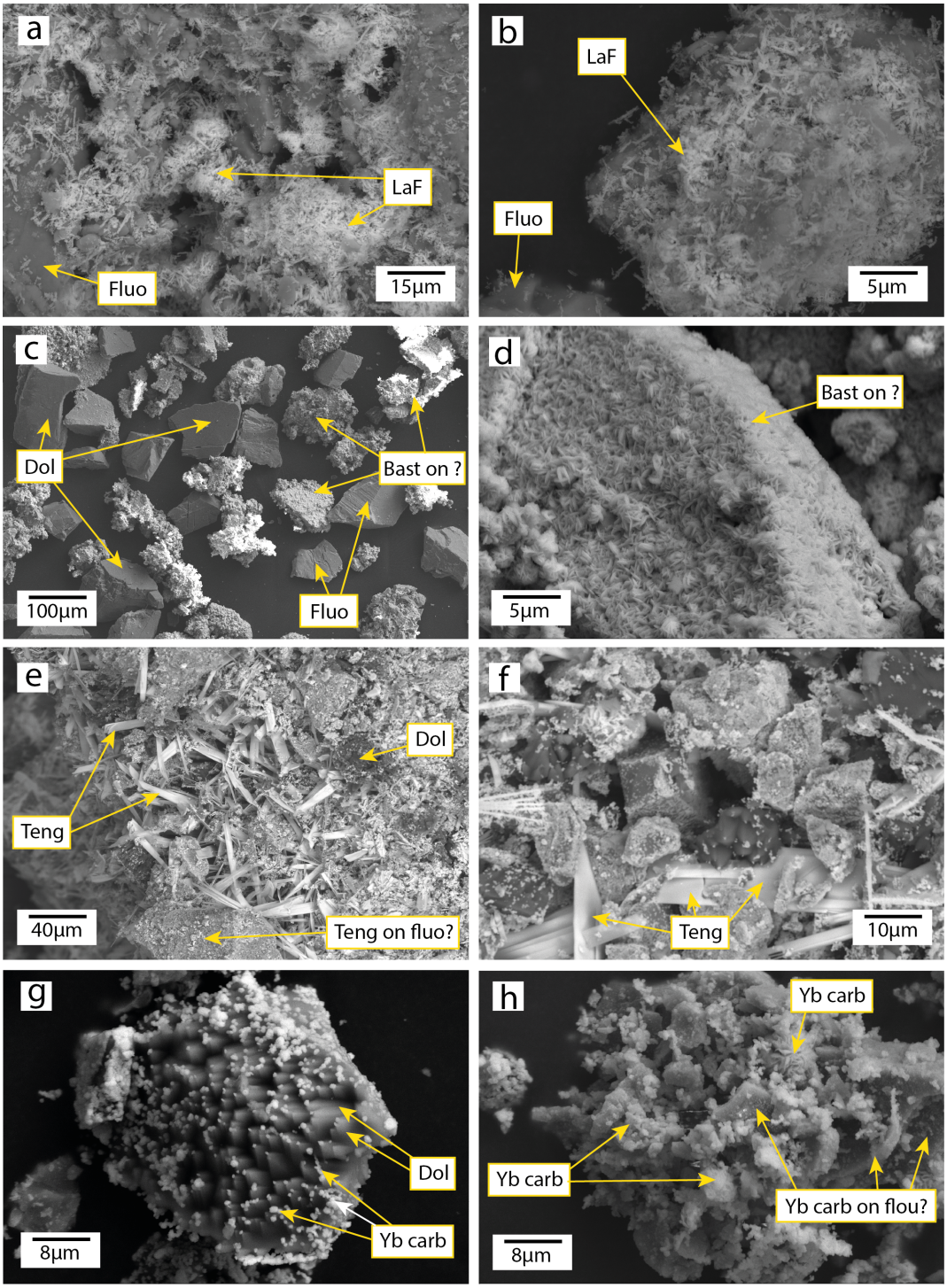

Figure 7.6: SEM images for the products of reactions between dolomite + fluorite pellets with: a – b) La; c – d) Nd; e – f) Er; g- h) Yb. The identity of the host mineral to the neo-formed mineralisation was not always clear, which is represented by question marks. LaF = La fluoride; bast = bastnäsite; teng = tengerite; Yb carb = Yb carbonate (see text for detail); dol = dolomite; fluo = fluorite.

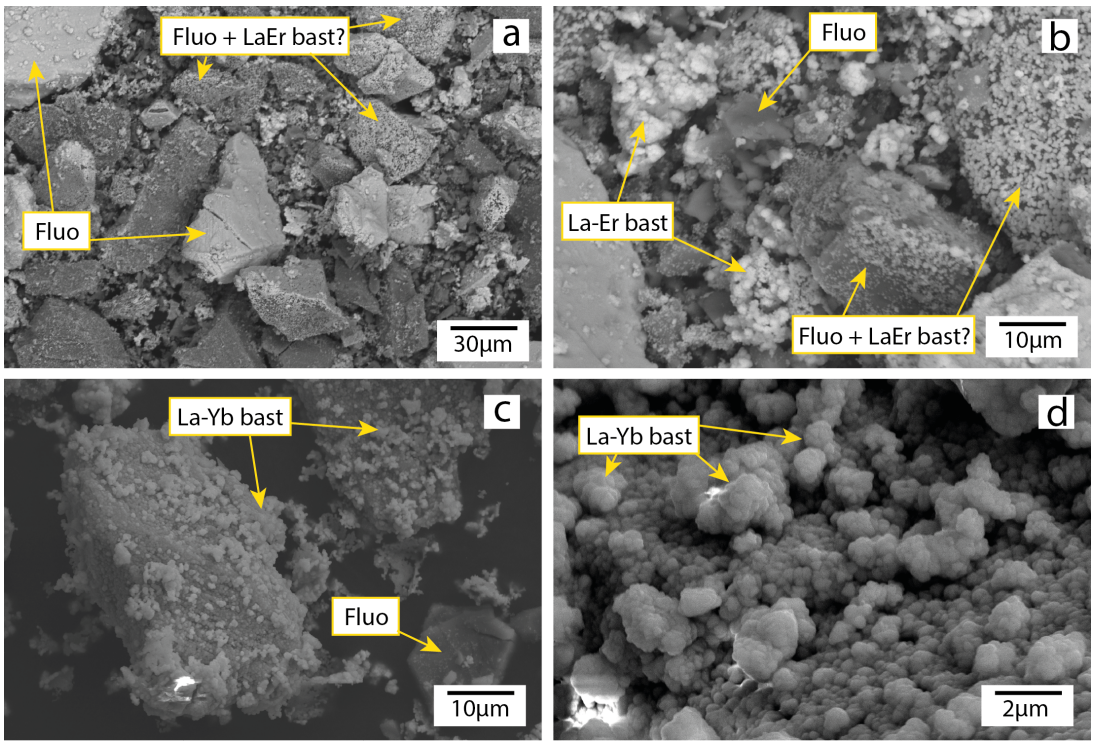

Figure 7.7: SEM images for the products of reactions between dolomite + fluorite pellets with: a – b) La+Er; c – d) La+Yb. Bast = bastnäsite; dol = dolomite; fluo = fluorite.

The SEM images of the La-fluoride (Figures 7.6a and b) reveal small needles (up to 3 μm in length) that cover the mineral on which they have formed. In almost all cases it is difficult/impossible to determine what the host mineral is because of the extent of product mineralisation. What is interesting, however, is the number of dolomite and fluorite grains (in all the experiments) that are devoid of neo-formed material. It is unknown why this has occurred, but is most likely a result of increased dolomite and fluorite dissolution on the faces of the pellets, while the pieces at greater depth have not been/less affected by the REE solutions. This is supported by Figure 7.6c (Nd experiment), in which smoothed-faced, unaltered pieces of both dolomite and fluorite are in the presence of material coated in what is assumed to be bastnäsite. A close-up of this material (Figure 7.6d) reveals tiny ($<$ 1 μm) plates. Because of the extent of bastnäsite mineralisation, the identity of the underlying mineral is unclear - this recurring problem is discussed, along with potential remedies, in the final synthesis chapter of this thesis. The morphology of the mixed LaEr (Figure 7.7a – b) and LaYb (Figure 7.7c – d) fluorocarbonate is not the same as that in the Nd-only experiment, despite all three identified as bastnäsite. This suggests a change in morphology related to the incorporation of both light and heavy REEs. In both mixed REE examples, small sphere-like masses (approximately 500 nm to 1 μm) have formed, neither of which resemble any of the morphologies seen in Chapter 6. In these samples the underlying mineral is easier to see, and examples of both fluorite and dolomite can be observed.

In the case of mixed-REE experiments, the EDS spectra of all the new material was found to contain both REEs used in each experiment, and no phase(s) containing only one REE was found.

The tengerite, identified in the Er-only solution, had the same elongate, blade morphology as that formed in the dolomite wall rock reactions at 90 and 130 °C of Chapter 6. Individual blades can reach up to 50 μm in length, which is far larger than any neo-formed material in any of the other elements investigated in the current chapter. There was also some fine-grained material located throughout the sample (Figure 7.6e – f), which cannot be excluded as an Er fluorocarbonate since EDS analyses detected Er, O, F, Ca and C. However, this material was very small and not homogeneously spread on its host mineral (fluorite), and it therefore seems more likely it is REE carbonate forming on fluorite. This seems to be supported further by the lack of unindexed Bragg peaks, or those attributable to an additional known phase (Figure 7.5).

In the Yb-only run, the PXRD identified a (calcium?)-REE-fluoride, but the SEM/EDS seems to favour most of the material, which is 'fluffy' in habit (as seen in Chapter 4), as being Yb carbonate. However, for the same reasons as the minor Er material, the intimate association with underlying fluorite (Figure 7.6h) makes EDS unreliable. Despite this, Yb carbonate is definitely present, forming on the altered face of dolomite (Figure 7.6g); no F was detected at these sites. This material may be responsible for the unindexed Bragg peaks in Figure 7.5, none of which match any of the previously unindexed Yb reflections in the previous chapters. What is unclear from the SEM images is whether the material formed in both multi-REE experiments is La fluorocarbonate admixed with some Er or Yb phase, or it is indeed a fluorocarbonate mineral into which both have incorporated. The latter is certainly possible, as some bastnäsites have documented Y content of up to 6 wt.% (e.g. Kalatha et al., 2017), and the type mineral bastnäsite-(Y) was reported as containing 40.1 % Y_2O_3 (Fleischer, 1972); both are secondary, alteration minerals.

The filters were assessed by optical microscopy and found not to contain detectable neo-formed material, from which it is inferred that all mineralisation was restricted to the dolomite and fluorite pieces.

Synthetic bastnäsite has been documented on several occasions (e.g. Haschke, 1975; Hsu, 1992), although the number of studies as compared with those focussed on REE carbonates is minimal. In almost all cases, the conditions of synthesis involve temperatures and pressures far in excess of those used in this investigation ($>$ 400 °C, $>$ 1 kbar – e.g. Hsu, 1992), and a search of the relevant literature did not find a method like that presented above. There are numerous high T and P studies of REE fluorocarbonate

synthesis that involve additional cations, most often Na and K, which are reviewed in Grice et al. (2007). The heaviest REE synthesised as a 'pure' bastnäsite is Eu, while those with additional cations extend to the heaviest REE, Lu. It does not appear that multi-REE-bearing fluorocarbonates have been synthesised previously, making the results presented above unique.

The most similar study in terms of method is that of Pradip et al. (2013), who heated a small amount (approximately 1 g) of hydrous La carbonate or Ce carbonate in distilled water at 90 °C for 24 hours, slowly added dilute hydrofluoric acid, and constantly bubbled CO_2 through the system. The experiment was a refinement of the earliest known synthesis of bastnäsite by Jansen et al. (1959). Apart from these two examples, the only other study to have synthesised 'pure' bastnäasite at < 100 °C is that of Shivaramaiah et al. (2016), which involved the dropwise addition of REE nitrate solutions to a solution of ammonium fluoride, followed by urea addition and hydrolysis at 90 °C for 20 hours. In all three studies, attempts were made to synthesise only La and Ce bastnäsites (i.e. no other REEs were used).

Fluoro-bastnäsite is far more common in nature than the OH end member, with experiments showing the latter forms in lower temperature environments essentially devoid of fluoride (e.g. Haschke, 1975; Hsu, 1992; Gysi and Williams-Jones, 2015; Voigt et al., 2016; Shivaramaiah et al., 2016). The thermodynamic properties (enthalpies of formation) of synthetic end-member La and Ce fluorobastnäsite, La and Nd hydroxylbastnäsite, and La, Ce, Dy and Y kozoite have recently been calculated using high temperature (700 °C) calorimetry (Shivaramaiah et al., 2016). The results showed that the enthalpies of formation (from REE_2O_3, CO_2 and H_2O or HF) became more negative with decreasing Z, indicating greater stability of the LREE phases, while enthalpies of formation (from elements) showed the fluorobastnäsites are more thermodynamically stable than the OH end members. The same conclusion was made using solubility measurements at 25 °C of hydroxylbastnäsite-(La), -(Nd), kozoite-(Nd) and fluorobastnäsite (inferred from the data of Gysi and Williams-Jones, 2015), which showed the hydroxylbastnäsites to be more stable than kozoite, and fluorobastnäsite to be significantly more stable than both of those phases (Voigt et al., 2016). The results of the current investigation mostly agree with those findings, although the observation of Er and Yb carbonates and La and Yb fluorides needs further investigation – however, it is important to note that the current experiments/products are most likely not at equilibrium, and as such the of results thermodynamic studies cannot be directly comparable.

The study by Gysi and Williams-Jones (2015) also calculated the thermodynamic properties of some fluorocarbonate minerals, this time natural bastnäsite-(Ce) and parisite-(Ce) (containing La, Ce, Pr and Nd). Using decomposition enthalpies to calculate the enthalpies of formation for these two phases, mineral-fluid stability diagrams for the

Ca-REE-C-O-H-F system at 300 and 400 °C were constructed. These suggested that the activity of REE^{3+} (controlled by pH) has a considerable influence on the stability fields of bastnäsite-(Ce) and parisite-(Ce). The assemblage bastnäsite + fluorite is thought to form at relatively low REE^{3+} and high F^- activities, respectively, whereas parisite + calcite is favoured at higher REE^{3+} activity (lower pH), higher CO_3^{2-} and lower F^- activities, respectively, and higher temperature. The modelling suggested that a reduction in temperature (from 400 to 300 °C) caused the bastnäsite stability field to increase (at the expense of parisite). Although the temperatures investigated in both thermodynamic studies cited were far greater than in the fluorocarbonate experiments of the current chapter, if their results can be extrapolated to lower temperatures they might explain the predominance of bastnäsite and lack of Ca-REE fluorocarbonates observed presently.

The solubility of end-member REE fluorocarbonates of Er and Yb have not been previously documented, making comparison with LREE fluorocarbonates impossible. However, based on the trends seen from the limited data on fluorobastnäsites, hydroxylbastnäsites and kozoites in Shivaramaiah et al. (2016), the stability of HREE fluorocarbonates might be expected to be lower than their LREE counterparts. The observation of Nd fluorocarbonate in the current study, and the absence of Er or Yb fluorocarbonates, would support this theory, but the results of the La (only fluocerite) and mixed La+Er and La+Yb (both bastnäsite) do not. This may suggest that the heaviest REEs (Er and Yb in this study) cannot form a structure like that of LREE fluorocarbonates, and that in the case of mixed La+Er or La+Yb, the HREEs are somehow accommodated within the framework of the La fluorocarbonate. A further set of mixed LREE+HREE experiments would be desirable to test this theory.

Another conclusion by Gysi and Williams-Jones (2015) was that fluorite and fluocerite can coexist when the activity of CO_3^{2-} is low and that of F^- is high. The observation of fluocerite in two of the experiments of this chapter suggest that – at least locally – these conditions are met, and in the case of Er where only tengerite was observed, perhaps the opposite conditions prevail (i.e. high CO_3^{2-}, low F^-). This would be easier to prove if fluocerite and tengerite were forming solely on fluorite and dolomite, respectively, but as mentioned earlier, this cannot be stated definitively. Again, these models were completed at equilibrium conditions, meaning direct comparison with the results of the current investigation – for which it is unclear whether this is true or not – is difficult.

The solubility product constants of REE tri fluorides (i.e. $REEF_3$) have been calculated at 150, 200 and 250 °C, and extrapolated to 25 °C (Migdisov et al. 2009), and the only solubility product for fluorobastnäsite is that inferred by Voigt et al. (2016) from the results of Gysi and Williams-Jones (2015). Comparison of the two shows

the bastnäsite to be significantly more stable, which, although based only on a small number of results, may provide evidence as to why fluocerite is so uncommon relative to bastnäsite in natural REE deposits. However, this still doesn't satisfactorily explain the occurrence of bastnäsite in some of the results in this chapter, and fluocerite in others, although again the caution of not dealing with a system at equilibrium is noted.

Based on the results presented above, it is suggested that REE mineralisation is occurring only at the surface of the pellets, leaving the constituent pieces at greater depth unaltered. The occurrence of La fluoride, Nd bastnäsite, Er carbonate, and Yb fluoride and carbonate is not easy to explain, however. One theory is that mineralisation is occurring so close to the surface of the dolomite and fluorite that the mineral to form is based purely on the micro-localised change in solution conditions, for example fluorite dissolution is proceeded immediately by REE fluoride deposition:

$$\mathrm{CaF_{2(s)} + H^{+}_{(aq)} \longrightarrow Ca^{2+}_{(aq)} + HF^{0}_{(aq)}} \tag{7.1}$$

$$\mathrm{REECl^{2+}_{(aq)} + HF^{0}_{(aq)} \longrightarrow REEF_{3(s)} + H^{+}_{(aq)} + Cl^{-}_{(aq)}} \tag{7.2}$$

Previous modelling of fluids rich in REE, chloride and fluoride have demonstrated that dissolved REE concentrations are reduced to ppb level as a result of REE fluoride (and fluorocarbonate) precipitation, brought on by either increases in pH (or $\mathrm{HCO_3^-}$ activity) or reductions in temperature (Migdisov and Williams-Jones, 2014). In that study, the dissolved REE concentration reaches ppb levels at around 300 °C, and only 1 ppb at 200 °C. In the current experiments, the excess dissolved REE and presumably small, localised concentrations of fluoride, would result in the immediate deposition of REE fluoride, a reaction that produces protons and therefore sustains dissolution of either fluorite or dolomite.

In the case of REE carbonate mineralisation, the same localised reactions would be taking place as were presented in Chapter 6 for the precipitation of tengerite:

$$\mathrm{CaMg(CO_3)_{2(s)} + 2\,H^{+}_{(aq)} \longrightarrow Ca^{2+}_{(aq)} + Mg^{2+}_{(aq)} + 2\,HCO_3^{-}{}_{(aq)}} \tag{7.3}$$

$$\mathrm{2\,REECl^{2+}_{(aq)} + 3\,HCO_3^{-}{}_{(aq)} + 2\,OH^{-}_{(aq)} \longrightarrow REE_2(CO_3)_3 \cdot 2\,H_2O_{(s)} + H^{+}_{(aq)} + 2\,Cl^{-}_{(aq)}} \tag{7.4}$$

The difference in solubility of either the REE fluoride or REE carbonate is suggested to not be important at the scale of the whole solution, as they are both supersaturated

with respect to the solution (i.e. their solubilities are very low). Only the dolomite and fluorite would continue to dissolve, providing further precipitation ligands. However, although these reactions explain the formation of REE fluoride and REE carbonate in a sample, this line of thought does not satisfactorily explain why only REE fluoride and REE carbonate were found in the La and Er experiments, respectively, why both these minerals were detected in the Yb sample, and why only bastnäsite was found in the Nd, La+Er and La+Yb runs.

Based on the known constituents of the experiments, the overall reaction for the precipitation of bastnasite under the conditions of this chapter is proposed as:

$$\mathrm{CaMg(CO_3)_{2(s)} + CaF_{2(s)} + 4\,H^+{}_{(aq)} \longrightarrow} \\ \mathrm{2\,HCO_3{}^-{}_{(aq)} + 2\,HF^0{}_{(aq)} + 2\,Ca^{2+}{}_{(aq)} + Mg^{2+}{}_{(aq)} \quad (7.5)}$$

$$\mathrm{REECl^{2+}{}_{(aq)} + HCO_3{}^-{}_{(aq)} + HF^0{}_{(aq)} \longrightarrow REECO_3F_{(s)} + Cl^-{}_{(aq)} + 2\,H^+{}_{(aq)} \quad (7.6)}$$

The HF dissociates almost instantaneously because of the low temperature, and the dolomite dissolution provides dissolved carbonate, leading to bastnäsite deposition.

Although models have been proposed for the precipitation of REE fluorides, REE carbonates, and REE fluorocarbonates, there is still no clear explanation as to why example of each occur individually when using different REEs in the experimental solution. However, one clear pattern emerging from the results of this thesis is the difference in behaviour of multiple-REE-bearing systems compared to those containing only a single REE. Although only speculation at this point, the presence of more than one REE in solution may impose some sort of influence on nucleation/crystallisation kinetics. Clearly further work is required on these systems, particularly those containing multiple REEs. Thermodynamic studies of multi-REE bearing carbonates and fluorocarbonates are almost absent from the literature (e.g. Gysi and Williams-Jones, 2015), and experimental studies of the type presented in this chapter are non-existent.

The results demonstrate further the complex nature of REE transport and deposition in the presence of carbonate and fluoride, and although only conducted at low (i.e. below usual ore-forming) conditions, the experimental method is easily adaptable to higher temperatures. In natural REE-carbonate and fluorocarbonate deposits the systems are more complex, for example by the presence of additional minerals, different temperatures (and pressures - something not addressed in this thesis), multiple-fluid compositions, several stages of mineralisation, etc. Although natural and experimental

systems are difficult to compare, the observation of REE fluorides, carbonates and fluorocarbonates formed under known conditions in the experiments of this Chapter can provide a starting point for studying natural REE (and host/gangue) assemblages.

7.4.2 Natural samples

Four thin sections were studied in detail by EMPA, two each from and Bayan Obo (90/19 and 88/165) and Tundulu (U4905 and 278). EMPA analyses were made on REE fluorocarbonates, monazites, apatites, dolomites/calcites and fluorites, where present.

7.4.2.1 Bayan Obo

The two Bayan Obo samples studied are sufficiently different to be described separately. The accompanying information for these samples – provided by the Natural History Museum – was very limited. All samples (including those not studied by EMPA) came with the same coordinates, which suggested sampling a few km from the actual mine pits (despite the notes stating the samples were collected in the pits). The two samples studied by EMPA came with the information in Table 7.3.

Long name	**Short name**	**Rock type**	**Details**	**Coordinates**
BM.1999, P7(65)	90/19	Magnetite bastnäsite	West of dyke, Eastern orebody	110°E, 40° 45' N
BM.1999, P7(41)	88/165	Aegirine-REE-fluorite	North side of western Main orebody	110°E, 40° 45' N

Table 7.3: Details of the two samples analysed *via* EMPA as provided by the Natural History Museum. The 'short name' is that used throughout this chapter.

Using the information in Table 7.3, the mineralogy of the slides (see below), and by cross-referencing literature information, both samples were identified as representing the main stage 'banded' (as opposed to 'massive') ores. Both had been fluoritised.

Petrography and textural relationships

Sample 90/19

The thin section image (Figure 7.8a) shows strong banding, with veinlets of orange and greenish (aegirine), purple/clear (fluorite), and black (magnetite) minerals. Dispersed throughout the sample are white minerals, which are a mixture of apatite, barite, monazite and bastnäsite (and some Ca-REE fluorocarbonates). There are also some larger fragments of minerals at the top of the slide. These are Nb-bearing minerals, possibly aeschynite.

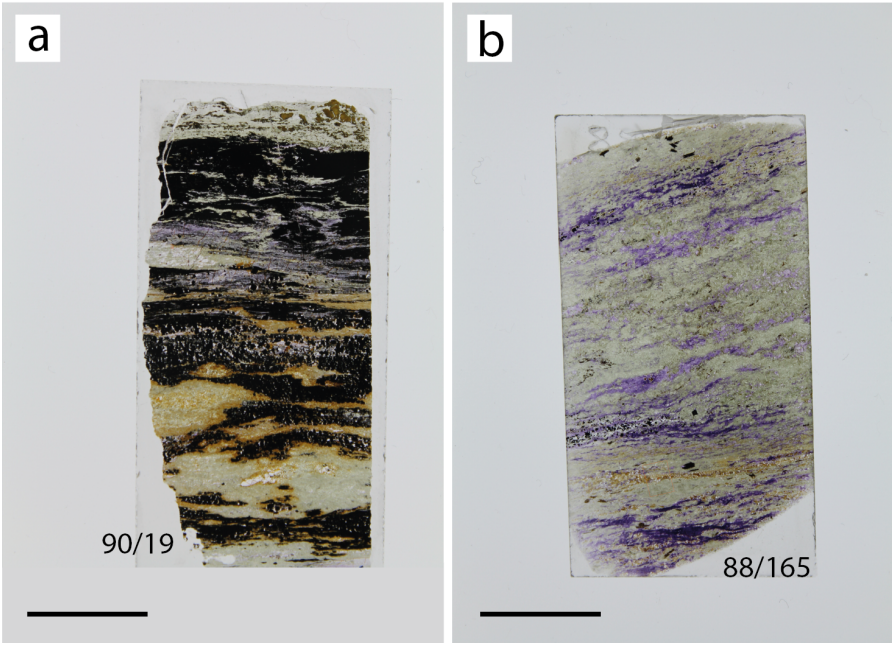

Figure 7.8: Photographs of the two Bayan Obo thin sections analysed *via* EMPA. a) sample 90/19 from the Eastern orebody, which contains bands of magnetite (black), aegirine (greenish) and fluorite (purple and clear). This sample also contains monazite, bastnäsite, Ca-REE fluorocarbonates, apatite and barite. The brown material in the upper-most part of the slide is the Nb-bearing mineral, possibly aeschynite. b) sample 88/165 from the Main orebody, which contains abundant aegirine (green) and fluorite (purple), with minor magnetite. The REE in this sample occurs almost exclusively as a Ba-REE fluorocarbonate, possibly huanghoite (brown veinlet in the lower third and disseminated throughout the slide). Scale bar = 1 cm.

SEM images of the larger scale textures in this sample are shown in Figure 7.9. They reveal the disseminated nature of the REE minerals, which occur as small (20 – 50 μm) grains most commonly concentrated in bands with fluorite and magnetite. The fluorite has a smooth, unaltered/unbroken surface, while the magnetite is more commonly pitted and contains inclusions. The other dominant mineral in this sample, aegirine, is relatively devoid of REE mineralisation and has a more broken-up surface. The Nb mineralisation was not studied in detail, but the large (700 μm length) minerals were surrounded by REE mineralisation and looked to be reacting to aegirine (Figure 7.9d), although there were also strong contacts between the Nb-bearing material and surrounding aegirine. Surprisingly, no calcite or dolomite were found anywhere in this sample.

Figure 7.10 presents pairs of SEM images, which detail the REE minerals and their textural relationships with host rocks. At these higher magnifications, it is clear that REE mineralisation is not restricted to a single host mineral, although it is more commonly associated with magnetite and fluorite. In Figures 7.10a and b, the REE mineralisation (bastnäsite) is intimately associated with barite, with both appearing to have formed

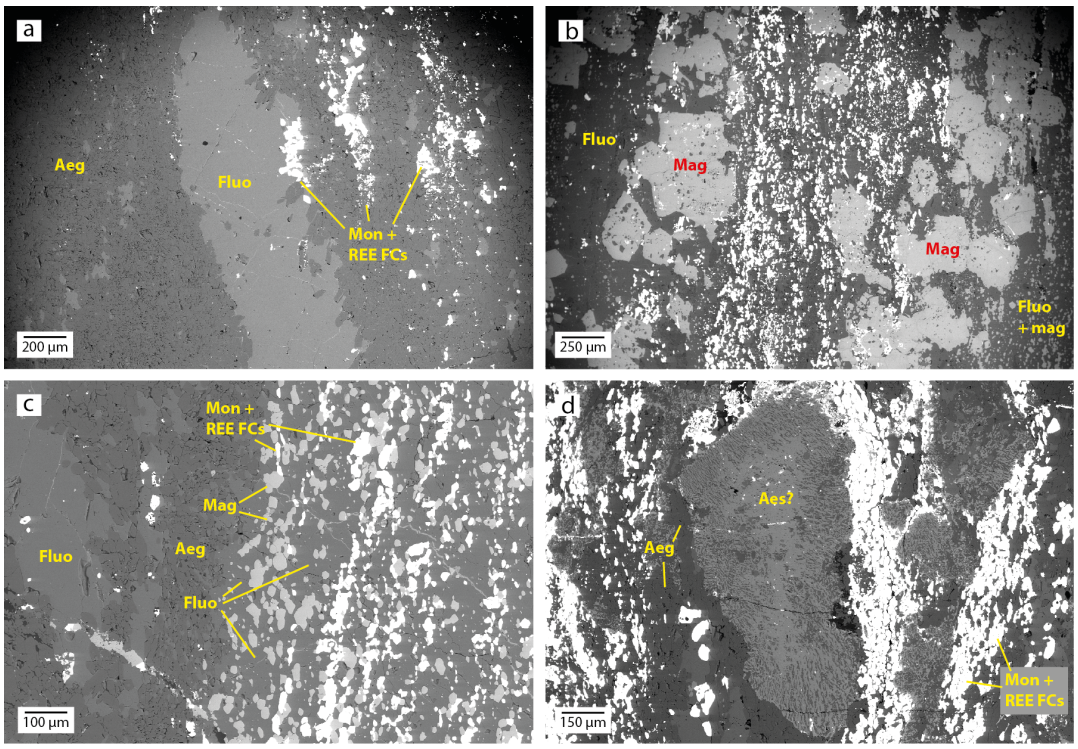

Figure 7.9: SEM image examples of the larger-scale textures seen in the banded magnetite-fluorite-aegirine-bastnäsite-monazite sample (90/19) from the Eastern orebody, Bayan Obo. The images highlight the disseminated, fine-grained nature of the REE minerals (b and c). Also present is an example of the Nb-bearing mineral, possibly aeschynite (d). Fluo = fluorite; Mag = magnetite; Aeg = aegiring; Mon = monazite; Bast = bastnäsite; REE-FCs = REE fluorocarbonates; Aes = aeschynite.

at the expense of some larger phase; it is not clear which of these two has formed first. In Figures 7.10d and f there are darker areas and small bands within the bastnäsite, which result from additional Ca. Interestingly, these Ca-bearing areas occur almost exclusively when in contact with apatite. The apatites also appear slightly zoned (apatites in middle of Figure 7.10c and bottom left in Figure 7.10g), although it is difficult to see in these images. In Figure 7.10h, there is a clear contact between the Ca-REE-FC and the barite, with no immediate suggestion as to which is oldest, perhaps suggesting the two formed contemporaneously. No Ba-REE-fluorocarbonates were found in this sample, nor were any sulfides. Although closely associated, there were no instances where bastnäsite (or Ca-REE fluorocarbonate) was found in contact with monazite. Fluorite and apatite are commonly in contact with each other. Despite widespread fluorite, no REE fluoride minerals were identified - this is relevant in comparison to the experiments presented earlier: if fluorite pre-dates the REE mineralisation, the precipitation of bastnäsite may have proceeded *via* the dissolution of fluorite (and dolomite/calcite - although this was not observed). However, there is no clear evidence for this based on the textures in Figures 7.9 and 7.10. There was no indication of any REE carbonates (i.e. other than the fluorocarbonates).

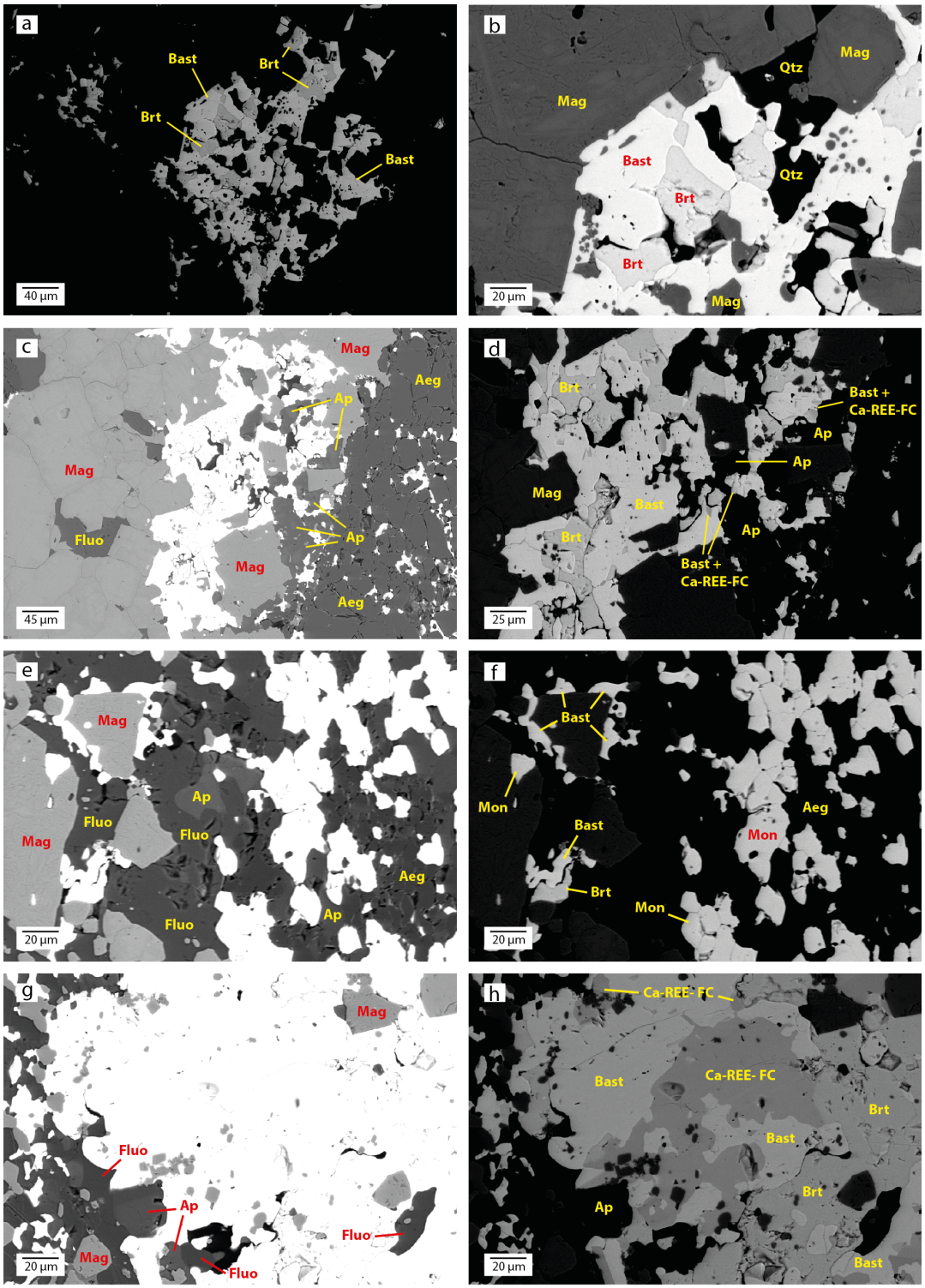

Figure 7.10: Pairs of SEM images showing examples of the textures between REE minerals and host rocks in Bayan Obo sample 90/19. b) and d) are slightly enlarged areas of a) and c), respectively; e) is at the same magnification as f); g) is the same magnification as h). Fluo = fluorite; Ap = apatite; Mag = magnetite; Aeg = aegiring; Dol = dolomite; Mon = monazite; Bast = bastnäsite; Brt = barite; Qtz = quartz; Ca-REE-FC = Ca-REE fluorocarbonate.

Sample 88/165

The photograph of this thin section (shown a few pages ago, Figure 7.8b) revealed bands and veinlets similar to the previous sample, although here the magnetite is almost absent and green aegirine and purple fluorite are more abundant. The brown veinlet near the bottom of the slide is a concentration of the REE mineralisation, which is almost exclusively in the form of a Ba-REE fluorocarbonate. This mineral is also dispersed through the sample. A white mineral is also visible, which is mostly apatite and some barite.

SEM images show the fluorite and aegirine to be similar in appearance to sample 90/19, i.e. smooth-faced and broken-up, respectively (Figures 7.11a – c). The REE mineralisation is mostly concentrated into thin veinlets (500 μm combined width), with the areas distant from these almost devoid of REE minerals. There are very clear areas in which large phases/minerals have been completely altered, with the pseudo-mineral filled with an assemblage of quartz, barite, magnetite and dolomite (Figure 7.11b-f). It is extremely difficult to identify the precursor mineral, although it is likely to be the original host rock (fluorite or aegirine), given that these are infilled veins. In Figure 7.11c and d, the infill contains a large amount of dolomite and magnetite, whereas in the Figures 7.11e and f there is an assortment of minerals including apatite, barite, Ba-REE fluorocarbonate (huanghoite?), monazite and a fine-grained material containing Nb, Ti and Ba. This latter phase is unidentified but may be the mineral baotite, $Ba_4(Ti,Nb)_8Si_4O_{22}Cl$, which has been described from this deposit previously (Smith et al., 2015). Within one of the altered areas there is an example of monazite surrounded by apatite, which forms a rim between the monazite and Ba-REE-FC.

Apatite is quite common in this sample, but only associated – and commonly enclosed by – Ba-REE fluorocarbonate (Figure 7.11g and h). The apatite is concentrically zoned, with REEs detected in the lighter regions (Figure 7.11h) but not in the darker bands. The most common configuration was a dark centre (no REE), surrounded by a light ring (REE detected), which was itself surrounded by another dark ring (usually in contact with Ba-REE-fluorocarbonate).

As with the previous sample, no sulfide minerals, REE fluorides or REE carbonates were identified.

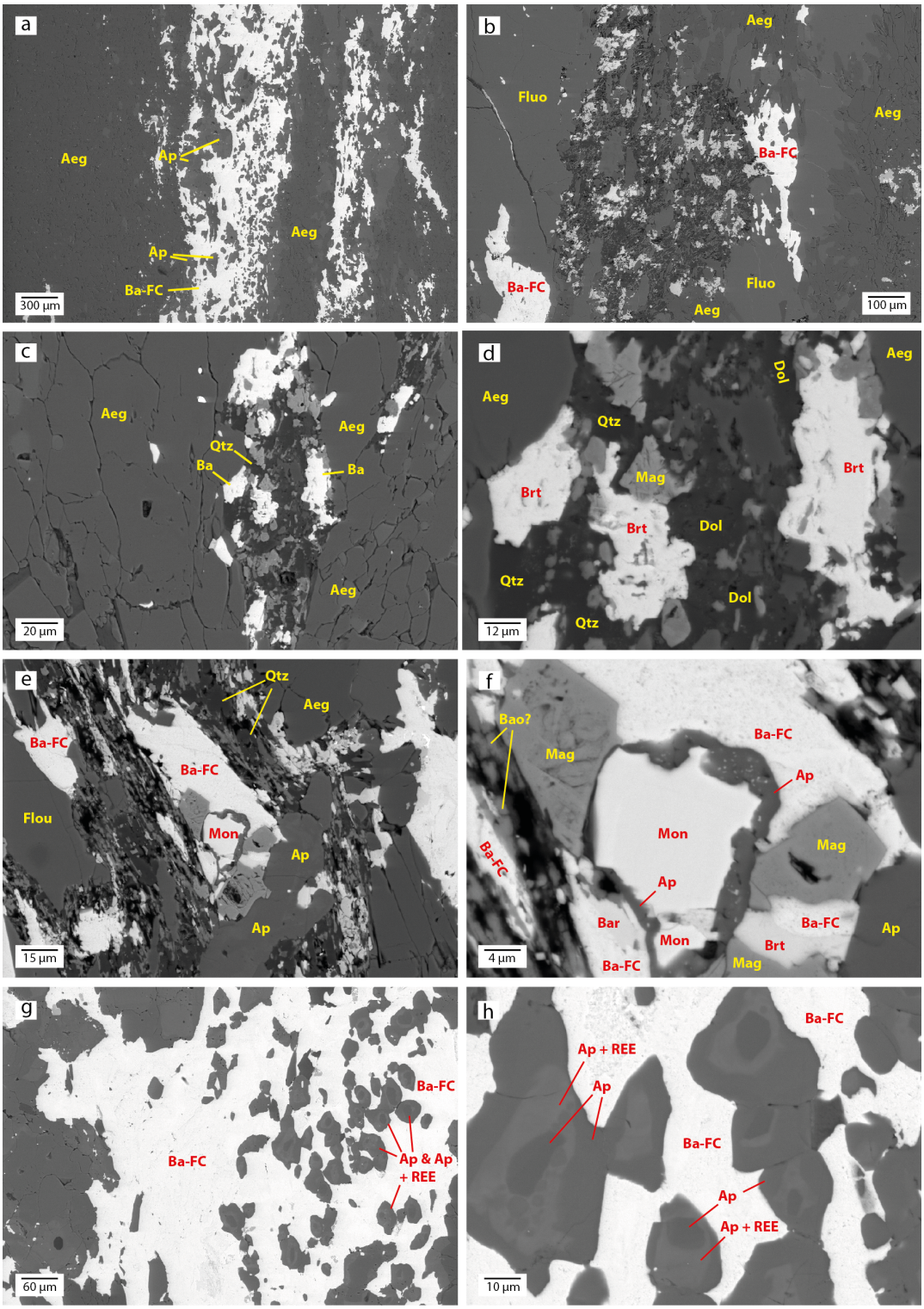

Figure 7.11: SEM images of sample 88/165 from the Main ore body at Bayan Obo showing the larger scale textures (a and b), replacement textures (b – f), and the relationship between the Ba-REE fluorocarbonates and apatite, including the REE-bearing (lighter) and REE-devoid (darker) concentric banding of apatite. Fluo = fluorite; Ap = apatite; Mag = magnetite; Aeg = aegiring; Dol = dolomite; Mon = monazite; Ba-FC = barium-REE fluorocarbonate; Qtz = quartz; Brt = barite; Bao = baotite.

Mineral compositions

Average mineral compositions and calculated formulae are presented in Tables 7.4 and 7.5, respectively. Results for Gd have not been included, as discussed in the methods section. All results can be found in Appendix A.

Fluorite was almost REE-barren, although Y was detected in almost all samples (max 0.08 % Y_2O_3), La in two, and Ce one. The average $\sum REE_2O_3$ was < 0.1, which is in agreement with previous analyses of fluorite from Bayan Obo (Xu et al., 2012).

EMPA results for all bastnäsite and monazite analyses have Ce as the dominant REE (therefore bastnäsite-(Ce) and monazite-(Ce)), followed by La > Nd > Pr. They contain very similar total REE_2O_3 concentrations, at around 70 %, which is in agreement with previously published results for natural and synthetic examples (e.g. Ngwenya, 1994; Smith and Campbell, 2000; Guastoni et al., 2009; Sheard et al., 2012; Pradip et al., 2013). Both minerals are LREE-enriched and have typical REE distributions (chondrite-normalised plots are shown in Figure 7.12 and discussed below). Calcium concentrations are low in both bastnäsite and monazite, as expected (max 1 % CaO). Thorium was detected only in monazite, but was low at around 0.2 % ThO_2, comparable to previous Bayan Obo studies. Ba-REE-fluorocarbonate results are mostly in agreement with previous results from Bayan Obo in terms of individual REE concentrations (Smith and Campbell, 2000). However, attempts to calculate the number of cations based on 7 oxygens (as was done for synchysite) was not successful, possibly a result of analytical error. Previous analyses of Ba-REE fluorocarbonates have shown these minerals may contain Na, P, Al, Si, Mn, Fe, Sr, Th and U (Zaitsev et al., 1996; Smith and Campbell, 2000; Trofanenko et al., 2016), however, these elements were not analysed in the current investigation. If these or any other cations are present in the samples at appreciable concentrations, then their absence from the results would throw the formula calculations. Nevertheless, the minerals were identified as Ba-REE-fluorocarbonates. As with the bastnäsite and monazite, Ce is the dominant REE, followed by La then Nd, however, no Pr was detected.

Apatite was only analysed from sample 88/165, but unfortunately the beam diameter was too wide to pick out the individual light and dark bands. Despite this, apatite was found to be a significant host for REEs, with an average REE_2O_3 concentration of 2.49 weight % (max 5.7 weight %), a figure comparable to some previously published data at Bayan Obo (Smith et al., 1999), and other deposits (e.g. Chakhmouradian and Wall, 2012; Goodenough et al., 2015; Broom-Fendley et al., 2016). The apatite contains an average of 3.61 weight % fluorine, making this fluorapatite. The calculated stoichiometry suggests a near perfect apatite formula; this would suggest the REE-richer bands are not separate monazite.

Bastnäsite		**Ba-REE-FC**		**Monazite**		**Apatite**		**Fluorite**	
$n = 16$		$n = 8$		$n = 11$		$n = 10$		$n = 11$	
F	6.18	F	2.34	P_2O_5	29.46	F	3.61	F	44.02
CaO	0.23	MgO	0.03	SiO_2	0.06	P_2O_5	40.25	SiO_2	0.03
Y_2O_3	0.17	CaO	1.17	CaO	0.40	CaO	52.13	CaO	74.51
La_2O_3	24.11	BaO	38.71	Y_2O_3	0.14	MnO	0.09	Y_2O_3	0.06
Ce_2O_3	33.72	Y_2O_3	0.09	La_2O_3	20.90	FeO	0.11	La_2O_3	0.09
Pr_2O_3	2.70	La_2O_3	6.50	Ce_2O_3	16.25	SrO	0.28	Ce_2O_3	0.14
Nd_2O_3	8.37	Ce_2O_3	16.25	Pr_2O_3	3.01	Y_2O_3	0.30	Total	119.59
Sm_2O_3	0.41	Nd_2O_3	5.39	Nd_2O_3	9.38	La_2O_3	0.25	O≡F	18.97
Dy_2O_3	0.09	Sm_2O_3	0.28	Sm_2O_3	0.51	Ce_2O_3	1.02	Total	100.62
Er_2O_3	0.07	Er_2O_3	0.07	Dy_2O_3	0.10	Pr_2O_3	0.30	$\sum REE_2O_3$	0.06
CO_2*	21.24	CO_2*	27.74	ThO_2	0.22	Nd_2O_3	1.00		
Total	100.00	Total	100.00	Total	100.82	Sm_2O_3	0.16		
O≡F	2.60	O≡F	0.99	$\sum REE_2O_3$	68.70	Total	99.11		
Total	97.40	Total	99.01			O≡F	1.52		
$\sum REE_2O_3$	69.48	$\sum REE_2O_3$	28.51			Total	97.59		
						$\sum REE_2O_3$	2.49		

Table 7.4: Average EMPA analyses (weight %) of the minerals Bayan Obo samples. Gd has been omitted due to potential interferences.

Bastnäsite		**Ba-REE-FC**		**Monazite**		**Apatite**	
Cations based on 4 O		Cations based on 7 O		Cations based on 4 O		Cations based on 12.5 O	
F	0.73	F	0.46	P	0.98	F	1.02
Ca	0.01	Mg	0.0	Si	0.00	P	2.87
Y	0.00	Ca	0.08	Ca	0.02	Ca	4.70
La	0.33	Ba	0.95	Y	0.00	Mn	0.01
Ce	0.46	Y	0.00	La	0.30	Fe	0.01
Pr	0.04	La	0.15	Ce	0.50	Sr	0.01
Nd	0.11	Ce	0.37	Pr	0.04	Y	0.01
Sm	0.01	Nd	0.12	Nd	0.13	La	0.01
Dy	0.00	Sm	0.01	Sm	0.01	Ce	0.03
Er	0.00	Er	0.00	Dy	0.00	Pr	0.01
C	1.07	C	2.36	Th	0.00	Nd	0.03
$\sum$REE	0.99	$\sum$REE	0.68	$\sum$REE	1.02	Sm	0.00
						$\sum$REE	0.09

Table 7.5: APFU of Bayan Obo minerals calculated from the average EMPA values in Table 7.4.

Chondrite-normalised plots of the REE minerals (bastnäsite, monazite and huanghoite) and apatite are shown in Figure 7.12. Although some elements were below the detection limit of the EDS, the plots demonstrate extreme LREE-enrichment of REE minerals, and the plots presented here are almost identical to those previously published (Smith and Campbell, 2000). In contrast, the apatites are relatively enriched in middle and heavy REEs, such that the slopes of the plots are less severe (i.e. flatter profile). This pattern has also been observed previously at Bayan Obo.

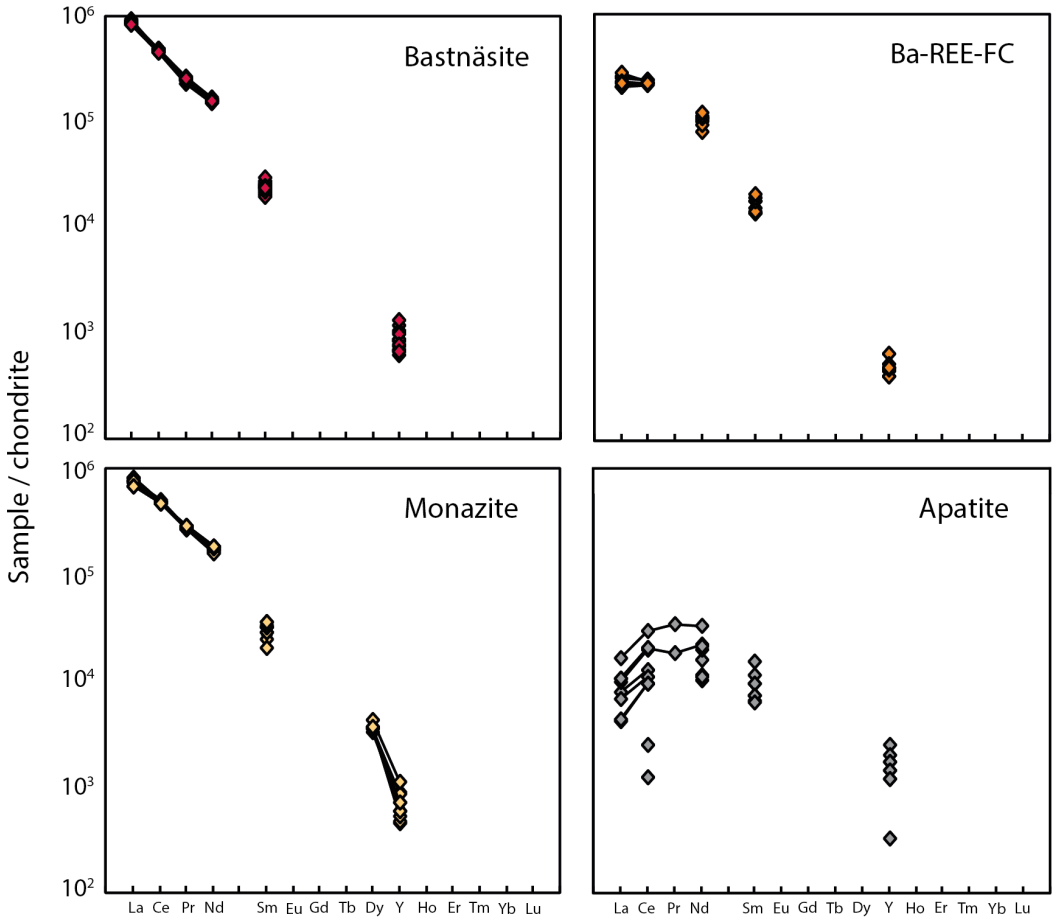

Figure 7.12: Chondrite-normalised REE concentrations of bastnäsite, Ba-REE-fluorocarbonate (huanghoite?), monazite and apatite from Bayan Obo. Chondrite values of McDonough and Sun (1995) used for normalisation.

Discussion

Previous studies on the textural relationships at Bayan Obo have shown a relationship between the REE minerals and host rocks (e.g. Smith et al., 1999; Smith and Campbell, 2000). In those studies, apatite + bastnäsite rims occurred around monazite, and

monazite + fluorite formed between bastnäasite and apatite. Calcite was also intimately associated with all minerals. The textures led the authors to propose the following reactions:

$$3\,\mathrm{REEPO_{4(s)}} + 5\,\mathrm{CaCO_{3(s)}} + 4\,\mathrm{HF^0_{(aq)}} \longrightarrow \mathrm{Ca_5(PO_4)_3F_{(s)}} + 3\,\mathrm{REECO_3F_{(s)}} + \mathrm{H_2O_{(aq)}} + 2\,\mathrm{CO_{2(aq)}} \quad (7.7)$$

$$\mathrm{Ca_5(PO_4)_3F_{(s)}} + 3\,\mathrm{REECO_3F_{(s)}} + \mathrm{H_2CO_{3(aq)}} \longrightarrow 3\,\mathrm{REEPO_{4(s)}} + 5\,\mathrm{CaCO_{3(s)}} + 4\,\mathrm{HF^0_{(aq)}} \quad (7.8)$$

$$\mathrm{Ca_5(PO_4)_3F_{(s)}} + 3\,\mathrm{REECO_3F_{(s)}} + 6\,\mathrm{HF^0_{(aq)}} \longrightarrow 3\,\mathrm{REEPO_{4(s)}} + 5\,\mathrm{CaF_{2(s)}} + 3\,\mathrm{H_2O_{(aq)}} \quad (7.9)$$

The direction of reactions was thought to be controlled by the pH and chemistry of the fluid. Monazite forming at the expense of bastnäsite and apatite (reactions 7.8 and 7.9) was suggested as occurring at low pH and high phosphate activities, while the reaction of monazite to bastnasite (reaction 7.7) occurred at higher pH and high CO_3^{2-} and F^- activities. During periods of excess carbonate (the deposit is hosted by dolomite/calcite), the conditions favour monazite breakdown and bastnäsite + apatite formation, but as the carbonate is limited and the F^- activity is high, monazite + fluorite would form at the expense of bastnäsite and apatite.

The assessment of the two samples in the current study did not identify dolomite or calcite (except in tiny quantities in replacement features of larger phases – e.g. Figure 7.11d), but there is abundant fluorite and evidence of reactions between apatite and the REE fluorocarbonate minerals. In sample 90/19 the occurrence of Ca-REE fluorocarbonates is almost always associated with apatite contacts, but there is no associated monazite or calcite, making the reactions above difficult to justify. In sample 88/165, however, there are examples of monazite associated with REE fluorocarbonates and apatite, in proximity to dolomite (Figure 7.11e and f). Here, apatite occurs as a rim around monazite, separating the latter from Ba-REE-FC, and all of which is found within one of the larger replacement textures mentioned earlier. Although the identity of the precursor phase is unknown, the presence of dolomite may suggest it as the parent mineral. If this is true, then reaction 7.7 would be applicable, and would account for the monazite breakdown to apatite + Ca-REE-FC; there would have been high Ca^{2+} and CO_3^{2-} activity for Ca-REE-FCs to form (Williams-Jones and Wood, 1992; Smith et al., 1999). In most accepted paragenesis models, Ba-REE-FCs formed *via* the transformation of earlier Ca-REE-FCs, suggesting multiple phases of fluid influx.

The banded apatite is more difficult to explain, particularly as there is no dolomite associated with these features. Banding may suggest multiple periods of fluid influx, with the conditions of that fluid being significantly different each time as to promote either apatite deposition or dissolution. Certainly there are known to have been several periods of mineralisation and fluid influx, as evidenced in particular by the banding of ores and host rocks, and it has been noted that apatite shows 'compositional variations that are consistent with multiple generations of fluid influx into the system, even within a single paragenetic stage' (Campbell and Henderson, 1997). Perhaps the core of these features is original apatite, which was associated with bastnäsite. The conditions of the fluid then changed, initiating the breakdown of apatite (+ bastnäsite) to monazite (+ calcite). However, before this reaction could go to completion, the fluid conditions changed back to that in which apatite was stable, perhaps when the widespread Ca- or Ba-REE-FC mineralisation was deposited.

A very common mineral in both samples not addressed thus far is magnetite. In previous studies of Bayan Obo, the formation of magnetite is suggested as either slightly pre-dating and/or contemporaneous with REE mineralisation (e.g. Smith et al., 2015; Yang et al., 2017). Despite widespread Fe oxides throughout the deposit, and Fe actually being the main element mined at Bayan Obo (REEs are recovered in most instances as a by-product), there has been little research on the genesis of Fe mineralisation. A recent study by Huang et al. (2015) used LA-ICP-MS to analyse the trace element content of magnetite and hematite grains from the different stages of mineralisation at Bayan Obo (i.e. disseminated, massive and banded ores), with the aim of better understanding the processes involved in their formation, and by inference, constraints on the conditions of REE mineralisation. The results of that study showed two generations of magnetite: those related to sedimentary processes and those of hydrothermal origin (determined by their REE and trace element content). The formation of magnetite from hydrothermal fluids would imply a redox control to their precipitation, as it contains both Fe^{2+} and Fe^{3+}. Based on the textures in Figures 7.9 and 7.10, it is difficult to determine whether the REE mineralisation postdates or is contemporaneous with the magnetite, but it appears hydrothermal in origin; these minerals were not analysed during the current investigation. The possible control of changing oxygen fugacity in the solutions as a trigger for Fe and REE mineralisation must, therefore, be noted, but cannot be determined here. However, such an event could be achieved *via* solution mixing (perhaps with a meteoric water?), something that could also provide additional ligands (e.g. carbonate, phosphate) necessary for the precipitation of observed fluorocarbonate and phosphate minerals.

The lack of dolomite and abundance of fluorite in these samples makes comparison with the experimental results difficult. There is no clear evidence for the dissolved carbonate and fluoride required for REE-FC deposition being sourced from calcite/dolomite

and fluorite, respectively. However, there is evidence highlighting the importance of calcite/dolomite, fluorite, apatite and monazite, and therefore experiments including dissolved phosphate in the presence of carbonate and fluoride would be the logical next step for better understanding the reactions seen at Bayan Obo.

7.4.2.2 Tundulu

The mineralogy and paragenesis at Tundulu were simpler than at Bayan Obo, and both samples studied were similar enough to be described together. Both are carbonate carbonatites (ankerite/Fe dolomite, calcite), with variable amounts of apatite, minor quartz and barite, and abundant REE fluorocarbonate mineralisation (synchysite).

Photographs of the two thin sections are shown in Figure 7.13. One (278) contained a much larger proportion of a dark material (about 80 %) with pockets of a greenish mineral, and minor white material. The other sample (4905) contained the same minerals, but these were finer-grained and more evenly distributed.

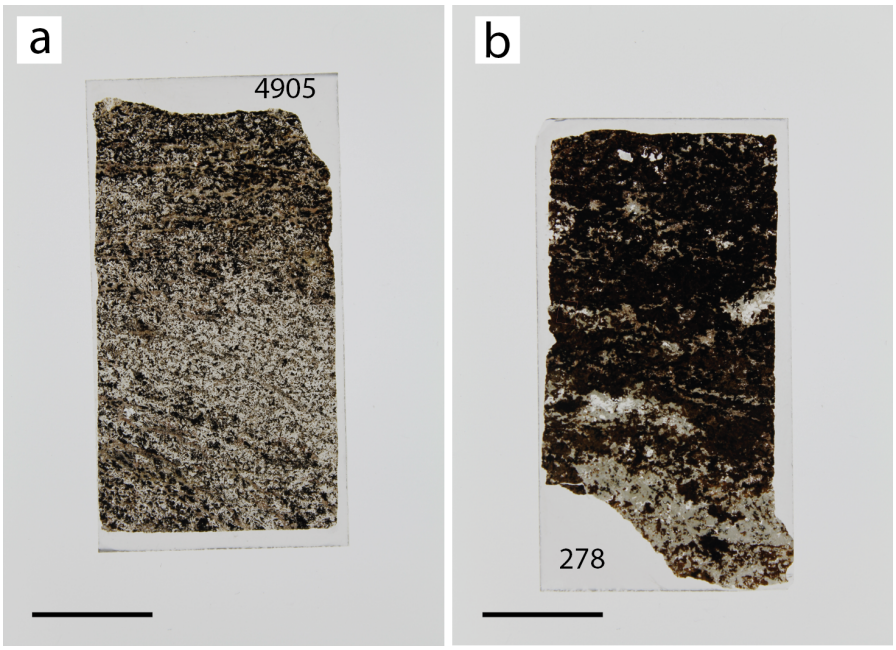

Figure 7.13: Photographs of the two Tundulu thin sections analysed *via* EMPA. Both samples contained the same mineralogy but in different proportions. The dark mineral was an altered carbonate rock (dolomite with exsolved Fe-oxide), possibly after ferroan dolomite or ankerite; the white phases were apatite, quartz (both samples) and minor barite (sample 278 only). The more greenish phase (especially at the bottom of 278) was synchysite. Scale bar = 1 cm.

SEM images of the larger-scale textures are shown in Figure 7.14, and more detailed images of the REE mineralisation are shown in Figure 7.15.

EDS revealed the dark material to be a carbonate mineral, heavily altered to iron oxides (grey specks in Figure 7.14a). The remaining carbonate (darker parts) phase contained Mg and Mn, possibly after ankerite (this carbonate plus Fe-oxides is herein named 'C1' carbonate). In places, the rhombic habit of the reactant carbonate was clearly visible (Figure 7.14a). A second carbonate phase was present in both samples, which could be sub-divided into two types: one was widespread and commonly heavily pitted (Figure 7.14a and d – herein named 'C2'), and the other was almost completely unaltered and occurs intimately with Ca-REE fluorocarbonate mineralisation (Figure 7.14a and f – herein named 'C3').

The white mineral in the thin section photos is mostly apatite, but also quartz (both samples) and barite (278 only, Figure 7.14c and d). Apatite makes up at least 40 % of sample 4905 and about 10 % of 278. In both, the SEM reveals heavily pitted surfaces and some crystals with perfect hexagonal form (Figure 7.14e). In places, the surrounding carbonate is heavily altered to iron oxides but the apatite appears unaffected, and in most cases the boundaries between these two minerals are unaltered (e.g. Figure 7.15e). The pitted apatite is the same as 'turbid' apatite described previously in Ngwenya (1994) and Broom-Fendley et al. (2016), although there was less evidence for the 'late overgrowth' stage of apatite described in the latter (i.e. less-altered, euhedral rims up to 100 μm thick). Broom-Fendley et al. (2016) used cold-cathode-luminescence to easily identify these overgrowths, a technique not used in the current investigation. Barite is uncommon, but always found within C2 or C3 carbonate and associated with the Ca-REE fluorocarbonates and quartz. Quartz is a minor phase throughout the samples, often making up the groundmass to REE mineralisation, but equally found unrelated with it (e.g. Figure 7.14f and Figure 7.15a and g).

The greenish mineral in thin section photos is Ca-REE fluorocarbonates. These occur throughout sample 4905, but are concentrated together into pockets in sample 278 (Figure 7.14b). The major host to these minerals is C2 and C3 carbonate. In places the host appears to have been completely altered to Fe oxide (Figure 7.15c). The fluorocarbonates form acicular crystals up to 200 μm that are mostly randomly orientated, and are always truncated by apatite and C1 carbonate, indicating they are younger (Figure 7.15e). In the larger pockets of mineralisation in sample 278, the crystals are commonly shorter (20 μm or less) pseudo-rectangles or shapeless masses. The latter are possibly the result of alteration during later fluid flow, as evidenced by Fe oxides (thought to be an alteration product of an earlier carbonate) commonly hosting them. This observation is not universal, however. The Ca-REE fluorocarbonates show pitting and alteration, particularly at contacts with all others minerals, and along possible cleavage (Figure 7.15d – h). Although alteration of these phases is common, there are many examples where the opposite is true. The textures and formation of brighter areas (higher Z) are identical to those seen at the Barra Do Itapipapuã carbonatite in

Brazil (Ruberti et al., 2008). There are a few examples where a fibrous material has formed between the laths of REE fluorocarbonate, which appear to be Mn oxide that also contains Ba and K (Figure 7.15f). This phase may be one of the psilomelane group minerals, although its identity could not be established.

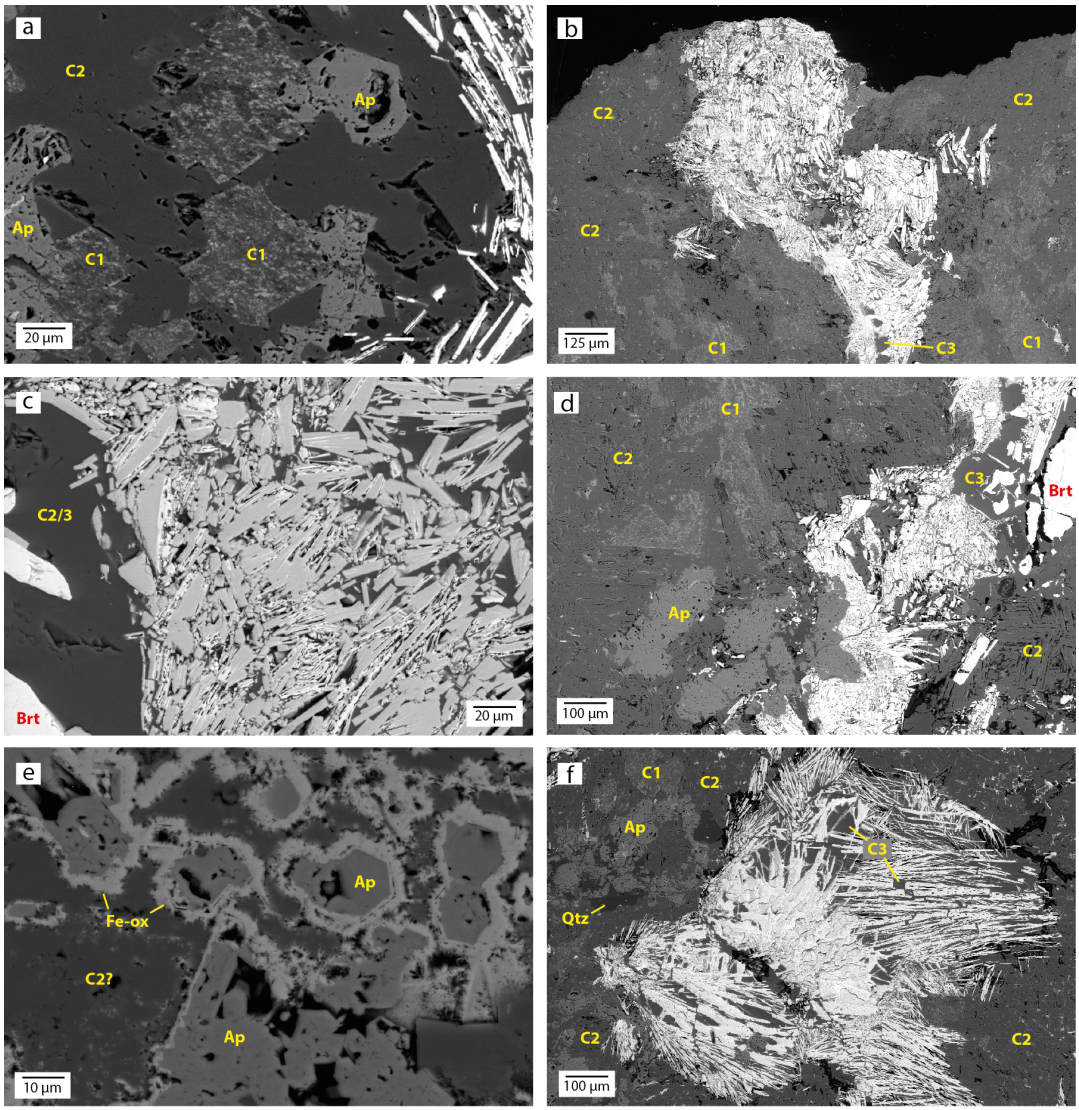

Figure 7.14: SEM images showing examples of the larger scale textures between the host rock and synchysite (all white material not labelled as barite) in both Tundulu samples (a – d and f), and the reaction of carbonate around apatite (e). The pseudomorphs after rhombic carbonate are clearly visible in a). Note the altered/pitted nature of the C2 carbonate. C1, C2 and C3 = three carbonate stages described in text; Ap = apatite; Brt = barite; Fe-ox = iron oxide.

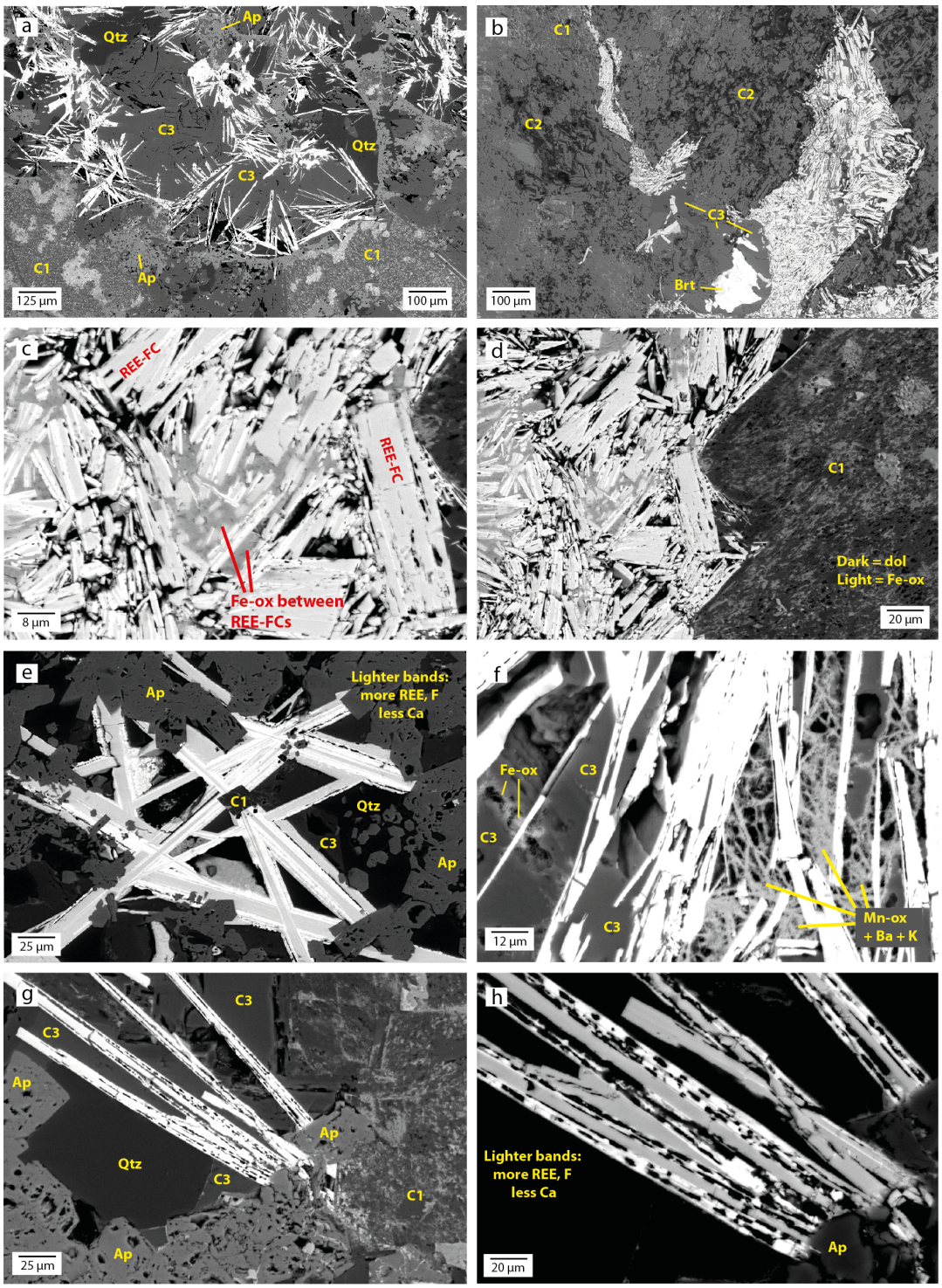

Figure 7.15: SEM images showing examples of the textures described in text for the Ca-REE fluorocarbonates and their host minerals at Tundulu. a), e) and g) clearly show the truncation of Ca-REE fluorocarbonate by apatite; c) shows an example of the Fe-oxide material playing host to the REE mineralisation, possibly because of earlier carbonate alteration; d) shows the C1 carbonate truncating REE mineralisation, the darker areas being dolomite and the lighter specks Fe-oxide; e and h) Ca-REE fluorocarbonate with alteration (brighter) to areas relatively more enriched in REEs and F, and relatively depleted in Ca; f) heavy alteration of some unknown phase to Mn-oxide with minor Ba and K detected. C1, C2 and C3 = three carbonate stages described in text; Ap = apatite; Brt = barite; Fe-ox = iron oxide; Qtz = quartz

Rhabdophane and pyrochlore, as observed by Ngwenya (1994) and Broom-Fendley et al. (2016), respectively, were not found in the current samples.

Mineral compositions

Average mineral compositions and calculated formulae are presented in Tables 7.6 and 7.7, respectively. All results can be found in Appendix A. EMPA analyses were made only on C2 and C3 examples (i.e. not the heavily altered C1 material). Based on their appearance and textures the carbonates were classified into three groups, however, the EMPA revealed very similar chemistries within a sample, but quite different between them. The carbonates in sample 4905 were dolomite/ferroan dolomite (up to 4.87 weight % FeO), while all examples from sample 278 were calcite. In all cases the carbonates were low in REEs (max $\sum REE_2O_3$ = 1.61 weight %). The composition of synchysite was very consistent across both samples. Cerium was the dominant REE, followed by La > Nd > Pr. Some of the middle and heavier REEs not detected in the bastnäsite from Bayan Obo (e.g. Eu, Tb) were present here, but only in very small concentrations (< 0.2 weight % oxide). The synchysite was strongly LREE-enriched, and the individual REE concentrations were in agreement with previous studies (Ngwenya, 1994; Broom-Fendley et al., 2016). The calculated mineral formula was near ideal. Attempts were made to analyse the brighter bands/parts of the synchysite minerals (thought to be parisite), but were unsuccessful due to overlap of the electron beam.

Apatite, a mineral shown previously to contain considerable REE content, was found here to have average $\sum REE_2O_3$ of 2.38 weight % (up to 2.67 %), made up of lighter REEs (Sm was the heaviest REE detected).

Chondrite-normalised plots for synchysite and apatite are shown in Figure 7.16. The LREE-enrichment of synchysite is extreme, but typical for carbonatite-hosted REE fluorocarbonates. Apatite displays flatter profiles (less La, Ce and Nd enrichment), but the MREE enrichment is less extreme than in the Bayan Obo samples. Plots presented here are most similar to some of the 'turbid core' analyses of Broom-Fendley et al. (2016), although the large number of missing REE analyses (i.e. below detection limits) from this mineral in the current investigation hampers comparison.

Synchysite		**Dolomite**		**Calcite**		**Apatite**	
$n = 24$		$n = 5$		$n = 11$		$n = 19$	
F	4.03	MgO	14.95	MgO	2.24	F	3.72
MgO	0.00	CaO	33.30	CaO	53.25	P_2O_5	38.59
CaO	17.02	MnO	0.97	MnO	0.20	CaO	51.93
Y_2O_3	0.30	FeO	4.06	FeO	1.08	MnO	0.08
La_2O_3	14.18	La_2O_3	0.05	Y_2O_3	0.02	FeO	0.25
Ce_2O_3	24.21	Ce_2O_3	0.07	La_2O_3	0.23	SrO	0.98
Pr_2O_3	2.31	CO_2*	53.34	Ce_2O_3	0.22	Y_2O_3	0.46
Nd_2O_3	7.47	Total	100.00	Nd_2O_3	0.16	La_2O_3	0.37
Sm_2O_3	0.72	$\sum REE_2O_3$	0.11	CO_2*	56.24	Ce_2O_3	0.87
Eu_2O_3	0.09			Total	43.76	Nd_2O_3	0.52
Tb_2O_3	0.08			$\sum REE_2O_3$	0.63	Sm_2O_3	0.16
Dy_2O_3	0.16					Total	97.93
Er_2O_3	0.09					O≡F	1.57
CO_2*	29.58					Total	96.37
Total	100.00					$\sum REE_2O_3$	2.38
O≡F	1.70						
Total	98.30						
$\sum REE_2O_3$	49.61						

Table 7.6: Average EMPA analyses (weight %) of the minerals at Tundulu samples. Gd has been omitted due to potential interferences.

Synchysite		**Dolomite**		**Calcite**		**Apatite**	
Cations based on 7 O		Cations based on 6 O		Cations based on 3 O		Cations based on 12.5 O	
F	0.71	Mg	0.70	Mg	0.06	F	1.01
Mg	0.00	Ca	1.13	Ca	0.06	F	1.01
Ca	1.01	Mn	0.03	Mn	0.06	F	1.01
Y	0.01	Fe	0.13	Fe	0.06	F	1.01
La	0.29	La	0.00	Y	0.06	F	1.01
Ce	0.49	Ce	0.00	La	0.06	F	1.01
Pr	0.05	C	2.02	Ce	0.06	F	1.01
Nd	0.15	$\sum$REE	0.00	Nd	0.00	La	0.01
Sm	0.01			C	0.99	Ce	0.03
Eu	0.00			$\sum$REE	0.00	Nd	0.02
Tb	0.00					Sm	0.00
Dy	0.00					$\sum$REE	0.08
Er	0.00						
C	2.03						
$\sum$REE	1.01						

Table 7.7: APFU of Tundulu minerals calculated from the average EMPA values in Table 7.6.

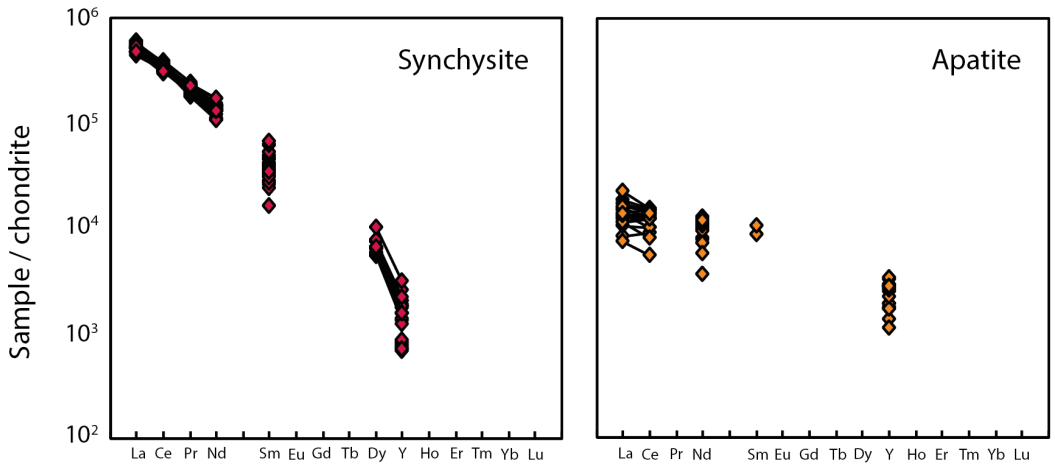

Figure 7.16: Chondrite-normalised REE concentrations in synchysite and apatite at Tundulu. Chondrite values of McDonough and Sun (1995) used for normalisation.

Discussion

The textures displayed in these samples indicate disequilibrium either between the constituent minerals, or the fluid in contact with them. In both samples the apatite and C1 carbonate (heavily altered) are clearly older than the REE mineralisation, which itself seems to be older than C3 carbonate). The C2 carbonate, if it is distinct from C3, is probably older than the synchysite, although this is not easy to determine from the evidence provided here.

The observed mineralogy and textures agree with the paragenesis as proposed by Broom-Fendley et al. (2016), although here more emphasis was placed on the carbonate and fluorocarbonate phases. This has led to a slight modification of his interpretation, as presented in Figure 7.17 (a revised version of Figure 7.4). Apatite and C1 carbonate are proposed as being earliest, both of which were altered by later fluids – this may coincide with the initial breakdown of apatite and formation of turbid cores in Broom-Fendley et al. (2016). Then came C2 carbonate, followed by synchysite. Dissolution of C2 carbonate may have aided synchysite precipitation, as the former shows heavily pitted/altered textures in contact with large areas of the latter (e.g. Figure 7.15b). However, if this was the case, the difference in chemistry between C2 carbonate from sample 278 (calcite) and 4905 (ferroan dolomite) did not affect the composition of the synchysite. It is unclear whether C3 carbonate is later or contemporaneous with REE mineralisation, but further changes to the system caused the breakdown of synchysite and C3 carbonate (to Fe and Mn oxides), which increased the Ca^{2+} and CO_3^{2-} activity and led to the transformation of synchysite to parisite(?) at the contacts of the synchysite and C3 carbonate. C3 carbonate is therefore proposed as being hydrothermal in origin, with C1 and C2 likely primary but altered by hydrothermal fluids.

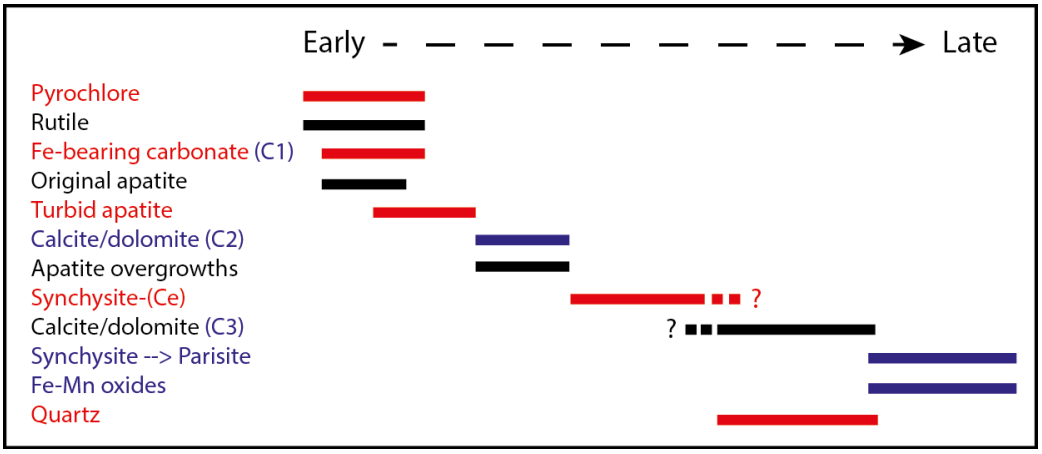

Figure 7.17: Revised paragenetic sequence for the mineralisation seen at Tundulu based on the findings of the current investigation, updated from that of (Broom-Fendley et al., 2016). The new observations are in purple, and the updated carbonate classifications are shown in parentheses.

This interpretation agrees with the findings of Ngwenya (1994) insofar as the breakdown of Ca-bearing carbonate wall rock supplied the Ca^{2+} and $CO_3{}^{2-}$ necessary for Ca-REE fluorocarbonate formation. However, the idea of different wall rock compositions (calcite or ankerite) limiting the supply of Ca^{2+} and $CO_3{}^{2-}$, and therefore controlling whether bastnäsite or synchysite/parisite formed, cannot be explored because no bastnäsite was identified in either of the samples studied here. The absence of this mineral does follow the hypothesis though.

In Ngwenya (1994), parisite was suggested to have possibly formed from the breakdown of synchysite to produce calcite:

$$2\,\mathrm{CaREE(CO_3)_2F_{(s)}} \longrightarrow \mathrm{CaREE_2(CO_3)_3F_{2(s)}} + \mathrm{CaCO_{3(s)}} \tag{7.10}$$

The problem was, the calcite expected from this reaction was not found. In the current study, there is abundant calcite intimately associated with synchysite/altered synchysite. However, based on the textures seen in the current investigation, the following reaction of synchysite to parisite is suggested:

$$2\,\mathrm{CaREE(CO_3)_2F_{(s)}} + \mathrm{CaCO_{3(s)}} + \mathrm{H^+_{(aq)}} \longrightarrow \mathrm{CaREE_2(CO_3)F_{2(s)}} + +\mathrm{Ca^{2+}_{(aq)}} + \mathrm{HCO_3{}^-{}_{(aq)}} \tag{7.11}$$

Which requires the solution causing alteration to be acidic, something that cannot be proven here, although the widespread pitting/alteration of the other carbonate phases is suggestive of such conditions. The consistent chemistry displayed by the synchysite suggests its deposition from a single source/fluid.

The source of fluoride necessary for the precipitation of synchysite is unknown, but the lack of fluorite in these samples does not suggest high levels of fluorine (presumably there is fairly high Ca^{2+} given all the carbonates?). In his study, Broom-Fendley et al. (2016) inferred the fluid composition as being high in chloride based on the alteration of apatite but absence of monazite, something only reported-previously during experiments with NaCl or $CaCl_2$ (albeit at much higher temperatures, 900 °C - Harlov and Forster, 2003). This was also used to infer REE-chloride complexation in these fluids, leading to greater stability of LREEs (Migdisov and Williams-Jones, 2014) and therefore explain the HREE-rich cores, and LREE-rich rims, of altered apatite. The fluoride source was not mentioned in that study. In contrast, Ngwenya (1994) proposed REE transport in the form of fluoride complexes (although this was based on the theoretical predictions of Wood, 1990b), or by a hypothetical $REECO_3F$ complex. However, as noted earlier, the existence of this latter complex has to this day not be proven. The transport of REEs as complexes with fluoride, given the new data of Migdisov and Williams-Jones (2014), seems unlikely at Tundulu, particularly as significant carbonate exists in this system capable of buffering the fluids and promoting REE precipitation. An alternative source could be from the breakdown of primary fluo-apatite, particularly as the latter is known to be earlier than REE mineralisation.

7.5 Comparison of results and chapter conclusions

Comparison of experimental data with interpretations made from natural samples is very challenging due to differences in fluid conditions and REE concentrations. The paragenesis of Bayan Obo is very complex and includes multiple mineralisation events, however, fluid inclusion data suggests temperatures around 460 °C (aegirine alteration) and 150 °C (late stage Ba mineralisation – e.g. Smith and Campbell, 2000). No direct temperature data exist for Tundulu, although 160 °C has been calculated as the minimum formation temperature of HREE mineralisation in a carbonatite located in the same province (Broom-Fendley et al., 2017), and may be significantly higher. Despite this, a few general comments can be made about processes occurring in both.

Results from the experiments have demonstrated the effectiveness of the method at precipitating REEs, and although only conducted at low temperature (< 100 °C), act as a starting point further investigation. Examples of REE carbonate, REE fluoride and REE fluorocarbonate precipitation in the presence of dolomite and fluorite dissolution have been observed; the occurrence of more than one of these phases in the same experiment, however, was confirmed only once (Yb-bearing solution). In the other experiments (La, Nd, Er, La+Er, La+Yb) only one of these products was detected, but no clear pattern was seen. Perhaps the most interesting observation, and in line with many of the results from the previous chapters, was the difference in the products from

single- vs multi-REE solutions. In this chapter, both multi-REE solutions resulted in the formation of REE fluorocarbonates, in comparison with only one of single-REE experiments (Nd). The reasons for this are currently unclear, but it would be interesting to take these experiments to higher temperatures and see if the results at 90 °C are reproduced.

The textures observed in the Bayan Obo thin sections point to disequilibrium between the minerals and the fluids, but the proposed reactions from previous studies (with which the current study mostly agree) do not match any of those for the experimental data, primarily because the natural system is more complex (particularly the presence of the phosphate-bearing minerals monazite and apatite). Despite the presence of large volumes of fluorite at Bayan Obo, there is no indication of REE fluoride minerals, nor of the formation of REE fluorocarbonates at the expense of fluorite (or fluorite and carbonate). As the latter reaction has been shown possible experimentally, this indicates either these reactions are not applicable at the conditions of formation at Bayan Obo, or it is a paragenetic issue in that fluorite post-dates REE mineralisation (at least in the studied samples). Clearly further experiments in which phosphate was somehow included (either in dissolved form or as a reactive mineral, like fluorite was here) would be required to better understand mineralisation at Bayan Obo (and other deposits in which these minerals coexist).

Although the system responsible for the mineralisation at Tundulu was also more complex than the experiments presented here, the proposed dissolution of carbonate rocks and subsequent release of dissolved carbonate and calcium required for REE fluorocarbonate precipitation is similar. However, in the natural case, synchysite (i.e. Ca-bearing) was the only REE fluorocarbonate to form, yet none was observed experimentally. This might be explained by higher Ca^{2+} activity in the natural system (perhaps the REE-bearing solutions were Ca-rich too?) or differences in solubility of Ca- and non-Ca-bearing fluorocarbonates (which is likely influenced by the temperature and solution chemistry). The significance of temperature during the formation of discrete LREE and HREE-enriched carbonate phases was demonstrated in Chapter 6, and highlights the need for more experiments in which fluoride is included. Perhaps at higher temperatures the REE fluorocarbonate to form is synchysite, which would make these experiments more applicable to the study of mineralisation at Tundulu. Nevertheless, the results presented in this chapter provide a simple and easily-reproduced method on which to base further REE fluorocarbonate synthesis experiments.

Chapter 8

Synthesis, conclusions and ideas for future work

8.1 Chapter conclusions

The principal goal of this research project was to better understand the conditions at which REE carbonates and fluorocarbonates are formed, the influence that single- vs multi-REE systems have on this process, and the whether the results are at all comparable to natural deposits. To this end, two main experimental pathways were taken, with the aim of synthesising first REE carbonate, then fluorocarbonates. The results of these experiments are summarised below, and combined and compared with each other and with previous work. This thesis is closed by a critical review of the experimental setup and procedures, followed, based on that review, by some ideas for future work.

8.1.1 Chapter 4 - REE chloride titrations

Chapter 4 detailed the results of experiments in which REE chloride solutions were titrated with sodium carbonate, followed by ageing at temperature. The objectives here were:

1. Synthesise REE carbonates *via* titration experiments, and assess the influence of temperature on the product (e.g. crystallinity, morphology);
2. Use representatives from across the REE series to assess any influence Z might have on the products;
3. Determine the influence that single- and multi-REE-bearing systems have on the products.

The results from single-REE-bearing experiments with LREEs were in excellent agreement with recent work (e.g. Vallina et al., 2014; Rodriguez-Blanco et al., 2014; Vallina

et al., 2015), where crystallisation of lanthanite, kozoite and hydroxylbastnäsite was observed. The structure and morphology of crystals depended on the temperature and length of ageing. Experiments involving the HREEs were less consistent, with crystalline material formed only at > 90 °C for Yb (although the structure formed at 130 °C was unidentified). Results from Er experiments revealed the reaction is strongly influence by kinetic factors, as a crystalline phase was only observed in the sample analysed after 84 days; at all other experimental conditions the material was X-ray amorphous (even at 200 °C).

Perhaps the most interesting observation from this chapter were the results of mixed-REE experiments. When LREEs were mixed the products were highly crystalline, and when HREEs were mixed the material was X-ray amorphous, but when mixed LREE+HREE solutions were used, the precipitates exhibited properties more akin to the HREE-only runs.

In all but two examples, the 'fresh precipitate' (i.e. that formed at the end of an approximately 10-minute titration) was found to be X-ray amorphous, indicating a non-classical crystallisation pathway for REE carbonates, consistent with Ostwald's step rule. In the LREE system, the formation of this material is either followed by its dissolution-precipitation to hydrated normal carbonates (e.g. lanthanite), or based on the results in Chapter 5, potentially formed directly from the X-ray amorphous precursor. With increased temperature, these hydrated phases dehydrate, leading to tengerite, then kozoite and finally hydroxylbastnäsite. In the HREE system, the Yb phases to form at 130 °C and higher did not contain water molecules (only hydroxyl ions were detected with FTIR).

New contributions to the literature from this chapter:

1. A linear relationship between REE atomic number and dehydration energy of the X-ray amorphous precursor had been previously proposed based on results from La, Ce, Pr, Nd, Dy and Yb carbonates (Nagashima et al., 1973; Vallina et al., 2013; Rodriguez-Blanco et al., 2014; Vallina et al., 2015). The results of Er and Yb experiments demonstrate this trend is not in fact linear, as Er appears to behave anomalously, at least under the conditions of this study;

2. Mixed-REE systems behave quite differently to their single-REE counterparts. The characteristics of precipitates are dominated by that of the heaviest REE in the mix (in the case of two element systems). Even in the case of La+Nd, the presence of Nd inhibited the growth of lanthanite in the fresh precipitates (the Bragg peaks were weaker than in the La-only example; the Nd-only sample was X-ray amorphous). Two-REE mixes containing Er or Yb were X-ray amorphous, including those taken up to 200 °C (Nd+Er). These observations may have

implications for the controlled growth of crystals in which different REEs are doped.

8.1.2 Chapter 5 - XAS study of solution, fresh and aged precipitates

The observation of X-ray amorphous precursor phases during the titrations of Chapter 4 led to a more detailed investigation of their properties in Chapter 5. XAS (XANES and EXAFS) was used to probe the local structures of the X-ray amorphous Nd, Er and Yb 'fresh precipitates', and the Er and Yb aged products. A few of the crystalline materials (La and Nd) were analysed for reference. In addition, new titrations were undertaken, this time at temperature, with two aliquots obtained: once during the initial period of rapid pH rise (pre-stat), and the other when pH remained static despite significant dissolved carbonate addition (stat). The objectives were:

1. Determine the local structure of solution precipitates and X-ray amorphous materials, and compare the two;
2. Identify whether the structure of bulk X-ray amorphous material was the same as solution precipitates – i.e. is the structure of the bulk predetermined by that of the earlier precipitates?;
3. Determine if the structure of X-ray amorphous material is similar to crystalline materials into which that element it is known to crystallise?

It was not possible to model the La solutions beyond first-shell oxygens, which although not much information, was enough to confirm these phases to be neither lanthanite-(La) nor hydroxylbastnäsite-(La). The 'fresh precipitate' of this sample, obtained at the end of the titration, was lanthanite. The X-ray amorphous La phase was not observed in this study because the titration method was used (it was observed by Vallina et al., 2015 after direct solution mixing).

The Nd 'fresh precipitate' had a short-range structure containing mixed mono and bidentate carbonates, potentially analogous to lanthanite. Given this material went on the form well crystalline lanthanite-(Nd) (Chapter 4), it is postulated that the X-ray amorphous material may not dissolve then reprecipitate, as previously suggest, but instead lanthanite forms directly from it.

In the Er experiments, the solution precipitates were thought to be Er carbonates, although it was not conclusive. This material had a different structure to the 'fresh precipitate', which itself was similar to (but not the same as) the aged product (which went on to crystallise as tengerite). Results of Yb suggested the same structure from solution to aged material (except perhaps in the Yb 90 stat sample), and was therefore

the only REE studied in which the solution precipitates/clusters were shown to have the same local structure as the X-ray amorphous phase.

New contributions from this chapter:

1. First (local) structural study of the X-ray amorphous 'precursor' or 'fresh precipitates';
2. The results of mixed REE (Nd+Er) precipitation have shown that when Er is included and the precipitates are X-ray amorphous, the distribution of the different REEs is even (opposed to Nd- and Er-rich areas). This would account for the X-ray amorphousness, as Nd-rich clusters might be expected to crystallise as discrete phases admixed with X-ray amorphous Er. Such observations would also have implications for controlled synthesis of multi-REE carbonates.

8.1.3 Chapter 6 - Wall rock reactions with dolomite

Fluid-rock reaction experiments are common in the literature, but those related to REE carbonate synthesis are not. The objectives of this chapter were:

1. Determine whether the reaction of a REE-rich solution with a carbonate rock results in the precipitation of a REE carbonate mineral;
2. As in previous chapter, assess the influence of temperature on the characteristics of the product;
3. Identify any cross-series trends or patterns; single- vs multi-REE solution comparisons; comparisons with titration experiment results.

REE-rich solutions were reacted with dolomite at temperatures ranging from 90 to 200 °C, with the products characterised by PXRD and SEM. In contrast to the results of titrations, here crystallisation was observed in all but one of the experiments, including those conducted with Er, Yb and multi-REEs (three- and five-REEs).

La and Nd experiments produced the familiar set of minerals (lanthanite, kozoite, hydroxylbastnäsite) in varying proportions depending on temperature and length of ageing, albeit with different morphologies to Chapter 4. These followed the same sequence as before (lanthanite → kozoite → hydroxylbastnäsite). Er produced large (100s μm length), acicular crystals of tengerite at temperatures as low as 90 °C, and a kozoite-type phase at 130 °C and higher. The latter has not been identified in nature, but has been previously synthesised (Tahara et al., 2007). A 90 °C experiment with Yb was the only to not produce any new mineralisation; at 170 and 200 °C widespread crystallisation of a material(s?) with an unidentified structure was detected.

Two multi-REE systems were explored (Nd+Er and five-REE mix). Nd+Er experiments resulted in widespread mineralisation with varied morphologies from 90 to 200 °C. There was evidence of both Nd- and Er-rich phases, although this would require a more detailed study to make any further conclusions, as it is currently unclear if minerals are zoned, if there is preferential dissolution (and reprecipitation?) of either REEs, or if they exhibit consistent behaviour. In the five-REE experiments (only conducted at 130 °C and higher), discrete LREE- and HREE-enriched phases were identified. The crystallisation sequence was unclear from the SEM images, with a few suggested options: 1) was an initial five-REE-bearing carbonate (as seen at 130 °C) formed first, followed by its complete dissolution, then precipitation of the L- and HREE phases?; 2) did a relatively LREE-enriched phase form first (but still containing some HREEs), followed by a relatively HREE-enriched phase at higher temperatures (i.e. similar to the titration results)? Although these questions remain unanswered, the observation of discrete phases at the higher temperatures and the lower abundance of HREE-phases may be of relevance to natural REE deposits.

Mineralisation in all but one of the experiments, when compared to the common X-ray amorphous material formed during titrations, points to the rate of dissolution having a major control on crystallinity. The slower rate experienced in the wall rock reactions (controlled by the dissolution of dolomite) would result in only localised supersaturation of the solution with respect to the REE carbonate, and therefore promote growth rather than multiple nucleation events – this would certainly account for the large acicular crystals of Er tengerite. The formation of the same X-ray amorphous precursor material as seen in Chapters 4 and 5 cannot be ruled out, but seems unlikely given its absence in the 90 °C Yb dolomite experiment (and lack of other crystals).

New contributions to the literature from this chapter:

1. The reaction of a REE-rich solution with a carbonate rock does result in the precipitation of a REE carbonate mineral. This is a common reaction quoted throughout the literature, but has until now not been determined experimentally;
2. Temperature has a significant control on the morphology of the new minerals;
3. In multi-REE systems, discrete L- and HREE-enriched phases form, which may have implication for natural deposits;
4. HREE carbonates are valid species under these conditions, and their absence from natural sites is therefore likely a consequence of the (relatively) HREE-depleted fluids, and not structural constraints (except perhaps for the heaviest REEs).

8.1.4 Chapter 7 - Wall rock reactions with dolomite plus fluorite, and EMPA of carbonatites

A continuation of Chapter 6, here a preliminary set of wall rock experiments were conducted but this time in the presence of a fluoride source (fluorite). The objectives were:

1. To assess whether a REE fluorocarbonate could be formed by the reaction of REE-rich solutions with dolomite and fluorite;
2. Determine any cross-series changes in the characteristics of the products;
3. Compare results (and consequent models/reactions of their formation) with previously suggested ideas of wall rock compositional control to observed REE fluorocarbonate species in natural deposits.

This last point was assessed not only by comparison with the literature, but also a small mineralogical and textural study (using EMPA) of two REE fluorocarbonate-bearing carbonatite deposits (Tundulu, Malawi, and Bayan Obo, China).

The results from wall rock experiments were interesting. It was thought the LREEs (La and Nd) would synthesise bastnäsite, but instead this mineral only formed in the Nd experiments, with La fluoride the sole product in La run. In the Er experiment only tengerite was observed (with the same acicular morphology as Chapter 6), and both Yb fluoride and Yb carbonate were formed from the Yb solution. Most interestingly, the mixed La+Er and La+Yb products were bastnäsite, with no other phases detected. No Ca-REE fluorocarbonates were formed. The reasons for these results are currently unexplained, but the differing behaviour of single- and multi-REE systems is in accordance with the other data chapters in this thesis. These experiments were only conducted up to 90 °C, and are at most a preliminary look at this system, but the few results obtained certainly set the stage for future investigation.

The EMPA studies revealed little new information for the Bayan Obo samples, but a small adjustment to the paragenesis at Tundulu was presented based on the identification of a potential new carbonate deposition stage. The REE minerals at both sites were strongly LREE-enriched, while apatite displayed flatter chondrite-normalised plots. Fluorite and carbonates were almost REE-barren. No REE carbonates or REE fluorides were found. These results, as expected, revealed the experimental conditions and results were not directly applicable to the study of natural deposits. Conducting experiments at higher temperatures, and a greater number of reactive products (a notable one being apatite) would be the first steps towards closing the gap between lab and real-life.

The results of Chapters 6 and 7 point to REE solution concentrations being the major control to HREE carbonate and fluorocarbonate mineralisation, as both have been shown possible to synthesise, even at low-end hydrothermal conditions.

New contributions:

1. REE fluorocarbonates can be synthesised *via* the reaction of REE-rich chloride solutions with a reactive carbonate and fluoride source, although the new mineralisation appears to be very localised with respect to the point of reactant supply;

2. Preliminary results suggest single-HREE fluorocarbonates are not formed, but that HREEs can be accommodated when in the presence of LREEs (suggesting HREEs are too small to form fluorocarbonates on their own?).

8.2 Final synthesis and comments

Taken altogether, the results from this investigation reveal some new information on the geochemistry of REEs in the presence of carbonate and fluoride, and the subsequent precipitation of REE carbonate and/or REE fluorocarbonates. A summary of results from the titration and wall rock experiments (excluding those involving dolomite + fluorite) is shown in Figure 8.1 to aid the comparison of results between the two main experimental methods used in this thesis.

An obvious observation from Figure 8.1 is the difference between the presence and absence of X-ray amorphous results ('A') during titration and wall rock experiments, respectively. This X-ray amorphous phase was identified, during Chapter 5 (XAS), to in some cases possess short-range structure similar to the first mineral to form in the crystallisation sequence for that particular REE (e.g. the X-ray amorphous fresh precipitate for Nd had a similar structure to lanthanite; X-ray amorphous Er precipitates had a similar structure to tengerite). Another observation from Figure 8.1 with regard to this X-ray amorphous material is that it is more common for HREEs and mixed precipitates in which HREEs are included. This was suggested as being a consequence of the greater energy required to dehydrate this material when formed from heavier REEs (although the linear relationship with atomic number, as previously suggested, appears not valid). The lack of X-ray amorphous material identified during wall rock experiments is suggested as being a consequence of the rate at which dissolved carbonate is delivered to the system, and, therefore, the rate at which supersaturation with respect to the first precipitated phase occurs. The relative difference in rates at which supersaturation are suggested to be achieved is demonstrated in Figure 8.2.

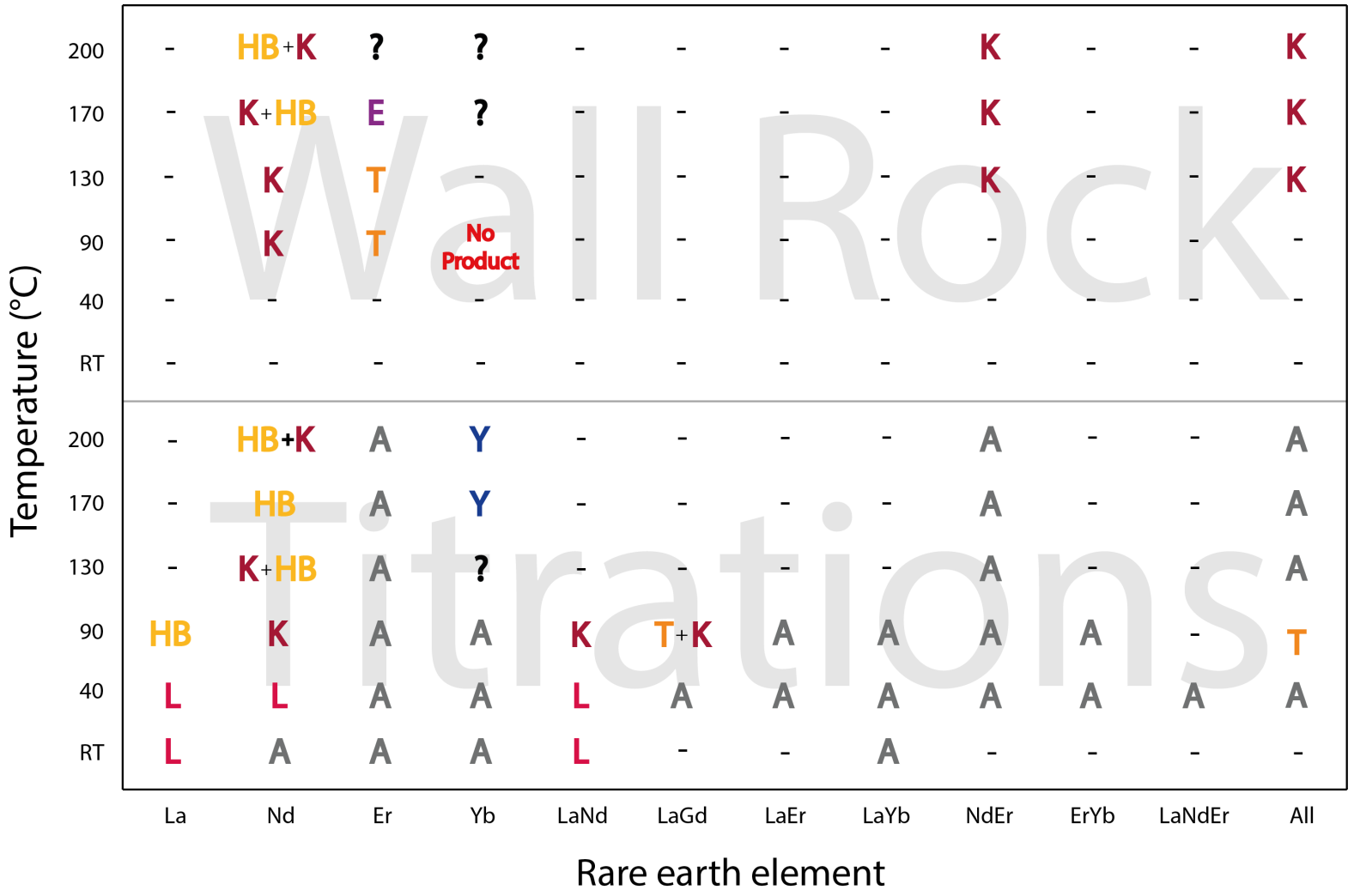

Figure 8.1: Summary and comparison of results for all the titration (bottom) and wall rock experiments (top), excluding those in which fluorite was also used. A hyphen denotes no experiment; L = lanthanite; K = kozoite; HB = hydroxylbastnäsite; T = tengerite; E = orthorhombic $ErCO_3OH$; Y = monoclinic $Yb_2O(OH)_2CO_3$; ? = crystalline but unidentified phase; A = X-ray amorphous. RT = room temperature; All = La + Nd + Gd + Er + Yb. Specific experimental conditions can be found in the relevant data chapter (4 and 6).

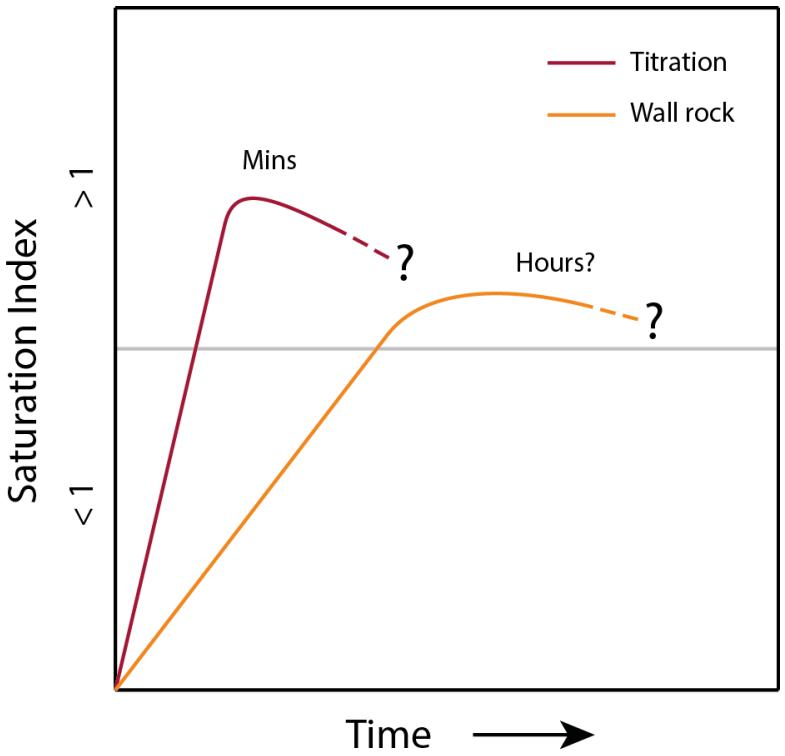

Figure 8.2: Relative estimations of the rate at which the solutions reach supersaturation with respect to the first-formed phase in titration and wall rock experiments. The time scales in the wall rock experiments are unknown, but preliminary runs (mentioned in Chapter 3) indicated no neo-formed phases after three hours at 90 °C (in a 0.02M Nd chloride solution). This diagram is not representative of a particular temperature, and as such the question marks simply indicate the variable fate of the first-formed material, the lifetime of which was strongly controlled by the temperature at which the solutions were heated. The first-formed product in the case of all titrations was an X-ray amorphous material (Chapter 5). Details of the products formed after heating are shown in Figure 8.1.

In the titration experiments, supersaturation is reached solution-wide within only a few minutes (once the low-pH REE solutions were buffered by carbonate addition to below the solubility levels of the first REE precipitate in the sequence - the X-ray amorphous material identified in Chapters 4 and 5), whereas in wall rock reactions supersaturation is only reached once the dolomite starts to dissolve, and is likely only to occur locally, at least during the initial phases of dissolution. The change in pH during titration experiments was documented as a function of Na_2CO_3 addition, and was seen to follow a pattern of 'rapid-rise - static period - raid-rise', the middle of which was attributed to REE carbonate formation (as discussed in Chapters 3 and 4). The rapid addition of dissolved carbonate in titrations meant that pH rose quickly from the start point of around 0.8, which would have promoted the widespread nucleation of initial phases, and ultimately REE carbonate formation (*via* the X-ray amorphous material). During exploratory experiments (mentioned in Chapter 3) it was found that no neo-formed mineralisation was identified on the dolomite surfaces after reaction with a 0.02M Nd chloride solution for three hours at 90 °C. This would suggest that, at least under those conditions, supersaturation of the solution with respect to the first-formed mineral (suggested here as being lanthanite, and not the X-ray amorphous material) takes

longer than three hours (i.e. significantly longer than in titrations). Given the lack of X-ray amorphous material identified in any of the wall rock experiments, it is further suggested that crystallisation of lanthanite (La and Nd) and tengerite (Er) may form directly on the dolomite surfaces, which occur due to local increases in dissolved carbonate and pH. It is still unclear as to whether the crystallisation of phases seen at higher temperatures results from dissolution-precipitation of earlier phases, or directly from solutions (this was discussed in the crystallisation model in Chapter 6). However, it is also noted that a scenario in which the X-ray amorphous material is formed at the dolomite surface and subsequently crystallises into the phases just mentioned cannot be ruled out.

Nucleation of initial phases in solution is aided by the presence of impurities, for example dust particles, mineral and container surfaces, grain boundaries, etc (this is known as heterogeneous nucleation, e.g. Thanh et al., 2014; Karthika et al., 2016). In the case of wall rock experiments it is clear that nucleation is heterogeneous (as indicated by the formation of minerals on the dolomite and fluorite surfaces, especially along cleavage of the former), whereas in the titration experiments homogeneous nucleation (uniform formation of nuclei throughout the solution) may be applicable. However, the solutions used (i.e. the REE chloride and sodium carbonate) were not filtered prior to titrations, and, therefore, are likely to contain microscopic impurities, particularly dust. Therefore, in addition to the rapid increase in carbonate ion activity experienced during titrations relative to that during dissolution of dolomite, there were likely abundant nucleation sites throughout the solutions, aiding the rapid formation of the first-formed, X-ray amorphous material. In wall rock reactions, the same impurities are likely to exist, but dissolved carbonate addition is slower, and more local to the dolomite surface, leading to crystal growth at these sites and not in solution. The same applies to the mineralisation in the dolomite + fluorite reactions.

Perhaps the most obvious observation from Figure 8.1 is the change in structure of minerals as a function of both ageing temperature and the constituent REE(s). However, even between methods, a consistent pattern for LREE carbonate crystallisation pathways is emerging. In the case of La this starts with the formation of orthorhombic lanthanite ($REE_2(CO_3)_3 \cdot 8\,H_2O$), and is terminated (under the conditions of this study) by hexagonal hydroxylbastnäsite ($REECO_3OH$). In the Nd system an additional phase, orthorhombic kozoite ($REECO_3OH$), was identified as forming between lanthanite and hydroxylbastnäsite. These results are in excellent agreement with recent work (e.g. Vallina et al., 2015), and represent a dehydration reaction followed by a change in crystal system. In the current study, mixtures of kozoite and hydroxylbastnäsite were identified at 130 °C in titration experiments, but only kozoite was detected at the same temperature in wall rock reactions; at 170 °C only hydroxylbastnäsite was detected in titration results, but a mixture of kozoite and hydroxylbastnäsite was seen in wall

rocks. These results suggest that the rate at which the crystallisation sequence (lanthanite → kozoite → hydroxylbastnäsite) occurs/progresses is greater in the titration experiments, which in turn implies that dehydration of the X-ray amorphous precursor phase in titrations is faster than the dissolution-precipitation of dolomite and REE carbonate phases in wall rocks reactions.

With an increase in atomic number of the REE investigated comes a more complicated story, with contrasting results for titrations and wall rock experiments (Figure 8.1). The results of titrations demonstrate that Er and Yb are unsuitable for the low-temperature precipitation of crystalline carbonates with controlled morphologies required for nano- and micro-technologies (e.g. Kaczmarek et al., 2015), at least under the conditions employed here. This is in contrast to room temperature synthesis of HREE carbonates (Tb, Er, Ho, Yb, Lu and Y - Liu and Ma, 1996a, 1997b,a; Liu et al., 2000; Liu and Ma, 2007) produced by leaving (for one week) a mixture of ammonium bicarbonate and REE chloride solutions, which highlights the influence of carbonate source to product crystallinity during these reactions. However, the study of Nagashima et al. (1973) (mentioned in Chapter 3), during which the methods for REE carbonate precipitation were compared, concluded that changes in structure of products were not influenced by the preparation technique (which included different carbonate sources), but only by the temperature at which solutions were heated. The results of that study are shown again in Figure 8.3 (a repeat of Figure 2.4). The reasons for contrasting behaviour of HREE precipitates from the titrations of the current investigation, those of Nagashima et al. (1973), and the other studies mentioned earlier in this paragraph are unknown, and further highlights to complexity of these reactions. However, given the suggested role that the first-formed phase in titration experiments imposes a significant influence on the crystallinity (or rate at which crystalline material is formed) of products, it would be reasonable to invoke this as significant in those other studies. It would, therefore, be interesting to repeat the experiments mentioned above in which both X-ray amorphous and crystalline HREE carbonates were identified, but analyse the first-formed phase (as was done in the current investigation) to assess whether there is any difference as a function of carbonate source.

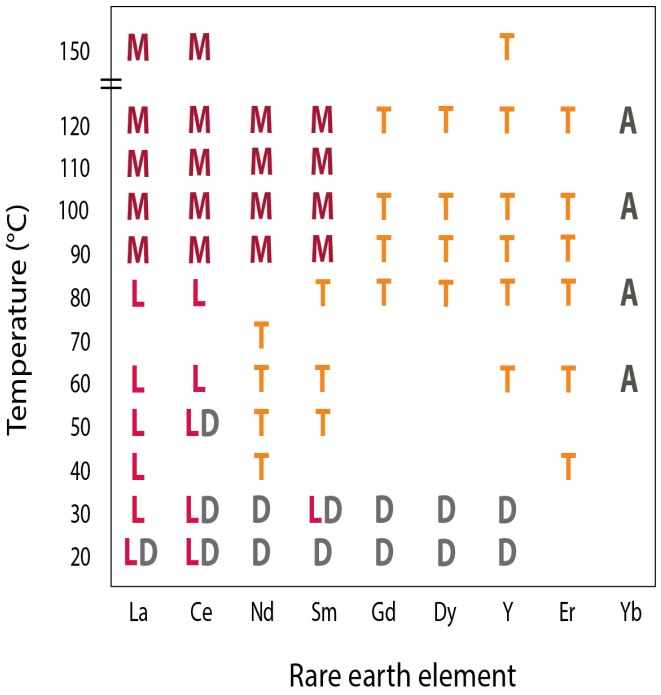

Figure 8.3: Summary of the results obtained by Nagashima et al. (1973), highlighting the different structures formed as a function of REE Z and temperature. M = monoxocarbonate; T = tengerite; L = lanthanite; D = double carbonate (e.g. hydrated carbonate of REE anf Na); A = amorphous.

Results of the titration experiments are in contrast to those of wall rock reactions for HREEs (Figure 8.1). Excellent crystallisation was observed in the latter, although the Yb mineralisation was unidentified at all temperatures (it was not the same as monoclinic $Yb_2O(OH)_2CO_3$ identified at $>$ 130 °C in the titrations). In the case of Er, the low temperature structure to form is not lanthanite as seen for La and Nd, but orthorhombic tengerite ($REE_2(CO_3)_3 \cdot 2{-}3\,H_2O$), which is in agreement with Nagashima et al. (1973) (Figure 8.3), and also Liu and Ma (2007). This change in structure has been suggested as being a consequence of the lanthanite contraction - i.e. that only REEs with radii larger than about Sm may form lanthanite. At higher temperatures the Er phase detected was first orthorhombic $ErCO_3OH$ (a modification of the kozoite structure), and finally an unidentified phase (at 200 °C). The lanthanide contraction is also the reason why Yb does not form the tengerite structure. In fact, based on the results/conditions of this investigation, it might be possible that no stable phase of Yb carbonate can form at temperatures below 130 °C. This is supported by Nagashima et al. (1973) (Figure 8.3), who only identified an X-ray amorphous material (their highest temperature was 120 °C) The relative lack of HREE mineralisation during titrations experiments is again suggested as being a consequence of the increased energy required to dehydrate the X-ray amorphous precursor phase - i.e. that in contrast to the LREEs, the time taken/energy required to dehydrate this phase is longer/greater than the rate at which crystallisation can form directly on the dolomite surfaces.

Differences in crystal morphologies between titrations from the current study and the results of e.g. Vallina et al. (2015) and Vallina et al. (2014) - despite both studies using very similar methods – demonstrates another experimental variable of importance to crystal morphology, i.e. heating rates. The differing behaviour of REEs when in the presence of one or more REE is yet another variable, and while this appears to have implications for the controlled growth of multi-REE or REE-doped materials (e.g. Bhargava, 1996; Bunzli and Piguet, 2005; Kaczmarek et al., 2015), it does not influence the ability of multi-REE-bearing carbonates to precipitate during carbonate rock dissolution. Another important variable in the starting concentration of REEs in solution, particularly as, for example, Zhang et al. (2009) have shown that the morphology of yttrium carbonates changes when precipitated under the same conditions other than varying molar ratios of $Y(NO_3)_3 \cdot 6\,H_2O$ to urea. In the experiments undertaken during the present work, REE concentrations varied from 0.1 M to 0.02 M, which was a consequence of the original experimental design not including > two REEs in solution (i.e. this was only decided once the one- and two-REE titration experiments were planned and completed). Further into the project it became apparent that use of lower concentrations still afforded a high enough yield for the successful characterisation of any product material, and, therefore, these experimental conditions were implemented as standard during the later stages of the work.

Based on the results from Figure 8.1, and the subsequent discussion in the previous paragraphs, a general pattern for the structure of REE carbonate precipitates is orthorhombic into hexagonal (confirmed for LREEs and LREE mixed precipitates). The presence of HREE(s) appears to retard this transformation, as evidenced by the formation of a kozoite-type structure at temperatures up to 200 °C when all five REEs investigated presently were in solution. These observations appear to be in contrast with the results of synthetic REE fluoride precipitation, which found hexagonal crystals for REEs La - Eu, and the orthorhombic system for Eu - Lu (Wang et al., 2006). In that study REE nitrate solutions were heated with sodium fluoride or ammonium bifluoride at 100 - 200 °C for 8 - 10 hours, however, it is noted that the large temperature range stated makes direct comparison with the current investigation unreliable. In fact, if the temperatures were in the region of 150 °Cor greater, the results of REE fluoride precipitation are almost the same as that of REE carbonates in the current work.

The reaction between REE chloride and carbonate rocks has been suggested as a major control to REE transport/deposition in natural systems (e.g. Ngwenya, 1994; Smith et al., 1999; Williams-Jones and Palmer, 2002; Migdisov and Williams-Jones, 2014; Graupner et al., 2015; Migdisov et al., 2016; Trofanenko et al., 2016; Benaouda et al., 2017; Broom-Fendley et al., 2017). Although the temperatures employed in the current investigation are lower than those suspected of forming ores/REE mineralisation, and the fluid compositions are likely far simpler than in nature, the experiments presented

in this thesis provide a simple yet effective method that go some way to confirming those previously proposed theories. In addition, the system can be easily adapted and expanded to increase its complexity. The preliminary experiments in which fluorite was used also provide a potential new method for studying these systems, although the low solubility of REE fluorides (e.g. Migdisov et al., 2009) still makes this challenging.

8.3 Critical review

A notable drawback to this project was not having any data on the solubility of the X-ray amorphous precursor material. Knowing this would allow for comparison with the recent solubility data for hydroxylbastnästie-(La), -(Nd) and kozoite-(Nd) (Voigt et al., 2016), and help determine the rates at which supersaturation is reached within the solution. This is important to understand when controlled synthesis of crystals of certain morphologies is desired – e.g. for nano- and micro-technologies. However, determining the solubility of the X-ray amorphous material is inherently difficult given its metastability. Solubility measurements of the other commonly referenced minerals, particularly the HREE species (e.g. tengerite), would also be highly beneficial for determining crystallisation pathways.

Analysis of the solutions post-experiment (all experiments) is something that would have provided a wealth of important and interesting information. The carbonate was added in excess during titrations (and the final pH was around 8.5), indicating the REEs were quantitatively precipitated, but the pH of wall rock experiments was unknown. Knowing the REE concentration post-experiments would be particularly interesting in the mixed-REE solutions, as it may shed light on whether initial precipitates remove LREEs and HREEs equally from solution or not. In wall rock reactions, determining the dissolved carbonate concentration (and pH) may help to explain why HREE and mixed-REE carbonates formed at (almost) all temperatures investigated, as it was postulated this was controlled by the rate at which supersaturation with respect to the minerals was achieved. The same is true of the experiments in which fluorite was used as a reactant (i.e. monitoring dissolved fluoride concentrations).

Another obvious step to take, given the variable results between LREEs, HREEs, and mixed solutions, would be to increase the experimental matrix, as the solutions used in this study were restricted to those containing REE chlorides, and the number of reactant phases did not exceed two, which most likely is an oversimplification of natural systems. This would also include extending the temperatures explored into the range thought most likely to be responsible for hydrothermal mineralisation (not just of REEs, but other metals also), perhaps up to 500 °C, as previous works are mostly restricted to low (up to about 250 °C) or very high (> 700 °C). However, as noted

throughout this work, there are significant issues associated with other REE-ligand pairings such as fluorides or carbonates, which is a shame given their potential importance to the precipitation of REE carbonates and fluorocarbonates. These difficulties were the principal reason for the use of chloride-rich solutions, but also the fact that REE chlorides are thought to be the most likely agent of transport in hydrothermal fluids. Unfortunately, there are few published studies in which solution chemistries - including REE concentrations - are reported for natural systems (i.e. from fluid inclusion data - e.g. Banks et al., 1994), which hampers direct comparison with controlled experimental conditions. As discussed in Chapters 3 and 4, a large number of solution mixing experiments have been conducted for single-REE solutions, but the results of those containing mixed-REEs in the current investigation are some of the first. In two of the mixed-REE titration experiments (Chapter 4), crystalline material was emerging (6 weeks at 90 °C), which demonstrates the reaction is strongly influenced by kinetic factors. It would clearly have been beneficial to run aliquots for significantly longer periods of time in those cases. The textural study in Chapter 7 also highlighted the importance of other minerals, particularly apatite. Wall rock experiments in which apatite, ankerite or some other common minerals in carbonatites are reacted in the presence of dissolved REE would take the setup another step closer to natural systems.

Although the results of Chapter 5 (XAS study) suggested the REE in mixed Nd+Er samples were mostly well dispersed (i.e. not Nd- or Er-rich clusters), it would still be interesting to make micro-X-ray maps of these (and other mixed precipitates), especially sampled from the dolomite experiments. Analyses of products of wall rock experiments, especially in those samples containing multiple crystal morphologies, might reveal migration of REEs during dissolution-precipitation or diffusional transformation from one form to another.

A final must for any future work of this flavour should be the running of repeats (duplicates, triplicates or more) for each experiment. As mentioned in the methods chapter and the previous section, solution concentration was varied between the titration, low temperature batch and higher temperature 'flow-through' reactions. This is important to note as a potential critical review because previous work has demonstrated a change in morphology and composition of yttrium carbonates precipitated under the same conditions other than varying molar ratios of $Y(NO_3)_3 \cdot 6\,H_2O$ to urea (e.g. Zhang et al., 2009). It would, therefore, be of importance to not only run duplicates/triplicates of samples, but to also conduct experiments of the same type under different molar ratios of REE chloride to sodium carbonate during titration experiments.

Combining the novel outcomes of this investigation with those areas identified as requiring improvement naturally leads to thoughts of potential future studies. A few ideas are presented in final section below.

8.4 Future work

In this work, the geochemistry of REE carbonate and fluorocarbonate synthesis has been investigated, with the results highlighting the complex nature of these reactions. Although a consistent pattern is emerging of behavioural differences between single- and multi-REE systems, there are some instances of inconsistent or contradictory results that warrant further investigation.

A key area for future study is the determination of REE mineral solubilities, including those of the X-ray amorphous precursor phases identified here and in previous works. Recent solubility measurements have been made for some synthetic REE carbonate phases (e.g. hydroxylbastnäsite and kozoite - Voigt et al., 2016), and the thermodynamic properties of some synthetic (bastnäsite – e.g. Pradip et al., 2013; Shivaramaiah et al., 2016) and natural REE fluorocarbonates (bastnäsite and parisite - Gysi and Williams-Jones, 2015) have been determined. These studies are an important step in the right direction, but the data are currently limited to a few compositions and temperatures. A first step would be to synthesise fluorocarbonates with only a single REE (i.e. $LaCO_3F$, $LaCO_3F$, $NdCO_3F$ $GdCO_3F$, $TbCO_3F$, $YbCO_3F$, etc.) and determine their solubilities and other thermodynamic properties, so that data exist for each of the 'end member' species. This data is a vital for comparison with that measured for natural fluorocarbonates (e.g. Gysi and Williams-Jones, 2015; Shivaramaiah et al., 2016).

The results of the current study indicate differing behaviour of the REEs between precipitation methods, single- and multi-REE systems, and with temperature. In the case of titration experiments combined with the XAS study, the crystallisation pathway for the X-ray amorphous precursor phase of La and Nd has been called into question. If the precursor phase is transforming directly into lanthanite (and not through its complete dissolution-precipitation), then a higher resolution sampling regime would be required. This would involve a similar experiment to those undertaken already, but during which aliquots are collected perhaps every ten seconds (La is shown to be fully crystalline after approximately two minutes – e.g. Rodriguez-Blanco et al., 2014). This could easily be achieved with a hand-operated mechanical pipette, although the volume within the experimental beaker would need to be greater than used in the current investigation to avoid significant changes to the REE solution concentration and pH. ICP-MS analyses could then be used to track the REE solution concentration with time, which, combined with SEM or TEM, may help identify whether the lanthanite forms directly from the X-ray amorphous precursor. Alternatively, a time-resolved *in-situ* XAS analyses, using the diamond-anvil cell setup described in Bassett et al. (2000), may identify the evolution of these materials, although it would be more applicable to studying the HREE systems (i.e. they don't transform as quickly).

A mention was made during the methods chapter to the fact that sodium carbonate addition to the REE chloride solutions was recorded by eye, and not automated. This could of course be easily remedied with an automated burette paired with a pH meter for automated recording of pH vs sodium carbonate addition. This information would be useful for more accurately determining the amount of H^+ buffering as a function of dissolved carbonate addition, which itself could help determine the REE species in solution and ultimately the precipitation of REEs as solid carbonate phases.

The HREE results presented in Chapters 4 and 5 suggest the proposed linear relationship of REE atomic number with the lifetime of the precursor phase (e.g. Vallina et al., 2013; Rodriguez-Blanco et al., 2014; Vallina et al., 2015) is not valid. An extended experimental matrix, including more of the REEs, additional multi-REE solutions (particularly containing HREEs) and higher temperatures are required. In the titration experiments this is necessary because of the difference in crystallinity and morphology of products, while in the wall rock reactions it was the observation of discrete L- and HREE-rich phases forming at the higher temperatures investigated. The wall rock reactions as completed in this study are unlike those previously published, and as such make direct comparison difficult. However, based on virtually all the literature, future works should build upon the preliminary experiments of this work in which equi-molar concentrations of each REEs were used, and instead adapt this to better reflect natural ore-forming compositions – i.e. significantly lower HREE concentrations.

Given the issues surrounding the use of soluble fluoride in the presence of REE (i.e. low solubility of REE-fluoride solids), fluorite was used as a reactant phase in Chapter 7. However, there are several possible methods for reacting REE, F^- and CO_3^{2-} in circumstances where it is not possible to achieve a suitable starting solution containing all those components at room temperature. A simple idea would be to flow dilute hydrofluoric acid through a system containing a solid REE carbonate, much like the study of Pradip et al. (2013). The requirement for this a non-reactive fluid path able to withstand hydrofluoric acid. A second modification of that method would be to heat (in a HCl solution) a REE carbonate in the presence of fluorite, or a REE fluoride in the presence of dolomite. A further method could be to introduce an acidic solution (devoid of REEs) into a vessel containing dolomite and fluorite, allowing the minerals to dissolve. This solution would then be pumped into a new vessel containing a REE chloride solution. Such a setup would avoid the immediate precipitation of REE fluoride and/or REE carbonate as experienced in some of the experiments of Chapter 7. Mineral reactants as sources of fluoride mean that concentrations remain low, limiting the potential for equipment degradation, although this may limit the volume of product and therefore hinder characterisation.

The preliminary wall rock experiments of this study have proven the method and demonstrated the effectiveness of dissolved carbonate to the precipitation of REEs from solution. Previous studies have modelled the progressive reaction of REE-bearing fluids with phosphate rocks (Williams-Jones et al., 2012), with results suggesting the fractionation of L- and HREEs is a consequence of preferential LREE complex stability. Results of the current investigation provide a simple, empirical method for studying these reactions that could easily be adapted to include additional phases of interest, for example apatite, monazite, calcite, ankerite and Fe-oxides, thereby better representing natural systems. A potential idea for testing the fractionation of REEs would be to react a REE solution (containing all the REEs in more natural concentrations/abundances) with the rock(s) of choice in a setup identical to that in Chapter 6, however, this time instead of the outlet tube going to waste, it feeds into a second reactor cell with fresh chips of the reactant rock. A setup like this could be repeated with more cells, or continual flushes of solution, thereby mimicking a more open system. The results of the current investigation have shown even small volumes of dolomite (0.5 g) and REE solution (about 10 ml) are sufficient to form enough material for characterisation without exhausting the dolomite supply, making it easily scalable and potentially useful for moving towards ore-forming conditions.

Analyses and discussion of the natural Bayan Obo samples noted the ubiquitous nature of magnetite, and therefore inferences were made as to the possible importance of oxygen fugacity during REE mineralisation. In the potential wall rock experiments proposed in the previous paragraph it may be interesting to include the mineral magnetite as a reactant phase and see how the behaviour of REEs differ when in the presence of this mineral under different oxygen fugacity conditions. A continuation of this theme would be to attempt both magnetite and REE carbonate (and fluorocarboante) precipitation *via* reaction with a carbonate rock, which would require the initial solution to be reduced as to facilitate iron mobility as Fe^{2+}, which would require the use of redox buffers. Comparison of produced assemblages and textures could be compared directly with those from natural deposits, helping to aid paragenetic interpretations and formation conditions.

During the dolomite + fluorite wall rock experiments, the difficulty in identifying the underlying mineral to neo-formed mineralisation was mentioned. This issue significantly hampered the ability to determine the true identity of the neo-formed minerals (i.e. because the components of the potential products were the same as the reactants - making EDS analyses unreliable). In these cases it would be beneficial to have sectioned a number of individual chips (after mounting them in epoxy resin). This would permit SEM/EDS analyses of their cross-sections, making identification of the underlying mineral straightforward, ultimately helping to determine the neo-formed minerals. This information could also be used to identify whether the respective structures of ei-

ther the dolomite or fluorite impose any influence on the orientation of the neo-formed material, and help to support the conclusions that dissolution of wall rock provides the ligands necessary for certain phases to form, but that this is only a local phenomenon (i.e. in contrast to the solution-wide supersaturation of REE chloride solutions during the titration experiments).

Bibliography

Adachi, G.-Y., Imanaka, N., and Tamura, S. (2010). Research trends in rare earths: A preliminary analysis. *Journal of Rare Earths*, 28(6):843–846.

Adler, H., Kerr, and P.F. (1963). Infrared spectra, symmetry and structure relations of some carbonate minerals. *The American Mineralogist*, 48:839–853.

Allen, P., Bucher, J., Shuh, D., Edelstein, N., and Craig, I. (2000). Coordination chemistry of trivalent lanthanide and actinide ions in dilute and concentrated chloride solutions. *Inorganic Chemistry*, 39:595–601.

Alonso, E., Sherman, A., Wallington, T., Everson, M., Field, F., Roth, R., and Kirchain, R. (2012). Evaluating rare earth element availability: A case with revolutionary demand from clean technologies. *Environmental Science and Technology*, 46(6):3406–3414.

Anderson, A., Jayanetti, S., Mayanovic, R., Bassett, W., and Chou, I.-M. (2002). X-ray spectroscopic investigations of fluids in the hydrothermal diamond anvil cell: The hydration structure of aqueous La 3+ up to 300 C and 1600 bars. *American Mineralogist*, 87:262–268.

Ani, T. and Sarapaa, O. (2013). Geochemistry and mineral phases of REE in Jammi carbonatite veins and fenites, southern end of the Sokli complex, NE Finland. *Geochemistry: Exploration, Environment, Analysis*, 13:217–224.

Asakura, H., Shishido, T., Fuchi, S., Teramura, K., and Tanaka, T. (2014a). Local Structure of Pr, Nd, and Sm Complex Oxides and Their X-ray Absorption Near Edge Structure Spectra. *The Journal of Physical Chemistry C*, 118(36):20881–20888.

Asakura, H., Shishido, T., Teramura, K., and Tanaka, T. (2014b). Local structure and La L1 and L3-edge XANES spectra of lanthanum complex oxides. *Inorganic chemistry*, 53(12):6048–53.

Asakura, H., Shishido, T., Teramura, K., and Tanaka, T. (2015). Local structure and L1 - and L3-edge X-ray absorption near edge structure of late lanthanide elements (Ho, Er, Yb) in their complex oxides. *The Journal of Physical Chemistry C*, 119(15):8070–8077.

Bach, S., Celinski, V., Dietzsch, M., Panth??fer, M., Bienert, R., Emmerling, F., auf der Gunne, J., and Tremel, W. (2015). Thermally highly stable amorphous zinc phos-

phate intermediates during the formation of zinc phosphate hydrate. *Journal of the American Chemical Society*, 137(6):2285–2294.

Bach, S., Panthofer, M., Bienert, R., Buzanich, A.-O., Emmerling, F., and Tremel, W. (2016). Role of water during crystallization of amorphous cobalt phosphate nanoparticles. *Crystal Growth and Design*, 16(8):4232–4239.

Banks, D., Yardley, B., Campbell, A., and Jarvis, K. (1994). REE composition of an aqueous magmatic fluid: a fluid inclusion study from the Capitan Pluton, New Mexico, USA. *Chemical Geology*, 113:259–272.

Bassett, W., Anderson, A., Mayanovic, R., and Chou, I.-M. (2000). Hydrothermal diamond anvil cell for XAFS studies of first-row transition elements in aqueous solution up to supercritical conditions. *Chemical Geology*, 167:3–10.

Beck, R. and Andreassen, J. (2010). Spherulitic growth of calcium carbonate. *Crystal Growth and Design*, 10(7):2934–2947.

Benaouda, R., Devey, C., Badra, L., and Ennaciri, A. (2017). Light rare-earth element mineralization in hydrothermal veins related to the Jbel Boho alkaline igneous complex, AntiAtlas/Morocco: The role of fluid-carbonate interactions in the deposition of synchysite-(Ce). *Journal of Geochemical Exploration*, 177:28–44.

Bevins, R., Rowbotham, G., Stephens, F., Turgoose, S., and Williams, P. (1985). Lanthanite-(Ce), (Ce, La, Nd)2.8H2O, a new mineral from Wales, U.K. *American Mineralogist*, 70:411–413.

Bhargava, R. (1996). Doped nanocrystalline materials - Physics and applications. *Journal of Luminescence*, 70(1):85–94.

Biagioni, C., Bonaccorsi, E., Cámara, F., Cadoni, M., Ciriotti, M., Bersani, D., and Kolitsch, U. (2013). Lusernaite-(Y), Y4Al(CO3)2(OH,F)11.6H2O, a new mineral species from Luserna Valley, Piedmont, Italy: Description and crystal structure. *American Mineralogist*, 98(Sandrone 2001):1322–1329.

Bond, D., Clark, D., Donohoe, R., Gordon, J., Gordon, P., Keogh, D., Scott, B., Tait, C., and Watkin, J. (2000). A new structural class of lanthanide carbonates: synthesis, properties, and X-ray structure of the one-dimensional chain complex [Co(NH3)6]6[K2(H2O)10]- [Nd2(CO3)8]2.20H2O. *Inorganic Chemistry*, 39:3934–3937.

Bond, D., Clark, D., Donohoe, R., Gordon, J., Gordon, P., Keogh, D., Scott, B., Tait, C., and Watkin, J. (2001). A model for trivalent actinides in media containing high carbonate concentrations - structural characterization of the lanthanide tetracarbonate [Co(NH3)6][Na(H2O)(H2O)4]2 [Ho(CO3)4].4H2O. *European Journal of Inorganic Chemistry*, 2001(15):2921–2926.

Bots, P., Benning, L., Rodriguez-Blanco, J., Roncal-Herrero, T., and Shaw, S. (2012). Mechanistic insights into the crystallization of amorphous calcium carbonate (ACC). *Crystal Growth and Design*, 12(7):3806–3814.

Broom-Fendley, S., Brady, A., Wall, F., Gunn, G., and Dawes, W. (2017). REE minerals at the Songwe Hill carbonatite, Malawi: HREE-enrichment in late-stage apatite. *Ore Geology Reviews*, 81:23–41.

Broom-Fendley, S., Styles, M., Appleton, J., Gunn, G., and Wall, F. (2016). Evidence for dissolution-reprecipitation of apatite and preferential LREE mobility in carbonatite-derived late-stage hydrothermal processes. *American Mineralogist*, 101(3):596–611.

Buhn, B., Rankin, A., Schneider, J., and Dulski, P. (2002). The nature of orthomagmatic, carbonatitic fluids precipitating REE, Sr-rich fluorite: fluid-inclusion evidence from the Okorusu fluorite deposit, Namibia. *Chemical Geology*, 186:75–98.

Bunzli, J. and Piguet, C. (2005). Taking advantage of luminescent lanthanide ions. *Chemical Soc.Rev.*, 34(12):1048–1077.

Buzko, V., Sukhno, I., and Buzko, M. (2009). Ab initio and DFT study of Lu3+ hydration. *Journal of Molecular Structure: THEOCHEM*, 894(1-3):75–79.

Byrne, R. and Li, B. (1995). Comparative complexation behaviour of the rare earths. *Geochimica et Cosmochimica Acta*, 59:4575–4589.

Campbell, L. and Henderson, P. (1997). Apatite paragenesis in the Bayan Obo REE-Nb-Fe ore deposit, Inner Mongolia, China. *Lithos*, 42:89–103.

Caro, P., Sawyer, J., and Eyring, L. (1972). The infrared spectra of rare earth carbonates. *Spectrochimica Acta*, 28:1167–1173.

Castor, S. B. (2008). The Mountain Pass rare-earth carbonatite and associated ultrapotassic rocks, California. *The Canadian Mineralogist*, 46:779–806.

Chakhmouradian, A. and Wall, F. (2012). Rare earth elements: minerals, mines, magnets (and more). *Elements*, 8(5):333–340.

Chakhmouradian, A. and Zaitsev, A. (2012). Rare earth mineralization in igneous rocks: sources and processes. *Elements*, 8(5):347–353.

Chang, H.-Y., Chen, F.-S., and Lu, C.-H. (2011). Preparation and luminescence characterization of new carbonate (Y2(CO3).nH2O:Eu3+) phosphors via the hydrothermal route. *Journal of Alloys and Compounds*, 509(41):10014–10019.

Chao, E., Back, J., and Minkin, J. (1992). Host-rock controlled epigenetic, hydrothermal metasomatic origin of the Bayan Obo REE-Fe-Nb ore deposit, Inner Mongolia, P.R.C. *Applied Geochemistry*, 7:443–458.

Charalampides, G., Vatalis, K., Apostoplos, B., and Ploutarch-Nikolas, B. (2015). Rare earth elements: Industrial applications and economic dependency of Europe. *Procedia Economics and Finance*, 24(15):126–135.

Charles, R. (1965). Rare earth carbonates prepared by homogenous precipitation. *Journal of Inorganic Nuclear Chemistry*, 27:1489–1493.

Cho, S., Jang, J.-W., Jung, A., Lee, S.-H., Lee, J., Lee, J.-S., and Lee, K.-H. (2011). Formation of amorphous zinc citrate spheres and their conversion to crystalline ZnO nanostructures. *Langmuir*, 27(1):371–378.

Christensen, A. (1973a). Hydrothermal perparation and magnetic properties of Dy2O2CO3, Ho2O2CO3, Er2O2CO3 and Yb2O2CO3. *Acta Chemica Scandinavica*, 27(5):1835–1837.

Christensen, A. (1973b). Hydrothermal preperation of rare earth hydroxy-carbonates. The crystal structure of NdOHCO3. *Acta Chemica Scandinavica*, 27:2973–2982.

Chukanov, N. and Chervonnyi, A. (2014). *Infrared spectroscopy of minerals and related compounds*. Springer International Publishing.

Clark, A. (1984). Mineralogy of the rare earth elements. In Henderson, P., editor, *Rare earth element geochemistry*, pages 33–61. Elsevier Science Publishers, Amsterdam.

Clegg, W. (2003). X-ray diffraction. In McCleverly, J. and Meyer, T., editors, *Comprehensive Coordination Chemistry II: from biology to nanotechnology*, chapter 2.4, pages 57–64. Elsevier Ltd, 2 edition.

Colfen, H. (2003). Synthesis of ordered mesoporous materials using surfactant liquid crystals or micellar solutions. *Current opinion in colloid and interface science*, 8:23–31.

Corbel, G., Courbion, G., Le Berre, F., Leblanc, M., Le Meins, J., Maisonneuve, V., and Mercier, N. (2001). Synthesis from solutions and properties of various metal fluorides and fluoride salts. *Journal of Fluorine Chemistry*, 107(2):193–198.

Coulson, M. (2012). *The History of Mining: The events, technology and people involced in the industry that forged the modern world*. Harriman House, Petersfield, Hampshire, UK., first edit edition.

Dal Negro, A., Rossi, G., and Tazzoli, V. (1975). The Crystal Structure of Ancylite, (RE)x(Ca,Sr)2-x(CO3)2(OH)x(2-x)H2O. *American Mineralogist*, 60:280–284.

Dal Negro, A., Rossi, G., and Tazzoli, V. (1977). The crystal structure of lanthanite. *American Mineralogist*, 62:142–146.

D'Angelo, P., De Panfillis, S., Fillipponi, A., and Persson, I. (2008). high-energy X-ray absorption spectroscopy: a new tool for structural investigations of lanthanoids and third-row transition elements. *Chemistry - A European Journal*, 14(10):3045–3055.

D'Angelo, P. and Spezia, R. (2012). Hydration of lanthanoids(III) and actinoids(III): an experimental/theoretical saga. *Chemistry - A European Journal*, 18(36):11162–78.

D'Angelo, P., Zitolo, A., Migliorati, V., Chillemi, G., Duvail, M., Vitorge, P., Abadie, S., Spezia, R., Mitterrand, B., Cedex, E., and Speciation, L. D. (2011). Revised ionic radii of lanthanoid (III) ions in aqueous solution. *Inorganic chemistry*, 50:4572–4579.

Deer, W., Howie, R., and Zussman, J. (2013). *An introduction to rock-forming minerals*. Mineralogical Society of Great Britain and Ireland, London, third edition.

del Tanago, J. G., La Iglesia, A., and Delgado, A. (2006). Kamphaugite-(Y) from La Cabrera massif, Spain: a low-temperature hydrothermal Y-REE carbonate. *Mineralogical Magazine*, 70(4):397–404.

Dey, A., Bomans, P., Muller, F., Will, J., Frederik, P., de With, G., and Sommerdijk, N. (2010). The role of prenucleation clusters in surface-induced calcium phosphate crystallization. *Nature Materials*, 9(12):1010–1014.

Dietzsch, M., Andrusenko, I., Branscheid, R., Emmerling, F., Kolb, U., and Tremel, W. (2017). Snapshots of calcium carbonate formation – a step by step analysis. *Zeitschrift für Kristallographie - Crystalline Materials*, 232(1-3):255–265.

Duraiswami, R. and Shaikh, T. (2014). Fluid-rock interaction in the Kangankunde Carbonatite Complex, Malawi: SEM based evidence for late stage pervasive hydrothermal mineralisation. *Central European Journal of Geosciences*, 6(4):476–491.

Duvail, M., Vitorge, P., and Spezia, R. (2010). Temperature influence on lanthanoids (III) hydration from molecular dynamics simulations. *Chemical Physics Letters*, 498(1-3):90–96.

Elzinga, E., Reeder, R., Withers, S., Peale, R., Mason, R., Beck, K., and Hess, W. (2002). EXAFS study of rare-earth element coordination in calcite. *Geochimica et Cosmochimica Acta*, 66(16):2875–2885.

European Commission (2011). Communication from the Commission: Tackling the challenges in commodity markets and on raw materials. Technical report, European Commission, Brussels.

European Commission (2014). Communication from the Commission: On the review of the list of critical raw materials for the EU and the implementation of the Raw Materials Initiative COM(2014). Technical report, European Commission, Brussels.

Fan, H., Yang, K., Hu, F., Liu, S., and Wang, K. (2016). The giant Bayan Obo REE-Nb-Fe deposit, China: Controversy and ore genesis. *Geoscience Frontiers*, 7(3):335–344.

Firsching, H. and Mohammadzadel, J. (1986). Solubillty products of rare earth carbonates. *Journal of Chemical Engineering Data*, 31:40–42.

Fleischer, M. (1972). Bastnaesite-(Y). *American Mineralogist*, 57:594–598.

Foger, K., Hoang, M., and Turney, T. (1992). Formation and thermal decomposition of rare-earth carbonates. *Journal of Material Science*, 27:77–82.

Forster, H.-J. (2001). Synchysite-(Y)-synchysite-(Ce) solid solutions from Markersbach, Erzgebirge, Germany: REE and Th mobility during high-T alteration of highly fractionated aluminous A-type granites. *Mineralogy and Petrology*, 72:259–280.

Frenkel, A., Yevick, A., Cooper, C., and Vasic, R. (2011). Modeling the structure and composition of nanoparticles by extended X-ray absorption fine-structure spectroscopy. *Annual Reviews in Analytical Chemistry (Palo Alto Calif)*, 4:23–39.

Frost, R., Lopez, A., Scholz, R., Xi, Y., and Belotti, F. (2013). Infrared and Raman spectroscopic characterization of the carbonate mineral huanghoite – and in comparison with selected rare earth carbonates. *Journal of Molecular Structure*, 1051:221–225.

Gebauer, D. and Cölfen, H. (2011). Prenucleation clusters and non-classical nucleation. *Nano Today*, 6:564–584.

Gebauer, D., Volkel, A., and Colfen, H. (2008). Stable prenucleation calcium carbonate clusters. *Science*, 322(5909):1819–1822.

Giebel, R., Gauert, C., Marks, M., Costin, G., and Markl, G. (2017). Multi-stage formation of REE minerals in the Palabora Carbonatite Complex , South Africa. *American Mineralogist*, 102:1218–1233.

Gill, R. (1997). *Modern analytical geochemistry: an introduction to quantitative chemical analysis techniques for earth, environmental and materials scientists*. Longman, Harlow, England.

Gob, S., Wenzel, T., Bau, M., Jacob, D., Loges, A., and Markl, G. (2011). The redistribution of rare-earth elements in secondary minerals of hydrothermal veins, Schwarzwald, southwestern Germany. *The Canadian Mineralogist*, 49:1305–1333.

Goff, G., Cisneros, M., Kluk, C., Williamson, K., Scott, B., Reilly, S., and Runde, W. (2010). Synthesis and structural characterization of molecular Dy(III) and Er(III) tetra-carbonates. *Inorganic Chemistry*, 49(14):6558–6564.

Goldstein, J., Newbury, D., Joy, D., Lyman, C., Echlin, P., Lifshin, E., Sawyer, L., and Michael, J. (2017). *Scanning Electron Microscopy and X-ray Microanalysis*. Springer Science, New York, third edition.

Golev, A., Scott, M., Erskine, P., Ali, S., and Ballantyne, G. (2014). Rare earths supply chains: Current status, constraints and opportunities. *Resources Policy*, 41(1):52–59.

Goodenough, K., Schilling, J., Jonsson, E., Kalvig, P., Charles, N., Tuduri, J., Deady, E., Sadeghi, M., Schiellerup, H., Müller, A., Bertrand, G., Arvanitidis, N., Eliopoulos, D., Shaw, R., Thrane, K., and Keulen, N. (2015). Europe's rare earth element resource potential: An overview of REE metallogenetic provinces and their geodynamic setting. *Ore Geology Reviews*, 72:838–856.

Graham, I., Pogson, R., Colchester, D., Hergt, J., Martin, R., and Williams, P. (2007). Pink lanthanite-(Nd) from Whitianga quarry, Coromandel Peninsula, New Zealand. *The Canadian Mineralogist*, 45:1389–1396.

Granasy, L., Pusztai, T., Tegze, G., Warren, J., and Douglas, J. (2005). Growth and form of spherulites. *Physical Review E - Statistical, Nonlinear, and Soft Matter Physics*, 72(1):1–15.

Graupner, T., Muhlbach, C., Schwarz-Schampera, U., Henjes-Kunst, F., Melcher, F., and Terblanche, H. (2015). Mineralogy of high-field-strength elements (Y, Nb, REE) in the world-class Vergenoeg fluorite deposit, South Africa. *Ore Geology Reviews*, 64:583–601.

Gregory, M. (2017). A fluid inclusion and stable isotope study of the Pebble porphyry copper-gold-molybdenum deposit, Alaska. *Ore Geology Reviews*, 80:1279–1303.

Grice, J., Maisonneuve, V., and Leblanc, M. (2007). Natural and synthetic fluoride carbonates. *Chemical Reviews*, 107:114–32.

Grice, J., Van Velthuizen, J., and Gault, R. (1994). Petersenite-(Ce), a new mineral from Mont Saint-Hilaire, and its structural relationship to other REE carbonates. *The Canadian Mineralogist*, 32:405–414.

Guastoni, A., Nestola, F., and Giaretta, A. (2009). Mineral chemistry and alteration of rare earth element (REE) carbonates from alkaline pegmatites of Mount Malosa, Malawi. *American Mineralogist*, 94:1216–1222.

Gueta, R., Natan, A., Addadi, L., Weiner, S., Refson, K., and Kronik, L. (2007). Local atomic order and infrared spectra of biogenic calcite. *Angewandte Chemie - International Edition*, 46(1-2):291–294.

Gysi, A. and Williams-Jones, A. (2013). Hydrothermal mobilization of pegmatite-hosted REE and Zr at Strange Lake, Canada: A reaction path model. *Geochimica et Cosmochimica Acta*, 122:324–352.

Gysi, A. and Williams-Jones, A. (2015). The thermodynamic properties of bastnäsite-(Ce) and parisite-(Ce). *Chemical Geology*, 392:87–101.

Ha, D.-H., Moreau, L., Bealing, C., Zhang, H., Hennig, R., and Robinson, R. (2011). The structural evolution and diffusion during the chemical transformation from cobalt to cobalt phosphide nanoparticles. *Journal of Materials Chemistry*, 21(31):11498–11510.

Haas, J., Shock, E., and Sassani, D. (1995). Rare earth elements in hydrothermal systems: Estimates of standard partial molal thermodynamic properties of aqueous complexes of the rare earth elements at high pressures and temperatures. *Geochimica et Cosmochimica Acta*, 59(21):4329–4350.

Harlov, D. and Forster, H.-J. (2003). Fluid-induced nucleation of (Y+REE)-phosphate minerals within apatite: Nature and experiment. Part II. Fluorapatite. *American Mineralogist*, 88:1209–1229.

Hartman, K. and Hisatsune, I. (1966). Infrared spectrum of carbon dioxide anion radical. *Journal of Chemical Physics*, 44:1913.

Haschke, J. (1975). The lanthanum hydroxide fluoride carbonate system: The preparation of synthetic bastnaesite. *Journal of Solid State Chemistry*, 12:115–121.

Heberling, F., Denecke, M., and Bosbach, D. (2008). Neptunium(V) coprecipitation with calcite. *Environmental Science and Technology*, 42(2):471–476.

Henderson, G., de Groot, F., and Moulton, J. (2014). X-ray absorption near edge structure (XANES) spectroscopy. In Henderson, G., Neuville, D., and Downs, R., editors, *Reviews in Mineralogy and Geochemistry: Spectroscopic methods in mineralogy and materials sciences*, page 800. Mineralogical Society of America, Virginia.

Henderson, P. (1984). *Rare earth element geochemistry*. Elsevier.

Hofer, T., Scharnagl, H., Randolf, B., and Rode, B. (2006). Structure and dynamics of La(III) in aqueous solution - An ab initio QM/MM MD approach. *Chemical Physics*, 327(1):31–42.

Hövelmann, J., Putnis, A., Geisler, T., Schmidt, B., and Golla-Schindler, U. (2010). The replacement of plagioclase feldspars by albite: Observations from hydrothermal experiments. *Contributions to Mineralogy and Petrology*, 159(1):43–59.

Hsu, L. (1992). Synthesis and Stability of Bastnaesites in a Part of the System (Ce, La)-F-H-C-O. *Mineralogy and Petrology*, 47:87–101.

Huang, X., Zhou, M., Qiu, Y., and Qi, L. (2015). In-situ LA-ICP-MS trace elemental analyses of magnetite: The Bayan Obo Fe-REE-Nb deposit, North China. *Ore Geology Reviews*, 65(P4):884–899.

Hughes, S., Nguyen, T.-N., Capobianco, J., and Peslherbe, G. (2005). A theoretical study of trivalent lanthanide ion microsolvation in water clusters from first principles. *International Journal of Mass Spectrometry*, 241:283–294.

Humphries, M. (2013). Rare Earth Elements: The Global Supply Chain. Technical report, Congressional Research Report R41347.

Ikuma, Y., Oosawa, H., Shimada, E., and Kamiya, M. (2002). Effect of microwave radiation on the formation of Ce2O(CO3)2.H2O. *Solid State Ionics*, 151:347–352.

Isobe, H. and Yoshizawa, M. (2014). Formation of iron mineral fine particles by acidic hydrothermal alteration experiments of synthetic martian basalt. *Journal of Mineralogical and Petrological Sciences*, 109(2):62–73.

Jaireth, S., Hoatson, D., and Miezitis, Y. (2014). Geological setting and resources of the major rare-earth-element deposits in Australia. *Ore Geology Reviews*, 62:72–128.

Janicki, R., Starynowicz, P., and Mondry, A. (2011). Lanthanide carbonates. *European Journal of Inorganic Chemistry*, 2011:3601–3616.

Jansen, G., Magin, G., and Levin, B. (1959). Synthesis of bastnaesite. *American Mineralogist*, 44:180–181.

Jeevanandam, P., Koltypin, Y., Palchik, O., and Gedanken, A. (2001). Synthesis of morphologically controlled lanthanum carbonate particles using ultrasound irradiation. *Journal of Materials Chemistry*, 11(3):869–873.

Jin, Y., Liu, J., Zheng, Q., Xu, J., Sharma, B., He, G., Yan, M., Zhang, L., Song, Y., Li, T., Yuan, Q., and Sun, Y. (2013). One pot synthesis of waters-stable gadolinium-doped Yb(OH)CO3 nanoprobes for in vivo dial MR and CT imaging. *New Journal of Chemistry*, 37:3024–3029.

Johannesson, K., Stetzenbach, K., and Hodge, V. (1997). Rare earth elements as geochemical tracers of regional groundwater mixing. *Geochimica et Cosmochimica Acta*, 61(17):3605–3618.

Kaczmarek, A., Van Hecke, K., and Van Deun, R. (2015). Nano- and micro-sized rare-earth carbonates and their use as precursors and sacrificial templates for the synthesis of new innovative materials. *Chemical Society reviews*, 44(8):2032–59.

Kalatha, S., Perraki, M., Economou-Eliopoulos, M., and Mitsis, I. (2017). On the origin of bastnaesite-(La,Nd,Y) in the Nissi (Patitira) Bauxite laterite Deposit, Lokris, Greece. *Minerals*, 7(3):45.

Karthika, S., Radhakrishnan, T., and Kalaichelvi, P. (2016). A review of classical and nonclassical nucleation theories. *Crystal Growth and Design*, 16(11):6663–6681.

Kato, S., Shibuya, T., Nakamura, K., Suzuki, K., Rejishkumar, V., and Yamagishi, A. (2013). Elemental dissolution of basalts with ultra-pure water at 340 C and 40 MPa in a newly developed flow-type hydrothermal apparatus. *Geochemical Journal*, 47:89–92.

Katz, L., Dewan, K., and Bronaugh, R. (2015). Nanotechnology in cosmetics. *Food and Chemical Toxicology*, 85:127–137.

Kesler, S. and Simon, A. (2016). *Mineral Resources, Economics and the Environment*. Cambridge University Press, Cambridge, second edi edition.

Koyabu, K., Mayama, Y., Masui, T., and Imanaka, N. (2006). Synthesis of new green emitting phosphors based on rare earth oxycarbonates. *Journal of Alloys and Compounds*, 418:230–233.

Kutlu, I., Kalz, H.-J., Wartchow, R., Ehrhardt, H., Seidel, H., and Meyer, G. (1997). Potassium lanthanoid carboantes, KM(CO3)2 (M = Nd, Gd, Dy, Ho, Yb). *Zeitschrift für Kristallographie*, 623:1753–1758.

Kynicky, J., Smith, M., and Xu, C. (2012). Diversity of Rare Earth Deposits: The Key Example of China. *Elements*, 8(5):361–367.

Lai, X. and Yang, X. (2013). Geochemical characteristics of the Bayan Obo giant REE–Nb–Fe deposit: Constraints on its genesis. *Journal of South American Earth Sciences*, 41:99–112.

Larsen, A. and Gault, R. (2002). Calcio-ancylite-(Ce) from syenite pegmatite at Tvedalen, Oslo Region, Norway. *Neues Jahrbuch fur Mineralogie, Monatshefte*, 9:411–423.

Lechevallier, S., Lecante, P., Mauricot, R., Dexpert, H., Dexpert-Ghys, J., Kong, H., Law, G., and Wong, K. (2010). Gadolinium-europium carbonate particles: Controlled precipitation for luminescent biolabeling. *Chemistry of Materials*, 22(22):6153–6161.

Levinson, A. (1966). A system of nomenclature for rare-earth minerals. *The American Mineralogist*, 51:152–158.

Lin, Y., Hu, C., and Mao, J. (2015). K2Pb3(CO3)3F2 and KCdCO3F: Novel fluoride carbonates with layered and 3D framework structures. *Inorganic Chemistry*, 54(21):10407–10414.

Ling, M., Liu, Y., Williams, I., Teng, F., Yang, X., Ding, X., Wei, G., Xie, L., Deng, W., and Sun, W. (2013). Formation of the world's largest REE deposit through protracted fluxing of carbonatite by subduction-derived fluids. *Scientific Reports*, 3:1776.

Liu, S. and Ma, R. (1996a). Synthesis and structure of hydrated europium carbonate. *Journal of Crystal Growth*, 169:190–192.

Liu, S. and Ma, R. (1996b). Synthesis and structure of hydrated terbium carbonate. *Indian Journal of Chemistry A*, 35(11):992–994.

Liu, S. and Ma, R. (1997a). Synthesis of a Crystalline Hydrated Basic Ytterbium Carbonate, Yb2O3·2.17CO2·6.17H2O. *Synthesis and Reactivity in Inorganic and Metal-Organic Chemistry*, 27(8):1183–1190.

Liu, S. and Ma, R. (1997b). Synthesis of lutetium carbonate. *Acta Chemica Scandinavica*, 51:893–895.

Liu, S. and Ma, R. (2007). Synthesis and characterisation of hydrated holmium and erbium carbonates. *Asian Journal of Chemistry*, 19(3):1883–1887.

Liu, S., Ma, R., Jiang, R., and Luo, F. (1999a). Precipitation and characterization of cerous carbonate. *Journal of Crystal Growth*, 206:88–92.

Liu, S., Ma, R., Jiang, R., and Luo, F. (1999b). Synthesis and structure of hydrated neodymium carbonate. *Journal of Crystal Growth*, 203:454–457.

Liu, S., Ma, R., Jiang, R., and Luo, F. (2000). Synthesis and Structure of Hydrated Yttrium Carbonate, Y2(Co3)33·2.79H2O. *Synthesis and Reactivity in Inorganic and Metal-Organic Chemistry*, 30(2):271–279.

Loges, A., Migdisov, A., Wagner, T., Williams-Jones, A., and Markl, G. (2013). An experimental study of the aqueous solubility and speciation of Y(III) fluoride at temperatures up to 250 C. *Geochimica et Cosmochimica Acta*, 123:403–415.

Louvel, M., Bordage, A., Testemale, D., Zhou, L., and Mavrogenes, J. (2015). Hydrothermal controls on the genesis of REE deposits: Insights from an in situ XAS study of Yb solubility and speciation in high temperature fluids (T <400 C). *Chemical Geology*, 417:228–237.

Lu, C.-H. and Wang, H.-C. (2002). Formation and microstructural variation of cerium carbonate hydroxide prepared by the hydrothermal process. *Materials Science and Engineering: B*, 90:138–141.

Luo, Y. and Millero, F. (2004). Effects of temperature and ionic strength on the stabilities of the first and second fluoride complexes of yttrium and the rare earth elements. *Geochimica et Cosmochimica Acta*, 68(21):4301–4308.

Luo, Y.-R. and Byrne, R. (2001). Yttrium and Rare Earth Element Complexation by Chloride Ions at 25 C. *Journal of Solution Chemistry*, 30(9):837–845.

Luo, Y.-R. and Byrne, R. (2004). Carbonate complexation of yttrium and the rare earth elements in natural waters. *Geochimica et Cosmochimica Acta*, 68(4):691–699.

Lv, J., Qiu, L., and Qu, B. (2004). Controlled growth of three morphological structures of magnesium hydroxide nanoparticles by wet precipitation method. *Journal of Crystal Growth*, 267(3-4):676–684.

Maksimovic, Z. (1985). Hydroxyl-bastnaesite-(Nd), a new mineral from Montenegro, Yugoslavia. *Mineralogical Magazine*, 49:717–720.

Malathi, S., Balakumaran, M., Kalaichelvan, P., and Balasubramanian, S. (2013). Green synthesis of gold nanoparticles for controlled delivery. *Advanced Materials*, 4(12):933–940.

Mao, Y., Bargar, J., Toney, M., and Chang, J. (2008). Correlation between luminescent properties and local coordination environment for erbium dopant in yttrium oxide nanotubes. *Journal of Applied Physics*, 103(9):094316.

Mariano, A. and Mariano, A. (2012). Rare earth mining and exploration in North America. *Elements*, 8(5):369–376.

Martelli, F., Jeanvoine, Y., Vercouter, T., Beuchat, C., Vuilleumier, R., and Spezia, R. (2014). Hydration properties of lanthanoid(III) carbonate complexes in liquid water determined by polarizable molecular dynamics simulations. *Physical Chemistry Chemical Physics: PCCP*, 16(8):3693–705.

Matijevic, E. (1988). Colloid science of ceramic powders. *Pure and Applied Chemistry*, 60(10):1479–1491.

Mayanovic, R., Anderson, A., Bassett, W., and Chou, I.-M. (2006). REE-chloride complexing in hydrothermal fluids with new data on Lanthanum chloroaqua complexes. *Geochemistry: Exploration, Environment, Analysis*, 72:A607.

Mayanovic, R., Anderson, A., Bassett, W., and Chou, I.-M. (2009a). Steric hindrance and the enhanced stability of light rare-earth elements in hydrothermal fluids. *American Mineralogist*, 94:1487–1490.

Mayanovic, R., Anderson, A., Bassett, W., and Chou, I.-M. (2009b). The structure and stability of aqueous rare-earth elements in hydrothermal fluids: New results on neodymium(III) aqua and chloroaqua complexes in aqueous solutions to 500 C and 520 MPa. *Chemical Geology*, 259:30–38.

Mayanovic, R., Jayanetti, S., Anderson, A., Bassett, W., and Chou, I.-M. (2002). The Structure of Yb 3+ Aquo Ion and Chloro Complexes in Aqueous Solutions at Up to 500 C and 270 MPa. *Journal of Physical Chemistry A*, 106:6591–6599.

McDonough, W. and Sun, S.-S. (1995). The composition of the Earth. *Chemical Geology*, 120:223–253.

Meekes, H., Boerrigter, S., Hollander, F., and Bennema, P. (2003). Needle crystal morphology explained. *Chemical Engineering and Technology*, 26(3):256–261.

Meldrum, F. and Cölfen, H. (2008). Controlling mineral morphologies and structures in biological and synthetic systems. *Chemical Reviews*, 108(11):4332–4432.

Meldrum, F. and Sear, R. (2008). Now you see them. *Science*, 322:1802–1803.

Michiba, K., Miyawaki, R., Minakawa, T., Terada, Y., Nakai, I., and Matsubara, S. (2013). Crystal structure of hydroxylbastnasite-(Ce) from Kamihouri, Miyazaki Prefecture, Japan. *Journal of Mineralogical and Petrological Sciences*, 108(6):326–334.

Michiba, K., Tahara, T., Nakai, I., Miyawaki, R., and Matsubara, S. (2011). Crystal structure of hexagonal RE(CO3)OH. *Zeitschrift fur Kristallographie*, 226(6):518–530.

Migdisov, A., Migdisov, A., Williams-Jones, A., and Williams-Jones, A. (2002). A spectrophotometric study of neodymium(III) complexation in chloride solutions. *Geochimica et Cosmochimica Acta*, 66(24):4311–4323.

Migdisov, A. and Williams-Jones, A. (2007). An experimental study of the solubility and speciation of neodymium(III) fluoride in F-bearing aqueous solutions. *Geochimica et Cosmochimica Acta*, 71:3056–3069.

Migdisov, A. and Williams-Jones, A. (2014). Hydrothermal transport and deposition of the rare earth elements by fluorine-bearing aqueous liquids. *Mineralium Deposita*, 49(8):987–997.

Migdisov, A., Williams-Jones, A., Normand, C., and Wood, S. (2008). A spectrophotometric study of samarium(III) speciation in chloride solutions at elevated temperatures. *Geochimica et Cosmochimica Acta*, 72(6):1611–1625.

Migdisov, A., Williams-Jones, A., and Wagner, T. (2009). An experimental study of the solubility and speciation of the Rare Earth Elements(III) in fluoride- and chloride-bearing aqueous solutions at temperatures up to 300 C. *Geochimica et Cosmochimica Acta*, 73:7087–7109.

Migdisov, A., Williams-Jones, A. E., Brugger, J., and Caporuscio, F. A. (2016). Hydrothermal transport, deposition, and fractionation of the REE: Experimental data and thermodynamic calculations. *Chemical Geology*, 439:13–42.

Mikhailova, J., Pakhomovsky, Y., Ivanyuk, G., Bazai, A., Yakovenchuk, V., Elizarova, I., and Kalashnikov, A. (2017). REE mineralogy and geochemistry of the Western Keivy peralkaline granite massif, Kola Peninsula, Russia. *Ore Geology Reviews*, 82:181–197.

Miyawaki, R., Kuriyama, J., and Nakai, I. (1993). The redefinition of tengerite-(Y), Y2(CO3)3.2-3H2O, and its crystal structure. *American Mineralogist*, 78:425–432.

Miyawaki, R., Matsubara, S., Yokoyama, K., Iwano, S., Hamasaki, K., and Yukinori, I. (2003). Kozoite-(La), La(C03)(0H), a new mineral from Mitsukoshi, Hizen-cho, Saga Prefecture, Japan. *Journal of Mineralogical and Petrological Sciences*, 98:137–141.

Miyawaki, R., Matsubara, S., Yokoyama, K., Takeuchi, K., Terada, Y., and Nakai, I. (2000). Kozoite-(Nd), Nd(CO3)(OH), a new mineral in an alkali olivine basalt from Hizen-cho , Saga Prefecture , Japan. *American Mineralogist*, 85:1076–1081.

Mondillo, N., Boni, M., Balassone, G., Spoleto, S., Stellato, F., Marino, A., Santoro, L., and Spratt, J. (2016). Rare earth elements (REE)-Minerals in the Silius fluorite vein system (Sardinia, Italy). *Ore Geology Reviews*, 74:211–224.

Morrison, S., Andrade, M., Wenz, M., Domanik, K., and Downs, R. (2013). Lanthanite-(Nd), Nd2(CO3)3·8H2O. *Acta crystallographica. Section E, Structure reports online*, 69(Pt 3):i15–i16.

Nadeau, O., Cayer, A., Pelletier, M., Stevenson, R., and Jébrak, M. (2015). The Paleoproterozoic Montviel carbonatite-hosted REE-Nb deposit, Abitibi, Canada: Geology, mineralogy, geochemistry and genesis. *Ore Geology Reviews*, 67:314–335.

Nagashima, K., Miyawaki, R., Takase, J., Nakai, I., Sakurai, K., Matsubara, S., Kato, A., and Iwano, S. (1986). Kimuraite, CaY2(CO3)4.6H2O, a new mineral from fissures in an alkali olivine basalt from Saga Prefecture, Japan, and new data on lokkaite. *American Mineralogist*, 71:1028–1033.

Nagashima, K., Wakita, H., and Mochizuki, A. (1973). The synthesis of crystalline rare earth carbonates. *Bulletin of the Chemical Society of Japan*, 46:152–156.

Nakamoto, K., Fujita, J., Tanaka, S., and Kobayashi, M. (1957). Infrared Spectra of Metallic Complexes. IV. Comparison of the Infrared Spectra of Unidentate and Bidentate Metallic Complexes. *J. Am. Chem. Soc.*, 79(18):4904–4908.

Newville, M. (2014). Fundamentals of XAFS. In Henderson, G., Neuville, R., and Downs, T., editors, *Reviews in Mineralogy and Geochemistry: Spectroscopic methods in mineralogy and materials sciences*, volume 78, page 800. Mineralogical Society of America, Virginia.

Ngwenya, B. (1994). Hydrothermal rare earth mineralisation in carbonatites of the Tundulu complex, Malawi: Processes at the fluid/rock interface. *Geochimica et Cosmochimica Acta*, 58(9):2061–2072.

Ohta, A., Kagi, H., Tsuno, H., Nomura, M., and Kawabe, I. (2008). Influence of multi-electron excitation on EXAFS spectroscopy of trivalent rare-earth ions and elucidation of change in hydration number through the series. *American Mineralogist*, 93(8-9):1384–1392.

Okamoto, A., Saishu, H., Hirano, N., and Tsuchiya, N. (2010). Mineralogical and textural variation of silica minerals in hydrothermal flow-through experiments: Implications for quartz vein formation. *Geochimica et Cosmochimica Acta*, 74(13):3692–3706.

Olson, J., Shawe, D., Pray, L., and Sharp, W. (1954). Rare-earth mineral deposits of the Mountain Pass District, San Bernardino County, California. Technical report, Washington D.C.

Orlandi, P., Pasero, M., and Vezzalini, G. (1990). Calcio-ancylite-(Nd), a new REE-carbonate from Baveno, Italy. *European Journal of Mineralogy*, 2(3):413–418.

Pearson, R. (1963). Hard and soft acids and bases. *Journal of the American Chemical Society*, 85:3533–3539.

PerkinElmer (2005). FT-IR Spectroscopy - Attenuated Total Reflectance (ATR).

Pingitore, N., Clague, J., and Gorski, D. (2014). Round Top Mountain rhyolite (Texas, USA), a massive, unique Y-bearing-fluorite-hosted heavy rare earth element (HREE) deposit. *Journal of Rare Earths*, 32(1):90–96.

Poitrasson, F., Chenery, S., and Bland, D. (1996). Contrasted monazite hydrothermal alteration mechanisms and their geochemical implications. *Earth and Planetary Science Letters*, 145:79–96.

Poty, B. and Pagel, M. (1988). Fluid inclusions related to uranium deposits: a review. *Journal of the Geological Society*, 145(1):157–162.

Pradip, Li, C., and Fuerstenau, D. (2013). The Synthesis and Characterization of Rare-Earth Fluocarbonates. *KONA Powder and Particle Journal*, 30(30):193–200.

Qian, L., Wang, X., and Zheng, H. (2012). Controlled synthesis of three-fold dendrites of Ce(OH)CO3 with multilayer caltrop and their thermal conversion to CeO 2. *Crystal Growth and Design*, 12(1):271–280.

Quartieri, S., Antonioli, G., Geiger, C., Artioli, G., and Lottici, P. (1999). XAFS characterization of the structural site of Yb in synthetic pyrope and grossular garnets. *Physics and Chemistry of Minerals*, 26:251–256.

Quill, L. and Salutsky, M. (1952). Separation of Praseodymium from Lanthanum. *Analytical Chemistry*, 24(9):1453–1455.

Ragnarsdottir, K., Oelkers, E., Sherman, D., and Collins, C. (1998). Aqueous speciation of yttrium at temperatures from 25 to 340 C at P sat: an in situ EXAFS study. *Chemical Geology*, 151:29–39.

Rahimi-Nasrabadi, M., Pourmortazavi, S., Aghazadeh, M., Ganjali, M., Karimi, M., and Norouzi, P. (2017). Fabrication, characterization and photochemical activity of ytterbium carbonate and ytterbium oxide nanoparticles. *Journal of Materials Science: Materials in Electronics*, 28(13):1–11.

Raiteri, P. and Gale, J. (2010). Water is the key to nonclassical nucleation of amorphous calcium carbonate. *Journal of the American Chemical Society*, 132(49):17623–17634.

Rasoamalala, V., Salvi, S., Béziat, D., Ursule, J.-P., Cuney, M., de Parseval, P., Guillaume, D., Moine, B., and Andriamampihantona, J. (2014). Geology of bastnaesite and monazite deposits in the Ambatofinandrahana area, central part of Madagascar: An overview. *Journal of African Earth Sciences*, 94:128–140.

Ravel, B. and Newville, M. (2005). ATHENA, ARTEMIS, HEPHAESTUS: Data analysis for X-ray absorption spectroscopy using IFEFFIT. *Journal of Synchrotron Radiation*, 12(4):537–541.

Reed, S. (2005). *Electron microprobe analysis and scanning electron microscopy in geology*. Cambridge University Press, Cambridge, second edition.

Refat, M. (2004). A Novel Method for the Synthesis of Rare Earth Carbonates. *Synthesis and Reactivity in Inorganic and Metal-Organic Chemistry*, 34(9):1605–1613.

Rickard, D. and Luther, G. (2006). Metal sulfide complexes and clusters. *Reviews in Mineralogy and Geochemistry*, 61(1):421–504.

Rieger, J., Frechen, T., Cox, G., Heckmann, W., Schmidt, C., and Thieme, J. (2007). Precursor structures in the crystallization/precipitation processes of CaCO3 and control of particle formation by polyelectrolytes. *Faraday discussions*, 136:265–277.

Rodriguez-Blanco, J., Shaw, S., and Benning, L. (2011). The kinetics and mechanisms of amorphous calcium carbonate (ACC) crystallization to calcite, via vaterite. *Nanoscale*, 3(1):265–271.

Rodriguez-Blanco, J., Vallina, B., Blanco, J., and Benning, L. (2014). The role of REE 3+ in the crystallization of lanthanites. *Mineralogical Magazine*, 78(6):1373–1380.

Roy, M. and Gurman, S. (1999). Amplitude reduction in EXAFS. *Journal of synchrotron radiation*, 6(Pt 3):228–230.

Ruberti, E., Enrich, G., and Gomes, C. (2008). Hydrothermal REE fluorocarbonate mineralization at Barra do Itapirapua, a multiple stockwork carbonatitie, southern Brazil. *The Canadian Mineralogist*, 46:901–914.

Rudnick, R. and Gau, S. (2003). Composition of the continental crust. In Rudnick, R., editor, *Treatise on Geochemistry 3: The Crust*. Elsevier.

Runde, W., Neu, M., Van Pelt, C., and Scott, B. (2000). Single crystal and solution complex structure of Nd(CO3)4. The first characterization of a mononuclear lanthanide(III) carbonato complex. *Inorganic Chemistry*, 39:1050–1051.

Salutsky, M. and Quill, L. (1950). The rare earth metals and their compounds XII: Carbonates of lanthanum, neodymiun and samarium. *Journal of the American Chemical Society*, 72:3306–3307.

Salvi, S. and Williams-Jones, A. (1996). The role of hydrothermal processes in concentrating high-field strength elements in the Strange Lake peralkaline complex, northeastern Canada. *Geochimica et Cosmochimica Acta*, 60(11):1917–1932.

Samson, I., Wood, S., and Finucane, K. (2004). Fluid inclusion characteristics and genesis of the fluorite-parisite mineralization in the Snowbird Deposit, Montana. *Economic Geology*, 99:1727–1744.

Sand, K., Rodriguez-Blanco, J., Makovicky, E., Benning, L., and Stipp, S. L. (2012). Crystallization of CaCO3 in water-alcohol mixtures: Spherulitic growth, polymorph stabilization, and morphology change. *Crystal Growth and Design*, 12(2):842–853.

Sarapaa, O., Ani, T., Lahti, S., Lauri, L., Sarala, P., Torppa, A., and Kontinen, A. (2013). Rare earth exploration potential in Finland. *Journal of Geochemical Exploration*, 133:25–41.

Sarp, H. and Bertrand, J. (1985). Gysinite , Pb(Nd,La)(CO3)2(OH).H2O, a new lead , rare-earth carbonate from Shinkolobwe, Shaba , Zaire and its relationship to ancylite. *American Mineralogist*, 70:1314–1317.

Sastry, R. L. N., Yoganarasimhant, S. R., Mehrotra, P. N., and Rao, C. N. R. (1966). Preparation, characterisation and thermal decomposition of praseodymium, terbium and neodymium carbonates. *Journal of Inorganic Nuclear Chemistry*, 28:1165–1177.

Savel, V., Bazarova, E., and Karmanov, N. (2011). Accessory minerals from the Primorsky Rapakivi Granite Complex, West Baikal Region. *Geology of Ore Deposits*, 53(8):708–722.

Schepers, A. and Milsch, H. (2013). Dissolution-precipitation reactions in hydrothermal experiments with quartz-feldspar aggregates. *Contributions to Mineralogy and Petrology*, 165(1):83–101.

Schijf, J. and Byrne, R. (2004). Determination of SO41 for yttrium and the rare earth elements at I = 0.66 m and t = 25 C - implications for YREE solution speciation in sulfate-rich waters. *Geochimica et Cosmochimica Acta*, 68(13):2825–2837.

Shang, X., Lu, W., Yue, B., Zhang, L., and Ni, J. (2009). Synthesis of three-dimensional hierarchical dendrites of NdOHCO3 via a facile hydrothermal method. *Crystal growth and design*, 9(3):1415–1420.

Shannon, R. (1976). Revised effective ionic radii and systematic studies of interatomic distances in halides and chalcogenides. *Acta Crystallographica Section A*, 32(5):751–767.

Sheard, E., Williams-Jones, A., Heiligmann, M., Pederson, C., and Trueman, D. (2012). Controls on the concentration of zirconium, niobium , and the rare earth elements in the Thor Lake Rare Metal Deposit, Northwest Territories, Canada. *Economic Geology*, 107:81–104.

Shivaramaiah, R., Anderko, A., Riman, R., and Navrotsky, A. (2016). Thermodynamics of bastnaesite: A major rare earth ore mineral. *American Mineralogist*, 101(5):1129–1134.

Sholkovitz, E. (1992). Chemical evolution of rare earth elements: fractionation between colloidal and solution phases of filtered river water. *Earth and Planetary Science Letters*, 114(1):77–84.

Sinha, S., Simas, A., and Moura, G. (2010). Molecular modeling of the octacoordinated tetracarbonato-Nd(III), [Nd(CO3)4]5-, complex and its nonacoordinated fluoro- and aquo-adducts. *Journal of Rare Earths*, 28(6):847–853.

Smirnov, P. and Grechin, O. (2015). Structural parameters of the nearest surrounding of ions in aqueous solutions of erbium chloride according to X-ray diffraction. *Russian Journal of Inorganic Chemistry*, 60(12):1514–1517.

Smirnov, P. and Trostin, V. (2012). Structural parameters of the nearest surrounding of lanthanide ions in aqueous solutions of their salts. *Russian Journal of General Chemistry*, 82(3):360–378.

Smith, M. and Campbell, L. (2000). Fractionation of the REE during hydrothermal processes: Constraints from the Bayan Obo Fe-REE-Nb deposit, Inner Mongolia, China. *Geochimica et Cosmochimica Acta*, 64(18):3141–3160.

Smith, M., Campbell, L., and Kynicky, J. (2015). A review of the genesis of the world class Bayan Obo Fe-REE-Nb deposits, Inner Mongolia, China: Multistage processes and outstanding questions. *Ore Geology Reviews*, 64:459–476.

Smith, M., Henderson, P., and Peisham, Z. (1999). Reaction relationships in the Bayan Obo Fe-REE-Nb deposit Inner Mongolia, China: implications for the relative stability of rare-earth element phosphates and fuorocarbonates. *Contributions to Mineralogy and Petrology*, 134:294–310.

Stepanchikova, S. and Kolonin, G. (2005). Spectrophotometric study of Nd, Sm, and Ho complexation in chloride solutions at 100–250 C. *Russian Journal of Coordination Chemistry*, 31(3):193–202.

Stuart, B. (2004). *Infrared Spectroscopy: fundamentals and applications*. John Wiley and Sons, Ltd.

Tahara, T., Nakai, I., Miyawaki, R., and Matsubara, S. (2007). Crystal chemistry of RE(CO3)OH. *Zeitschrift für Kristallographie*, 222(7):326 – 334.

Tan, T. (2012). *Rare earth nanotechnology*. Pan Stanford Publishing, Singapore.

Tanaka, K., Takahashi, Y., and Shimizu, H. (2008). Local structure of Y and Ho in calcite and its relevance to Y fractionation from Ho in partitioning between calcite and aqueous solution. *Chemical Geology*, 248(1-2):104–113.

Thanh, N., Maclean, N., and Mahiddine, S. (2014). Mechanisms of nucleation and growth of nanoparticles in solution. *Chemical Reviews*, 114(15):7610–7630.

Trofanenko, J., Williams-Jones, A., Simandl, G., and Migdisov, A. (2016). The nature and origin of the REE mineralization in the Wicheeda Carbonatite, British Columbia, Canada. *Economic Geology*, 111(1):199–223.

Trushina, D., Sulyanov, S., Bukreeva, T., and Kovalchuk, M. (2015). Size control and structure features of spherical calcium carbonate particles. *Crystallography Reports*, 60(4):570–577.

Tsuno, H., Kagi, H., Takahashi, Y., Akagi, T., and Nomura, M. (2003). Spontaneously induced reduction of trivalent ytterbium in synthesized crystal of calcite. *Chemistry Letters*, 32(6):500–501.

Tsuno, H., Kagi, H., Takahashi, Y., Akagi, T., and Nomura, M. (2005). XAFS study on the trace amounts of ytterbium ions incorporated in calcium carbonate crystal. *Physica Scripta*, 115:897–900.

Tu, T., Bargarjane, V., Van, T., and Bargar, J. (2006). Er coordination in thin films studied by extended x-ray absorption fine structure Er coordination in Y2O3 thin films studied by extended x-ray absorption fine structure. *Journal of Applied Physics*, 100(023115).

Tunsu, C., Petranikova, M., Gergorić, M., Ekberg, C., and Retegan, T. (2015). Reclaiming rare earth elements from end-of-life products: A review of the perspectives for urban mining using hydrometallurgical unit operations. *Hydrometallurgy*, 156:239–258.

USGS (2016). Mineral Commodity Summaries 2016: Rare Earth Elements. Technical report.

Vallina, B., Rodriguez-Blanco, J., Blanco, J., and Benning, L. (2014). The effect of heating on the morphology of crystalline neodymium hydroxycarbonate, NdCO3OH. *Mineralogical Magazine*, 78(6):1391–1397.

Vallina, B., Rodriguez-Blanco, J., Brown, A., Blanco, J., and Benning, L. (2013). Amorphous dysprosium carbonate: characterization, stability, and crystallization pathways. *Journal of Nanoparticle Research*, 15:1438.

Vallina, B., Rodriguez-Blanco, J., Brown, A., Blanco, J., and Benning, L. (2015). The role of amorphous precursors in the crystallization of La and Nd carbonates. *Nanoscale*, 7(28):12166–12179.

Van, T., Hoang, J., Ostroumov, R., Wang, K., Bargar, J., Lu, J., Blom, H., and Chang, J. (2006). Nanostructure and temperature-dependent photoluminescence of Er-doped Y2O3 thin films for micro-optoelectronic integrated circuits. *Journal of Applied Physics*, 100(073512).

Villa, A., Hess, B., and Saint-martin, H. (2009). Dynamics and structure of Ln (III) - aqua ions : A comparative molecular dynamics study using ab initio based flexible and polarizable model potentials. *Journal of Physical Chemistry B*, 113:7270–7281.

Voigt, M., Rodriguez-Blanco, J., Vallina, B., Benning, L., and Oelkers, E. (2016). An experimental study of hydroxylbastnasite solubility in aqueous solutions at 25 C. *Chemical Geology*, 430:70–77.

Wakita, H. and Nagashima, K. (1972). Synthesis of tengerite type REE carbonates. *Bulletin of the Chemical Society of Japan*, 45(8):2476–2479.

Wallwork, K., Kolitsch, U., Pring, A., and Nasdala, L. (2002). Decrespignyite-(Y), a new copper yttrium rare earth carbonate chloride hydrate from Paratoo, South Australia. *Mineralogical Magazine*, 66(1):181–188.

Walters, A. and Lusty, P. (2011). Rare Earth Elements. Technical Report November, British Geological Survey, Keyworth, Nottingham, U.K.

Wang, L. and Muhammed, M. (1999). Synthesis of zinc oxide nanoparticles with controlled morphology. *Journal of Materials Chemistry*, 9(11):2871–2878.

Wang, X., Zhuang, J., Peng, Q., and Li, Y. (2006). Hydrothermal synthesis of rare-earth fluoride nanocrystals. *Inorganic Chemistry*, 45(17):6661–6665.

Weng, Z., Jowitt, S., Mudd, G., and Haque, N. (2015). A detailed assessment of global rare earth element resources: Opportunities and challenges. *Economic Geology*, 110(8):1925–1952.

Wickleder, M. (2002). Inorganic lanthanide compounds with complex anions. *Chemical Reviews*, 102(6):2011–2088.

Wilkinson, J. J. (2010). A review of fluid inclusion constraints on mineralization in the Irish ore field and implications for the genesis of sediment-hosted Zn-Pb deposits. *Economic Geology*, 105(2):417–442.

Williams-Jones, A., Migdisov, A., and Samson, I. (2012). Hydrothermal Mobilisation of the Rare Earth Elements - a Tale of "Ceria" and "Yttria". *Elements*, 8(5):355–360.

Williams-Jones, A. and Palmer, D. (2002). The evolution of aqueous-carbonic fluids in the Amba Dongar carbonatite, India: implications for fenitisation. *Chemical Geology*, 185:283–301.

Williams-Jones, A., Samson, I., and Olivo, G. (2000). The genesis of hydrothermal fluorite-REE deposits in the Gallinas Mountains, New Mexico. *Economic Geology*, 95:327–342.

Williams-Jones, A. and Wood, S. (1992). A preliminary petrogenetic grid for REE fluorocarbonates and associated minerals. *Geochimica et Cosmochimica Acta*, 56(2):725–738.

Wolterbeek, T., Peach, C., Raoof, A., and Spiers, C. (2016). Reactive transport of CO2-rich fluids in simulated wellbore interfaces: Flow-through experiments on the 1-6m length scale. *International Journal of Greenhouse Gas Control*, 54:96–116.

Wood, S. (1990a). The aqueous geochemistry of the rare-earth elements and yttrium 1. Review of available low-temperature data for inorganic complexes and the inorganic REE speciation of natural waters. *Chemical Geology*, 82:159–186.

Wood, S. (1990b). The aqueous geochemistry of the rare-earth elements and yttrium 2. Theoretical predictions of speciation in hydrothermal solutions to 350 C at saturation water vapor pressure. *Chemical Geology*, 88:99–125.

Xu, C., Campbell, I., Kynicky, J., Allen, C., Chen, Y., Huang, Z., and Qi, L. (2008). Comparison of the Daluxiang and Maoniuping carbonatitic REE deposits with Bayan Obo REE deposit, China. *Lithos*, 106:12–24.

Xu, C., Taylor, R., Li, W., Kynicky, J., Chakhmouradian, A., and Song, W. (2012). Comparison of fluorite geochemistry from REE deposits in the Panxi region and Bayan Obo, China. *Journal of Asian Earth Sciences*, 57:76–89.

Yang, D., Kang, X., Ma, P., Dai, Y., Hou, Z., Cheng, Z., and Li, C. (2013). Hollow structured upconversion luminescent NaYF4:Yb3+, Er3+ nanospheres for cell imaging and targeted anti-cancer drug delivery. *Biomaterials*, 34:1601–1612.

Yang, H., Dembowski, R. F., Conrad, P. G., and Downs, R. T. (2008). Crystal structure and Raman spectrum of hydroxyl-bastnasite-(Ce), CeCO3(OH). *American Mineralogist*, 93(4):698–701.

Yang, X., Lai, X., Pirajno, F., Liu, Y., Mingxing, L., and Sun, W. (2017). Genesis of the Bayan Obo Fe-REE-Nb formation in Inner Mongolia, North China Craton: A perspective review. *Precambrian Research*, 288:39–71.

Zaitsev, A., Yakovenchuk, V., Chao, G., Gault, R., Subbotin, V., Pakhomosky, Y., and Bogdanova, A. (1996). Kukharenkoite-(Ce), Ba2Ce(CO3)3F a new mineral from Kola peninsula, Russia, and Quebec, Canada. *European Journal of Mineralogy*, 8:1327–1336.

Zhang, Y., Gao, M., Han, K., Fang, Z., Yin, X., and Xu, Z. (2009). Synthesis, characterization and formation mechanism of dumbbell-like YOHCO3 and rod-like Y2(CO3)3.2.5H2O. *Journal of Alloys and Compounds*, 474(1-2):598–604.

Zhang, Y., Han, K., Cheng, T., and Fang, Z. (2007). Synthesis, characterization , and photoluminescence property of LaCO3OH microspheres. *Inorganic chemistry*, 46(11):827–831.

Zhang, Y.-X., Zhou, X.-B., Liu, Z.-L., Liu, Q.-Z., Zhu, G.-P., Dai, K., Li, B., Sun, B., Jin, Z., and Li, X.-H. (2015). Green synthesis of monodispersed LaCO3OH micro-gears with novel plum blossom-like structure via a glycerol-mediated solvothermal method. *RSC Advances*, 5(28):21925–21930.

Zhao, D., Yang, Q., Han, Z., Zhou, J., Xu, S., and Sun, F. (2008). Biomolecule-assisted synthesis of rare earth hydroxycarbonates. *Solid State Sciences*, 10:31–39.

Zhou, L., Yang, J., Hu, S., Luo, Y., and Yang, J. (2015). Synthesis of 3D hierarchical architectures of Tb2(CO3)3: Eu3+ phosphor and its efficient energy transfer from Tb3+ to Eu3+. *Journal of Materials Science*, 50(13):4503–4515.

Appendix A

The full suite of EMPA results from Chapter 7 are presented in the following pages.

Sample	**90/19-1**	**90/19-2**	**90/19-3**	**90/19-5**	**90/19-6**	**90/19-7**
F	6.11	6.20	6.47	6.34	6.30	6.24
MgO	bdl	bdl	bdl	bdl	bdl	bdl
P_2O_5	na	na	na	na	na	na
SiO_2	na	na	na	na	na	na
SO_2	na	na	na	na	na	na
Cao	0.11	0.10	0.22	0.07	0.06	0.05
MnO	na	na	na	na	na	na
FeO	na	na	na	na	na	na
SrO	na	na	na	na	na	na
Y_2O_3	0.23	0.20	0.21	0.17	0.15	0.13
BaO	na	na	na	na	na	na
La_2O_3	24.12	23.93	24.51	24.86	24.20	23.97
Ce_2O_3	33.49	33.96	34.16	34.02	34.31	34.13
Pr_2O_3	2.70	2.75	2.66	2.64	2.70	2.76
Nd_2O_3	8.39	8.72	8.25	8.13	8.54	8.58
Sm_2O_3	0.40	0.43	0.35	0.34	0.43	0.47
Eu_2O_3	bdl	bdl	bdl	bdl	bdl	bdl
Gd_2O_3	3.09	3.09	2.98	3.07	3.10	3.09
Tb_2O_3	bdl	bdl	bdl	bdl	bdl	bdl
Dy_2O_3	bdl	bdl	bdl			bdl
Er_2O_3	bdl	bdl	bdl	bdl	bdl	bdl
Yb_2O_3	bdl	bdl	bdl	bdl	bdl	
ThO_2	na	na	na	na	na	na
Total	78.64	79.38	79.81	79.72	79.88	79.42
O≡F	2.57	2.61	2.72	2.67	2.65	2.63
Total	76.07	76.77	77.09	77.05	77.23	76.79
$\sum REE_2O_3$	72.42	73.08	73.32	73.32	73.52	73.55

Table A1: EMPA analyses (weight %) of bastnäsite in sample 90/19 from Bayan Obo

Sample	**90/19-8**	**90/19-9**	**90/19-11**	**90/19-12**	**90/19-13**	**90/19-31**
F	6.12	6.40	6.48	6.45	6.25	6.35
MgO	bdl	bdl	bdl	bdl	bdl	bdl
P_2O_5	na	na	na	na	na	na
SiO_2	na	na	na	na	na	na
SO_2	na	na	na	na	na	na
Cao	0.57	0.10	0.08	0.05	0.22	0.20
MnO	na	na	na	na	na	na
FeO	na	na	na	na	na	na
SrO	na	na	na	na	na	na
Y_2O_3	0.14	0.17	0.26	0.17	0.12	0.17
BaO	na	na	na	na	na	na
La_2O_3	24.91	25.43	23.88	23.59	25.13	23.49
Ce_2O_3	33.96	33.99	34.25	34.88	34.29	32.84
Pr_2O_3	2.72	2.62	2.74	2.83	2.72	2.75
Nd_2O_3	8.39	8.26	8.72	9.05	8.17	8.29
Sm_2O_3	0.33	0.41	0.45	0.51	0.42	0.39
Eu_2O_3	bdl	bdl	bdl	bdl	bdl	bdl
Gd_2O_3	3.10	3.09	3.14	3.13	3.12	3.10
Tb_2O_3	bdl	bdl	bdl	bdl	bdl	bdl
Dy_2O_3	bdl	bdl	bdl	bdl	bdl	bdl
Er_2O_3	bdl	bdl	bdl	bdl	bdl	bdl
Yb_2O_3	bdl	bdl	bdl	bdl	bdl	bdl
ThO_2	na	na	na	na	na	na
Total	80.34	80.47	79.98	80.65	80.45	77.66
O≡F	2.62	2.70	2.73	2.71	2.63	2.67
Total	77.72	77.77	77.25	77.93	77.82	74.99
$\sum REE_2O_3$	73.55	73.97	73.42	74.15	73.98	71.11

Table A1: *continued.*

Sample	**90/19-32**	**90/19-33**	**90/19-34**	**90/19-35**
F	4.60	6.28	6.07	6.05
MgO	0.03	bdl	bdl	bdl
P_2O_5	na	na	na	na
SiO_2	na	na	na	na
SO_2	na	na	na	na
Cao	0.22	0.89	0.44	0.24
MnO	na	na	na	na
FeO	na	na	na	na
SrO	na	na	na	na
Y_2O_3	0.19	0.14	0.15	0.13
BaO	na	na	na	na
La_2O_3	23.14	23.68	23.68	23.32
Ce_2O_3	32.50	32.10	32.74	32.82
Pr_2O_3	2.52	2.66	2.71	2.75
Nd_2O_3	7.90	8.11	8.17	8.24
Sm_2O_3	0.39	0.42	0.37	0.40
Eu_2O_3	bdl	bdl	bdl	bdl
Gd_2O_3	2.82	3.08	309	3.08
Tb_2O_3	bdl	bdl	bdl	bdl
Dy_2O_3	bdl	bdl	bdl	bdl
Er_2O_3	bdl	bdl	bdl	bdl
Yb_2O_3	bdl	bdl	bdl	bdl
ThO_2	na	na	na	na
Total	74.29	78.35	77.43	77.03
O≡F	1.94	2.65	2.56	2.55
Total	72.36	75.71	74.87	74.48
$\sum REE_2O_3$	69.45	71.18	70.92	70.74

Table A1: *continued.*

Sample	**90/19-4**	**90/19-14**	**90/19-15**	**90/19-16**	**90/19-17**	**90/19-18**
F	na	na	na	na	na	na
MgO	na	na	na	na	na	na
P_2O_5	29.27	29.55	29.38	29.57	29.47	29.59
SiO_2	0.06	0.06	bdl	bdl	bdl	bdl
SO_2	na	na	na	na	na	na
Cao	0.16	0.17	0.83	0.46	0.18	0.48
MnO	na	na	na	na	na	na
FeO	na	na	na	na	na	na
SrO	na	na	na	na	na	na
Y_2O_3	0.18	0.12	0.14	0.019	0.17	0.09
BaO	na	na	na	na	na	na
La_2O_3	22.17	21.40	20.64	22.68	21.09	22.91
Ce_2O_3	34.16	35.21	35.15	34.87	35.70	34.90
Pr_2O_3	2.87	3.00	3.01	2.89	3.01	2.86
Nd_2O_3	9.09	9.29	9.85	8.74	9.22	8.49
Sm_2O_3	0.55	0.48	0.60	0.42	0.49	0.35
Eu_2O_3	bdl	bdl	bdl	bdl	bdl	bdl
Gd_2O_3	3.08	3.14	3.14	3.04	3.15	3.04
Tb_2O_3	bdl	bdl	bdl	bdl	bdl	bdl
Dy_2O_3	bdl	bdl	0.09	bdl	0.10	bdl
Er_2O_3	bdl	bdl	bdl	bdl	bdl	bdl
Yb_2O_3	bdl	bdl	bdl	bdl	bdl	bdl
ThO_2	0.21	0.26	0.24	bdl	bdl	bdl
Total	101.79	102.68	103.08	102.76	102.57	102.70

Table A2: EMPA analyses (weight %) of monazite in sample 90/19 from Bayan Obo

Sample	**90/19-19**	**90/19-20**	**90/19-23**	**90/19-24**	**90/19-37**
F	na	na	na	na	na
MgO	na	na	na	na	na
P_2O_5	29.61	29.43	29.34	29.38	29.43
SiO_2	bdl	0.06	0.06	0.05	bdl
SO_2	na	na	na	na	na
Cao	1.08	0.24	0.11	0.08	0.67
MnO	na	na	na	na	na
FeO	na	na	na	na	na
SrO	na	na	na	na	na
Y_2O_3	0.12	0.10	0.12	0.22	0.14
BaO	na	na	na	na	na
La_2O_3	24.41	21.22	18.77	18.72	18.91
Ce_2O_3	35.12	35.23	34.03	33.91	33.39
Pr_2O_3	2.98	3.04	3.15	3.15	3.12
Nd_2O_3	9.38	9.52	9.76	9.93	9.94
Sm_2O_3	0.50	0.55	0.55	0.57	0.61
Eu_2O_3	bdl	bdl	na	na	na
Gd_2O_3	3.13	3.09	3.15	3.17	3.15
Tb_2O_3	bdl	bdl	bdl	bdl	bdl
Dy_2O_3	bdl	0.11	0.10	0.12	0.11
Er_2O_3	bdl	bdl	bdl	bdl	bdl
Yb_2O_3	bdl	bdl	bdl	bdl	bdl
ThO_2	0.27	0.17	0.18	bdl	bdl
Total	103.59	102.77	99.32	99.31	99.46

Table A2: *continued.*

Sample	**88/165-1**	**88/165-2**	**88/165-3**	**88/165-4**	**88/165-11**
F	2.35	2.36	2.19	2.64	2.18
MgO	bdl	bdl	bdl	bdl	bdl
P_2O_5	na	na	na	na	na
SiO_2	na	na	na	na	na
SO_2	na	na	na	na	na
Cao	0.97	0.83	0.51	5.00	0.38
MnO	na	na	na	na	na
FeO	na	na	na	na	na
SrO	na	na	na	na	na
Y_2O_3	0.09	0.08	0.08	0.13	0.09
BaO	36.25	36.92	40.12	40.27	40.37
La_2O_3	7.07	7.14	7.73	5.82	5.83
Ce_2O_3	17.01	17.02	16.58	15.78	15.76
Pr_2O_3	na	na	na	na	na
Nd_2O_3	5.28	5.34	4.23	4.89	5.62
Sm_2O_3	0.26	0.23	0.23	0.24	0.30
Eu_2O_3	na	na	na	na	na
Gd_2O_3	1.59	1.61	1.52	1.42	1.46
Tb_2O_3	bdl	bdl	bdl	bdl	bdl
Dy_2O_3	bdl	bdl	bdl	bdl	bdl
Er_2O_3	bdl	bdl	0.07	bdl	bdl
Yb_2O_3	bdl	bdl	bdl	bdl	bdl
ThO_2	na	na	na	na	na
Total	70.85	71.53	73.25	76.20	72.00
O≡F	0.99	0.99	0.92	1.11	0.92
Total	69.86	70.54	72.33	75.09	71.08
$\sum REE_2O_3$	31.28	31.42	30.43	28.29	29.07

Table A3: EMPA analyses (weight %) of Ba-REE fluorocarbonates in sample 88/165 from Bayan Obo

Sample	**88/165-12**	**88/165-13**	**88/165-14**
F	2.28	2.44	2.29
MgO	bdl	bdl	bdl
P_2O_5	na	na	na
SiO_2	na	na	na
SO_2	na	na	na
Cao	0.52	0.66	0.48
MnO	na	na	na
FeO	na	na	na
SrO	na	na	na
Y_2O_3	0.09	0.10	0.09
BaO	40.94	36.72	38.10
La_2O_3	5.77	6.34	6.26
Ce_2O_3	15.52	16.18	16.13
Pr_2O_3	na	na	na
Nd_2O_3	5.67	5.90	6.20
Sm_2O_3	0.30	0.32	0.35
Eu_2O_3	na	na	na
Gd_2O_3	1.48	1.55	1.56
Tb_2O_3	bdl	bdl	bdl
Dy_2O_3	bdl	bdl	bdl
Er_2O_3	bdl	bdl	bdl
Yb_2O_3	bdl	bdl	bdl
ThO_2	na	na	na
Total	72.57	70.22	71.45
O≡F	0.96	1.03	0.97
Total	71.61	69.19	70.49
$\sum REE_2O_3$	28.83	30.39	30.59

Table A3: *continued.*

Sample	**88/165-15**	**88/165-16**	**88/165-17**	**88/165-18**	**88/165-19**
F	3.59	2.89	3.93	3.48	3.88
MgO	na	na	na	na	na
P_2O_5	39.84	38.66	37.88	39.09	41.06
SiO_2	na	na	na	na	na
SO_2	na	na	na	na	na
Cao	51.80	47.94	50.12	50.82	52.43
MnO	0.09	0.11	0.10	0.08	0.06
FeO	0.14	0.07	bdl	0.05	0.04
SrO	0.50	0.50	0.40	0.20	0.09
Y_2O_3	0.29	0.50	0.40	0.35	0.24
BaO	na	na	na	na	na
La_2O_3	0.23	0.48	0.31	0.28	0.19
Ce_2O_3	0.96	2.24	1.54	1.47	0.82
Pr_2O_3	bdl	0.39	0.21	bdl	bdl
Nd_2O_3	0.87	1.84	1.20	1.11	0.56
Sm_2O_3	0.13	0.27	0.20	0.17	0.12
Eu_2O_3	na	na	na	na	na
Gd_2O_3	0.24	0.42	0.30	0.27	0.19
Tb_2O_3	na	na	na	na	na
Dy_2O_3	bdl	bdl	bdl	bdl	bdl
Er_2O_3	bdl	bdl	bdl	bdl	bdl
Yb_2O_3	bdl	bdl	bdl	bdl	bdl
ThO_2	na	na	na	na	na
Total	98.69	96.31	96.58	97.36	99.69
O≡F	1.51	1.22	1.65	1.46	1.63
Total	97.17	95.09	94.93	95.89	98.06
$\sum REE_2O_3$	2.72	6.13	4.15	3.64	3.81

Table A4: EMPA analyses (weight %) of apatite in sample 88/165 from Bayan Obo

Sample	**88/165-20**	**88/165-21**	**88/165-22**	**88/165-23**	**88/165-24**
F	3.63	3.52	3.63	4.10	3.42
MgO	na	na	na	na	na
P_2O_5	39.28	41.21	43.41	41.11	40.92
SiO_2	na	na	na	na	na
SO_2	na	na	na	na	na
Cao	50.32	55.97	55.21	54.25	52.39
MnO	0.09	bdl	0.08	bdl	0.10
FeO	0.18	0.10	0.16	0.09	0.15
SrO	0.22	0.06	0.33	0.06	0.48
Y_2O_3	0.34	bdl	0.29	0.06	0.24
BaO	na	na	na	na	na
La_2O_3	0.30	bdl	0.12	bdl	0.12
Ce_2O_3	1.54	0.09	0.70	0.18	0.70
Pr_2O_3	bdl	bdl	bdl	bdl	bdl
Nd_2O_3	1.18	bdl	0.62	bdl	0.60
Sm_2O_3	0.17	bdl	0.13	bdl	0.11
Eu_2O_3	na	na	na	na	na
Gd_2O_3	0.27	bdl	0.17	bdl	0.15
Tb_2O_3	na	na	na	na	na
Dy_2O_3	bdl	bdl	bdl	bdl	bdl
Er_2O_3	bdl	bdl	bdl	bdl	bdl
Yb_2O_3	bdl	bdl	bdl	bdl	bdl
ThO_2	na	na	na	na	na
Total	97.53	100.95	104.85	99.86	99.38
O≡F	1.53	1.48	1.53	1.73	1.44
Total	96.01	99.47	103.32	98.13	97.94
$\sum REE_2O_3$	3.81	0.09	2.02	0.24	1.93

Table A4: *continued.*

Sample	**4905-1**	**4905-2**	**4905-3**	**4905-4**	**4905-5**
F	4.31	4.23	4.39	4.39	4.46
MgO	bdl	bdl	bdl	bdl	bdl
P_2O_5	na	na	na	na	na
SiO_2	na	na	na	na	na
SO_2	na	na	na	na	na
Cao	16.94	16.73	17.00	16.88	16.91
MnO	na	na	na	na	na
FeO	na	na	na	na	na
SrO	na	na	na	na	na
Y_2O_3	0.27	0.31	0.41	0.35	0.37
BaO	na	na	na	na	na
La_2O_3	13.12	13.07	13.21	14.31	14.46
Ce_2O_3	24.22	24.28	23.71	24.28	23.99
Pr_2O_3	2.39	2.31	2.35	2.25	2.21
Nd_2O_3	7.90	7.78	7.91	6.90	7.07
Sm_2O_3	0.80	0.73	0.90	0.62	0.77
Eu_2O_3	0.09	bdl	0.08	bdl	0.10
Gd_2O_3	2.58	2.53	2.66	2.54	2.60
Tb_2O_3	bdl	bdl	bdl	bdl	bdl
Dy_2O_3	0.15	0.18	0.18	0.12	0.13
Er_2O_3	0.09	bdl	bdl	bdl	bdl
Yb_2O_3	bdl	bdl	bdl	bdl	bdl
ThO_2	na	na	na	na	na
Total	72.88	72.13	72.90	72.63	73.06
O≡F	1.82	1.78	1.85	1.85	1.88
Total	71.06	70.36	71.05	70.78	71.19
$\sum REE_2O_3$	51.63	51.18	51.51	51.36	51.70

Table A5: EMPA analyses (weight %) of synchysite in sample 4905 from Tundulu

Sample	**4905-6**	**4905-7**	**4905-8**	**4905-14**	**4905-15**
F					
MgO	bdl	bdl	bdl	bdl	bdl
P_2O_5	na	na	na	na	na
SiO_2	na	na	na	na	na
SO_2	na	na	na	na	na
Cao	17.16	16.77	17.10	16.45	16.76
MnO	na	na	na	na	na
FeO	na	na	na	na	na
SrO	na	na	na	na	na
Y_2O_3	0.15	0.31	0.36	0.52	0.40
BaO	na	na	na	na	na
La_2O_3	13.08	15.32	14.06	14.00	14.49
Ce_2O_3	25.91	24.74	24.6	24.33	22.78
Pr_2O_3	2.42	2.09	2.26	2.35	2.17
Nd_2O_3	7.09	6.31	7.07	7.33	7.28
Sm_2O_3	0.45	0.57	0.64	0.55	0.84
Eu_2O_3	bdl	bdl	bdl	na	na
Gd_2O_3	2.42	2.54	2.55	2.62	2.74
Tb_2O_3	bdl	0.08	bdl	bdl	bdl
Dy_2O_3	bdl	0.16	0.16	0.09	0.15
Er_2O_3	bdl	bdl	bdl	0.08	0.07
Yb_2O_3	bdl	bdl	bdl	bdl	bdl
ThO_2	na	na	na	na	na
Total	73.11	73.40	73.39	72.03	71.63
O≡F	1.86	1.90	1.90	1.55	1.67
Total	71.24	71.50	71.48	70.47	69.96
$\sum REE_2O_3$	51.52	52.14	51.77	51.89	50.96

Table A5: *continued.*

Sample	**4905-16**	**4905-18**	**4905-20**
F	3.74	3.87	3.86
MgO	bdl	bdl	bdl
P_2O_5	na	na	na
SiO_2	na	na	na
SO_2	na	na	na
Cao	16.45	17.09	17.02
MnO	na	na	na
FeO	na	na	na
SrO	na	na	na
Y_2O_3	0.28	0.36	0.25
BaO	na	na	na
La_2O_3	13.24	12.00	12.87
Ce_2O_3	24.74	23.31	24.35
Pr_2O_3	2.43	2.55	2.50
Nd_2O_3	7.87	8.98	8.17
Sm_2O_3	0.69	1.07	0.67
Eu_2O_3	na	na	na
Gd_2O_3	2.66	2.86	2.68
Tb_2O_3	bdl	bdl	bdl
Dy_2O_3	0.16	0.18	0.10
Er_2O_3	0.10	bdl	0.07
Yb_2O_3	bdl	bdl	bdl
ThO_2	na	na	na
Total	72.37	72.26	72.53
O≡F	1.58	1.63	1.62
Total	70.79	70.64	70.91
$\sum REE_2O_3$	52.17	52.17	51.66

Table A5: *continued.*

Sample	**278-3**	**278-4-2**	**278-18**	**278-19**	**278-20**
F	4.40	4.47	3.74	3.89	4.01
MgO	bdl	bdl	bdl	bdl	bdl
P_2O_5	na	na	na	na	na
SiO_2	na	na	na	na	na
SO_2	na	na	na	na	na
Cao	16.63	16.57	17.24	16.64	16.17
MnO	na	na	na	na	na
FeO	na	na	na	na	na
SrO	na	na	na	na	na
Y_2O_3	0.16	0.17	0.44	0.31	0.32
BaO	na	na	na	na	na
La_2O_3	16.36	15.94	13.42	15.35	14.99
Ce_2O_3	24.24	25.07	21.64	22.21	22.25
Pr_2O_3	2.05	2.02	2.50	2.12	2.15
Nd_2O_3	6.02	5.74	9.21	7.53	7.65
Sm_2O_3	0.48	0.28	1.07	0.91	1.05
Eu_2O_3	bdl	bdl	na	na	na
Gd_2O_3	2.46	2.44	2.90	2.78	2.94
Tb_2O_3	bdl	bdl	0.08	0bdl	bdl
Dy_2O_3	0.08	bdl	0.21	0.22	0.19
Er_2O_3	bdl	bdl	bdl	bdl	0.09
Yb_2O_3	bdl	bdl	bdl	bdl	bdl
ThO_2	na	na	na	na	na
Total	72.87	72.70	72.46	71.96	71.80
O≡F	1.85	1.88	1.58	1.64	1.69
Total	71.02	70.82	70.89	70.32	70.11
$\sum REE_2O_3$	51.84	51.66	51.47	51.43	51.62

Table A6: EMPA analyses (weight %) of synchysite in sample 278 from Tundulu

Sample	**278-30**	**278-31**	**278-32**	**278-33**
F	3.77	3.85	3.85	3.70
MgO	bdl	bdl	bdl	bdl
P_2O_5	na	na	na	na
SiO_2	na	na	na	na
SO_2	na	na	na	na
Cao	16.88	17.38	17.38	17.17
MnO	na	na	na	na
FeO	na	na	na	na
SrO	na	na	na	na
Y_2O_3	0.14	0.14	0.14	0.64
BaO	na	na	na	na
La_2O_3	14.54	14.17	15.08	12.97
Ce_2O_3	23.92	24.36	24.12	22.50
Pr_2O_3	2.26	2.31	2.22	2.45
Nd_2O_3	6.92	7.21	6.89	9.14
Sm_2O_3	0.53	0.63	0.60	1.16
Eu_2O_3	na	na	na	na
Gd_2O_3	2.66	2.66	2.62	3.00
Tb_2O_3	bdl	bdl	bdl	bdl
Dy_2O_3	bdl	bdl	bdl	bdl
Er_2O_3	bdl	bdl	bdl	bdl
Yb_2O_3	bdl	bdl	bdl	bdl
ThO_2	na	na	na	na
Total	71.62	72.71	72.88	73.24
O≡F	1.59	1.62	1.62	1.56
Total	70.03	71.1	71.10	71.68
$\sum REE_2O_3$	50.97	51.49	51.49	52.38

Table A6: *continued.*

Sample	**4905-21**	**4905-22**	**4905-23**	**4905-24**	**4905-25**
F	4.14	3.58	3.64	3.40	3.42
MgO	na	na	na	na	na
P_2O_5	39.81	38.60	38.88	40.72	35.71
SiO_2	na	na	na	na	na
SO_2	na	na	na	na	na
Cao	53.01	52.95	51.12	53.78	49.08
MnO	0.07	bdl	bdl	bdl	bdl
FeO	0.12	0.24	0.19	0.07	0.66
SrO	0.81	0.89	0.85	0.64	0.92
Y_2O_3	0.52	0.55	0.49	0.57	0.37
BaO	na	na	na	na	na
La_2O_3	0.34	0.23	0.41	0.34	0.51
Ce_2O_3	0.96	0.64	1.06	0.99	1.08
Pr_2O_3	bdl	bdl	bdl	bdl	bdl
Nd_2O_3	0.64	0.38	0.66	0.67	0.53
Sm_2O_3	bdl	bdl	bdl	bdl	bdl
Eu_2O_3	na	na	na	na	na
Gd_2O_3	0.19	0.13	0.19	0.19	0.18
Tb_2O_3	na	na	na	na	na
Dy_2O_3	bdl	bdl	bdl	bdl	bdl
Er_2O_3	bdl	bdl	bdl	bdl	bdl
Yb_2O_3	bdl	bdl	bdl	bdl	bdl
ThO_2	na	na	na	na	na
Total	100.61	98.18	97.49	101.37	92.46
O≡F	1.74	1.51	1.53	1.43	1.44
Total	98.86	96.68	95.96	99.94	91.02
$\sum REE_2O_3$	2.66	1.93	2.81	2.76	2.67

Table A7: EMPA analyses (weight %) of apatite in sample 4905 from Tundulu

Sample	**4905-26**	**4905-27**	**4905-28**	**4905-29**	**4905-30**
F	3.29	3.99	3.86	4.04	3.83
MgO	na	na	na	na	na
P_2O_5					
SiO_2	na	na	na	na	na
SO_2	na	na	na	na	na
Cao	50.59	52.81	51.24	51.58	51.08
MnO	0.12	bdl	bdl	bdl	bdl
FeO	1.42	bdl	0.11	0.05	0.04
SrO	1.07	1.39	1.14	1.22	1.28
Y_2O_3	0.33	0.35	0.37	0.26	0.55
BaO	na	na	na	na	na
La_2O_3	0.42	0.20	0.47	0.60	0.29
Ce_2O_3	0.88	0.39	1.04	1.10	0.72
Pr_2O_3	bdl	bdl	bdl	bdl	bdl
Nd_2O_3	0.42	0.19	0.52	0.41	0.49
Sm_2O_3	bdl	bdl	bdl	bdl	bdl
Eu_2O_3	ns	na	na	na	na
Gd_2O_3	0.16	bdl	0.17	0.18	0.17
Tb_2O_3	na	na	na	na	na
Dy_2O_3	bdl	bdl	bdl	bdl	bdl
Er_2O_3	bdl	bdl	bdl	bdl	bdl
Yb_2O_3	bdl	bdl	bdl	bdl	bdl
ThO_2	na	na	na	na	na
Total	96.26	99.92	96.99	97.70	96.79
O≡F	1.38	1.68	1.62	1.70	1.61
Total	94.87	98.24	95.37	96.00	95.18
$\sum REE_2O_3$	2.21	1.13	2.57	2.56	2.22

Table A7: *continued.*

Sample	**278-21**	**278-22**	**278-23**	**278-24**	**278-25**
F	3.72	3.38	3.83	3.52	3.76
MgO	na	na	na	na	na
P_2O_5	38.87	39.29	38.42	38.03	38.35
SiO_2	na	na	na	na	na
SO_2	na	na	na	na	na
Cao	52.22	51.76	52.53	52.17	52.52
MnO	bdl	0.04	0.08	0.07	0.11
FeO	0.08	bdl	0.09	0.07	0.25
SrO	0.85	0.66	1.29	1.02	1.34
Y_2O_3	0.57	0.64	0.33	0.43	0.22
BaO	na	na	na	na	na
La_2O_3	0.36	0.31	0.37	0.36	0.31
Ce_2O_3	0.87	0.92	0.72	0.86	0.56
Pr_2O_3	bdl	bdl	bdl	bdl	bdl
Nd_2O_3	0.58	0.63	0.38	0.55	0.30
Sm_2O_3	0.15	bdl	bdl	bdl	bdl
Eu_2O_3	na	na	na	na	na
Gd_2O_3	0.20	0.21	0.15	0.19	0.12
Tb_2O_3	na	na	na	na	na
Dy_2O_3	bdl	bdl	bdl	bdl	bdl
Er_2O_3	bdl	bdl	bdl	bdl	bdl
Yb_2O_3	bdl	bdl	bdl	bdl	bdl
ThO_2	na	na	na	na	na
Total	98.46	97.84	98.19	97.27	97.83
O≡F	1.57	1.42	1.61	1.48	1.58
Total	96.90	96.42	96.57	95.79	96.25
$\sum REE_2O_3$	2.73	2.72	1.94	2.40	1.51

Table A8: EMPA analyses (weight %) of apatite in sample 278 from Tundulu

Sample	**278-26**	**278-27**	**278-28**	**278-29**
F	4.06	3.90	3.66	3.64
MgO	na	na	na	na
P_2O_5	39.96	38.64	37.47	37.70
SiO_2	na	na	na	na
SO_2	na	na	na	na
Cao	52.12	52.75	51.44	51.89
MnO	bdl	bdl	0.06	bdl
FeO	0.06	0.07	0.21	bdl
SrO	0.71	0.83	0.94	0.84
Y_2O_3	0.66	0.50	0.54	0.54
BaO	na	na	na	na
La_2O_3	0.31	0.36	0.43	0.38
Ce_2O_3	0.85	0.87	1.03	0.96
Pr_2O_3	bdl	bdl	bdl	bdl
Nd_2O_3	0.67	0.65	0.59	0.61
Sm_2O_3	0.18	bdl	bdl	bdl
Eu_2O_3	na	na	na	na
Gd_2O_3	0.20			
Tb_2O_3	na	na	na	na
Dy_2O_3	bdl	bdl	bdl	bdl
Er_2O_3	bdl	bdl	bdl	bdl
Yb_2O_3	bdl	bdl	bdl	bdl
ThO_2	na	na	na	na
Total	99.79	98.75	96.57	96.75
O≡F	1.71	1.64	1.54	1.53
Total	98.08	97.11	95.02	95.21
$\sum REE_2O_3$	2.87	2.58	2.79	2.68

Table A8: *continued.*

Sample	**4905-11**	**4905-12**	**4905-13**	**4905-17**	**4905-19**
F	na	na	na	na	na
MgO	14.47	15.07	15.41	15.08	14.73
P_2O_5	na	na	na	na	na
SiO_2	na	na	na	na	na
SO_2	na	na	na	na	na
Cao	33.23	33.32	32.87	33.80	33.28
MnO	1.04	0.86	0.77	1.00	1.17
FeO	3.92	3.56	3.72	4.25	4.87
SrO	na	na	na	na	na
Y_2O_3	bdl	bdl	bdl	bdl	bdl
BaO	na	na	na	na	na
La_2O_3	bdl	bdl	bdl	0.05	
Ce_2O_3	bdl	0.04	0.05	0.12	0.05
Pr_2O_3	bdl	bdl	bdl	bdl	bdl
Nd_2O_3	bdl	bdl	bdl	bdl	bdl
Sm_2O_3	bdl	bdl	bdl	bdl	bdl
Eu_2O_3	na	na	na	na	na
Gd_2O_3	bdl	bdl	bdl	bdl	bdl
Tb_2O_3	na	na	na	na	na
Dy_2O_3	bdl	bdl	bdl	bdl	bdl
Er_2O_3	bdl	bdl	bdl	bdl	bdl
Yb_2O_3	bdl	bdl	bdl	bdl	bdl
ThO_2	na	na	na	na	na
Total	52.66	52.85	52.82	54.30	54.10
$\sum REE_2O_3$	bdl	0.04	0.0.5	0.09	0.05

Table A9: EMPA analyses (weight %) of dolomite in sample 4905 from Tundulu

Sample	**278-6**	**4278-7**	**278-8**	**278-9**	**278-10**	**278-11**
F	na	na	na	na	na	na
MgO	1.43	1.72	1.92	2.32	2.49	3.08
P_2O_5	na	na	na	na	na	na
SiO_2	na	na	na	na	na	na
SO_2	na	na	na	na	na	na
Cao	49.93	55.05	55.09	53.49	53.25	5416
MnO	0.44	0.06	bdl	bdl	bdl	bdl
FeO	2.72	0.88	0.22	bdl	bdl	bdl
SrO	na	na	na	na	na	na
Y_2O_3	bdl	bdl	bdl	bdl	bdl	bdl
BaO	na	na	na	na	na	na
La_2O_3	0.10	bdl	bdl	0.14	0.35	bdl
Ce_2O_3	bdl	bdl	bdl	0.30	0.07	0.04
Pr_2O_3	bdl	bdl	bdl	bdl	bdl	bdl
Nd_2O_3	bdl	bdl	bdl	0.12	0.11	bdl
Sm_2O_3	bdl	bdl	bdl	bdl	bdl	bdl
Eu_2O_3	na	na	na	na	na	na
Gd_2O_3	bdl	bdl	bdl	bdl	bdl	bdl
Tb_2O_3	na	na	na	na	na	na
Dy_2O_3	bdl	bdl	bdl	bdl	bdl	bdl
Er_2O_3	bdl	bdl	bdl	bdl	bdl	bdl
Yb_2O_3	bdl	bdl	bdl	bdl	bdl	bdl
ThO_2	na	na	na	na	na	na
Total	54.63	57.70	57.23	56.38	56.26	57.29
$\sum REE_2O_3$	0.10	bdl	bdl	0.17	0.18	0.04

Table A10: EMPA analyses (weight %) of calcite in sample 278 from Tundulu

Sample	**278-12**	**278-13**	**278-14**	**278-15**	**278-16**
F	na	na	na	na	na
MgO	2.68	2.16	2.51	2.68	1.67
P_2O_5	na	na	na	na	na
SiO_2	na	na	na	na	na
SO_2	na	na	na	na	na
Cao	54.68	51.11	53.10	51.30	54.57
MnO	bdl	bdl	bdl	0.20	0.10
FeO	bdl	bdl	bdl	bdl	0.51
SrO	na	na	na	na	na
Y_2O_3	0.02	bdl	bdl	bdl	bdl
BaO	na	na	na	na	na
La_2O_3	bdl	0.41	bdl	0.13	bdl
Ce_2O_3	bdl	0.95	0.05	0.06	0.05
Pr_2O_3	bdl	bdl	bdl	bdl	bdl
Nd_2O_3	bdl	0.25	bdl	bdl	bdl
Sm_2O_3	bdl	bdl	bdl	bdl	bdl
Eu_2O_3	na	na	na	na	na
Gd_2O_3	bdl	bdl	bdl	bdl	bdl
Tb_2O_3	na	na	na	na	na
Dy_2O_3	bdl	bdl	bdl	bdl	bdl
Er_2O_3	bdl	bdl	bdl	bdl	bdl
Yb_2O_3	bdl	bdl	bdl	bdl	bdl
ThO_2	na	na	na	na	na
Total	57.37	54.88	55.66	54.36	56.90
$\sum REE_2O_3$	0.02	0.54	0.05	0.10	0.05

Table A10: *continued.*